

Computational Approach to Electron Charge Transfer Reactions

Jónsson, Elvar Örn; Jacobsen, Karsten Wedel; Thygesen, Kristian Sommer; Ulstrup, Jens

Publication date:
2013

Document Version
Publisher's PDF, also known as Version of record

[Link back to DTU Orbit](#)

Citation (APA):

Jónsson, E. Ö., Jacobsen, K. W., Thygesen, K. S., & Ulstrup, J. (2013). Computational Approach to Electron Charge Transfer Reactions. Department of Physics, Technical University of Denmark.

DTU Library

Technical Information Center of Denmark

General rights

Copyright and moral rights for the publications made accessible in the public portal are retained by the authors and/or other copyright owners and it is a condition of accessing publications that users recognise and abide by the legal requirements associated with these rights.

- Users may download and print one copy of any publication from the public portal for the purpose of private study or research.
- You may not further distribute the material or use it for any profit-making activity or commercial gain
- You may freely distribute the URL identifying the publication in the public portal

If you believe that this document breaches copyright please contact us providing details, and we will remove access to the work immediately and investigate your claim.

COMPUTATIONAL APPROACH TO ELECTRON CHARGE
TRANSFER REACTIONS

ELVAR ÖRN JÓNSSON

PhD Thesis

Center for Atomic-scale Material Design
Department of Physics
Technical University of Denmark

PREFACE

This thesis is submitted in the candidacy for the Ph.D degree from the Technical University of Denmark (DTU). The work was carried out in the period from September 2010 to February 2014 at the Center for Atomic-scale Material Design (CAMD), Department of Physics, DTU, under the supervision of Professor Karsten W. Jacobsen, Professor Kristian S. Thygesen and Professor Jens Ulstrup.

First and foremost I would like to express my gratitude to my supervisors for the opportunity to work on this Ph.D project - the wide variety of methods and topics addressed has left this particular student feeling confident in his abilities to tackle a vast range of complex problems. The discussion during meetings - although sometimes mildly off topic - were always interesting and a major source of inspiration. Their support and understanding during trying times were admirable, to say the least.

I would also like to thank Marianne Ærsø, Ole H. Nielsen and Marcin Dulak of CAMD for their always positive and helpful attitude towards the range of issues I brought to their attention. Without administration and IT I would be truly lost.

The research, discussions, implementations, debugging, lunches, more debugging and general shenanigans were made so much more enjoyable with by Asmus O. Dohn. Thank you for 'ze' good times! And to my new and former office mates, in particular Kristian B. Ørnso, for the always interesting discussions on research, travel and other non-physics related topics. Oh, and the proofreading was nice as well.

To my friends near and far, and in particular here at DTU - Pétur and Nonni B. - the DTU lunches were essential. Birkir Veigarsson for the proofreading, intense gym sessions, the crazy power-hours and overall support and of course to my second half Bjarki M. Elíasson - my circumstantial partner in life.

Copenhagen, February 2014
Elvar Örn Jónsson

ABSTRACT

The step from *ab initio* atomic and molecular properties to thermodynamic - or macroscopic - properties requires the combination of several theoretical tools. This dissertation presents constant temperature molecular dynamics with bond length constraints, a hybrid quantum mechanics-molecular mechanics scheme, and tools to analyse statistical data and generate relative free energies and free energy surfaces. The methodology is applied to several charge transfer species and reactions in chemical environments - chemical in the sense that solvent, counter ions and substrate surfaces are taken in to account - which directly influence the reactants and resulting reaction through both physical and chemical interactions. All methods are though general and can be applied to different types of chemistry.

First, the basis of the various theoretical tools is presented and applied to several test systems to show general (or expected) properties. Properties such as in the physical and (semi-)chemical interface between classical and quantum systems and the effects of molecular bond length constraints on the temperature during simulations.

As a second step the methodology is applied to the symmetric and asymmetric charge transfer reactions between several first-row transition metals in water. The results are compared to experiments and rationalised with classical analytic expressions. Shortcomings of the methods are accounted for with clear steps towards improved accuracy.

Later the analysis is extended to more complex systems composed of a larger osmium complex in solution and at the solute-substrate interfaces, where in particular the redox state of the complex is controlled through chemical means. The efficiency of the hybrid-classical and quantum mechanics method is used to generate adequate statistics and a simple post-sampling scheme used to generate free energy surfaces - which compare to full *ab initio* calculations.

In the last part both the molecular dynamics and hybrid classical and quantum mechanics method are used to generate a vast data set for the accurate analysis of dynamical structure modes. This is for a large iridium-iridium dimer complex which shows a dramatic structural (and vibrational) change upon electronic excitation.

RÉSUMÉ

At tage skridtet fra de ab-initio atomare og molekylære egenskaber til termodynamiske - eller makroskopiske - kræver en kombination af mange forskellige teoretiske værktøjer. Denne afhandling præsenterer konstant-temperatur molekylær dynamik med muligheden for at fastholde bindingslængder, en hybrid kvantemekanisk-klassisk mekanisk metode, og værktøjer til at analysere statistisk data og generere fri-energi og fri-energi-flader. Metoden er blevet anvendt til flere forskellige ladningsoverførselssystemer og på reaktioner i kemiske omgivelser - kemisk i den forståelse at solventet, modioner og substratoverflader direkte påvirker reaktanterne og den resulterede reaktion, både igennem kemiske og fysiske interaktioner. Alle metoder er generelle og kan anvendes på mange forskellige kemiske systemer.

Først præsenteres de grundlæggende teoretiske værktøjer, hvorefter de anvendes til flere forskellige test-systemer, for at vise generelle (eller forventede) egenskaber. Egenskaber såsom den fysiske og (semi-)kemiske interaktion i interfacet mellem den klassisk beskrevne- og kvantemekanisk beskrevne del, og effekterne af fastholdte bindingslængder på temperaturen under simuleringerne.

Som det næste skridt bliver metoden anvendt til at beskrive den symmetriske- og asymmetriske ladningsoverførsel mellem flere overgangsmetaller i vand. Resultaterne sammenlignes med eksperimentelle resultater og klassiske, analytiske modeller. De forskellige metoders mangler redegøres for, hvilket resulterer i klare skridt imod bedre præcision.

Analysen udvides til mere komplekse systemer, bestående af osmium komplekser i opløsning, og solut-substrat interfaces, hvor specielt kompleksets redox-tilstand er kontrolleret via de kemiske betingelser. Den hybride kvante/klassiske metodes effektivitet anvendes til at generere tilstrækkelig statistik, og en simpelt 'post-sampling' metode er blevet brugt til at opnå fri-energi flader - som sammenlignes med fulde, ab-initio beregninger.

I den sidste del af afhandlingen bliver kvante/klassisk dynamik hybrid metoden anvendt til at generere et stort dataset til en præcis analyse af de dynamiske strukturændringer i et iridium-iridium kompleks. Resultaterne viser en dramatisk ændring under eksitation af komplekset.

PUBLICATIONS

Paper I

AB INITIO CALCULATIONS OF THE ELECTRONIC PROPERTIES OF POLYPYRIDINE TRANSITION METAL COMPLEXES AND THEIR ADSORPTION ON METAL SURFACES IN THE PRESENCE OF SOLVENT AND COUNTERIONS

Elvar Ö. Jónsson, Kristian S. Thygesen, Jens Ulstrup, and Karsten W. Jacobsen, *J. Phys. Chem. B* **115**(30), 9410-6 (2011), doi: 10.1021/jp200893w

Paper II

AN EFFICIENT QM/MM SCHEME TO EXPLORE ELECTRON TRANSFER REACTIONS IN SOLUTION

Elvar Ö. Jónsson, Asmus O. Dohn, Klaus B. Møller, Kristian S. Thygesen, Jens Ulstrup, and Karsten W. Jacobsen, in preparation (2014)

Paper III

DIRECT MEASUREMENT AND MODULATION OF SINGLE-MOLECULE COORDINATIVE BONDING FORCES IN A TRANSITION METAL COMPLEX

Xian Hao, Nan Zhu, Tina Gschneidtner, Elvar Ö. Jónsson, Jingdong Zhang, Kasper Moth-Poulsen, Hongda Wang, Kristian S. Thygesen, Karsten W. Jacobsen, Jens Ulstrup, and Qijin Chi, *Nat. Comm.* (2013), doi: 10.1038/ncomms3121

Paper IV

DIRECT DYNAMICS STUDIES OF A BINUCLEAR METAL COMPLEX IN SOLUTION: THE INTERPLAY BETWEEN VIBRATIONAL RELAXATION, COHERENCE, AND SOLVENT EFFECTS

Asmus O. Dohn, Elvar Ö. Jónsson, Kasper S. Kjær, Tim B. van Driel, Martin M. Nielsen, Karsten W. Jacobsen, Niels E. Henriksen, and Klaus B. Møller, in preparation (2014)

CONTENTS

I	INTRODUCTION	1
1	INTRODUCTION	3
1.1	Outline	4
II	THEORY	5
2	THE ELECTRONIC STRUCTURE PROBLEM	7
2.1	The Many-Body Problem	7
2.2	Density Functional Theory	8
2.2.1	Kohn-Sham Theory	9
2.2.2	Exchange Correlation	10
2.2.3	Core-Electron Description	12
2.2.4	Valence Electrons	13
2.3	From the Electronic Ground State to Potential Energy Surfaces	15
2.3.1	Hellmann-Feynman Theorem	15
2.4	The Electronic Structure and Atomic Charges	16
3	CLASSICAL POTENTIALS	19
3.1	The Classical Pairwise Additive Potential	19
3.1.1	Lennard-Jones Terms	20
3.1.2	Selected Parameters	22
4	QUANTUM MECHANICS / MOLECULAR MECHANICS	25
4.1	The Hybrid QM/MM Scheme	25
4.1.1	Short-Range Electrostatics	27
4.2	Long-Range Electrostatics	30
4.2.1	The Wolf Scheme	33
4.2.2	Periodic Summation	34
4.3	Forces	36
5	MOLECULAR DYNAMICS	41
5.1	Constant Temperature Molecular Dynamics	41
5.1.1	Langevin Integrator with Holonomic-Constraints	42
5.1.2	Molecular Constraints and Instantaneous Temperature	45
5.1.3	Radial Distribution Functions	48
6	FREE ENERGY ANALYSIS	51
6.1	Free Energy Surfaces	51
6.1.1	The Free Energy Function	52
6.2	Biased or Driven Sampling Methods	53
6.2.1	Fractional Number of Electrons	55
6.2.2	Coupling Parameter	56
6.3	Weighted Histogram Analysis Method	56
6.3.1	Application of WHAM	58

III	APPLICATION	59
7	AQUEOUS TRANSITION METAL COMPLEXES	61
7.1	Computational Details	61
7.2	Structures and Redox Induced Structural Changes	62
7.3	Free Energies Surfaces	65
7.3.1	Internal Reorganization Energy	68
7.3.2	Comparison to Experiment	72
7.4	Redox Potentials	73
7.5	QM/MM Simulations	74
7.6	Conclusion and Outlook	76
8	OSMIUM COMPLEXES	79
8.1	Osmium Polypyridine	79
8.2	Computational Parameters	80
8.2.1	Redox State Control	80
8.2.2	Free Energy Surfaces	82
8.2.3	Conclusion and Outlook	85
8.3	Osmium Terpyridine	86
8.3.1	DFT Simulations	87
8.3.2	Rotational PES of Terpyridine	87
8.3.3	Magnetic States and Charge	89
8.3.4	Simulated Bond Breaking	90
8.3.5	Conclusion and Outlook	91
9	IRIDIUM-IRIDIUM DIMER	95
9.1	Computational Methods	95
9.2	Results	96
9.3	Final Remarks	98
IV	SUMMARY	99
10	SUMMARY	101
	BIBLIOGRAPHY	103
	Paper I	111
	Paper II	123
	Paper III	177
	Paper IV	205

Part I

INTRODUCTION

INTRODUCTION

The electron transfer (ET) reaction, albeit conceptually the simplest of the chemical reactions, still presents a considerable computational challenge. This is due to electrostatic coupling, or response, of the surrounding condensed matter environment and hence requires considerable configurational sampling. Furthermore, the species involved in the charge transfer process can be chemically linked, and the initial and final electronic states overlap. In this regard charge transfer reactions are divided into two categories - diabatic and adiabatic - and it is understood that the transition state barrier is almost purely due to the environmental response in the former case, whereas the transition barrier is strongly affected in the latter case due to said chemical link, or electronic state overlap.

ET reactions are encountered, and are of fundamental importance to the chemical processes in biochemistry, (photo-)electrochemistry, homo- and heterogeneous (surface) catalysis, and to the relatively new experimental field of Scanning Tunneling Spectroscopy (STS), which is a two step interfacial charge transfer process with electrochemical control. This unique method has unprecedented operational control over the electrochemistry, particularly in the sense of 'smart' molecules where the redox state of the molecule and surface-electrode to tip-electrode potential bias are controlled separately. This control has been demonstrated for osmium and cobalt polypyridine transition metal complexes, which showed transistor-like and rectifying behavior [1, 2, 3, 4, 5]. The observed functionality is, furthermore, explained with the phenomenological theory of interfacial electrochemical ET theory [1, 6, 7, 8, 9] with well defined parameters accessible through experimental work and both first principles and hybrid classical and quantum mechanical calculations, such as presented in this work.

Combined Quantum Mechanics / Molecular Mechanics (QM/MM) methods provide an efficient and, often, accurate potential energy description of chemical and biological systems. Such methods have been essential in simulating and understanding solution and biological reactions [10, 11, 12, 13, 14, 15], where it is common to describe the chemically active center(s) (e.g. transition metal complex) with QM and the enclosing environment with MM. The obvious gain there is, for example, that one can greatly speed up configurational sampling of the environment as the ET reaction takes place, facilitated by molec-

ular dynamics simulations.

This thesis presents several computational tools aimed for efficient configuration sampling in the context of electron charge transfer. This includes a constant temperature molecular dynamics with molecular bond constraints - where the simulations are stable well beyond 1 fs in the time step - and a hybrid-classical and quantum mechanics interface - where the bulk solvent is treated with simple classical potentials in diverse systems. The tools are general for other applications, and are used for example in a detailed analysis of excited-state dynamics of a complex system.

1.1 OUTLINE

The thesis is organized as follows:

CHAPTER 2 briefly introduces density functional theory and common approximations, which are used to calculate the electronic structure and potential energy surfaces of atomistic systems.

CHAPTER 3 presents the classical molecular mechanics scheme implemented for this work, which is used mainly for the description of simple solvents in mixed classical and quantum systems.

CHAPTER 4 outlines the quantum mechanics-molecular mechanics method implemented and used for this work.

CHAPTER 5 presents the particular constant temperature molecular dynamics method - with molecular bond constraints - implemented and used for this work.

CHAPTER 6 introduces simple diabatic electron charge transfer and resulting relative free energy surfaces. This includes a method to generate free energy surfaces from molecular dynamics simulations.

CHAPTER 7 presents molecular dynamics and free energy surface analysis for symmetric and asymmetric charge transfer reactions of first-row transition metals in water.

CHAPTER 8 is divided into two parts: 1) reports on the redox state control, molecular dynamics and free energy surface analysis of a large osmium polypyridine complex. 2) presents an analysis on the binding properties of an osmium terpyridine complex.

CHAPTER 9 reports on the detailed analysis of dynamical structure modes of an iridium-iridium dimer complex.

Part II

THEORY

THE ELECTRONIC STRUCTURE PROBLEM

The problem of solving for the electronic structure of atomistic systems is a long standing one and falls under the many-body problem [16] and computational difficulties thereof, where no exact and feasible solution exists to date. In the combined real of quantum chemistry and solid state physics most approaches to the electronic structure rely on efficient methods to solve single-particle wave mechanics expressions with various correlation and/or perturbation schemes to account for the complicated many-body interactions. A multitude of approaches are available in modern computational packages available to academia: Gaussian 09 [17], GPAW [18, 19], Siesta [20], Vasp [21] - all with their own flavour added to the solution of the electronic structure and in many cases a unique and efficient approaches to other ground- and excited-state properties. The core fundamentals behind these approaches, namely DENSITY FUNCTIONAL THEORY (DFT) will be discussed in this Chapter, and is the tool used to simulate the majority of the systems presented in the results section of this thesis.

2.1 THE MANY-BODY PROBLEM

The behavior of chemical systems can be modeled with the interactions of the electrons and nuclei which compose the system, including external perturbation such as an electric field. Such systems, composed of N_e electrons and N_α nuclei, pose a considerable computational challenge due to both their intra- and inter-specific interactions which depend on their spacial coordinates \mathbb{R}^3 and for the electron the spin index as well. For a modest system, say composed of a single transition metal complex adsorbed on a solid surface slab the number of degrees of freedom are in the thousands and hence pose a significant number of interconnected variables for any modern day processor to handle efficiently.

The most commonly applied simplification is to decouple the coordinate variables of the electron and nuclei and solve for the electronic structure for a fixed set of nuclear coordinates, \mathbf{R}_α . This is the well known Born-Oppenheimer approximation [22] and is justified when considering the different time scales of the motion of the electrons compared to a typical nuclei. In terms of their mass they relate by $m_e/M_{\text{nuc}} \approx 10^{-3} - 10^{-5}$, where m_e is the mass of the electron and M_{nuc} the mass range of the nuclei. Hence, one separates the total

wavefunction in to two components such that the motion of the electrons and nuclei are solved for separately, but not independently. The view is that any perturbation of the nuclear coordinates is met with an instantaneous adjustment (or relaxation) of the electronic degrees of freedom. However, any change in the electronic degrees of freedom sets up a different potential environment for the nuclei to move in.

The time independent many-body Schrödinger equation, for a given set of nuclear coordinates reads

$$\hat{H}[\mathbf{R}_\alpha, \mathbf{r}]\Psi(\mathbf{r}) = E[\mathbf{R}_\alpha, \mathbf{r}]\Psi(\mathbf{r}) \quad (1)$$

where for simplicity \mathbf{r} represents both spatial and spin variables of the electrons, and the wavefunction is a function of those variables only. The non-relativistic Hamiltonian is

$$\begin{aligned} \hat{H}[\mathbf{R}_\alpha, \mathbf{r}] &= -\frac{1}{2} \sum_{i=1}^{N_e} \nabla_i^2 - \frac{1}{2} \sum_i^{N_e} \sum_\alpha^{N_\alpha} \frac{Z_\alpha}{|\mathbf{r}_i - \mathbf{R}_\alpha|} + \sum_{i<j} \frac{1}{|\mathbf{r}_i - \mathbf{r}_j|} \\ &= \hat{T} + \hat{V}_{\text{ext}} + \hat{V}_{ee} \end{aligned} \quad (2)$$

where Z_α and \mathbf{R}_α are the charge and position of nuclei α . The first term on the rhs., \hat{T} , is the kinetic energy operator and the second and third term are the Coulomb attraction between the electrons and nuclei, \hat{V}_{ext} , and the Coulomb repulsion between electrons, \hat{V}_{ee} . The second term is denoted the external potential as other static fields such as an applied electromagnetic fields are convoluted in to that collective term. Finally, all the many-body effects are contained in the two-body operator \hat{V}_{ee} .

Several methods have been developed to solve for eq. 2, mainly in the Chemistry community, such as the Hartree-Fock [23] and configuration interaction [24] methods, where the many-body wavefunction is represented as a Slater-determinant or a linear combination thereof. The methods become extremely demanding with higher sophistication but the accuracy at the higher levels are unparalleled, and so are routinely applied for small molecules in the gaseous phase.

2.2 DENSITY FUNCTIONAL THEORY

DENSITY FUNCTIONAL THEORY stands uncontested as the means to solve the electronic structure problem, eq. 2 - when efficiency and accuracy are both taken into account. In 1964 Hohenberg and Kohn [25] reformulated the electronic structure problem in terms of the electronic density

$$\begin{aligned}
E[\mathbf{n}(\mathbf{r})] &= \langle \Psi[\mathbf{n}(\mathbf{r})] | \hat{H} | \Psi[\mathbf{n}(\mathbf{r})] \rangle \\
&= \langle \Psi[\mathbf{n}(\mathbf{r})] | \hat{T} + \hat{V}_{ee} | \Psi[\mathbf{n}(\mathbf{r})] \rangle + \int d\mathbf{r} v_{\text{ext}}(\mathbf{r}) n(\mathbf{r}) \quad (3)
\end{aligned}$$

such that the electronic energy is here a functional of the electronic density, which is in terms of the wavefunctions

$$n(\mathbf{r}) = N_e \sum_{s_1} \cdots \sum_{s_N} \int d(\mathbf{r}_2) \cdots \int d(\mathbf{r}_N) |\Psi(\mathbf{r}, s_1, \mathbf{r}_2, s_2, \dots, \mathbf{r}_N, s_N)|^2 \quad (4)$$

Furthermore, Hohenberg and Kohn, postulated that there is a one-to-one correspondence between the observed electronic density and the external potential of eq. 3, which means that a unique electronic density exists for a given external potential which differs by no more than a constant.

To define the ground state electronic density Hohenberg and Kohn also postulated a variational scheme which states that for a given electronic density $n'(\mathbf{r})$ the ground state energy, E_0 , is the the minimum value of the functional $E[n(\mathbf{r})]$ of eq. 3, or

$$E_0 = \min_{n'(\mathbf{r})} E[n'(\mathbf{r})] \quad (5)$$

Together eq. 3 and 5 provide the basis for DFT. For a given external potential a unique energy functional is defined which can be minimized for the ground state electronic density.

2.2.1 Kohn-Sham Theory

In 1965 Kohn and Sham [26] re-formulated DFT to circumvent the many-body interactions by mapping the interacting electrons on to a system of non interacting electrons.

Kohn and Sham showed that for a given ground state electronic density, $n_0(\mathbf{r})$, there exists an effective potential V_{eff} which, if constructed correctly, gives the same electronic density, $n(\mathbf{r}) \equiv n_0(\mathbf{r})$, when applied through the non-interacting single particle KOHN-SHAM Hamiltonian $H_{KS} = T + V_{\text{eff}}$. For a set of N_e non-interacting single particle states, $\psi_i(\mathbf{r})$, eq. 1 can be written as

$$\hat{H}_{KS} \psi_i(\mathbf{r}) = \epsilon_i \psi_i(\mathbf{r}) \quad (6)$$

and the electronic density in terms of the single particle states is

$$n(\mathbf{r}) = \sum_i^{N_e} |\psi_i(\mathbf{r})|^2 \quad (7)$$

Given that the Hohenberg-Kohn formulation is valid for any electronic density eq. 3 becomes

$$E_{\text{KS}}[n(\mathbf{r})] = T_s[n(\mathbf{r})] + \int d\mathbf{r} v_{\text{eff}}(\mathbf{r})n(\mathbf{r}) \quad (8)$$

where T_s is the single particle kinetic energy operator. More explicitly standard DFT is usually denoted as

$$\begin{aligned} E_{\text{KS}}[n(\mathbf{r})] &= T_s[n(\mathbf{r})] + E_{\text{H}}[n(\mathbf{r})] + E_{\text{xc}}[n(\mathbf{r})] + E_{\text{ext}}[n(\mathbf{r})] \\ &= T_s[n(\mathbf{r})] + G[n(\mathbf{r})] \end{aligned} \quad (9)$$

where E_{H} is the Hartree energy, E_{ext} is the electron-nuclei interaction energy and E_{xc} is the exchange-correlation energy, which recovers many-body effects. Finally, the potential energy terms are collected in to $G[n(\mathbf{r})]$, which is denoted the universal functional. The effective external potential, which acts on the single particle states, can then be defined as the functional derivative with respect to the density

$$v_{\text{eff}} = \frac{\delta G[n(\mathbf{r})]}{\delta n[\mathbf{r}]} = v_{\text{H}} + v_{\text{xc}} + v_{\text{ext}} \quad (10)$$

The Hartree potential accounts for the Coulomb repulsion between the electrons

$$v_{\text{H}} = \frac{1}{2} \iint \frac{n(\mathbf{r})n(\mathbf{r}')}{|\mathbf{r} - \mathbf{r}'|} d\mathbf{r}d\mathbf{r}' \quad (11)$$

and v_{ext} accounts for the electron-nuclei and other static sources as before. Finally, the complicated many-body effects are collected into v_{xc} which is the subject of the next section.

As a final note of this section, since the effective potential depends on the electronic density the Kohn-Sham scheme is solved self-consistently; first by defining an initial density, calculating the effective potential and then by solving the single particle equation 6. With the aim of minimizing the energy functional of eq. 8 the initial density is permuted with an appropriate scheme and the cycle is started again with the new density until convergence is achieved.

2.2.2 Exchange Correlation

Although KOHN-SHAM theory is formally exact the term denoted exchange-correlation (xc) is unknown. This term can be approximated in numerous ways with each improvement usually resulting in increased computational cost. A formal definition of the xc-functional, which in turn defines the xc-potential in eq. 10, is

$$E_{\text{xc}}[n(\mathbf{r})] = T[n(\mathbf{r})] - T_s[n(\mathbf{r})] + V_{ee}[n(\mathbf{r})] - V_{\text{H}}[n(\mathbf{r})] \quad (12)$$

where $T[n(\mathbf{r})] - T_s[n(\mathbf{r})]$ recovers correlation contribution to the kinetic energy density and $V_{ee}[n(\mathbf{r})] - V_H[n(\mathbf{r})]$ introduces many-body electronic effects beyond the Hartree term.

The xc-functionals themselves are divided into hierarchies ranging from low to high computational cost and the accuracy closely follows from poor to good [27]. At the lower end the most commonly used functionals are found - the LOCAL DENSITY APPROXIMATION (LDA) and the GENERALIZED GRADIENT APPROXIMATION (GGA). Higher up in the hierarchy are the hybrid functionals where the exact treatment of the exchange term (see for example [28]) is added to some extent.

THE LOCAL DENSITY APPROXIMATION: Building on the initial self-consistent treatment of DFT by Kohn and Sham [26], the LDA approximates the xc-energy density as for a uniform electron gas, $\epsilon([n(\mathbf{r})], \mathbf{r})_{xc}^{uni}$

$$E_{xc}^{LDA}[n(\mathbf{r})] = \int d\mathbf{r} n(\mathbf{r}) \epsilon([n(\mathbf{r})], \mathbf{r})_{xc}^{uni} \quad (13)$$

The exchange part is known analytically, whereas the correlation part is only known at certain limits. Fitted correlation expressions are used from extensive quantum Monte-Carlo calculations of Ceperley and Alder [29] where the most common parameters are from Perdew-Wang [30] and Perdew-Zunger [31].

LDA is fairly successful for solid-state systems as the density in bulk systems varies slowly, and a xc functional aimed at describing a uniform electron gas works intuitively well for such systems. LDA has also been found to be somewhat successful for molecular systems as well due to spurious self-error cancellations .

GENERALIZED GRADIENT APPROXIMATION: For a more structure dependent density the GGAs utilize the local density gradient, $|\nabla n(\mathbf{r})|$, such that the xc-energy density becomes $\epsilon([n(\mathbf{r})], |\nabla n(\mathbf{r})|)_{xc}^{GGA}$ and

$$E_{xc}^{GGA}[n(\mathbf{r})] = \int d\mathbf{r} n(\mathbf{r}) \epsilon([n(\mathbf{r})], |\nabla n(\mathbf{r})|)_{xc}^{GGA} \quad (14)$$

effectively making the functional semi-local. The use of the full gradient has proved to be troublesome as it varies greatly in systems and can break down the expression, hence a scaled relation to the gradient is used through an additional term $F_{xc}(s)$,

$$E_{xc}^{GGA}[n(\mathbf{r})] = \int d\mathbf{r} n(\mathbf{r}) \epsilon([n(\mathbf{r})], \mathbf{r})_{xc}^{LDA} F_{xc}(n(\mathbf{r}), s(|\nabla n(\mathbf{r})|)) \quad (15)$$

and the various GGAs differ with the choice of the exchange part of $F_{xc}(\mathbf{s})$ [32]. Due to the semi-local nature of the functional it has been found to be quite successful for molecular systems as well as bulk systems, hence the GGAs are the most widely used functionals to date.

Most commonly applied GGA in the Physics community is with the scaling of Perdew, Burke and Ernzerhof (PBE) [33]. The combination of Becke's 88 exchange functional [34] and Lee, Yang and Parr 88 (LYP) correlation functional [35], denoted BLYP, is the most common GGA choice in the Chemistry community. Of the two PBE performs better for molecular systems and almost always for bulk systems, whereas BLYP is apt for molecules only [36]. Other common choices are for example the revised PBEs, revPBE [37] and RPBE [38], where the scaling factor is adjusted to best fit experimental data and in these cases provide a more accurate energetics regarding substrate-surface adsorption and molecular bonds.

2.2.3 Core-Electron Description

Full core-electron description is expensive due to the rapid oscillation of wave-functions near the nuclei core. Such closely bound states require a considerable number of basis functions to describe accurately, yet often have little effect on the chemistry between neighboring atoms - such as charge transfer or bond formation. A very common approximation is to treat these chemically irrelevant core electrons *a priori* either by replacing their collective effect by a suitable potential or by calculating, and fixing, the electronic structure of the core electrons under suitable boundary conditions, hence retain an all-electron (AE) description.

PSUEDOPOTENTIALS: In the pseudopotential approach the effects of the core electrons are replaced with a smooth potential which is easy to describe numerically, and is fitted to reproduce the correct scattering effect on the remaining valence electrons - in this form it is attributed to Hans Hellman [39]. One drawback of this approach is that the atom specific pseudopotentials do not work equally well in different chemical environments.

PROJECTOR AUGMENTED WAVE (PAW): In the PAW method, as presented by Blöchl in 1994, the information on the core electron states are retained, yet the treatment of the core region remains computationally convenient. This is achieved by replacing the true AE single electron KS wavefunction of eq. 6, $\psi_i(\mathbf{r})$, with a

smooth pseudo-wavefunction - i.e. having smooth core states - and a transformation operator

$$|\psi_i(\mathbf{r})\rangle = \tilde{\mathcal{T}}|\tilde{\psi}_i(\mathbf{r})\rangle \quad (16)$$

The transformation operator $\tilde{\mathcal{T}}$ is defined in such way that it only modifies the pseudo-wavefunction when it crosses a boundary at a given cut-off radius centered on atom α

$$\tilde{\mathcal{T}} = 1 + \sum_{\alpha} \tilde{\mathcal{T}}^{\alpha} \quad (17)$$

and in this way only acts on the pseudo-wavefunction in the approximate smooth region - termed the augmentation region - see Figure 1. The resulting form is [40]

$$\psi_i(\mathbf{r}) = \tilde{\psi}_i(\mathbf{r}) + \sum_{\alpha} \sum_n (\phi_n^{\alpha}(\mathbf{r}) - \tilde{\phi}_n^{\alpha}(\mathbf{r})) \langle \tilde{p}_n^{\alpha} | \tilde{\psi}_i \rangle \quad (18)$$

where $\phi_n^{\alpha}(\mathbf{r})$ and $\tilde{\phi}_n^{\alpha}(\mathbf{r})$ are basis expansions of the AE KS wavefunctions and the pseudo-wavefunctions within the augmentation region, respectively, and $\langle \tilde{p}_n^{\alpha} | \tilde{\psi}_i \rangle$ determines the expansion coefficients with a projector function \tilde{p}_n^{α} satisfying $\langle \tilde{p}_n^{\alpha} | \tilde{\phi}_{n'}^{\alpha} \rangle = \delta_{n,n'}$.

Before a calculation the expansions within the augmentation sphere are calculated and saved as 'PAW objects' [18] and the Kohn-Sham equations are then solved as before but now with

$$\tilde{\mathcal{T}}^{\dagger} \hat{H} \tilde{\mathcal{T}} |\tilde{\psi}_i\rangle = \epsilon_i \tilde{\mathcal{T}}^{\dagger} \tilde{\mathcal{T}} |\tilde{\psi}_i\rangle \quad (19)$$

The PAW method is as accurate as full all electron calculations [41], and outperforms pseudopotential methods most notably due to the fact that the PAW objects are easier to construct and transferable between various chemical environments.

2.2.4 Valence Electrons

The wave-functions for the valence electrons are relatively smooth compared to the aforementioned core-electron functions - hence, they are described with a finite basis of numerically convenient functions or forms.

LOCALIZED ATOMIC ORBITALS: The numerical localized atomic orbital (AO) basis sets are the most popular among the chemists as they provide a compact and efficient basis for small and large

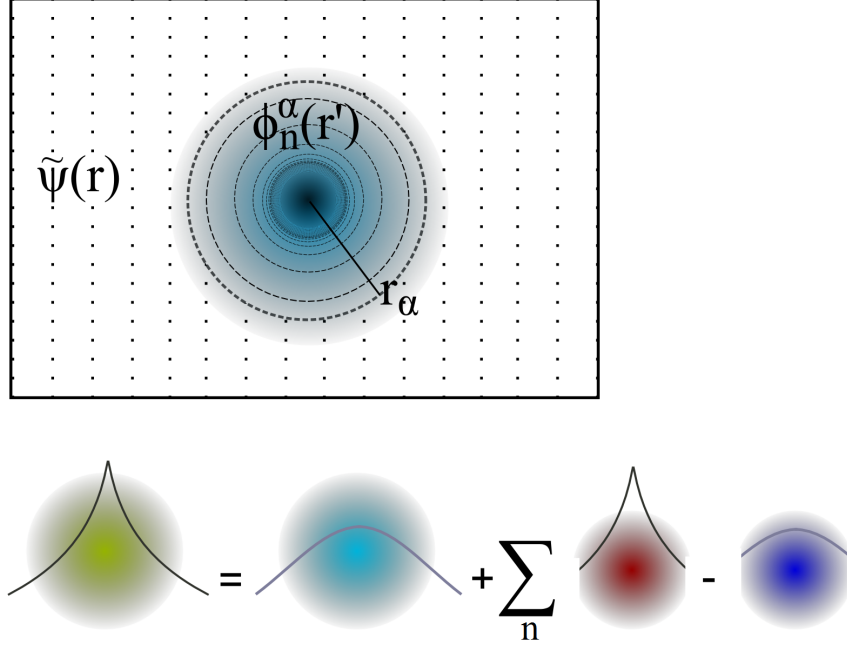


Figure 1: **Top:** in GPAW the pseudo-wavefunctions, $\tilde{\psi}(\mathbf{r})$ are described numerically on a grid, and the pseudo and all-electron core electrons, $\tilde{\phi}^\alpha(\mathbf{r})$ and $\phi^\alpha(\mathbf{r}')$, are described on a finer logarithmic radial grid within the boundary defined by r_α - or the augmentation region. **Bottom:** the all electron wave-function around an arbitrary nuclei is constructed by adding the all electron core electron wave functions and subtracting the smooth pseudo core electron wave function to the pseudo-electron wave function where the valence and core electrons are matched at the boundary with the projector functions (eq. 18).

molecular systems. The Kohn-Sham states are represented as a linear combination of n AO functions

$$|\psi_i(\mathbf{r})\rangle = \sum_n c_{ni} |\phi_n(\mathbf{r})\rangle \quad (20)$$

and as such the method is most commonly referred to as 'linear-combination of atomic orbitals' (LCAO) - where ϕ are composed of the spherical and radial harmonics. During a self-consistent calculations the variational parameter for the electronic density are simply the expansion coefficients c_{ni} , and for greater accuracy the number of AOs can be increased without drastic change in computational cost. The implementation of LCAO in to GPAW can be found here [42] along with benchmark results.

REAL-SPACE GRID: Here the wavefunctions are represented numerically on a three-dimensional real space grid - hence termed "grid mode". Constructing pair-potentials is straightforward and the differential operators of the Hamiltonian are based on fi-

nite difference methods. The accuracy can be systematically controlled with a single parameter, the grid spacing (see for example Figure 1). Moreover, grid based methods can be parallelized very efficiently by dividing the real space grid into domains.

2.3 FROM THE ELECTRONIC GROUND STATE TO POTENTIAL ENERGY SURFACES

Although the computational path towards the electronic ground structure is not unique, the basis of success is that the electronic structure is unique to the surroundings composed of the nuclei through $v_{\text{ext}}[\mathbf{R}_\alpha]$ in eq. 10. For a given xc-functional and core- and valence-electron basis, the resulting potential energy is unique to the particular arrangement of the nuclei. Hence one can with an appropriate scheme propagate or mutate the arrangement of the nuclei and map the so called POTENTIAL ENERGY SURFACE (PES) - which is the electronic ground state energy as a function of nuclei coordinates.

2.3.1 Hellmann-Feynman Theorem

The path from the electronic ground state density to the PES, $E_{\text{KS}}(\mathbf{R}_{\alpha,j})$, is provided by considering the gradient of the function. The gradient itself point towards increase of the potential energy and hence for minimization or traversing within the PES one can define the forces as the negative gradient

$$\mathbf{F}(\mathbf{R}_\alpha) = -\nabla E(\mathbf{R}_\alpha) \quad (21)$$

However, the gradient is not directly available from KS-DFT and so the Hellmann-Feynman theorem [43, 44] is used where it states that the partial derivative of the potential energy as a function of a continuous parameter, $\partial E/\partial \eta$, can be evaluated if the wave-functions depend implicitly on the parameter, $\psi(\eta)$, or

$$\begin{aligned} \frac{\partial E}{\partial \eta} &= \left\langle \frac{\partial \psi(\eta)}{\partial \eta} \mid \hat{H} \mid \psi(\eta) \right\rangle + \left\langle \psi(\eta) \mid \frac{\partial \hat{H}}{\partial \eta} \mid \psi(\eta) \right\rangle + \left\langle \psi(\eta) \mid \hat{H} \mid \frac{\partial \psi(\eta)}{\partial \eta} \right\rangle \\ &= E \frac{\partial}{\partial \eta} \langle \psi(\eta) \mid \psi(\eta) \rangle + \left\langle \psi(\eta) \mid \frac{\partial \hat{H}}{\partial \eta} \mid \psi(\eta) \right\rangle \\ &= \left\langle \psi(\eta) \mid \frac{\partial \hat{H}}{\partial \eta} \mid \psi(\eta) \right\rangle \end{aligned} \quad (22)$$

where in the first line the Hermitian properties of the Hamiltonian is used to arrive at line two, and in the second line orthonormality of the wave-functions is assumed making the first term zero - leading to the last line.

For the KS-DFT Hamiltonian, under the Born-Oppenheimer approximation, the continuous parameter is chosen as the nuclei coordinates. In this way $E_{\text{KS}}(\mathbf{R}_{\alpha,j})$ can be generated using the resulting forces and the appropriate scheme to propagate the nuclei. This can be used for structural minimization following the negative gradient until a minimum on the PES is reached, or molecular dynamics (discussed in Chapter 4.).

As discussed in Section 2.2.1 the wave-functions, or the electronic density, is solved for using variational minimization hence the accuracy of the forces is not guaranteed and they will contain numerical noise [18].

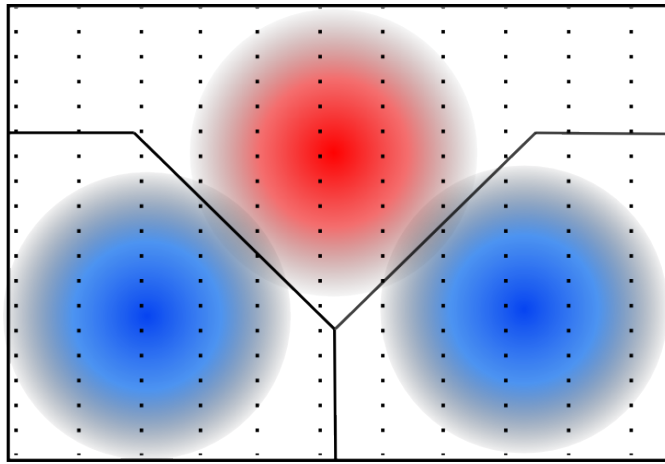


Figure 2: In Bader's analysis the electronic density is divided among the nuclei which are enclosed by surfaces where the gradient of the electronic density vanishes normal to the surface. As an arbitrary example the resulting charge density composed of the electronic density from say a GPAW calculation - where $n(\mathbf{r}) = \tilde{n}(\mathbf{r}) + \sum_{\alpha} [n^{\alpha}(\mathbf{r}) - \tilde{n}^{\alpha}(\mathbf{r})]$ - is divided approximately at the middle of the overlap between the blue and red distributions.

2.4 THE ELECTRONIC STRUCTURE AND ATOMIC CHARGES

With the electronic ground state solved, and the electronic density available it is of interest to analyze the charge on specific molecules of the respective computational system. Such analysis can provide direct insight into the chemistry between atoms and molecules, particularly for charge transfer systems where the redox states of molecules are changed. To this end various charge partitioning schemes have been developed based either on the single-particle wfs. (7) or the charge density

$$\rho(\mathbf{r}, \mathbf{R}_{\alpha}) = n(\mathbf{r}) + \sum_{\alpha}^{N_{\alpha}} Z_i \delta(\mathbf{r} - \mathbf{R}_{\alpha}) \quad (23)$$

which are both readily available after completing an SCF cycle in modern DFT codes. The disadvantage of orbital based methods, such as the Mulliken population analysis [45], is that they are heavily basis set dependent. Methods based on the resulting charge density are not as sensitive to the basis are most commonly used. Here the method of Bader's "atoms in molecules" [46] topological approach is used, see Figure 2.

Bader's analysis has been found to give too ionic character when addressing bonds between specific atoms compared to other charge density such as the VORONOI DEFORMATION DENSITY (VDD) method, as well as others assessed here [47]. However, it is not of interest to analyse specific bonds rather the localization of charge on well separated molecules or ions where Bader's analysis suits well. For this work the grid-based algorithm of Tang et. al. [48] is used.

CLASSICAL POTENTIALS

Although DFT presents an efficient way to obtain the electronic structure for a given nuclear configuration of a microscopic system composed of thousands of individual particles, and hence the potential energy and resulting forces, it is still limited. Macroscopic (thermodynamic) properties, which are readily available through experimental means, requires an analysis of thousands of independent nuclear configurations to study accurately at the theoretical level. Classical potentials have here been favored as they are most often composed of pairwise additive potentials as functions of the nuclear positions, with the electronic degrees of freedom skipped entirely. Complicated electronic terms are re-introduced through simple pair potentials such as the Coulomb and Lennard-Jones potential [49], where the latter mimics important many-body correlations like van der Waals interactions [50] and fundamental quantum principles like Pauli repulsion. In the static picture the atoms comprising the classical molecules are given partial charge values, q_i , which represent in one term the number of electrons and the nuclear charge, along with specific van der Waals coefficients to describe quantum and many-body effects. These parameters are fitted to match PESs for the same (or similar) systems simulated by more accurate means such as with Monte Carlo simulations or full quantum mechanical calculations.

3.1 THE CLASSICAL PAIRWISE ADDITIVE POTENTIAL

Classical potentials are divided in to two parts; a non-covalent part which describes the pairwise interactions between individual molecules, and a covalent part which describes the internal structure of the molecules

$$E_{MM} = E_{\text{covalent}} + E_{\text{non-covalent}} \quad (24)$$

The classical potential or force field most commonly employed in molecular mechanics (MM) of small and large (bio-) molecules are of the general form of Wang et. al. [10, 11, 51]

$$\begin{aligned}
E_{\text{MM}} = & \sum_{\text{bonds}} K_r (\mathbf{r} - \mathbf{r}_{\text{eq}})^2 + \sum_{\text{angles}} K_\Phi (\Phi - \Phi_{\text{eq}})^2 \\
& + \sum_{\text{dihedrals}} \frac{V_n}{2} [1 + \cos(n\phi - \gamma)] \\
& + \sum_{i < j} \left[\frac{q_i q_j}{\tau_{ij}} + 4\epsilon_{ij} \left\{ \left(\frac{\sigma_{ij}}{\tau_{ij}} \right)^{12} - \left(\frac{\sigma_{ij}}{\tau_{ij}} \right)^6 \right\} \right] \quad (25)
\end{aligned}$$

The first three parts on the right hand side describes the energy dependence of the internal structure of the classical molecule (covalent part) and a visual description is provided in Figure 3 along with the definition of the parameters. The last part represents the interactions among the molecules in terms of a Coulomb potential and the well known 12-6 LJ potential. The main tests and applications of the MM code in this work employ a simple three-site model of water, or the well known TIP3P [52], and similarly for acetonitrile (methyl-cyanide) [53] where the internal structure is kept fixed, hence the focus is on the last part of eq. 25. However, internal bonds are though left as an option for use in the MM or QM/MM code (described in Chapter 4).

3.1.1 Lennard-Jones Terms

The LJ potential encountered in eq. 25 is an important part for both the QM/MM (see Chapter 4) and MM/MM interspecies interactions as they approximate physically important short and long range interactions. Specifically the general pair potential reads

$$E_{\text{LJ}} = \sum_{i < j}^{N_i} 4\epsilon_{ij} \left[\left(\frac{\sigma_{ij}}{|\tau_i - \tau_j|} \right)^{12} - \left(\frac{\sigma_{ij}}{|\tau_i - \tau_j|} \right)^6 \right] \quad (26)$$

where ϵ_{ij} and σ_{ij} are the energy and size parameters, respectively, controlling the pair potential depth and minimum position. The r^{-12} term on the right hand side of eq. 26 is attributed to Pauli repulsion but is an approximation only, while the r^{-6} term describes long range attraction, or van der Waals (vdW) interactions, with some theoretical justification [50].

Due to the very short range of r^{-6} this term is not given a special treatment in the case of periodically repeated systems, and interactions are simply cut-off beyond nearest neighbor cells. However, the energy and size parameters need to be constructed for the cross-relation between point charges i and j . Several combination rules exist which have been systematically tested [54, 55, 56], and are often based on the simple arithmetic or geometric mean rules by Lorentz and Berth-

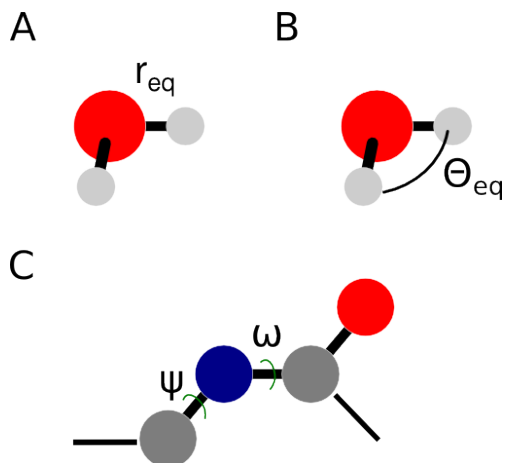


Figure 3: The molecular mechanics model of eq. 25 includes electrostatic, van der Waals, bond, bond angle and dihedral terms. **A:** Atom-to-atom bond lengths, r , are modeled with harmonic oscillators of force constant K_r and equilibrium bond length r_{eq} . **B:** the second part describes bond angles, Φ , between two atoms linked through a third atom (e.g. such as hydrogens in a water molecule) with a force constant K_Φ and equilibrium angle Φ_{eq} . **C** the third term describes dihedral angles between, for example, protein residues. ψ is the dihedral angle and V_n is the corresponding force constant. γ , or the phase angle, takes values of either 0° or 180° . The last term of eq. 25 is discussed extensively in the text, particularly in Chapter 4, with strategies to model solvents. More detailed strategies for everything from small molecules, to proteins and other large bio-molecules can be found here [10, 11, 12, 13, 14, 15], where modulations of the electrostatic terms are considered, and a multitude of electrostatic parameters are listed for specific purposes.

elot [57, 58].

More in depth studies [55] have focused on a simple rule by Waldman-Hagler (WH) [59]

$$\sigma_{ij} = \left[\frac{\sigma_{ii}^6 + \sigma_{jj}^6}{2} \right]^{\frac{1}{6}}$$

$$\epsilon_{ij} = \frac{2\sigma_{ii}^3 \sigma_{jj}^3}{\sigma_{ii}^6 + \sigma_{jj}^6} \sqrt{\epsilon_{ii} \epsilon_{jj}} \quad (27)$$

with no added computational complexity. Classical simulations where energy and size parameters are evaluated with the WH method above were found to reproduce experimental rare-gas binding curves, yet retain the same relative accuracy in more complex systems compared to simulations using the simpler combination schemes [55, 59].

A general code to deal with classical force fields, or rather the SIMPLE POINT CHARGE POTENTIALS has been implemented and tested exten-

sively on both water and acetonitrile. Molecular dynamics and resulting radial distribution functions are presented in various chapters of this thesis - Chapter 5 for example, two methods to treat periodic boundary conditions are compared, or the MINIMUM IMAGE CONVENTION (MIC) and the WOLF method, which is a simplified variant of the Ewald summation method [60]. The WOLF method is the subject of the next Chapter where it is applied on a variety of potentials with focus on the point-charge to point-charge Coulomb potential.

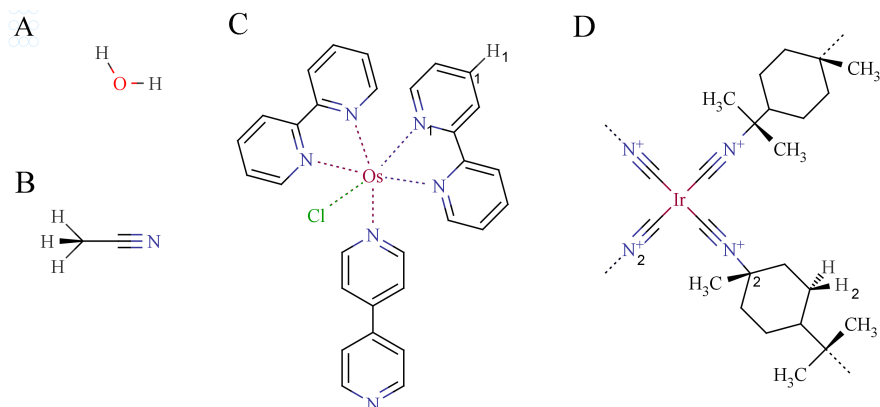


Figure 4: Systems **A-D** represent the majority of the systems studied. The carbons, nitrogens and hydrogens in the various environments require specific parameters to describe classically with eq. 26, as well as in hybrid-quantum and classical system discussed in Chapter 4 - where a Lennard-Jones pair potential (and other potentials) couple the two parts. All values are collected in Table 1. The electronic structure of the complexes depicted in **C** and **D** are always treated with quantum mechanics - but the solvents are either QM or MM. In the MM case water has fixed bond lengths and angles: $r_{\text{OH}} = 0.958 \text{ \AA}$, $\angle(\text{H-O-H}) = 104.4^\circ$ - and point charge values $q_{\text{O}} = -0.834$ and $q_{\text{H}} = 0.417$. For MM acetonitrile the following constraints and charge values apply: $r_{\text{NC}} = 1.146$, $r_{\text{CC}^{\text{M}}} = 1.157$, $r_{\text{NC}^{\text{M}}} = 2.303$, $q_{\text{N}} = 0.206$, $q_{\text{C}} = 0.247$ and $q_{\text{C}^{\text{M}}} = -0.453$. Note that the hydrogens of the methyl group in acetonitrile are entirely omitted - and their effects convoluted into the effective charge values and vdW parameters of the methyl-carbon, C^{M} .

3.1.2 Selected Parameters

Figure 4 presents a schematic of the various molecules and solvents studied in this thesis. Table 1 collects and references the Lennard-Jones parameters, ϵ_{ii} and σ_{ii} , which are used in both full classical and hybrid-quantum mechanical/molecular mechanical simulations (which is the subject of the next chapter) - or wherever there is a Lennard-Jones pair potential term.

The LJ parameters for the polypyridine and dimen groups of the osmium and iridium complexes, respectively, which are composed of carbon, hydrogen and nitrogen, are from Cornell et. al. [14]. In their work a multitude of generic parameters are presented for various constituents - such as for sp^2 and sp^3 hybridized carbons - in nucleic acid, protein and organic molecules alike. For water and acetonitrile the parameter sets are, as noted before, the TIP3P [52] and the one of Guardia et. al. [53], respectively. The TIP3P requires little introduction as it is one of the most widely used three-point classical potential. The acetonitrile is described with a three-site point charge potential - with parameters for the nitrogen, carbon and methyl group where the methyl group is represented with a single carbon atom only - and the vdW and charge parameters adjusted to best represent the 'presence' of the hydrogen atoms as well.

For the counter-anion chloride (used to control redox state of osmium, Chapter 8) optimized parameters for aqueous simulations are used from Jensen et. al. [61]. The transition metal complexes which are treated with QM/MM in this thesis; iron (Chapter 7), osmium (Chapter 8) and iridium (Chapter 9), are all embedded into structures described with QM. The LJ potential is very short range and since the distance to the solvent is shortest 4 Å (case of iron) they will not perturb the metal, particularly where it is central. In some cases the metals are described with LJ parameters from Allinger et. al. [62] - and in their work parameters for a range of transition metals are reported, and many are derived by simply extrapolating from known crystallographic data.

Table 1: The Lennard-Jones pair potential energy, ϵ_{ii} , and size parameters, σ_{ii} , in units eV and Å, respectively. These parameters are used for the various constituents of the osmium and iridium complexes (Figure 4) studied in this work with classical and hybrid quantum-classical methods. The last column collects the values for the water (w) and acetonitrile (a) solvents.

Atom	ϵ_{ii}	σ_{ii}	Atom	ϵ_{ii}	σ_{ii}
H ₁	1.30e-3	2.42	O _w	6.59e-3	3.15
H ₂	6.81e-4	1.49	N _a	6.50e-3	3.20
C ₁ ^{sp2}	3.30e-3	3.55	C _a	5.63e-3	3.65
C ₂ ^{sp3}	4.74e-3	1.91	(CH ₃) _a	8.11e-3	3.78
N _{1,2}	7.37e-3	2.96	Os	0.019	2.31
Cl ⁻	3.08e-2	4.02	Ir	0.025	2.31

This chapter explores the combination of quantum mechanics and molecular mechanics, here with the focus on efficiency. QUANTUM MECHANICS/MOLECULAR MECHANICS or QM/MM methods, first established by Warshel and Levitt [63], are today widely used in the study of microscopic systems with recent work within the field of solvation reactions [64, 65], redox chemistry [66] and enzymology [67, 68, 69], where more often than not these fields overlap within the same study. The advantage of combined QM/MM methods is first and foremost the option of treating the chemically interesting, or reactive, part of the microscopic system with QM, whereas the solvent or the bulk of a protein is treated with classical force fields. This **a)** minimizes the quantum mechanical system and **b)** offers the possibility of performing molecular dynamics on otherwise heavily resource demanding or even inaccessible systems. As discussed in Chapter 2, DFT is an efficient and often accurate approach to the electronic structure problem thus it is a popular choice for many QM/MM studies [70, 71, 68, 72, 73]. This is an appealing combination when considering the multitude and time scale for configuration sampling for free energy analysis.

4.1 THE HYBRID QM/MM SCHEME

In DFT the total energy is obtained by minimizing a density functional with respect to the electronic density. This provides a convenient framework for describing systems containing both quantum parts with a certain electronic density and classical degrees of freedom which couple to the quantum system through the electronic density. The following total energy expression is thus used

$$E_{\text{tot}} = E_{\text{KS}} + E_{\text{QM/MM}} + E_{\text{MM}} \quad (28)$$

where the total energy functional is given by the usual Kohn-Sham functional for the QM part of the system, E_{KS} eq. 9, a classical part, E_{MM} as given by eq. 25, and only depends on the classical degrees of freedom, and a mixed term, $E_{\text{QM/MM}}$, which couples the quantum and classical degrees of freedom.

As discussed in Chapter 3 a point charge value, q_i , and Cartesian coordinates τ_i is assigned to the C atoms comprising the MM part, and write the QM/MM interactions as

$$E_{\text{QM/MM}} = \sum_{i=1}^C q_i \int \frac{n(\mathbf{r})}{|\mathbf{r} - \boldsymbol{\tau}_i|} d\mathbf{r} + \sum_{i=1}^C \sum_{\alpha=1}^A \frac{q_i Z_\alpha}{|\mathbf{R}_\alpha - \boldsymbol{\tau}_i|} + E_{\text{LJ}} \quad (29)$$

where $n(\mathbf{r})$ is here the spatial electronic density of the quantum region, and Z_α and \mathbf{R}_α are the charge and Cartesian coordinates of the quantum nuclei, respectively. Together, the first two terms on the right hand side in the equation above are the Coulombic interactions between the point charges of the MM part, and the charge density, $\rho(\mathbf{r}, \mathbf{R}_\alpha)$, of the QM part as defined in eq. 23

$$E_{\text{QM/MM}}^{\text{coul}} = \sum_{i=1}^C q_i \int \rho(\mathbf{r}, \mathbf{R}_\alpha) \quad (30)$$

This term leads to an additional contribution to the potential which acts on the QM system

$$v_{\text{MM}} = \frac{\delta E_{\text{QM/MM}}}{\delta n(\mathbf{r})} = \sum_{i=1}^C \frac{q_i}{|\mathbf{r} - \boldsymbol{\tau}_i|} \quad (31)$$

so that the effective external potential of the Kohn-Sham scheme solved with GPAW becomes

$$v_{\text{eff}}^{\text{tot}} = v_{\text{H}} + v_{\text{xc}} + v_{\text{ext}} + v_{\text{MM}} \quad (32)$$

where v_{H} , v_{ext} and v_{xc} are the Hartree, electron-quantum nuclei and exchange-correlation potentials, respectively. In this way the ground state electronic density is solved for with the electrostatic effects due to the presence of the MM system by the self-consistent cycle in GPAW. This includes the electronic contribution to the forces exerted on the quantum nuclei, F_α^{ele} . Similarly for a quantum nuclei, α , the classical potential is defined as

$$v_{\text{MM}}^\alpha = \frac{\delta E_{\text{QM/MM}}}{\delta Z_\alpha} = \sum_{i=1}^C \frac{q_i}{|\mathbf{R}_\alpha - \boldsymbol{\tau}_i|} \quad (33)$$

which is evaluate analytically but with modifications described in following subsections.

Finally E_{LJ} , the last term on the right hand side of eq. 29, denotes the Lennard-Jones potential interactions with the same generic 12-6 repulsive-attractive form as in eq. 26, but here explicitly between point charge i and quantum nuclei α

$$E_{\text{LJ}} = \sum_{i=1}^C \sum_{\alpha=1}^A 4\epsilon_{\alpha i} \left[\left(\frac{\sigma_{\alpha i}}{|\mathbf{R}_\alpha - \boldsymbol{\tau}_i|} \right)^{12} - \left(\frac{\sigma_{\alpha i}}{|\mathbf{R}_\alpha - \boldsymbol{\tau}_i|} \right)^6 \right] \quad (34)$$

The same combination scheme is employed as in eq. 27, and the same ϵ and σ parameters are used when combining, say, QM water described with the PBE functional with a classical water described with the TIP3P parameter set (listed in Table 1).

Finally, to complete the set of potentials the point-charge potential acting on point charge j is defined as

$$v_{\text{MM}}^j = \sum_{i \neq j}^c \frac{q_i}{|\tau_i - \tau_j|} \quad (35)$$

The potentials in eq. 31, eq. 33 and eq. 35 are all of the r^{-1} form and hence require special treatment in both the short and long range limits, discussed in the following sections.

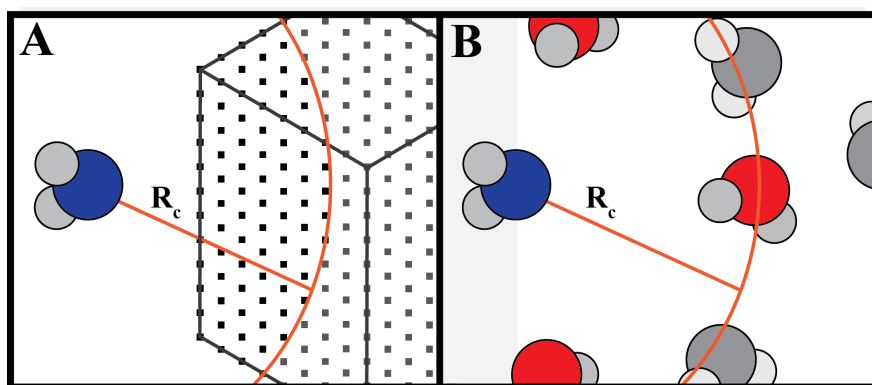


Figure 5: The electrostatic interactions of the classical solvent molecules are truncated at R_c ; here they are depicted as water with the oxygen blue, and the hydrogens grey. **Case A:** In this example the point charge is outside the quantum potential grid space, and due to the cut-off only gives weight to v_{MM} (see eq. 32) at the points within the truncated sphere defined by R_c . **Case B:** Here the electrostatic interaction between point charge to quantum nuclei, or point charge to point charge, are cut off at R_c . However, if the principal atom of a simple molecule like water (i.e. oxygen) lies within the sphere the whole molecule is taken in to account, such that the hydrogens are evaluated within $|R_c + \Delta_H|$.

4.1.1 Short-Range Electrostatics

The classical electrostatic potential of eq. 31 requires special treatment at both the short and long distance limits. In the short-range case the point-charges will sometimes be within the grid space of the QM system (see Figure 5 and top of Figure 6). One must take care if the divergence of the potential associated with a point charge is close to a grid point. This is also known as the charge spill out effect [74, 75, 76], where electronic density clusters around such artificial potential wells.

To avoid this problem a simple smoothing form of Laio et al. [74] and transform the potential of eq. 31 to

$$v_{\text{MM}}(\mathbf{r}^\gamma) = \sum_{i=1}^C \frac{q_i}{r^\gamma} \quad (36)$$

with

$$\frac{1}{r^\gamma} = \frac{\gamma^4 - |\mathbf{r} - \tau_i|^4}{\gamma^5 - |\mathbf{r} - \tau_i|^5} \quad (37)$$

The value of γ which controls the smoothing of the potential near the origin is 0.20 Å in this work, which was found to give a consistent potential minimum between the different atoms of a classical molecule interacting with the different atoms of a quantum molecule (see for example Figure 6, and discussion below). Other convenient forms and suggestions for smoothing can be found here [70, 75, 76].

The basic Coulomb form (r^{-1}) is encountered in both the QM/MM and MM/MM potential energy descriptions, eq. 33 and eq. 35. For simplicity and consistency in the derivation of the long-range approximations which follows, all classical potentials are smoothed in the same way; eq. 33 and eq. 35 then become

$$v_{\text{MM}}^\alpha(\mathbf{R}_\alpha) \rightarrow v_{\text{MM}}^\alpha(\mathbf{R}_\alpha^\gamma) \quad (38)$$

with

$$\frac{1}{\mathbf{R}_\alpha^\gamma} = \frac{\gamma^4 - |\mathbf{R}_\alpha - \tau_i|^4}{\gamma^5 - |\mathbf{R}_\alpha - \tau_i|^5} \quad (39)$$

and, similarly

$$v_{\text{MM}}^j(\tau_j) \rightarrow v_{\text{MM}}^j(\tau_j^\gamma) \quad (40)$$

with

$$\frac{1}{\tau_j^\gamma} = \frac{\gamma^4 - |\tau_j - \tau_i|^4}{\gamma^5 - |\tau_j - \tau_i|^5} \quad (41)$$

Figure 6 presents hydrogen binding curves for the MM/MM case versus the QM/MM case employing the smoothed potentials described above. The hydrogen binding energy for the MM/MM case is simply evaluated with the last part of eq. 25 with the smoothing for consistency

$$E_{\text{MM/MM}}^{\text{bond}} = \sum_j^{C'} q_j v_{\text{MM}}^j(\tau_j^\gamma) + \sum_i^C \sum_j^{C'} E_{\text{LJ}} \quad (42)$$

where C and C' simply indexes the atoms in the different water molecules. The parameters of the TIP3P model [52] are used to describe the classical molecules. The QM/MM hydrogen binding energy is here given by

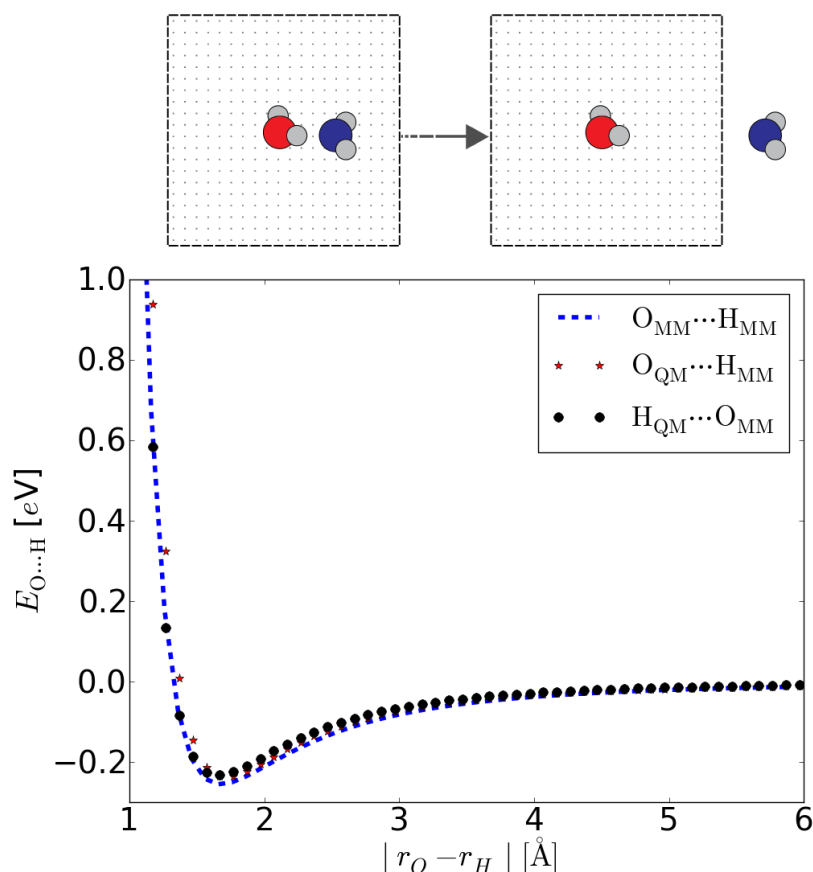


Figure 6: **Top:** The computational setup for the hydrogen bond analysis between a classical and quantum water molecule. The classical point charges begin within the grid space of the QM system which extends to 4.0 Å in xyz, viewed from the quantum oxygen. The classical molecule is systematically moved away until the quantum-hydrogen to classical-oxygen length is 6.0 Å which brings it well outside the quantum grid space. **Bottom:** The hydrogen binding energy between a classical and quantum molecule, compared to the classical to classical case. The classical to quantum is furthermore split in to two cases; first a quantum oxygen interacts with a classical hydrogen, and second, a quantum hydrogen interacts with a classical oxygen. The blue broken curve is the electrostatic potential of eq. 25, using the TIP3P parameters. The red stars and black dots are the electrostatic QM/MM cases, $O_{QM} \cdots H_{MM}$ and $H_{QM} \cdots O_{MM}$ respectively, where $E_{\text{bond}} = E_{QM/MM} - E_{KS}(H_2O)$, or eq. 29 with the smoothed coulomb potential of eq. 36, minus the potential energy of quantum water in vacuum. The full QM-QM hydrogen bond is not presented but the minimum of the potential profile in that case was found to be about -0.36 eV, which is a significant increase compared to the cases presented here. This is a known property of GGA described water [77, 78, 79] - and results in a near 'ice'-like behavior for molecular dynamics simulations at 300 K.

$$E_{\text{bond}} = E_{\text{KS}}[\text{H}_2\text{O}, v_{\text{MM}}(\mathbf{r}^\gamma)] + \sum_{\alpha}^A Z_{\alpha} v_{\text{MM}}(\mathbf{R}_{\alpha}^{\gamma}) + E_{\text{LJ}} - E_{\text{KS}}[\text{H}_2\text{O}] \quad (43)$$

where $E_{\text{KS}}[\text{H}_2\text{O}]$ and $E_{\text{KS}}[\text{H}_2\text{O}, v_{\text{MM}}(\mathbf{r}^\gamma)]$ are the potential energy of a water molecule in vacuum and the potential energy of water influenced by the point charges through the smoothed potential - where eq. 36 is added to the effective external potential of eq. 32. The second and third term on the rhs. are the point charge-quantum nuclei and LJ interactions. The same TIP3P Lennard-Jones parameters are used for the intra-point charges interactions and the point charges to quantum nuclei interactions.

Two QM/MM cases are presented in Figure 6 where in one case a quantum hydrogen points towards a classical oxygen, and in the second case a quantum oxygen points towards a classical hydrogen. There is a very smooth transition between the two cases with only a minor difference at very short and unrealistic distances at room temperature. Furthermore the QM/MM and MM/MM cures are very similar with only a 0.02 eV difference at the minimum, with the MM/MM interactions stronger.

Figure 7 presents radial distribution functions (see eq. 96 pg. 48) of oxygen-to-oxygen distances between a single quantum water molecule and classical solvent molecules - where two different smoothing approaches are compared.

4.2 LONG-RANGE ELECTROSTATICS

The aim is to describe systems containing molecules and solvent interacting with a solid surface and it is therefore preferable to be able to treat periodically repeated systems. The objective is to approximate the external potentials of eqs. 36, 38 and 40 on the periodic lattice common to the real-space grid, quantum nuclei, and point-charges, respectively. The long-range truncation which follows is applied to the Coulombic part of E_{MM} only, and the associate long-range potential form of $v_{\text{MM}}^j(\tau_j^\gamma)$ derived. All steps in the derivation are applicable to the other Coulomb potentials of eq. 36 and 38, unless stated otherwise.

The summation over the periodic lattice is considered $\mathbf{a} = n\mathbf{l} = \{nl_x, nl_y, nl_z\}$ (see Figure 8) such that

$$E_{\text{MM}}^{\text{coul}} = \frac{1}{2} \sum_{i,j}^C \sum_{n=0} \frac{q_i q_j}{|\tau_{ij} + \mathbf{a}|} \quad (44)$$

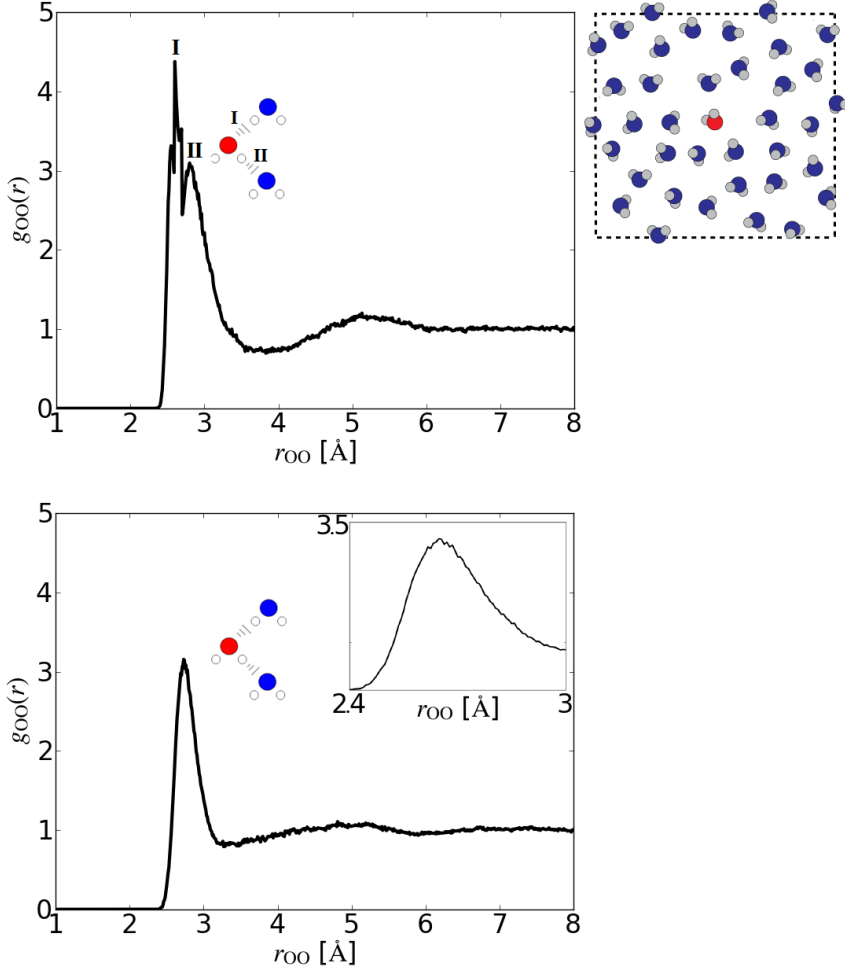


Figure 7: Radial distribution functions of a single quantum oxygen to classical oxygen atoms. **Top:** The smoothing of the potential via eq. 37 is atom specific - different γ_i values are used for different types of atoms. This is the form presented by Laio et. al. [74], but in our case gives very asymmetric hydrogen bonds when I) a quantum oxygen interacts with a classical hydrogen and II) a quantum hydrogen binds with a classical oxygen. **Bottom:** A single value is used for γ , here 0.2 \AA . This was found to give a consistent hydrogen binding energy between the two cases, as evident in the smooth first peak as well as the potential energy presented in Figure 6.

where the vector $\mathbf{n} = (n_x, n_y, n_z)$ denotes the three-dimensional periodicity of the simulation cell, of side lengths $\mathbf{l} = (l_x, l_y, l_z)$. The prime indicates that at $\mathbf{n} = 0$ one has $i \neq j$, and $\sum_{i,j}^C = \sum_i^C \sum_j^C$. It is well known that a direct truncation at some R_c of eq. 44

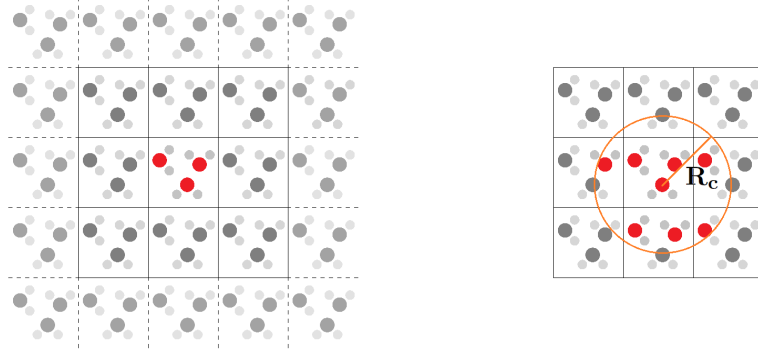


Figure 8: A typical simulation consist of atomic objects, and a well defined simulation cell of dimension l_x , l_y and l_z . For a (semi-)infinite simulation the periodic lattice is referred to as $\mathbf{a} = n\mathbf{l} = \{nl_x, nl_y, nl_z\}$. **Left:** Schematic of the real-reciprocal space Ewald summation. Depending on the system, a typical Ewald summation includes at least the nearest neighbors in the real space part, plus a reciprocal sum which extends much greater (e.g. $n = 9$). **Right:** Truncated Wolf scheme. For a system where $R_c < l_x, l_y, l_z$, the Wolf method amounts to a single real-space summation over the nearest neighbor cells only. All interactions are treated within the given sphere, which is the true form of the Coulomb potential, whereas Ewald methods have a cubic cut-off scheme. A spherical scheme also comes more naturally to disordered (dynamic) systems.

$$E_{MM}^{\text{coul}} \approx \frac{1}{2} \sum_{\substack{i,j \neq i \\ \tau_{ij} \leq R_c}}^C \sum_{\substack{n=0 \\ |\tau_{ij} + \mathbf{a}| \leq R_c}} \frac{q_i q_j}{|\tau_{ij} + \mathbf{a}|} \quad (45)$$

leads to severe errors in the electrostatics between periodically repeated images. The problem of approximating such infinite summations is a most often solved with the Ewald summation technique (original paper [60]) [80, 81, 82, 83, 84, 85, 86]. The general strategy here is to recast eq. 44 to a manageable form with separate short and long range components

$$E_{MM}^{\text{coul}} = \frac{1}{2} \sum_{n=0}^C \left[\sum_{i,j} \frac{q_i q_j}{\tau_{ij}} d(\tau_{ij}) + \sum_{i,j} \frac{q_i q_j}{\tau_{ij}} [1 - d(\tau_{ij})] \right]_{\tau_{ij} = |\tau_{ij} + \mathbf{a}|} \quad (46)$$

and the idea is that the first part converges rapidly in real-space, and the latter in reciprocal space. Such convergence is achieved defining

$$d(\tau_{ij}) = \text{erf}(\kappa \tau_{ij}) \quad (47)$$

consequently

$$[1 - d(\tau_{ij})] = \text{erfc}(\kappa \tau_{ij}) \quad (48)$$

in eq. 46. A Fourier transform of the error function gives a reciprocal sum, and finally κ is the splitting coefficient which controls how rapidly the real and reciprocal sums converge. This parameter is often optimized to minimize or divide equally the computational load for the real and reciprocal space sums of eq. 46.

Instead, the strategies of [74, 87, 81, 80, 88] are followed, who use a simpler scheme yet retain comparable accuracy in ionic and polar solvent systems compared to the full Ewald summation. The scheme is based on the work of Wolf et. al. [89], and presents a direct summation of the Coulomb terms with linear scaling ($O(N)$). Further implementations and comparisons between the Ewald and Wolf method can also be found here [90, 91, 92]. In their original work they noted that the Coulomb interactions of the systems under scrutiny; systems comprised of ordered and disordered polar media like crystals, liquids and interfaces; showed Coulomb asymptotic behavior of order r^{-5} due to strong charge screening effects. By applying a careful charge neutralization procedure for each particle of the system nice asymptotic behavior was realized, and a suitable real-space cut-off, R_c , found.

4.2.1 The Wolf Scheme

First the electrostatic energy as felt by a single point-charge j is considered

$$E_j^{\text{coul}} = \sum_{i \neq j}^{C'} \frac{q_i q_j}{\tau_{ij}} \quad (49)$$

where C' indexes the point charges in the original cell plus all point charges in neighbor cells (see Figure 8). Simply truncating at some cut-off value R_c leads to well known error, but here Wolf et. al. introduced a charge neutralization term specific to each particle j of the system, E_j^{neu}

$$E_j^{\text{coul}} = \sum_{\substack{i \neq j \\ \tau_{ij} \leq R_c}}^{C'} \frac{q_i q_j}{\tau_{ij}} - E_j^{\text{neu}} + O(R_c^{-2}) \quad (50)$$

with errors of the order of R_c^{-2} . What the charge neutralization amounts to is to find the limit of the potential in eq. 49 at the cut-off distance. This defines the image charge on the truncation surface around point charge j as

$$\Phi_j = \sum_{\substack{i \neq j \\ \tau_{ij} \leq R_c}}^{C'} \frac{q_i}{R_c} \quad (51)$$

and the correction term becomes simply

$$E_j^{\text{neu}} \equiv q_j \Phi_j \quad (52)$$

So to sum up, the electrostatic potential energy as felt by point charge j is corrected with the image charge potential on the truncation surface defined by R_c centered on j .

4.2.2 Periodic Summation

Continuing on with the periodic treatment of eq. 44 a cut-off at R_c is applied to the smoothed potential form of eq. 40 without the Wolf correction, and retain the basic non-smoothed Coulomb summation beyond the cut-off

$$E_{\text{MM}}^{\text{coul}} = \frac{1}{2} \sum_i^{C'} \left(\sum_{\substack{j \neq i \\ \tau_{ij} \leq R_c}}^{C'} \frac{q_i q_j}{\tau_{ij}^\gamma} + \sum_{\substack{j \neq i \\ \tau_{ij} > R_c}}^{C'} \frac{q_i q_j}{\tau_{ij}} \right) \quad (53)$$

with the view that at a sufficient cut-off length $1/\tau_{ij}^\gamma \approx 1/\tau_{ij}$. Here one is free to add and subtract the Coulomb interactions within the cut-off sphere defined by R_c such that

$$E_{\text{MM}}^{\text{coul}} = \frac{1}{2} \sum_i^{C'} \left(\sum_{\substack{j \neq i \\ \tau_{ij} \leq R_c}}^{C'} \frac{q_i q_j}{\tau_{ij}^\gamma} + \sum_{\substack{j \neq i \\ \tau_{ij} > R_c}}^{C'} \frac{q_i q_j}{\tau_{ij}} + \sum_{\substack{j \neq i \\ \tau_{ij} \leq R_c}}^{C'} \frac{q_i q_j}{\tau_{ij}} - \sum_{\substack{j \neq i \\ \tau_{ij} \leq R_c}}^{C'} \frac{q_i q_j}{\tau_{ij}} \right) \quad (54)$$

Combining the two middle terms effectively recovers eq. 44, resulting in

$$E_{\text{MM}}^{\text{coul}} = \frac{1}{2} \sum_i^{C'} \left(\sum_{\substack{j \neq i \\ \tau_{ij} \leq R_c}}^{C'} \frac{q_i q_j}{\tau_{ij}^\gamma} - \sum_{\substack{j \neq i \\ \tau_{ij} \leq R_c}}^{C'} \frac{q_i q_j}{\tau_{ij}} \right) + \frac{1}{2} \sum_{i,j}^C \sum_{n=0}^{\infty} \frac{q_i q_j}{|\tau_{ij} + \mathbf{a}|} \quad (55)$$

The first two terms on the rhs. require the charge neutralization term of eq. 52 to complete, whereas the last part is here recast in to two parts as in eq. 46, which is the general procedure for the Ewald summation based methods

$$E_{(1)} = \frac{1}{2} \sum_{i,j}^C \sum_{n=0} \left(\frac{q_i q_j \operatorname{erfc}(\kappa |\tau_{ij} + \mathbf{a}|)}{|\tau_{ij} + \mathbf{a}|} - \lim_{\tau_{ij} \rightarrow 0} \left\{ \frac{1}{2} \sum_i^C \frac{q_i^2 \operatorname{erf}(\kappa \tau_{ij})}{\tau_{ij}} \right\} \right) \quad (56)$$

$$E_{(2)} = \frac{1}{2} \sum_{i,j}^C \sum_{n=0} \left(\frac{q_i q_j \operatorname{erf}(\kappa |\tau_{ij} + \mathbf{a}|)}{|\tau_{ij} + \mathbf{a}|} \right) \quad (57)$$

The second term on the rhs. of eq. 56 is the point self energy correction. Due to the Wolf correction method a proper choice of the splitting coefficient κ makes the $E_{(2)}$ term become negligible, and the more pronounced first term on the rhs. of $E_{(1)}$ can then be treated with the simple charge neutralization procedure along with the parenthesis on the rhs. of eq. 55.

Replacing the periodic summation in eq. 55 with eq. 56, and applying the truncation and neutralization one arrives at

$$E_{MM}^{\text{coul}} \approx \frac{1}{2} \sum_i^{C'} \sum_{\substack{j \neq i \\ \tau_{ij} \leq R_c}}^{C'} \left(\frac{q_i q_j}{\tau_{ij}^\gamma} - \frac{q_i q_j}{\tau_{ij}} + \frac{q_i q_j \operatorname{erfc}(\kappa \tau_{ij})}{\tau_{ij}} \right) \quad (58)$$

$$- \lim_{\tau_{ij} \rightarrow R_c} \left\{ \frac{q_i q_j}{\tau_{ij}^\gamma} - \frac{q_i q_j}{\tau_{ij}} + \frac{q_i q_j \operatorname{erfc}(\kappa \tau_{ij})}{\tau_{ij}} \right\} \quad (59)$$

$$- \left(\frac{1}{2R_c^\gamma} - \frac{1}{2R_c} + \frac{\operatorname{erfc}(\kappa R_c)}{2R_c} + \frac{\kappa}{\sqrt{\pi}} \right) \sum_i^C q_i^2 \quad (60)$$

where the last line represents the self-energy terms. Here, a general smoothed and truncated point charge potential can be defined, acting on some point r_j , as

$$v_{MM}(r_j) = \frac{\delta E_{MM}}{\delta q_j} = \sum_{\substack{i=1 \\ r_{ij} \leq R_c}}^{C'} q_i \left(\frac{1}{r_{ij}^\gamma} - \frac{1}{r_{ij}} + \frac{\operatorname{erfc}(\kappa r_{ij})}{r_{ij}} \right) \quad (61)$$

$$- \lim_{r_{ij} \rightarrow R_c} \left\{ \frac{1}{r_{ij}^\gamma} - \frac{1}{r_{ij}} + \frac{\operatorname{erfc}(\kappa r_{ij})}{r_{ij}} \right\} \quad (62)$$

which is also the final form for eq. 31 and eq. 33 in the periodic lattice, one simply changes the coordinate variable.

The total potential energy of the QM/MM system, eq. 28, with smearing and in a periodic lattice can then be written as

$$\begin{aligned}
E_{\text{tot}} = & E_{\text{KS}}[n(\mathbf{r}), v_{\text{MM}}[\mathbf{r}, \tau_i]] + \sum_{\alpha=1}^A Z_{\alpha} v_{\text{MM}}[\mathbf{R}_{\alpha}, \tau_i] + E_{\text{LJ}}[\mathbf{R}_{\alpha}, \tau_i] \\
& + \frac{1}{2} \sum_{j \neq i}^C q_j v_{\text{MM}}[\tau_j, \tau_i] + E_{\text{LJ}}[\tau_j, \tau_i] \quad (63)
\end{aligned}$$

4.3 FORCES

To derive the forces one first rewrites eq. 29 to include the general smoothed and truncated potential of eq. 62

$$E_{\text{QM/MM}} = \int d\mathbf{r} v_{\text{MM}}[\tau_i, \mathbf{r}] n(\mathbf{r}) + \sum_{\alpha=1}^A Z_{\alpha} v_{\text{MM}}[\tau_i, \mathbf{R}_{\alpha}] + E_{\text{LJ}}[\mathbf{R}_{\alpha}, \tau_i] \quad (64)$$

so for the quantum nuclei the forces are derivatives of eq. 28 with respect to their position, with the $E_{\text{QM/MM}}$ expression above

$$F_{\alpha} = -\frac{\delta E_{\text{KS}}[\mathbf{R}_{\alpha}]}{\delta \mathbf{R}_{\alpha}} - \frac{\delta E_{\text{QM/MM}}[\mathbf{R}_{\alpha}, \tau_i]}{\delta \mathbf{R}_{\alpha}} \quad (65)$$

The first term on the rhs. is solved for by GPAW, however with the point-charge potential included in the effective KS potential, eq. 32

$$E_{\text{KS}} = \dots - \frac{1}{2} \int v_{\text{eff}}^{\text{tot}}(\mathbf{r}) n(\mathbf{r}) d\mathbf{r} - \dots \quad (66)$$

Subsequently the force component due to the external potential becomes (cf. [18])

$$-\frac{E_{\text{KS}}[\mathbf{R}_{\alpha}]}{\delta \mathbf{R}_{\alpha}} = \dots - 2\Re \sum_{\mu \in \alpha; \nu} \left[\int \frac{d\Phi_{\mu}^*(\mathbf{r})}{d\mathbf{R}_{\alpha}} v_{\text{eff}}^{\text{tot}} \Phi_{\nu}(\mathbf{r}) d\mathbf{r} \right] n_{\mu\nu} - \dots \quad (67)$$

and so the action of the MM field on the quantum electronic density is felt by the nuclei through this electronic force term. The second term on the rhs. of eq. 65 reads

$$-\frac{\delta E_{\text{QM/MM}}[\mathbf{R}_{\alpha}, \tau_i]}{\delta \mathbf{R}_{\alpha}} = -Z_{\alpha} \frac{\delta v_{\text{MM}}[\mathbf{R}_{\alpha}, \tau_i]}{\delta \mathbf{R}_{\alpha}} - \frac{\delta E_{\text{LJ}}[\mathbf{R}_{\alpha}, \tau_i]}{\delta \mathbf{R}_{\alpha}} \quad (68)$$

so in total the force components for the quantum nuclei can be divided in to these three terms

$$F_{\alpha}^{\text{tot}} = F_{\alpha}^{\text{ele}} + F_{\alpha}^{\text{MM}} + F_{\alpha}^{\text{LJ}} \quad (69)$$

where F_{α}^{MM} and F_{α}^{LJ} are the derivatives on the rhs. of eq. 68. F_{α}^{LJ} is a simple derivative of the general LJ expression, and as noted before does not receive any special treatment when simulation periodically

repeated systems. The F_{α}^{MM} term is the derivative of eq. 62, which includes taking a limit at the cut-off. The work of Ma et. al. [81] is followed, and the derivative is first evaluated, followed by applying the limit, so this term becomes

$$F_{\alpha}^{\text{MM}} = -Z_{\alpha} \sum_{\substack{i=1 \\ r_{i\alpha} \leq R_c}}^{C'} q_i \left(\frac{1}{dr_{i\alpha}^{\gamma}} - \frac{1}{r_{i\alpha}^2} - \frac{\text{erfc}(\kappa r_{i\alpha})}{r_{i\alpha}^2} - \frac{2\kappa \exp(-\kappa^2 r_{i\alpha}^2)}{\sqrt{\pi} r_{i\alpha}} \right. \\ \left. + \frac{1}{dR_c^{\gamma}} + \frac{1}{R_c^2} - \frac{\text{erfc}(\kappa R_c)}{R_c^2} - \frac{2\kappa \exp(-\kappa^2 R_c^2)}{\sqrt{\pi} R_c} \right) \quad (70)$$

with $1/dr_{i\alpha}^{\gamma}$ referring to the derivative of the smearing expression in eq. 37 with respect to, here, the coordinate of the quantum nuclei.

Although such sequence of operations do not commute - finding the derivative and then applying the cut-off limit - Ma et. al. observed only a minor upward shift in the potential energy during the course of NVE molecular dynamics with the forces derived in analogous manner. Furthermore, Zahn et. al. [87] re-derived the potential expression by integrating over the forces derived in this fashion, such as to exactly match the potential to the forces, but for all intents and purposes the potential derived deviates only slightly from the potential in eq. 62. Figure 9 compares our potential descriptions to the one of Zahn et. al.

For the classical degrees of freedom the derivative of eq. 64 is again evaluated but now with respect to the position of the point charges

$$-\frac{\delta E_{\text{QM/MM}}[\mathbf{R}_{\alpha}, \tau_i]}{\delta \tau_i} = - \int n(\mathbf{r}) \frac{\delta v_{\text{MM}}[\mathbf{r}, \tau_i]}{\delta \tau_i} - Z_{\alpha} \frac{\delta v_{\text{MM}}[\mathbf{R}_{\alpha}, \tau_i]}{\delta \tau_i} - \frac{\delta E_{\text{LJ}}[\mathbf{R}_{\alpha}, \tau_i]}{\delta \tau_i} \quad (71)$$

Here the first term on the rhs. requires a numerical integration and is the most time consuming step of the QM/MM procedure. The second term is of the same generic form as in eq. 70, but now the sum runs over the quantum-nuclei

$$F_i^{\text{nuc}} = -q_i \sum_{\substack{\alpha=1 \\ r_{i\alpha} \leq R_c}}^{A'} Z_{\alpha} \left(\frac{1}{dr_{i\alpha}^{\gamma}} - \frac{1}{r_{i\alpha}^2} - \frac{\text{erfc}(\kappa r_{i\alpha})}{r_{i\alpha}^2} - \frac{2\kappa \exp(-\kappa^2 r_{i\alpha}^2)}{\sqrt{\pi} r_{i\alpha}} \right. \\ \left. + \frac{1}{dR_c^{\gamma}} + \frac{1}{R_c^2} - \frac{\text{erfc}(\kappa R_c)}{R_c^2} - \frac{2\kappa \exp(-\kappa^2 R_c^2)}{\sqrt{\pi} R_c} \right) \quad (72)$$

and it is understood that A' represents the expansion of quantum-nuclei in the origin of the periodic system as well as in nearest neighbor periodic images (see Figure 8). In addition to the QM/MM part

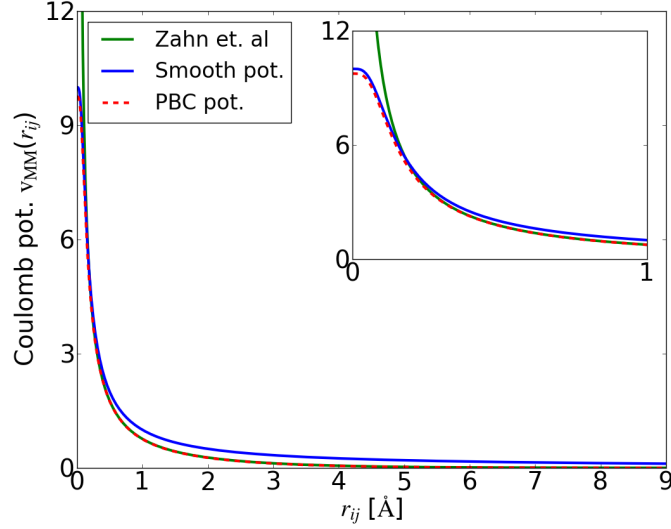


Figure 9: The blank potential expressions. Blue curve is the basic Coulomb potential including the smoothing - eq. 38. The red broken curve is the Coulomb potential with the charge neutralization and cut-off applied - eq. 62. The green curve is a similar potential where the Wolf method is used, but no smoothing - here they derived the forces first, which are analogous to our forces without the smoothing - and then derived the potential by integrating the resulting forces, resulting in the green curve. The inset shows the region where the smooth potential transition into the basic r^{-1} form.

the classical point charges interact with each other through the last two terms of eq. 63. The Coulomb part reads

$$\begin{aligned}
 F_i^{\text{MM}} = & -q_i \sum_{\substack{j \neq i \\ \tau_{ij} \leq R_c}}^{C'} q_j \left(\frac{1}{d\tau_{ij}^\gamma} - \frac{1}{\tau_{ij}^2} - \frac{\text{erfc}(\kappa\tau_{ij})}{\tau_{ij}^2} - \frac{2\kappa \exp(-\kappa^2\tau_{ij}^2)}{\sqrt{\pi} \tau_{ij}} \right. \\
 & \left. + \frac{1}{dR_c^\gamma} + \frac{1}{R_c^2} - \frac{\text{erfc}(\kappa R_c)}{R_c^2} - \frac{2\kappa \exp(-\kappa^2 R_c^2)}{\sqrt{\pi} R_c} \right) \quad (73)
 \end{aligned}$$

To sum up, one can write the total force acting on point charge i as

$$F_i^{\text{tot}} = F_i^{\text{ele}} + F_i^{\text{nuc}} + F_i^{\text{MM}} + F_i^{\text{LJ}} \quad (74)$$

where F_i^{ele} and F_i^{nuc} are the forces due to the interaction between the point charges and the charge density of the quantum system, F_i^{MM} the Coulomb interaction among the point charges, and finally both the QM/MM and MM/MM Lennard-Jones terms are collected in to F_i^{LJ} .

Figure 10 presents an analysis of the forces observed in a molecular dynamics simulation (discussed in Chapter 5) for a mixed QM/MM

system employing the Wolf scheme. The forces are summed over all of the atoms and ideally should sum up to zero, but due to computational noise, approximations in the QM/MM forces such as the cut-off scheme and the treatment of the forces in the QM code GPAW (see for example [18]) the forces from the various sources do not cancel, and potential energy is not conserved. This results in for example a steady increase in temperature (or rather potential energy) during molecular dynamics simulations of the fixed number of particle, volume and potential energy (NVE) type - the drift was recorded at 10^{-5} – 10^{-7} eV/ps per atom for simulations employing this particular QM/MM implementation.

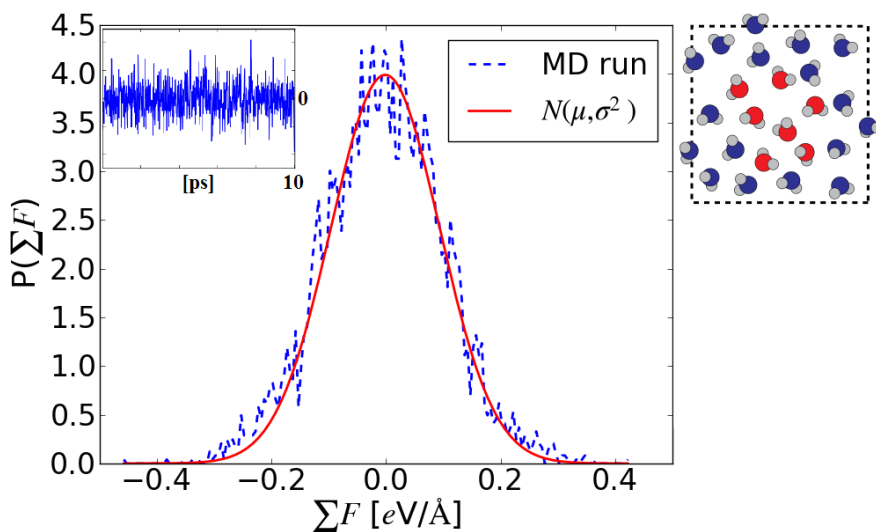


Figure 10: The distribution of the sum over all forces, $P(\sum \mathbf{F})$, for a typical QM/MM run; here of a cluster of quantum mechanically described water surrounded by a classical, or TIP3P, water. The inset shows the fluctuation over a 10 ps molecular dynamics simulation. A normal distribution, $N(\mu, \sigma^2)$, is fitted to the data giving $\mu = 0.005$ - hence, during NVE dynamics the potential energy increases in accordance with the residual value. Due to the friction and collision terms in the Langevin-dynamics (presented in Chapter 5) the sum over the forces have a normal distribution - this means that simulation employing the Langevin thermostat are very stable and, due to the temperature dependence of the basic Langevin equations any increase in the potential energy is dissipated.

MOLECULAR DYNAMICS

In molecular dynamics simulations the motion of the particles - point charges, quantum nuclei or the like - are calculated using the laws of classical mechanics. This involves solving a system of second-order differential equations that follow Newton's second law, which can be written for some particle i as

$$m_i \frac{d^2 x_i(t)}{dt^2} = \sum_j \mathbf{F}_{ij} + \sum_\alpha \mathbf{F}_{i\alpha} + \sum \mathbf{F}_{\text{ext},i} \quad (75)$$

where m_i and $x_i(t)$ are the mass of the particle and its position at time t . The force vectors are derived from the gradient of the various potential energy functions introduced in the previous sections; for example the \mathbf{F}_{ij} and $\mathbf{F}_{i\alpha}$ represent forces derived from two-body interactions such as the Coulomb and Lennard-Jones potentials of eq. 26. The $\mathbf{F}_{\text{ext},i}$ term accounts for the forces due to the electronic density of a coupled QM system acting on say point charge i (eq. 62), as well as other external sources if appropriate.

5.1 CONSTANT TEMPERATURE MOLECULAR DYNAMICS

Langevin dynamics approximate the canonical ensemble by including both a friction and collision term, which mediate kinetic energy in to the system. This allows one to control the average temperature during the dynamic simulation. The basic formulation is

$$m_i \frac{d^2 x_i(t)}{dt^2} = \mathbf{F}_i(x(t)) - \gamma m_i \frac{dx_i(t)}{dt} + \sqrt{2k_B T \gamma m_i} dW(t) \quad (76)$$

where $\mathbf{F}(x(t))$ are the forces collected in eq. 75 above, k_B is the Boltzmann constant, $\gamma > 0$ is a friction coefficient and $dW(t)$ is white noise - a stochastic process or Brownian motion. The second and third term on the rhs. describe friction and collision, respectively. T is here the desired temperature, which is usually reached in molecular dynamics simulations of this type after a few picoseconds of simulation time. In the canonical ensemble the number of particle, volume and temperature of the system is fixed. Under these conditions the partition function of the system is given by [93]

$$Z(N, V, T) = \frac{1}{\Lambda^{3N} N!} \int d\mathbf{R}^N e^{-\beta E(\mathbf{R}^N)} \quad (77)$$

where $\Lambda = \sqrt{\hbar^2/(2\pi m k_B T)}$ is the thermal de Broglie wavelength. This defines the absolute free energy of the system

$$F = -k_B T \ln(Z) \quad (78)$$

and probabilities of observing a particular coordinate R^N are given by

$$P(R^N) = \frac{e^{-\beta E(R^N)}}{Z} \quad (79)$$

Free energy analysis based on the canonical ensemble are then rooted in the simple relations above, and are discussed in more detail in Chapter 6.

The basic approach to eq. 76 is by solving a stochastic differential equation of the form

$$\begin{cases} dx_i(t) = v_i(t) dt \\ dv_i(t) = (m_i^{-1} F_i(x(t)) - \gamma v_i(t)) dt + \sqrt{2k_B T \gamma m_i^{-1}} dW_i(t) \end{cases} \quad (80)$$

and there are several accurate approximations in the literature to the trajectories of $x_i(t)$ and $v_i(t)$ via. time discretization of the equations above. The most popular being the ones of van Gunsteren and Berendsen (vGB) [94] and Brünger-Brook-Karplus (BBK) [95].

5.1.1 Langevin Integrator with Holonomic-Constraints

For this work a particular integrator is selected which is generalized to the case of holonomic-constraints. This is from the work of V.-Eijnden et. al. [96], which includes a step-by-step derivation and error analysis - and in the form presented there is accurate to second order in the time step dt . The integrator is in the following form

$$\begin{cases} x_i^{n+1} = x_i^n + v_i^n dt + A_i^n - \sum_{j=1}^{C'} \mu_{ij}^n r_{ij}(x_i^n) \\ v_i^{n+1} = v_i^n + \frac{1}{2}(f_i(x^{n+1}) + f_i(x^n)) dt - \gamma v_i^n dt + \sqrt{dt} \sigma_i \xi_i^n - \gamma A_i^n \\ \quad - dt^{-1} \sum_{j=1}^{C'} (\mu_{ij}^* r_{ij}(x^{n+1}) + \mu_{ij}^n r_{ij}(x^n)) \end{cases} \quad (81)$$

where $f_i(x^n) = m_i^{-1} F_i(x^n)$, $\sigma_i = \sqrt{2k_b T \gamma m_i^{-1}}$ and

$$A_i^n = \frac{1}{2}(f_i(x^n) + \gamma v_i^n) dt^2 + \sigma dt^{3/2} \left(\frac{1}{2} \xi_i^n + \frac{1}{2\sqrt{3}} \eta_i^n \right) \quad (82)$$

In the integrator above the white noise term has been replaced with (ξ_i^n, η_i^n) . These numbers are generated from a normal distribution $(N(\mu, \sigma^2))$, with mean zero and covariance

$$\mathbb{E}(\xi_i^n, \xi_j^n) = \mathbb{E}(\eta_i^n, \eta_j^n) = \delta_{ij}, \quad \mathbb{E}(\xi_i^n, \eta_j^n) = 0$$

Finally, the coefficients μ_{ij} and μ_{ij}^* - defined below - adjust the position and velocity vectors such that bond length constraints are conserved. Note that by setting $\gamma = 0$ the procedure above reduces to the well know Verlet-integrator [97], which can be used to sample the microcanonical ensemble - fixed number of particles, volume and potential energy ($Z(N, V, E)$).

In order to run an algorithm based on the expression above the forces are calculated for some initial coordinate, $x(t = 0)$, and the molecules of the system are given a thermal kick based on the Maxwell-Boltzmann distribution (see for example Figure 13 and eq. 94, pg. 47) to give $v_i(t = 0)$. Using this x_i^{n+1} are generated for all atoms i of the system and the next set of forces or f_i^{n+1} calculated - the velocity is then updated to v_i^{n+1} .

5.1.1.1 Holonomic-Constraints

Holonomic constraints are rigid - or fixed bond length constraints - which can be expressed as simple functions of the coordinates

$$f(x_1, x_2, \dots, x_N, t) = 0 \quad (83)$$

Velocity dependent constraints can be written as

$$f(x_1, x_2, \dots, x_N, v_1, v_2, \dots, v_N, t) = 0 \quad (84)$$

and are usually not holonomic unless the velocity dependence can be integrated out. The RATTLE scheme [98] is one such approach in which the constraints are of the following simple form

$$(x_i - x_j)^2 - d_{ij}^2 = 0 \quad (85)$$

where x_i and x_j are the position of particle i and j , and d_{ij} is the desired distance.

In the RATTLE scheme the approach is as follows; after generating the next set of coordinates, x^{n+1} , the current distance vector between pair i and j is tabulated, s_{ij} , and the coordinates x^{n+1} updated again using

$$\mu_{ij}^n = \frac{[s_{ij}^2 - d_{ij}^2]}{2dt |s_{ij} \cdot r_{ij}(x^n)| (m_i^{-1} + m_j^{-1})} \quad (86)$$

This process is iterated over all atom pairs where constraints apply - until a certain convergence criteria is met. With x^{n+1} available the velocities are updated to v^{n+1} , and the velocity dependent coefficients determined by

$$\mu_{ij}^* = r_{ij}(x^{n+1}) \cdot \frac{[v_i^{n+1} - v_j^{n+1}]}{d_{ij}^2 (m_i^{-1} + m_j^{-1})} \quad (87)$$

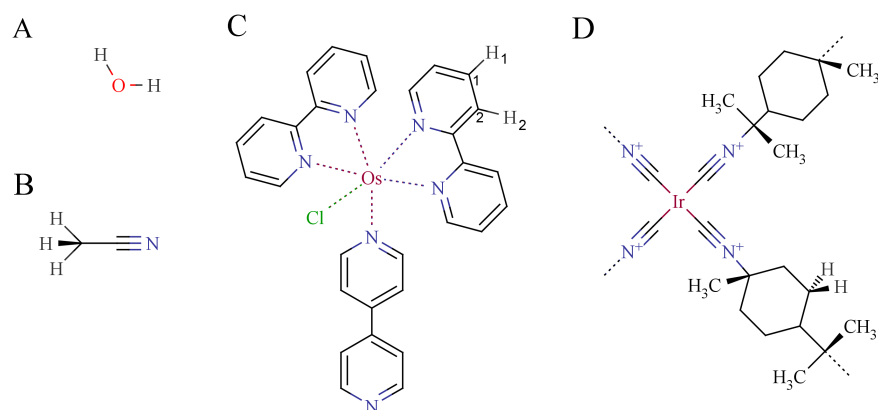


Figure 11: Schematic of the various molecules addressed in this study. With the hydrogen bond lengths fixed in the ways listed below molecular dynamics simulations with Langevin-RATTLE code are stable up to 6 fs in the time step (dt), although rarely exceed 2 fs in our simulations. **A:** Water is treated both quantum mechanically and classically in the various molecular dynamics runs presented in this thesis. In both cases the oxygen to hydrogen bond length and the hydrogen-to-hydrogen distance is fixed (which fixes the angle as well) - and set to the TIP3P [52] values in mixed QM/MM systems. **B:** Acetonitrile, which is also in parts treated fully quantum mechanically and classically, has the following constraints: the $C\equiv N$, H_3C-C and H_2C-H bond lengths are fixed, as well as the distance between the hydrogens in the methyl group. **C:** The polypyridine osmium complex has several carbon-hydrogen bonds which are constraint, but they are all a part of the same substructure $-HC=CH-$ and hence only a single constraint scheme is applied where the bond between H_1-C_1 and distance between H_1-C_2 is fixed (and similarly for H_2). The second constraint ensures that the distance between H_1 and H_2 has a minimum value, but does not suppress all vibrational modes. **D:** All C-H and H-H distances belonging to the same alkane group are fixed.

and a similar iterative process applies where each constraint in a pre-described list is treated until converged.

Figure 11 shows the solvents and complexes used and studied in the thesis and presents the various constraints applied to the hydrogens in different geometries. Figure 121 presents a typical temperature profile for a Langevin-RATTLE molecular dynamics run. The system is composed of a hexaaqua iron complex, which is described with QM, and 25 classical water molecules - the oxygen to hydrogen bond lengths and angles are fixed. The effects of the constraints on instantaneous temperature during simulations is discussed below.

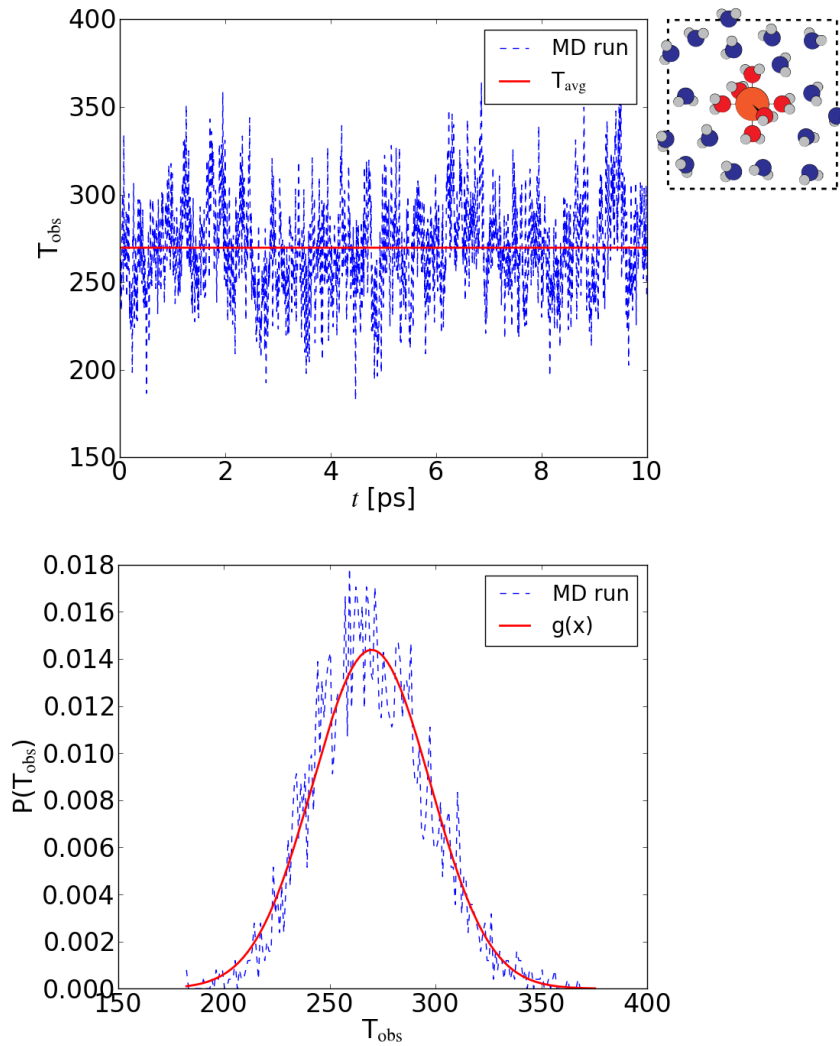


Figure 12: **Top:** A typical instantaneous temperature profile over the course of 10 ps of Langevin-RATTLE dynamics, blue broken line. The average temperature, T_{avg} - red line, is found to be 267.3 K and the target temperature is 268.3 K (400 K without the constraints, see text for details). A schematic of the system is presented to the right. **Bottom:** the normalized distribution of temperatures, which has a variance, σ_T , of here 27.7 K estimated from eq. 91. The red curve is the Gaussian distribution function which describes the density function of a normally distributed random variable - where the curves parameters are T_{avg} , and σ_T .

5.1.2 Molecular Constraints and Instantaneous Temperature

The observed temperature in simulations employing molecular constraints is directly proportional to the degrees of freedom. The instantaneous temperature at time step t , $T(t)$, follows directly from the kinetic energy

$$\frac{3}{2}Nk_B T(t) = \sum_{i=1}^N \frac{m_i v_i^2(t)}{2} = E_{\text{kin}}(t) \quad (88)$$

where k_B is the Boltzmann constant, N is the number of particles in the system and $v_i(t)$ is the velocity. The factor 3 on the lhs. accounts for the degrees of freedom associated with each particle.

The observed temperature in constraint MD runs - which is say is aimed at T' - is

$$T_{\text{obs}} = T' \frac{N_{\text{act}}}{N_{\text{TOT}}} \quad (89)$$

where N_{TOT} is simply $3N$, and N_{act} the number of active degrees of freedom - for example a water molecule has $N_{\text{TOT}} = 3 * 3$, which is reduced to $N_{\text{act}} = 3 * 3 - 3$ when the three vibrational modes are suppressed by fixing the bond lengths.

In constant temperature molecular dynamics which obey Boltzmann statistics the relative variance in the kinetic energy of each particle is

$$\frac{\sigma_p^2}{\langle p^2 \rangle^2} = \frac{2}{3} \quad (90)$$

where $p = mv$, and p^2 is the second moment of the Maxwell-Boltzmann velocity distribution (MBD) [93]. This means that for a finite system the instantaneous temperature fluctuates, with a relative variance of

$$\frac{\sigma_T^2}{\langle T \rangle^2} = \frac{2}{3N} \quad (91)$$

Figure 12 presents the probability of observing a particular temperature, $P(T_{\text{obs}})$, from the $T_{\text{obs}}(t)$ recorded from the molecular dynamics run. Also plotted is the probability density function of a normally distributed random variable, here T_{obs} , which is a Gaussian function

$$g(x) = \frac{1}{\sigma_T \sqrt{2\pi}} e^{-\frac{1}{2} \left(\frac{x - T_{\text{avg}}}{\sigma_T} \right)^2} \quad (92)$$

and is centered on T_{avg} with a variance estimated with eq. 91. Note that there is no fitting, the Gaussian function is plotted with these parameters alone which are estimated from the data set of the MD run. In this particular case the system is composed of the single metal ion and 31 water molecules - and each water molecule is constraint as discussed above such that the active degrees of freedom are $N_{\text{act}} = 3 + 6 * 31$.

The temperature is aimed at 400 K - but due to the constraints should be according to eq. 89 on average 268.3 K. From the actual simulations T_{avg} is found to be 267.3 K - with a variance of $\sigma_T = 27.7$ K.

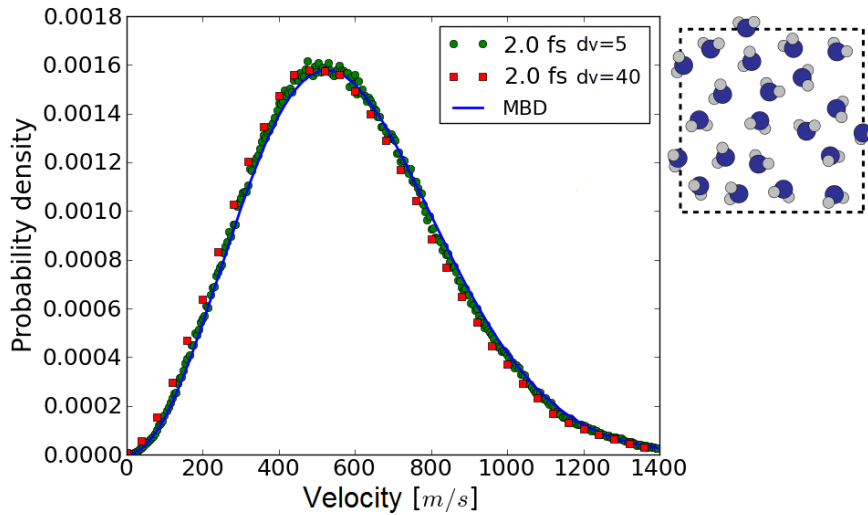


Figure 13: The Maxwell-Boltzmann distribution (MBD) of velocities, here for classical water described with the TIP₃P parameter set - during a typical constant temperature molecular dynamics simulation employing the Langevin-RATTLE constraint scheme. The variance in the observed distribution of temperatures, Figure 12, is directly proportional to the variance in momentum - derived from the analytical expression of the MBD - and as seen here the velocity profile for a typical simulation deviate only slightly.

These are the parameters used for the Gaussian distribution of eq. 92, which fits very nicely to the computational normalized distribution of observed temperature, $P(T_{\text{obs}})$.

As noted before the relative statistical variance of eq. 90 is derived from the second-moment of the Maxwell-Boltzmann velocity distribution

$$\langle p^2 \rangle = \int dp p^2 P(p) \quad (93)$$

and the distribution in analytic form is given by

$$P(p) = \left(\frac{\beta}{2\pi m} \right)^{3/2} e^{-\beta \frac{p^2}{2m}} \quad (94)$$

Figure 13 presents a comparison of the observed and analytical MBD for water molecules, where the distribution from the data is evaluated as

$$P(p') = \frac{1}{N_{\text{H}_2\text{O}} * n} \sum_{i=1}^{N_{\text{H}_2\text{O}}} \sum_{j=1}^n \delta(p' - p + dp) \quad (95)$$

where $N_{\text{H}_2\text{O}}$ and n are the number of unique water molecules and steps from the trajectory, and $dp = mdv$.

Simulations using the Langevin-RATTLE scheme implemented for this study do indeed produce the desired statistics; the observed temperature is directly related to the number of active degrees of freedom and vary in accordance with the second moment $\langle p^2 \rangle$ - statistical distribution produced during MD match the normal distribution of random variables.

5.1.3 Radial Distribution Functions

The radial distribution function (RDF) are generated for several systems - full quantum, classical and QM/MM - in the results section of this thesis, and are evaluated as

$$g(\mathbf{r}) = \sum_{\mathbf{I}} \sum_{\alpha} \frac{\delta(\mathbf{r} - \mathbf{r}_{i\alpha} \pm \mathbf{dr}) V_{\text{cell}}}{dV_{\text{sph}} N_{\alpha} N_{\mathbf{I}}} \quad (96)$$

where V_{cell} is the volume of the simulation cell, dV_{sph} is the spherical volume element: $4\pi r^2 dr$, and $N_{\mathbf{I}}$ and N_{α} are the number of images (configurations) and particles, respectively. The coordinate is the distance between a particular atom pair $i\alpha$.

5.1.3.1 QM/MM RDFs

Figures 14 and 15 presents radial distribution functions for water and acetonitrile - the solvents used in the majority of the simulations presented in later chapters. Both the systems and sampling methods are presented in the figure captions. The RDFs are compared between various MM and QM/MM levels. All in all there is good agreement between the various methods as well as to experiments or other computational work. Discrepancies are mainly due to, for example, the over-binding of hydrogen in GGA described water, as discussed in the caption of Figure 6.

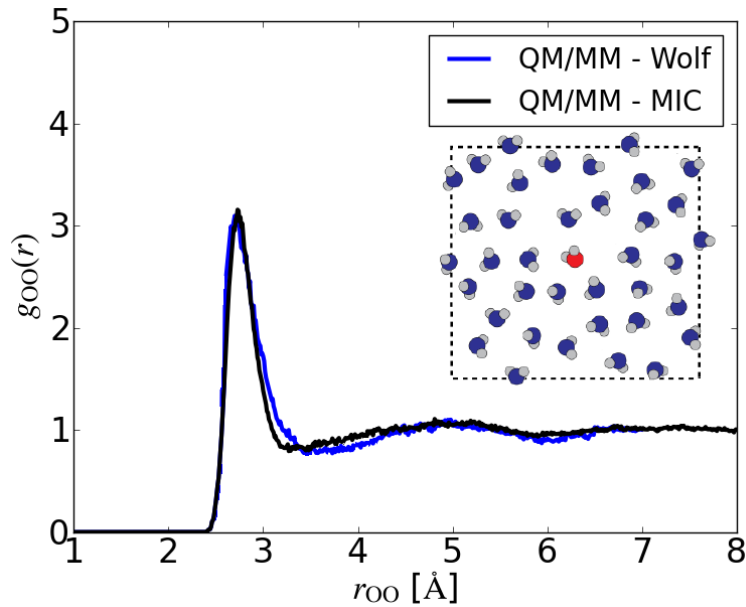


Figure 14: Radial distribution functions of the single quantum oxygen to all classical oxygen distances in mixed QM/MM calculations. Two periodic boundary conditions are employed - in the minimum image convention (MIC) no truncation is applied and the system interacts with nearest neighbor systems only. This is generally a good approximation when the system size is large (box sizes of at >18.0 Å in all directions). In such a simulation the system size can be in the thousands to tens of thousands of atoms since the bulk is treated classically - and is here for example for about 800 H_2O (but only a single quantum water molecule). The second simulation employs the Wolf truncation scheme - and is applied to a smaller system composed of 110 classical water molecules. The position of the first and second peak are almost the same in both cases - and are largely controlled by the interfacing hydrogen binding energy between the classical and quantum systems (Figure 6). The position of the maximum of the first peak is at 2.81 Å, with $g_{\text{OO}}(r)$ of value 3.13 . This compares nicely to experimental results which show a maximum for the first peak at 2.88 Å and $g_{\text{OO}}(r)$ of value 3.09 [99].

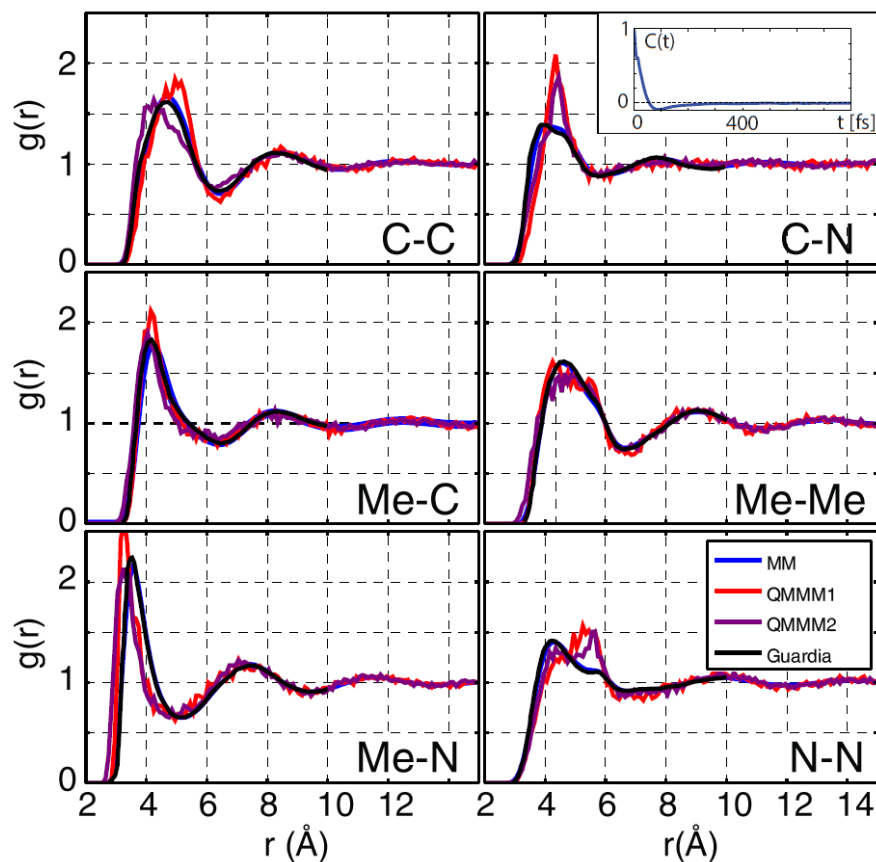


Figure 15: Radial distribution functions of the 6 intra-molecular distances in acetonitrile. The structural data used for the RDFs are taken from every 500th fs in molecular dynamics runs (Langevin-RATTLE) of 0.5 and 0.25 ns, for the MM and QM/MM systems, respectively. The QM/MM systems are comprised of a single QM acetonitrile in a bath of 290 classically described acetonitrile molecules. The thermostat is set to 300 K in. The inset depicts the velocity autocorrelation function which evens out to 0 at the 500th fs mark. Two sets of Lennard-Jones (LJ) parameters are used for the quantum mechanical acetonitrile: in QM/MM1 the parameters from the three-point interaction model of Guardia et. al. [53] are used. In QM/MM2 the LJ parameters for the methyl group are changed to the general sp^3 -carbon and hydrogen parameters (LJ parameters are presented in Table 1, pg. 23). The black curve is from the original paper on the three-point interaction model of acetonitrile [53]. In all cases there is a good agreement with the position and with of the first and second peak. The first peak is somewhat sharper in the case of nitrogen from the QM/MM simulations - but similar to water this is due to slight over binding.

In free energy analysis involving transition barriers and reorganization energy terms it is necessary to sample out of equilibrium configurations. Here the method to generate free energy surfaces in the context of electron charge transfer reactions is outlined, and two methods to efficiently sample the reaction coordinate discussed - which are compared in detail in Chapter 7. An optimized way of analyzing data from simulations of this type and to construct relative free energy surfaces is presented.

6.1 FREE ENERGY SURFACES

In diabatic ET theory a single charge is transferred from donor molecule or atom, D^1 , to acceptor molecule or atom of less absolute charge, A^0 . Together the donor and acceptor form the initial and final state



where in the final state the donor and acceptor have changed their electronic states. The potential energy of the initial state can be defined as

$$E_i(R^N) = U_i + V(R^N) + \epsilon_i(R^N) \quad (98)$$

where U_i is the gas phase energy of the solutes in the electronic configuration corresponding to the initial state. R^N denotes a nuclear configuration of solvent and solute. $\epsilon_i(R^N)$ denotes the interaction of the transferring charge with the solvent environment, and $V(R^N)$ is the solute-solvent interactions disregarding the transferring charge. The same definition is valid for the final state given that the chemical species D and A stay the same (i.e. no bond breaking or formation, nor magnetic state changes).

Assuming the above holds then for a given nuclear configuration R^N the solute-solvent interactions are the same in the initial and final state, so one can write

$$\begin{aligned} \Delta E(R^N) &= E_f(R^N) - E_i(R^N) \\ &= \Delta \epsilon(R^N) + U_f - U_i \end{aligned} \quad (99)$$

where

$$\Delta\epsilon(\mathbf{R}^N) = \epsilon_f(\mathbf{R}^N) - \epsilon_i(\mathbf{R}^N) \quad (100)$$

$\Delta\epsilon(\mathbf{R}^N)$ describes the difference between the interaction of the transferring charge with the solvent in initial and final state electronic configurations, for a given nuclear configuration \mathbf{R}^N .

The transition state nuclear coordinates can be defined in terms of the potential energy difference between the initial and final states as the configurations where the potential energy gap closes (Franck-Condon principle) $\Delta E(\mathbf{R}^N) = 0$. This means that at \mathbf{R}^\ddagger one has

$$\epsilon_f(\mathbf{R}^\ddagger) - \epsilon_i(\mathbf{R}^\ddagger) = -(\mathcal{U}_f - \mathcal{U}_i) \quad (101)$$

i.e. the nuclear configurations which close the initial-final state potential energy gap induce a change in the electronic interaction between the nuclear environment and transferring charge equal to the constant internal energy difference. To calculate the energy one must both sample numerous configurations as well as statistically unlikely configurations.

6.1.1 The Free Energy Function

Free energy is a thermodynamic state function, of e.g. $E_i(\mathbf{R}^N)$, and in the context of ET theory is a well defined free energy function of the potential energy difference of eq. 99

$$F_i(x) = -\frac{1}{\beta} \ln \int d\mathbf{R}^N \delta(x - \Delta E(\mathbf{R}^N)) \exp(-\beta E_i(\mathbf{R}^N)) \quad (102)$$

where $\beta = (k_B T)^{-1}$, the inverse of the thermal energy. The integral is the statistical mechanical probability of observing a particular value of x of the potential energy gap - which acts as the reaction coordinate - while the system is in the i state, or

$$F_i(x) = -\frac{1}{\beta} \ln[P_i(x)] + F_i^* \quad (103)$$

where F_i^* is the free energy of the state. This separation is achieved if one factors out the probability from eq. 102

$$P_i(x) = \frac{\int d\mathbf{R}^N \delta(x - \Delta E(\mathbf{R}^N)) \exp(-\beta E_i(\mathbf{R}^N))}{\int d\mathbf{R}^N \exp(-\beta E_i(\mathbf{R}^N))} \quad (104)$$

so the free energy can here be expressed as

$$F_i(x) = -\frac{1}{\beta} \ln[P_i(x)] - \frac{1}{\beta} \ln \int d\mathbf{R}^N \exp(-\beta E_i(\mathbf{R}^N)) \quad (105)$$

the second term on the rhs. defines F_i^* . This term is not computed in practice (or evaluate experimentally) but the first term and hence relative free energy and differences for this state are readily calculated. For example, the free energy transition state barrier is

$$\begin{aligned}\Delta F^\ddagger &= F_i(x^\ddagger) - F_i(x_{\min}) \\ &= F_i(\Delta E(R^\ddagger)) - F_i(\Delta E(R_{\min}^N))\end{aligned}\quad (106)$$

where x_{\min} gives the minimum of the F_i free energy surface.

The same definitions hold for the final state, e.g. it is a thermodynamic state function, and one can write the free energy function as

$$F_f(x) = -\frac{1}{\beta} \ln \int dR^N \delta(x - \Delta E(R^N)) \exp(-\beta E_f(R^N)) \quad (107)$$

which is analogous to eq. 102 and contains an unknown free energy for this state, F_f^* . Now by defining $E_f(R^N)$ in terms of $E_i(R^N)$ (rearranging eq. 99) and inserting in to the above one gets

$$\begin{aligned}F_f(x) &= -\frac{1}{\beta} \ln \int dR^N \delta(x - \Delta E(R^N)) \exp(-\beta(E_i(R^N) + \Delta E(R^N))) \\ F_f(x) &= x - \frac{1}{\beta} \ln \int dR^N \delta(x - \Delta E(R^N)) \exp(-\beta E_i(R^N)) \\ F_f(x) &= x + F_i(x)\end{aligned}\quad (108)$$

The last relation shows that the two surfaces cross at ΔF^\ddagger , or simply

$$F_f(x^\ddagger) - F_i(x^\ddagger) = 0 = \Delta E(R^\ddagger) = \Delta e(R^\ddagger) + (U_f - U_i) \quad (109)$$

which is a restatement of eq. 101. Furthermore, knowing one surface the other can be derived in relative terms. The rhs. of eq. 105, which defines F_i^* (and F_f^*), does not need to be known to get relative free energy differences between the states. They have the same free energy function with one translated by the coordinate x and vertically shifted by the constant internal energy difference $U_f - U_i$. Figure 16 presents two ideal free energy curves and their relations.

6.2 BIASED OR DRIVEN SAMPLING METHODS

In free energy analysis where one seeks to map the free energy change as a system goes from an initial to final state (eq. 97) a considerable sampling is required for accurate results. Furthermore, the system will spend most time near equilibrium so the reaction coordinate close to the final state is poorly sampled. To bridge the gap between

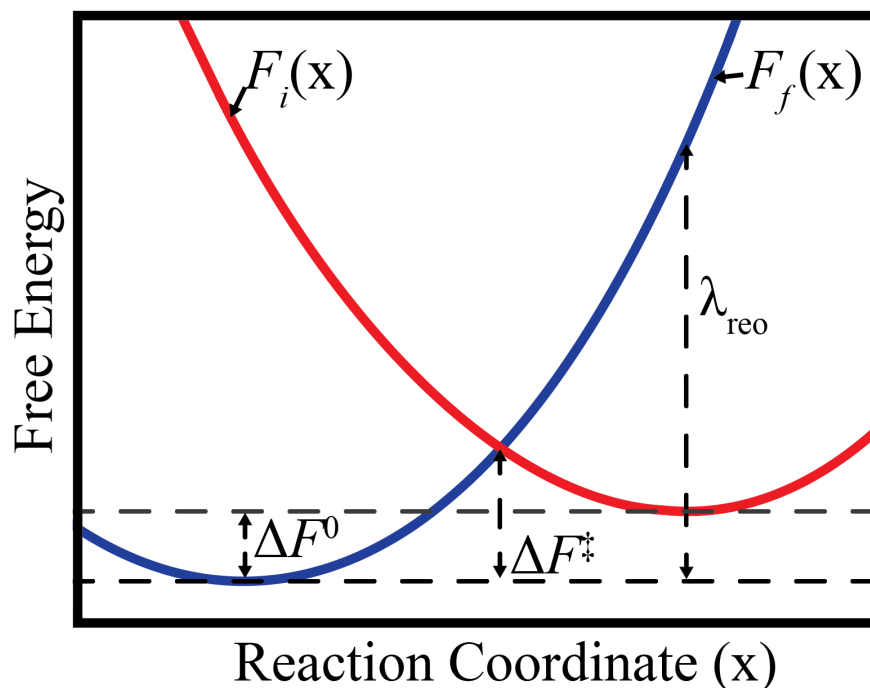


Figure 16: Free energy surfaces for the initial, $F_i(x)$, and the final, $F_f(x)$, states. The parameters pertinent to electron charge transfer are depicted on the graph: ΔF^0 - the free energy difference between the two states (redox potential difference); ΔF^\ddagger - the free energy barrier for the reaction; and λ_{reo} - the reorganization energy of the solvent (nuclear) environment including the internal reorganization of the chemical species under scrutiny.

the two states various methods have been devised to drive the reaction from one state to the other, hence allowing sampling in otherwise statistically unlikely regions along the reaction coordinate.

Accelerated sampling methods in this respect can be divided into two classes: (A) methods modifying the energy expression to reduce the thermodynamic barrier to overcome, hence allowing more frequent sampling of out of equilibrium coordinates or (B) restricting the sampling to all degrees of freedom except the reaction coordinate, which is then in some way systematically controlled [100, 93]. The Umbrella Sampling method (US) [101, 102] is one form of (A) where the reaction coordinate is sampled by "pulling" it from one state to the other by using a suitable biasing potential acting on one state. This does not restrict any degrees of freedom hence the full momentum space is sampled. In its rudimentary form it simply reads

$$E_j^b(\mathbf{R}^N) = E_i(\mathbf{R}^N) + W_j(\Delta E(\mathbf{R}^N)) \quad (110)$$

where $E_j^b(\mathbf{R}^N)$ is the energy of an intermediate state j , having mixed characteristics of the initial and final state - the superscript denotes

that it is a biased sampling - and $W_j(\Delta E(\mathbf{R}^N))$ is some biasing potential which brings the system from the initial state to intermediate states and is here a undefined function of the reaction coordinate which is to be sampled.

6.2.1 Fractional Number of Electrons

The transition from the initial to the final state is assumed to be purely electronic (eq. 99) - the charge transfers between the species without inducing any chemical change. In the FRACTIONAL NUMBER OF ELECTRONS (FNE) method [103] this is exploited by gradually (or rather manually) changing the charge on the donor and acceptor species to partial values, Δq_j , between the full redox states. For each Δq_j an intermediate state is created



so, in the FNE context a simulation consists of dividing the transferring charge into intervals, say $\Delta q_j = \{0, 0.25, 0.5, 0.75, 1.0\}$, and run molecular dynamics where the forces are derived from the electronic structure of those states. The definition of the energy gap is eq. 99 so after a suitable simulation time where typically tens of thousands of nuclear configurations are available the potential energy of the initial and final state, eq. 97, is calculated to give $\Delta E(\mathbf{R}^N)$ - this is again only for a subspace of the available simulated phase space to represent the statistical average. Note that the specific configurations, \mathbf{R}^N , are not specific to a particular intermediate state as all \mathbf{R}^N are in the phase-space of possible configurations for either states - they are just statistically unlikely.

In terms of a biasing potential eq. 110 is re-written as

$$\begin{aligned} E_j^b(\mathbf{R}^N) &= E_i(\mathbf{R}^N) + \frac{\Delta E_{q_j}(\mathbf{R}^N)}{\Delta E(\mathbf{R}^N)} \Delta E(\mathbf{R}^N) \\ &= E_i(\mathbf{R}^N) + \eta_{q_j} \Delta E(\mathbf{R}^N) \end{aligned} \quad (112)$$

where $\Delta E_{q_j}(\mathbf{R}^N) = E_{q_j}(\mathbf{R}^N) - E_i(\mathbf{R}^N)$, the potential energy difference between the partially charged state and the initial state. There is no guarantee that for a given partial charge that $\Delta q_j = \eta_j$, or in other words that the partial charge gap $\Delta E_{q_j}(\mathbf{R}^N)$ is a linear function of $\Delta E(\mathbf{R}^N)$, with an intersection at zero. As seen and discussed in the results section 7.3 applying eq. 112 requires additional steps when using the partial charge to drive the reaction.

6.2.2 Coupling Parameter

An alternative approach to drive the reactions is to use a suitable coupling parameter [104], η_j , which mixes the potential energy surfaces of the initial and final state in a straightforward way

$$\begin{aligned} E_j(\mathbf{R}^N) &= (1 - \eta_j)E_i(\mathbf{R}^N) + \eta_j E_f(\mathbf{R}^N) \\ &= E_i(\mathbf{R}^N) + \eta_j \Delta E(\mathbf{R}^N) \end{aligned} \quad (113)$$

and has values in the range $0 \leq \eta \leq 1$ which, similar to the partial charge, brings the system from the initial to final state. In this case the biasing potential has a simpler definition: $W_j(\Delta E(\mathbf{R}^N)) = \eta_j \Delta E(\mathbf{R}^N)$. The reaction coordinate can then be readily explored by doing calculations on the initial and final state in parallel, allowing transition into the intermediate state configurations by tuning η_j . This amounts to running molecular dynamics using the same linear combination of the forces

$$\begin{aligned} \mathbf{F}_j(\mathbf{R}^N) &= (1 - \eta_j)\mathbf{F}_i(\mathbf{R}^N) + \eta_j \mathbf{F}_f(\mathbf{R}^N) \\ &= \mathbf{F}_i(\mathbf{R}^N) + \eta_j (\mathbf{F}_f(\mathbf{R}^N) - \mathbf{F}_i(\mathbf{R}^N)) \end{aligned} \quad (114)$$

where \mathbf{F}_i and \mathbf{F}_f represent the force vectors of the atoms in the initial and final state electronic configurations, respectively.

In this context the potential energy of each and every configuration needs to be calculated for both the initial and final states, which makes this method close to twice as expensive compared to the FNE method. However, the biasing potential is well defined and one does not have to deal with unphysical partially charged states and additional complexity due to the well-known difficulty of treating such systems with DFT.

6.3 WEIGHTED HISTOGRAM ANALYSIS METHOD

The Weighted Histogram Analysis Method (WHAM) as first presented by Ferrenberg and Swendsen [105] is an optimized way to analyse data generated with Monte-Carlo simulations. This method was later extended to the general umbrella sampling and related methods [106, 107], which makes WHAM ideal for constant temperature MD simulation methods such as employed here, where biased sampling windows are used to bridge sampling between two states.

Here the basic formulation in [107] is followed and apply a self-consistent WHAM code to connect biased sampling windows using the coupling parameter, η_j , and partial charge, Δq_j . The probability of

observing a particular value of the reaction coordinate, $\Delta E(\mathbf{R}^N)$, from a sampling produced by running MD on biased systems, $E_j^b(\mathbf{R}^N)$, produces a biased probability - $P_j^b(\Delta E(\mathbf{R}^N))$. The relation of the biased probability to the unbiased one is given by

$$P_j^u(\Delta E(\mathbf{R}^N)) = e^{\beta[W_j(\Delta E(\mathbf{R}^N)) - f_j]} P_j^b(\Delta E(\mathbf{R}^N)) \quad (115)$$

where f_j is the free energy change in the system by introducing the biasing potential $W_j(\Delta E(\mathbf{R}^N))$. The total probability curve for the initial state can be written as linear combination of the unbiased probability distributions from the j simulation windows

$$P_i(\Delta E(\mathbf{R}^N)) = C \sum_{j=1}^N p_j(\Delta E(\mathbf{R}^N)) P_j^u(\Delta E(\mathbf{R}^N)) \quad (116)$$

where N runs over all simulation windows, C is a normalization constant, and $p_j(\Delta E(\mathbf{R}^N))$ are the weights of the sampling windows and are strongly dependent on the choice of the coupling parameter η_j , or the partial charge Δq_j .

Requiring the weights to be normalized

$$1 = \sum_j^N p_j(\Delta E(\mathbf{R}^N)) \quad (117)$$

and to minimize the statistical error results in [106, 107]

$$\begin{aligned} P_i(\Delta E(\mathbf{R}^N)) &= C \sum_{j=1}^N \frac{n_j e^{-\beta[W_j(\Delta E(\mathbf{R}^N)) - f_j]}}{\sum_{k=1}^N n_k e^{-\beta[W_k(\Delta E(\mathbf{R}^N)) - f_k]}} P_j^u(\Delta E(\mathbf{R}^N)) \\ &= C \sum_{j=1}^N \frac{n_j}{\sum_{k=1}^N n_k e^{-\beta[W_k(\Delta E(\mathbf{R}^N)) - f_k]}} P_j^b(\Delta E(\mathbf{R}^N)) \end{aligned} \quad (118)$$

where n_j are the number of unique samplings in window j . The free energy change due to the biasing potential in say window n can be solved for using the following equation

$$\begin{aligned} e^{-\beta f_n} &= \int d\mathbf{R}^N e^{-\beta[W_n(\Delta E(\mathbf{R}^N))]} P_i(\Delta E(\mathbf{R}^N)) \\ &= C \int d\mathbf{R}^N \sum_{j=1}^N \frac{n_j e^{-\beta[W_n(\Delta E(\mathbf{R}^N))]} }{\sum_{k=1}^N n_k e^{-\beta[W_k(\Delta E(\mathbf{R}^N)) - f_k]}} P_j^b(\Delta E(\mathbf{R}^N)) \end{aligned} \quad (119)$$

This equation presents a self-consistent way to solve for the free energies of perturbation.

6.3.1 Application of WHAM

The self-consistent solution to eq. 119 is achieved by first providing an initial guess to the f_j values - solving the equation until a consistency is achieved on both sides of the equal sign - and at the very end the value of f_i is subtracted from the array of f_j values. This ensures that the weights and probabilities are normalized, hence the C 's in eq. 118 and 119 are also solved for. For example, the biasing potentials corresponding to the initial state in eq. 112 and 113 are zero by construct - hence during the self-consistent cycle f_i approaches zero, but due to the nature of the problem when applying a convergence criteria has some residual value.

In practice the biased probabilities of the simulation window j are here computed as normalized histograms

$$P_j^b(x) \equiv \frac{1}{n_j} \sum_{l=1}^{n_j} \delta(x - \Delta E(R_{j,l}^N)) \quad (120)$$

where $R_{j,l}^N$ is a selection of coordinates from the configuration phase space and is generally (due to obvious limitations) not a complete sampling of the phase space.

Introducing eq. 120 in to eq. 119 results in

$$\begin{aligned} e^{-\beta f_n} &= \int dR^N \sum_{j=1}^N \frac{n_j e^{-\beta [W_n(\Delta E(R^N))]} }{\sum_{k=1}^N n_k e^{-\beta [W_k(\Delta E(R^N)) - f_k]} } \frac{1}{n_j} \sum_{l=1}^{n_j} \delta(x - \Delta E(R_{j,l}^N)) \\ &= \sum_{j=1}^N \sum_{l=1}^{n_j} \frac{e^{-\beta [W_n(\Delta E(R_{j,l}^N))]} }{\sum_{k=1}^N n_k e^{-\beta [W_k(\Delta E(R_{j,l}^N)) - f_k]} } \end{aligned} \quad (121)$$

where $R_{j,l}^N$ is a selection of configurations to best represent the statistical average from a limited sampling in simulation window j .

Part III

APPLICATION

In this Chapter various aspects of the free energy analysis are explored for symmetric and asymmetric electron charge transfer reactions between the first row transition metals: vanadium (V), chromium (Cr), manganese (Mn), iron (Fe) and cobalt (Co). Cobalt is furthermore analyzed for two different magnetic states - high- and low-spin. The general reaction is $D^{+2} - A^{+3} \rightarrow D^{+3} - A^{+2}$, where one transition metal acts as the donor in the +2 redox state, exchanging charge with another transition metal in the +3 redox state, acting as the acceptor. The majority of the results are generated at the full QM level with the symmetric reaction of iron explored at the QM/MM level in detail as well. The focus is on their coordination to water at the two redox states, redox potential differences and the reorganization energies - where the two methods of employing either a coupling parameter η_j or partial charge Δq_j to 'drive' the reaction are compared.

7.1 COMPUTATIONAL DETAILS

All electronic ground state calculations were performed with the real-space DFT code GPAW [18, 19, 42], where the core electrons are described with PROJECTOR AUGMENTED WAVE (PAW) method [40]. The electronic wave functions describing the valence-electrons are represented with a numerical atom-centered orbital basis corresponding to the double- ζ with polarization (dzp) quality. The effective external potential, and the grid-based wave functions, are represented on a real-space grid with a $0.18(\pm 0.01)$ Å spacing. Exchange-correlation energy is approximated with the GGA functional of Perdew-Burke-Ernzerhof (PBE) [32].

Structural relaxations and molecular dynamics are available in ASE [108]. A Quasi-Newton scheme is used to relax bulk systems with force tolerance of $0.05 \frac{eV}{\text{Å}}$ (e.g. a transition metal in bulk water), whereas vacuum systems are relaxed at a criteria of $0.01 \frac{eV}{\text{Å}}$. Constant temperature MD are run with the Langevin integrator with a friction coefficient of 0.01. The friction is only applied to the solvent molecules, not the metal and the six water ligands. The RATTLE scheme [109] is used to fix bond lengths - and all oxygen to hydrogen bond lengths and angles were constraint, which allowed for a MD step size of 1-2 fs (see Figure 11). For the phase space sampling each state (initial, intermediate(s) and final) were thermalized for 10 ps be-

fore data collection, which was also run for another set of 10 ps at 1 fs time steps. The temperature was set to 400 K in all cases - which is found to give a better agreement to experiment when simulating with GGA described water [79, 78].

In the QM/MM simulation the inner-sphere ligand structure of hexaaqua iron ($\text{Fe}(\text{H}_2\text{O})_6$) was treated at the same QM level as described above. The surrounding solvent was modeled with the TIP3P [52] parameter set. The same Lennard-Jones parameters are used to describe LJ-potential interaction between the classical and quantum water (ligands), but due to the very short range of the LJ-potential the interaction between the classical water and iron was omitted.

For the free energy analysis the energy gaps were analyzed for both the forward and reverse reaction (see Figure 17). At every tenth image (10th fs) $\Delta E(\text{R}^N)$ was calculated, providing 1000 conformations for each simulation window of each metal species, using both the coupling parameter or partial charge to gather intermediate state configurations. Since the donor and acceptor cells are independent the energy gaps of the donor site is combined with the energy gap at the acceptor site to give 10^6 'unique' values for the initial and final state potential energy gaps.

7.2 STRUCTURES AND REDOX INDUCED STRUCTURAL CHANGES

From the molecular dynamic trajectories which were run for 10 ps in each sampling window, after thermalization, the radial distribution functions (eq. 96) of metal to oxygen ($\text{M}(\text{OH}_2)_6$) distances were analyzed for the initial, intermediate and final states. All distributions at the +2 and +3 redox states are presented in Figures 18, which include indicators of the estimated centers of the peaks. In these relatively small systems only two peaks are observed. The first peak represents the metal to ligand bond lengths, and the second broad peak is the first solvation shell. Table 2 collects peak center estimates and compares to experiment, as well as bond lengths determined from structural relaxation in vacuum.

All in all there is a good agreement between the internal structure determined from the RDFs and experiment, with the computational values consistently larger but only by 0.01-0.06 Å. This is not surprising as PBE and related exchange-correlation functionals are in general accurate in determining bond lengths between transition metals and various ligands [117, 118]. Vacuum bond lengths are within 0.01-0.03 Å compared to the RDFs, with the +2 bond length shorter, whereas the +3 bond length slightly longer. This is more evident if one considers the change in the bond length, $\Delta R_{(\text{OH}_2)_6}$, between the two oxida-

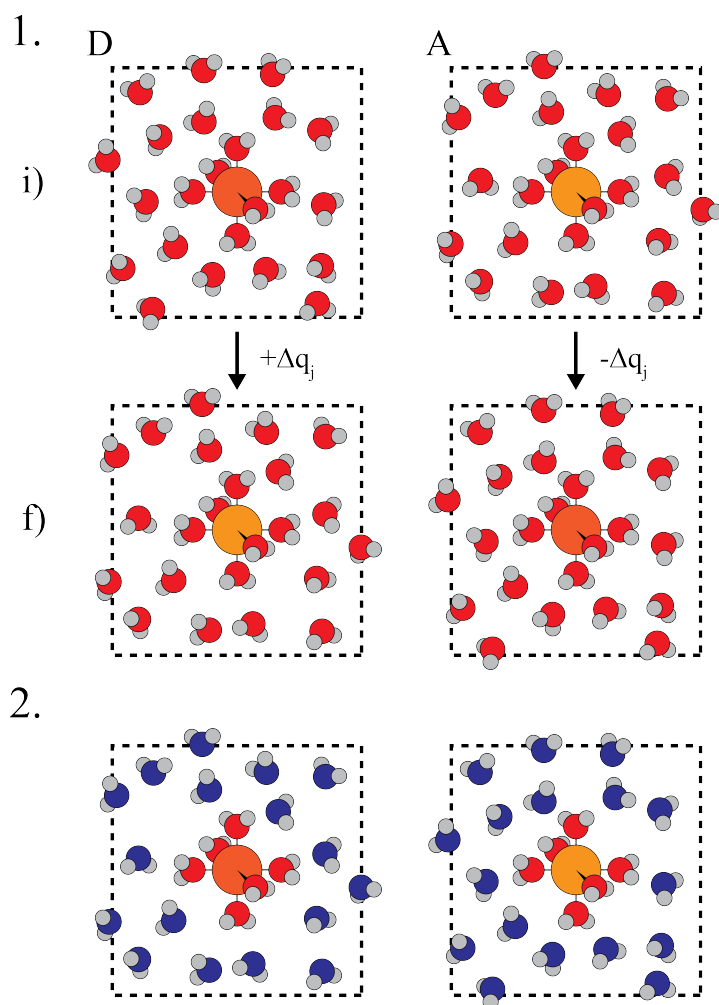


Figure 17: 1. Schematic of the biased sampling methods and reaction centers.

The i)ntial and f)inal states are a combination of two independent charge sites, Donor and Acceptor. The simulated reaction at **D** is $M^{2+} \rightarrow M^{3+}$ with the reverse reaction taking place at **A**. In 2) the solvent molecules are described classically - but the inner ligand sphere is kept QM. However, the QM/MM method can not predict accurate reorganization energies as it lacks description of the solvent polarizability, hence QM/MM is used to sample a large phase space, but potential energy values which enter the WHAM scheme are always evaluated with full QM on selected snapshots.

tion states - collected in Table 3.

The position of the peak of the first solvation shell, R_{sol} , was also analyzed for both redox states - which are presented in Table 2. The peak shift, ΔR_{sol} , between redox states is presented in Table 3. All in all there is a clear shift of the peak between the two redox states; at 2+ the peak is found within the range 4.20-4.33 Å, whereas for the +3 state it shifts to 4.05-4.17 Å. There is some correlation to the averaged

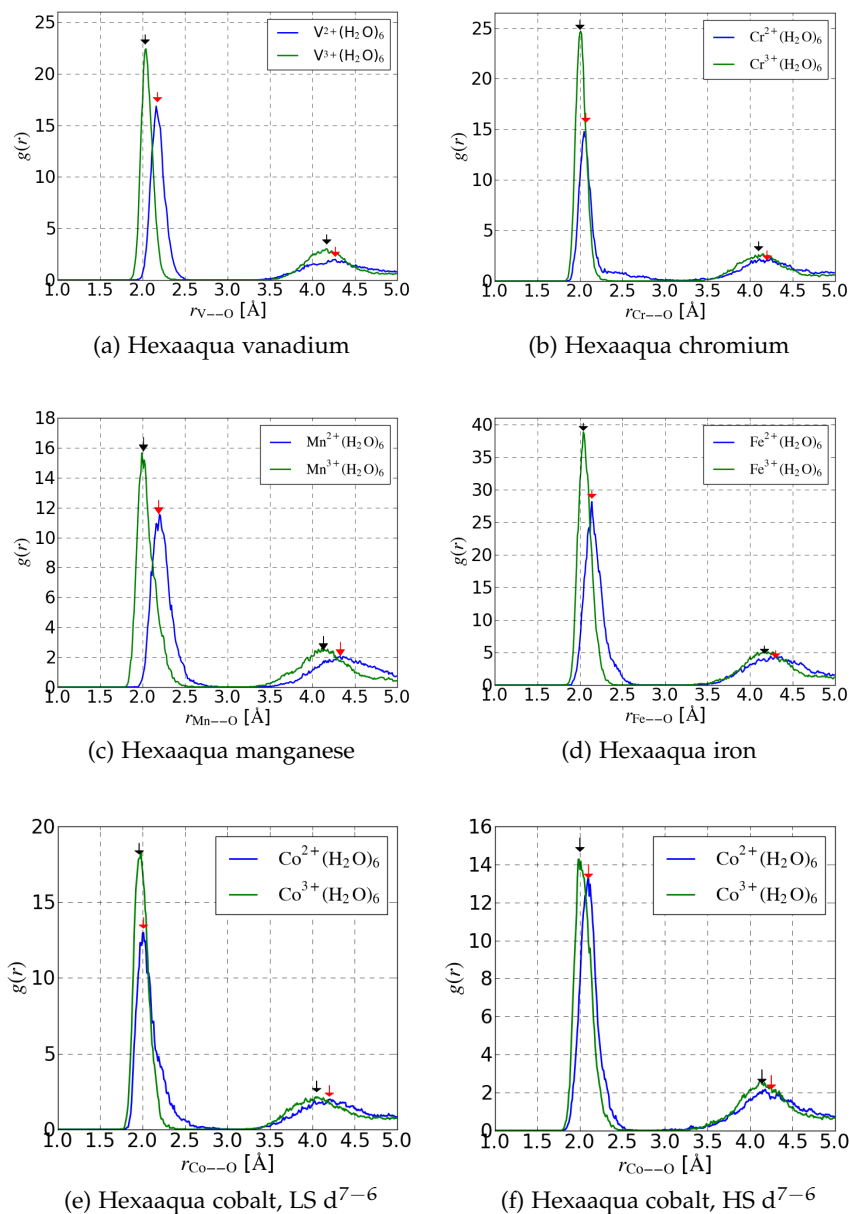


Figure 18: Radial distribution functions (RDFs) of the metal to oxygen distances for V, Cr, Mn and Fe, as well as both spin-state of Co. The RDFs are displayed for both the +2 and +3 charge states, blue and green curves respectively, and are collected over a 10 ps interval. The red and black arrows mark the center of the ligand sphere and first solvation shell peaks. In all cases the ligands and first solvation shell contract with increased positive charge on the metal atom. The Jahn-Teller effect is observed in the vacuum relaxed structures of hexaaqua $Cr(2+)$, $Mn(3+)$ and $Co(2+)$, which is strongly suppressed in the molecular dynamics runs. It is though evident in the second small peak of $Cr(2+)$ and the relatively broad peak of $Co(2+)$.

Table 2: The hexaaqua coordination, $R_{(\text{OH}_2)_6}$, and first solvation shell, R_{sol} , peak position of the transition metals at the +2 and +3 states. The hexaaqua coordination is compared to crystal structures of the metals at the two different redox states. The last column lists the computational metal to oxygen bond lengths for the complexes in vacuum, $R_{(\text{OH}_2)_6}^{\text{vac}}$. All values are in angstroms.

Metal	$R_{(\text{OH}_2)_6}$				R_{sol}		$R_{(\text{OH}_2)_6}^{\text{vac}}$	
	+2	Exp.	+3	Exp.	+2	+3	+2	+3
V	2.17	2.14 ^a	2.03	2.00 ^d	4.27	4.15	2.15	2.06
Cr	2.44	2.30 ^f	1.99	1.96 ^{d,g}	4.21	4.09	2.35	2.01
		2.07 ^f					2.09	
Mn	2.19	2.18 ^{a,b}	2.00	1.99 ^d	4.33	4.13	2.19	2.16
								2.00
Fe	2.13	2.12 ^a	2.03	1.99 ^e	4.30	4.17	2.13	2.05
Co(LS)	2.02		1.93	1.87 ^d	4.25	4.14	2.17	1.94
							2.00	
Co(HS)	2.10	2.09 ^a	2.03		4.20	4.05	2.10	2.04

(a) Johnson et. al. [110], references therein; (b,c) Montgomery et. al. [111, 112]; (d) Beattie et. al. [113]; (e) Best et. al. [114]; (f) Brunschwig et. al. [115]; (g) Eshel, Bino [116]

bond length of the species and the position and shift of the second peak. For example the average bond length of $\text{Mn}(\text{OH}_6)^{+2}$ is 2.19 Å, which changes to 2.00 at +3 - this species has both the longest bond length and the largest bond length change, resulting in a shift of 0.20 Å for the second peak. This shift is lower for the other complexes, or in the range 0.11-0.15 Å.

7.3 FREE ENERGIES SURFACES

Data for the free energy surface analysis was collected for both bias methods; eq. 112 and 113 - by running molecular dynamics on the states defined by $\Delta q_j, \eta_j = \{0, 0.25, 0.5, 0.75, 1.0\}$. Figure 19 presents radial distribution functions for the initial, intermediate and final states of the V^{2+} - V^{3+} transition.

In comparing the two methods one notes that a) the peak position are in general determined to be the same within ± 0.02 Å at any given $\Delta q_j = \eta_j$ and b) the peak position are furthermore shifted by the same fractional value as the bias parameters. For example the difference in peak position between the intermediate states at $\eta_j, \Delta q_j = 0.5$ to the initial state is 0.07 Å. This is exactly 0.5 of the peak shift when

Table 3: Metal to ligand bond length changes between the +2 and +3 redox states. Results from the RDFs and vacuum calculations are presented, along with the estimated shift from experimental bond lengths.

Metal	$\Delta R_{(\text{OH}_2)_6}$	$\Delta R_{(\text{OH}_2)_6}^{\text{vac}}$	Exp.*	ΔR_{sol}
V	0.14	0.09	0.14	0.12
Cr	0.08	0.08	0.11	0.12
Mn	0.19	0.19	0.19	0.20
Fe	0.10	0.08	0.13	0.13
Co(LS)	0.09	0.06	-	0.11
Co(HS)	0.07	0.06	-	0.15

* the experimental shift is simply taken as the difference between the +2 and +3 experimental results collected in Table 2. In the case of complexes which display the Jahn-Teller effect the equatorial bond length is used.

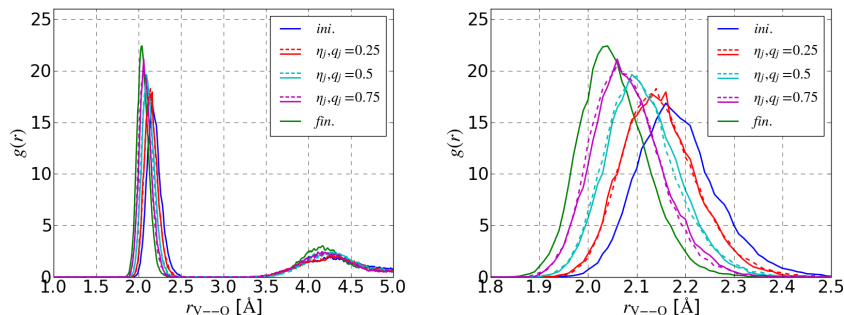


Figure 19: Radial distribution functions (RDFs) of the initial, intermediate and final states of hexaaqua vanadium. The intermediate states sampled by using both the coupling parameter, η_j (broken lines), and partial charge (solid line), Δq_j , are presented. Left: RDFs showing both the ligand and first solvation peaks. Right: zoom in of the ligand peaks, showing the overlap of the intermediate state peaks (broken lines of same color scheme shown in the legend).

comparing the initial and final state (0.14 Å). This was observed for all intermediate states of all of the metals, meaning that the internal structural change scales linearly in both η_j and Δq_j .

As discussed in section 6.2 application of WHAM requires knowing the value of the bias potential defined in eq. 113 and eq. 112. In the former case the bias potential is simply the coupling parameters times the potential energy gap - in the latter case however the bias is written as a simple function of the partial charge potential energy gap over the total gap, assuming linearity. This linearity is not observed and

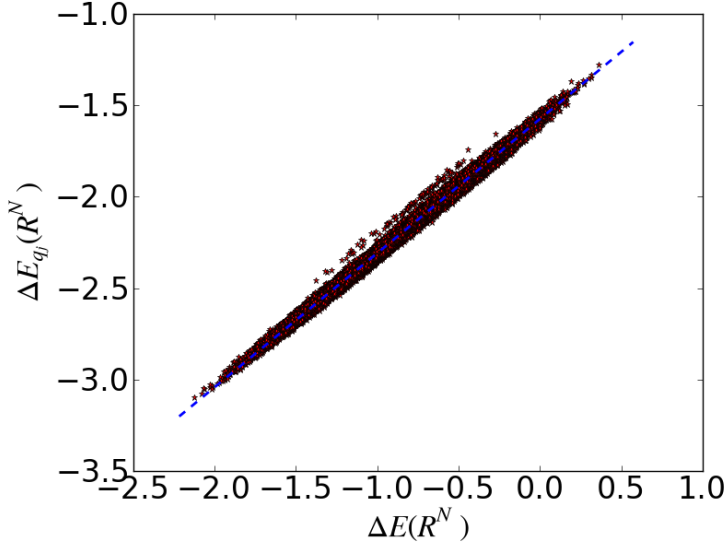


Figure 20: In order to evaluate the biasing potential of eq. 112 for the intermediate, or partially charged, systems the ratio of partial charge potential energy gap $\Delta E_{q_j}(R^N)$ to the initial-final state gap $\Delta E(R^N)$, red stars, is fitted with a first order linear equation, blue broken line. This particular example is from simulations with the $V^{+2.75} - V^{+2.25}$ intermediate state ($\Delta q_j = 0.75$, see Figure 17), where the slope of the best fit is $\eta_{q_j}^{\text{LIN}} = 0.74$, in line with the partial charge.

is severely skewed - which is mainly due to the self-interaction error inherent to DFT, see e.g. [31, 37]. Furthermore, application of eq. 121 requires terms of the form

$$\eta_{q_j} = \frac{\Delta E_{q_j}(R_{k,l}^N)}{\Delta E(R_{k,l}^N)} \quad (122)$$

or in other words knowing the potential energy gap of the partially charged systems in configuration generated at all other partial charges - hence a sampling of j^2 is implied. To solve for both issues making WHAM applicable to the partial charge case a trivial linearization is performed by first order fitting to the $\Delta E_{q_j}(R^N)/\Delta E(R^N)$ ratio, such that eq. 112 becomes

$$E_j^b(R^N) = E_i(R^N) + \eta_{q_j}^{\text{LIN}} \Delta E(R^N) + C_j \quad (123)$$

where η_j^{LIN} and C_j are the slope and intercept of the linear fitting for charge state j . Figure 20 presents a general sample of the fitting process, here for the $\Delta q_j = 0.75$ data set of vanadium. The slope is found, in all cases and for all metals, to be in accordance with the coupling parameter η_j within ± 0.03 . Fitting to vanadium gives $\eta_{q_j}^{\text{LIN}} = \{0.23, 0.5, 0.74\}$ for the intermediate states defined by

$q_j = \{0.25, 0.5, 0.75\}$, respectively.

Figure 21 presents free energy surfaces generated for each intermediate state unbiased probabilities (eq. 115) for vanadium and chromium, and compares the two bias methods. The free energies are evaluated as

$$F(P_j^u(x)) = -\frac{1}{\beta} \ln[P_j^u(x)] \quad (124)$$

The associated weights $p_j(x)$ are overlaid as well, which show clearly where each intermediate state is centered and their overlap - or in other words where each intermediate state has statistical significance in the full initial state probability curve (eq. 116).

Table 4: Free energy barrier, ΔF^\ddagger , and reorganization energy, λ_{reo} , collected from free energy surfaces created with intermediate states using either the coupling parameter η_j (eq. 113), or partial charge Δq_j (eq. 112).

Metal	ΔF^\ddagger		λ_{reo}	
	η_j	Δq_j	η_j	Δq_j
V	0.47	0.45	1.90	1.80
Cr	0.70	0.74	2.82	2.97
Mn	0.62	0.64	2.46	2.55
Fe	0.42	0.39	1.66	1.58
Co(HS)	0.44	0.45	1.84	1.80
Co(LS)	0.68	0.71	2.73	2.81

With the unbiased probabilities and weights readily available the initial state probability (eq. 116, pg 57) and the resulting free energy surface were generated. Figure 22 presents a sample analysis for vanadium where both the initial and final state curves are presented. Table 4 collects the free energy of reorganization and barrier, for all metals employing both bias methods. The free energy barrier varies by 0.42-0.70 eV over the range of metals, and deviates by $\pm 0.02 - 0.04$ eV when comparing the two bias methods. The free energy of reorganization ranges from 1.66-2.82 eV, and evidently varies quite a lot between metals. The two bias methods give similar results but vary by $\pm 0.06 - 0.15$ eV.

7.3.1 Internal Reorganization Energy

In the diabatic picture of electron transfer theory [7] the reorganization energy term is divided in to two components

$$\lambda_{\text{reo}} = \lambda_{\text{in}} + \lambda_{\text{out}} \quad (125)$$

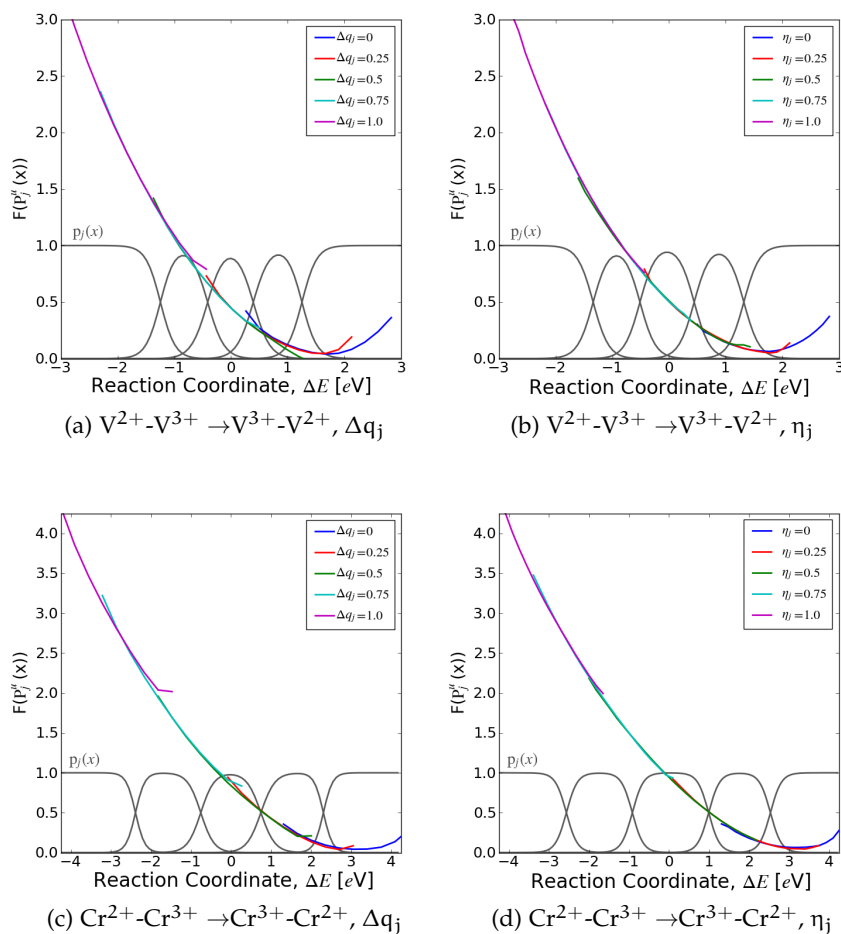


Figure 21: Example free energy surface analysis for (top-bottom) vanadium and chromium using (left-right) the partial charge or coupling parameter methods. The plots show the free energy of the unbiased probability distributions (eq. 115, pg. 57) sampled by running molecular dynamics on the intermediate states defined in the legend. Also plotted are the associated weights for each window $p_j(x)$, which are required to piece together the total initial state free energy curve (eq. 116, pg. 57). The free energy curves generated with the coupling parameter are smoother in all cases - as seen in the smoother tails of the intermediate state curve - but the total curves give very similar reorganization energy and barrier. All values are collected in Table 4, and Figure 22 presents a free energy surface generated from the total initial state probability curve for vanadium.

an internal reorganization term λ_{in} - as in the structural change of the $M(OH_2)_6$ species which is evident in the change of the first peak of the RDFs in Figure 18 - and an external term associated with the response of the bulk solvent, or the outer-sphere solvation, denoted λ_{out} .

Table 5: Free energy barrier, ΔF^\ddagger , energy of reorganization, λ_{reo} , and internal reorganization energy, λ_{in} , for the first row transition metals, estimated using the procedure described in section 5 and a single point vacuum calculation, respectively. (Quasi-)Experimental reorganization energies from the same source are found here [119, 120, 121] (exp. A), and a collection of more recent values from various sources here [122] (exp. B). Also presented are outer-sphere reorganization energy, $\lambda_{\text{out}} = \lambda_{\text{reo}} - \lambda_{\text{in}}$, and λ_{in} is calculated by eq. 126. The last column presents the outer sphere reorganization energy estimated with the Marcus model, eq. 129 (see text for details).

Metal	ΔF^\ddagger	λ_{reo}	exp. A	exp. B	λ_{int}	λ_{out}	calc.
V	0.47	1.90	2.13	2.69	0.72	1.18	1.50
Cr	0.70	2.82	2.05	3.47	1.68	1.14	1.54
Mn	0.62	2.46	2.02	3.26	1.26	1.20	1.48
Fe	0.42	1.66	2.11	2.10	0.48	1.18	1.55
Co(HS)	0.44	1.84	2.26	2.24	0.68	1.16	1.52
Co(LS)	0.68	2.73			1.38	1.25	1.59

The internal reorganization energy is estimated as the energy difference of a redox states in vacuum relaxed structures of both redox states; λ_{in} is then a sum of two components, one for the acceptor- and one for the donor-reaction site

$$\lambda_{\text{in}} = \lambda_{\text{in}}^0 + \lambda_{\text{in}}^1 \quad (126)$$

where

$$\lambda_{\text{in}}^0 = E^0(\text{R}[\text{M}(\text{OH}_6)]^1) - E^0(\text{R}[\text{M}(\text{OH}_6)]^0) \quad (127)$$

for example, and $\text{R}[\text{M}(\text{OH}_6)]^n$ denotes the structure relaxed for a given charge state. The same expression is used for λ_{in}^1 with appropriate changes in the charge indexes. These values are presented in Table 5, and it is clear that λ_{in} correlates well with the observed λ_{reo} - the metal with the largest internal reorganization energy displays the largest overall reorganization energy.

In Marcus' classical picture of the diabatic free energy of reorganization [123, 124, 125, 126, 127] the initial and final state free energy surfaces take the form of simple parabolas about their minimum

$$F_i(x) = \frac{1}{2}k(x - x_{i,\text{min}})^2 + F_i^* \quad (128)$$

with an analogous expression for the final state. The two parabolas - of equivalent curvature k - intersect at $\Delta F^\ddagger = (\lambda + \Delta F^0)^2/4\lambda_{\text{reo}}$ (and in all cases a parabola fits our data very accurately - and by construction (eq. 108, pg. 53) the parabolas of the initial and final state have the same curvature). Furthermore, based on the linear response

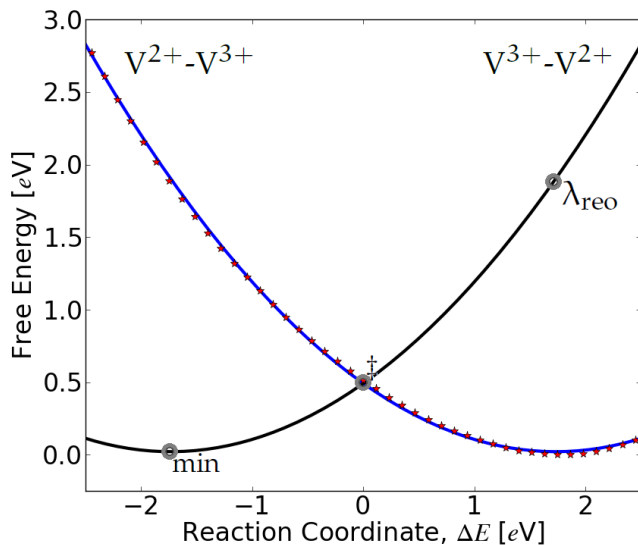


Figure 22: Applying the weights to the unbiased probability curves (see Figure 21) for each sampling window the final free energy surface is constructed. This particular example is for vanadium and the bias method here uses the coupling parameter η_j . The red stars are the WHAM data and the blue curve is a second order best fit - and as seen the data fits a parabola quite accurately in accordance with the Marcus model of the reorganization energy [123, 124, 125, 126, 127]. The black curve represents the final state free energy surface which is the same fitted curve but here translated by the reaction coordinate (see eq. 108, pg. 53). The equations of the resulting best fit and translation are used to solve for the reorganization energy and the free energy barrier - gray circles λ_{reo} and \ddagger , respectively - relative to the minimum (eq. 109, pg. 53). The values for both methods and all metals are presented in Table 4. The values presented in Table 5 are collected from the free energy surfaces composed of intermediate states made with the coupling parameter η_j , and are compared to experiment and the Marcus model.

assumption, λ_{out} can be derived in terms of a ion of finite radius R^q (representing the reactants) interacting with a continuous charge distribution (bulk solvent) extending to infinity. The model reads

$$\lambda_{\text{out}} = \frac{\Delta q^2}{4\pi\epsilon_0} \left(\frac{1}{\epsilon^{\text{op}}} - \frac{1}{\epsilon^s} \right) \left(\frac{1}{2R^1} + \frac{1}{2R^0} - \frac{1}{R_{\text{DA}}} \right) \quad (129)$$

where ϵ^0 is the permittivity of free space, and ϵ^{op} and ϵ^s are the optical and static dielectric constants of the solvent. R^1 and R^0 are the ionic radius of the donor and acceptor, respectively, and R_{DA} the distance between the reactants - which in our simulation set up is infinite, hence this term is omitted.

Using eq. 125 the contribution of the outer-sphere reorganization, λ_{out} , was calculated and is presented in Table 5. This value was found to be in very good agreement for all of the metals, in the range 1.14-1.25 eV. Also presented are the estimated outer-sphere contributions using the Marcus model, which range from 1.48-1.59 eV for the various metals, and differ by 0.28-0.36 eV compared to the computational results. In all cases the estimated center of the second solvation peak in the RFDs, Figure 19, are used for the ionic-radii.

The discrepancy has several sources. In the simulations the water is described with the PBE functional, which has an estimated optical dielectric constant of 2.0 at ambient temperatures [128] - but also using a very limited number of water molecules to represent the non-local dielectric - which may further effect the constant. For example, evaluation with $\epsilon^{\text{op}} = 2.2$ would give a very good agreement between the computations and Marcus model. The estimate of the ionic-radii (or the interface of the reactant and bulk solvent) is questionable at best, but then again this value has a range of definition in the literature.

7.3.2 Comparison to Experiment

Table 5 presents (quasi-)experimental reorganization energies from two sources; A) a collection of experiments employing the same set up - photo-emission experiments - and from same authors [119, 120, 121]; B) a collections of more recent work, which better represents accepted experimental values [122]. The experimental values from source A are all very close in value or 2.02-2.26 eV, with little correlation to the observed trend in the computational results - where it is clear that the internal reorganization energy differentiates between the metals. This trend is better reflected in the more recent experimental values (source B) - which range from 2.1-3.5 eV, and the relative value between metals compares very well to the computational series. The computational work of Rosso et. al. on the same series of metals revealed the same [129] - where both the internal- and external contributions are analyzed in detail.

This discrepancy between the computational and experimental free energies for these types of systems are well understood - first and foremost the two reactants are infinitely far apart in the simulations - but in the experiments and in ET theory there is an optimal distance between the reactants before charge transfer occurs (often taken as the hard-sphere distance between the reactant centers) - and a resulting electrostatic interaction and solvent shell overlaps which will effect the free energies. Moreover, the water is described with a GGA functional which gives too high dielectric constants compared to experimental water - and at ambient conditions is 1.77 and 78.4 [130].

This means, according to eq. 129, that the higher constant in our simulations results in an underestimation of the reorganization energy (this alone accounts for about 0.3 eV discrepancy). As a final note - although the computational bond lengths are in good agreement with experiment - the λ_{in} value is not necessarily accurate - and do account for a very large fraction of the total reorganization. For example in the study of Rosso et. al. [129] λ_{in} was found to be larger in all cases - about 0.1-0.2 eV in most cases - but there the complexes are described with a hybrid-GGA functional and a larger basis set.

Table 6: Initial-final state free energy difference, f_f , between $Fe^{2+} + M^{3+} \rightarrow Fe^{3+} + M^{2+}$. The free energy difference is solved for self-consistently using the WHAM method. From the difference the experimental redox potential of $Fe^{3+/2+}$: 0.771 eV [131] is added to give a computational estimate of the $M^{3+/2+}$ redox potential (see text for details), which is compared to experiments. The computational results are from [132], where the redox potential is estimated with a simpler scheme using DFT at a similar level of theory.

$M^{3+/2+}$	f_f	$E_M^{3+/2+}$	exp.	comp.
V	-0.98	-0.21	-0.26 ^{a,f}	-0.17
Cr	-1.15	-0.38	-0.42 ^{b,f}	-0.50
Mn	0.37	1.14	1.54 ^{c,f}	1.21
Co(HS)	1.05	1.82	1.92 ^{d,f}	1.75
Co(LS)	0.30	1.07		1.10

(a) Jones et. al. [133]; (b) von Grube et. al. [134]; (c) Ciavatta et. al. [135]; (d) Diebler et. al. [136]; (e) Bratsch et. al. [137]; (f) Bard, Parson and Jordan [138]

7.4 REDOX POTENTIALS

The QM calculations are on charged and periodic systems which employ the standard uniform neutralizing background. This shifts the relative potential of differently charged systems [139] hence the redox potential of the various $M^{2+/3+}$ reactions can not be accurately determined. However, using the known reduction potential of $Fe^{2+/3+}$ versus the standard hydrogen electrode (SHE), $E_{Fe,SHE}^{2+/3+} = -0.771$ eV, the redox potential of the other transition metals can be determined from the free energy difference between the initial and final states of asymmetric $Fe^{2+}-M^{3+} \rightarrow Fe^{3+}-M^{2+}$ reactions. In this way the redox potential of the other metals relative to SHE is solved with

$$E_{M,SHE}^{3+/2+} = \Delta F^0 - E_{Fe,SHE}^{2+/3+} \quad (130)$$

This difference is solved for self-consistently using the WHAM formalism in eq. 119. In order to solve it one starts with an initial array

of the f_j values corresponding to the $\eta_j = \{0, 0.25, 0.5, 0.75, 1.0\}$ states and at convergence subtracts any residual f_i (initial state $\eta_j = 0$). This gives the relative free energies of the intermediate, f_j , and final state f_f ($\eta_j = 1.0$). In that way $\Delta F^0 = f_f$. Table 6 collects the estimated redox potentials of the metals, and compares to experimental values and other computational results.

The relative redox potentials of V, Cr and Co are in fair agreement with experiment, differing by only 0.05-0.1 eV. Results for Mn are however not, and differ by 0.4 eV, but are in line in all cases with the trend and value of computational results employing a similar exchange-correlation functional (GGA) and a larger basis set [132]. In those simulations the transition metals were placed in an idealized cage consisting of eighteen water molecules and then embedded in to a continuous electrostatic media to represent the bulk solvent.

Table 7: Free energy barrier and reorganization energy for the $\text{Fe}^{2+} \rightarrow \text{Fe}^{3+}$ reaction. The fd results are on par with Sit et al. which is a plane-wave based DFT calculation employing the same xc functional. QM/MM parenthesis refers to the case where the phase space is first created with the WOLF-QM/MM method (see schematic Figure 17), but energy gaps and WHAM parameters are re-evaluated with full QM calculations at the indicated basis level.

	fd	fd(QM/MM)	dzp	dzp(QM/MM)	Sit et al.
ΔF^\ddagger	0.45	0.44	0.39	0.40	0.44
λ	1.80	1.75	1.58	1.60	1.77

7.5 QM/MM SIMULATIONS

Here the symmetric reaction of Fe^{2+} - Fe^{3+} is explored in more detail where first the difference of using a relatively cheap basis set versus a complete basis set is compared, and second where the cheaper QM/MM calculator is used (see Figure 172) to sample an adequate phase-space for free energy analysis. Note that the free energy analysis requires accurate potential energy gaps between the initial and final state, so after an adequate phase-space sampling with QM/MM a subspace is selected (every tenth image) the potential energy gap is evaluated with full QM calculations. The resulting potential energy gap from QM/MM calculations will be too large due to the role of dielectric response of the solvent, which is lacking in the simple three-site solvent model used here - e.g. for TIP3P ϵ^{op} is found to be approx. 1.1 [140, 141] which according to eq. 129 increases the reorganization energy and hence the potential energy gap considerably (or by a factor of 1.8).

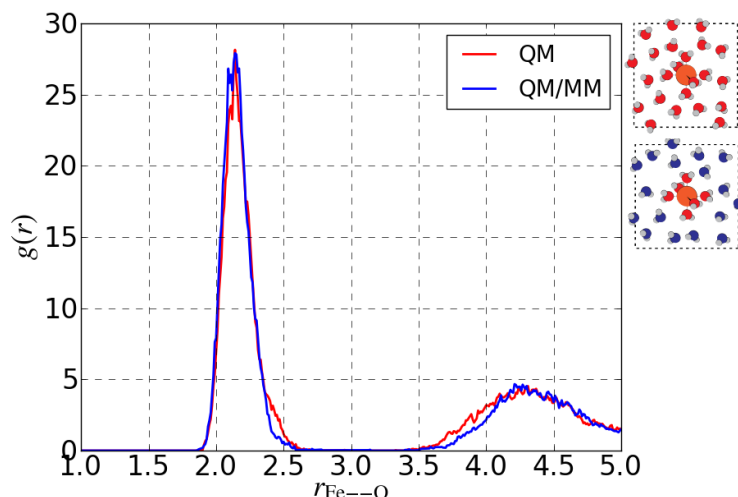


Figure 23: Radial distribution function of the iron to oxygen distances, analyzed from molecular dynamics simulations at the full QM (red) and QM/MM (blue) theoretical level. The $M(\text{OH}_2)_6$ complex is described with QM in the mixed QM/MM simulations, and as expected the first peak of both simulation overlap as it represents the distribution of metal to ligand bond lengths. The second peaks are also centered at a similar position with the QM/MM peak though shifted slightly to the further away from the metal. This is in line with the stronger hydrogen bond interaction between the QM solvent and QM ligands compared to a MM solvent interacting with a QM ligand (see Figure 6).

Figure 23 compares the radial distribution function of $\text{Fe}^{2+}(\text{OH}_2)_6$ in quantum and classical solvent. The first peak of both simulations are almost overlaid, as they should since the internal structure of the metal complex are treated at the same theoretical level. There is a difference in the second peak, which is slightly farther away from the metal center in the QM/MM case. An analysis of the +3 RDFs revealed more or less the same.

Figure 24 presents two free energy curves where the basis set dependence is compared. Table 7 collects the free energies of reorganization and barrier for both basis sets, and for the case where the phase-space is sampled with QM/MM. The results are compared to the simulations of Sit et. al. [142] where the system size, number of water molecules and exchange-correlation functional is matched. In their calculations they employ a plane-wave basis to describe the valence electrons, where here a comparable purely grid-based basis - where the only convergence parameter is the spacing between individual points [18, 19]. - is used.

All in all there is good agreement between the free energy barriers when comparing the two different basis sets, 0.45 eV vs. 0.39 eV for

the *fd* and *dzp* basis respectively, and only a slight difference when comparing the same basis but different sampling method. There is also excellent agreement between our results and the one of Sit et. al., and the cases where the phase space is generated with the QM/MM calculator. Considering the total reorganization energy there is a noticeable difference between the basis, or up to 0.22 eV.

This difference is largely explained with the difference in the internal reorganization. With the more complete grid-based basis the internal reorganization energy was found to be 0.56 eV - which is in a better agreement with computational work here [129] - and the resulting $\lambda_{\text{out}} = 1.24$ eV, in excellent agreement with the *dzp* results of 1.22 eV. The outer-sphere reorganization is due to the change in localized charge on the central metal surrounded by water ligands - so there is little to no overlap between the electronic state of the solvent and the charge carrying electronic state of the metal - hence it makes sense that there is little discrepancy in λ_{out} between the two basis.

7.6 CONCLUSION AND OUTLOOK

The free energy surfaces for several transition metals were generated with data gathered from first principles and hybrid-QM/MM calculations, using two variants of the umbrella sampling method. Both methods give more or less the same results but differ largely in the computational approach - in one method a non-physical partially charged intermediate state is used to sample out of equilibrium configurations, but it is well known that GGA based DFT calculations describe such partially charged system poorly. For example, during similar simulation on titanium and copper variants of the hexaaqua complexes, a spurious formation of pentaqua complexes was observed - but only in the partially charged systems, not in the fully charged initial or final state. The second approach employs a coupling parameter which mixes the forces of the well defined initial and final state in a straightforward manner. Although it is slightly more expensive (since each configuration in the intermediate states always requires two electronic ground state calculations) the coupling parameter method is more appealing as it circumvents the non-physical partially charged states.

A note on the relative computational time is certainly in order; the QM/MM, QM(*dzp*) and QM(*fd*) scale as 1:4:10 - for these relatively small systems. Although the *fd* is considerably more expensive - and too expensive for systems beyond a few hundred atoms particularly when one needs a considerable phase-space sampling - an optimal choice for further study is to use QM/MM to sample the phase space

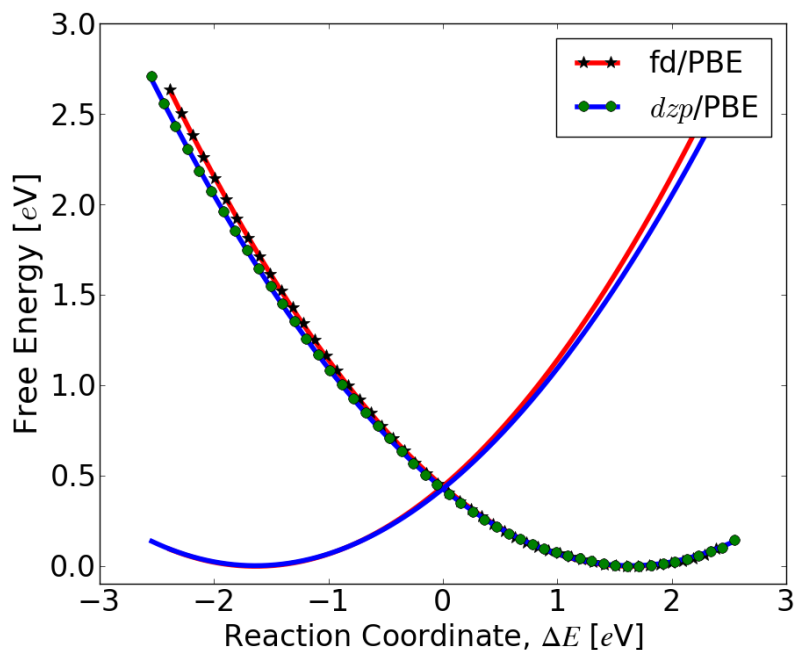


Figure 24: Diabatic free energy surfaces for the ferric-ferrous ($\text{Fe}^{+2}\text{-Fe}^{+3}$) charge transfer reaction. It is important to note that two different ways of describing the KS states are used: the finite difference (fd) mode, where the basis accuracy depends solely on the grid spacing, and a localized atomic orbital basis of *dzp* quality (a much cheaper option). Time scale of sampling an adequate phase space corresponding to 5 ps per bias window scales as follows: 1:4:10 for the QM/MM, QM(*dzp*) and QM(fd) methods, respectively. The black stars and green dots is the output from the WHAM method, and the red and green curves are second order fits to the data.

and then use the fd basis (or *dzp* basis if the internal energy reorganization is expected to be small) to analyze the potential energy gap.

As a final note - a major discrepancy is in the electrostatic constant of GGA described water compared to experiment - but after the generation of an adequate phase-space the with the QM/MM method accurate results were recovered by evaluating the electronic gaps with full QM. One can in a similar fashion explore exchange-correlation functionals beyond GGA, since the expensive phase-space sampling is avoided with QM/MM. A final step is to bring the reactants together in to a single simulation cell - and a simple way is already present in the current GPAW code - namely ΔSCF [143, 144] - where one has control over the electronic occupation in specific molecular orbitals.

OSMIUM COMPLEXES

The first part of this Chapter summarizes the results presented in paper **I** and expands upon those results to include analysis with the QM/MM code, as well as free energy surfaces which are partly presented in paper **II**. In the second part the experimental results from paper **III** are summarized and the DFT calculations presented in detail.

8.1 OSMIUM POLYPYRIDINE

Os(II)/(III) polypyridine complexes in aqueous solution are robust molecular entities both in freely solute state and adsorbed on Au(111)- and Pt(111)-electrode surfaces. This class of robust coordination chemical compounds have recently been characterized by electrochemical SCANNING TUNNELING MICROSCOPY (*in situ* STM) [1, 2, 3, 4, 5]. The Os-complexes were found to display strong SCANNING TUNNELING SPECTROSCOPY (STS) features at the level of resolution of the single molecule while STS features of a similar Co complexes, although clear, were much weaker. The data was framed by concise but phenomenological theory of interfacial electrochemical ELECTRON TRANSFER (ET) extended to the electrochemical *in situ* STM configuration [8, 6, 9].

With view on first-principles insight into the *in situ* STM behavior of this class of robust redox (as opposed to non-redox) molecules, this chapter presents both a DFT and QM/MM study on the systems presented in Figure 25. The aim is to address the following

- Redox state control, as to mimic the gate-potential control in the *in situ* STM experiments
- Classical versus quantum solvent description for stabilizing both counter-anions as well as the redox states of the target polypyridine transition metal species
- Thermodynamic values pertinent to their redox process, as outlined in previous chapters

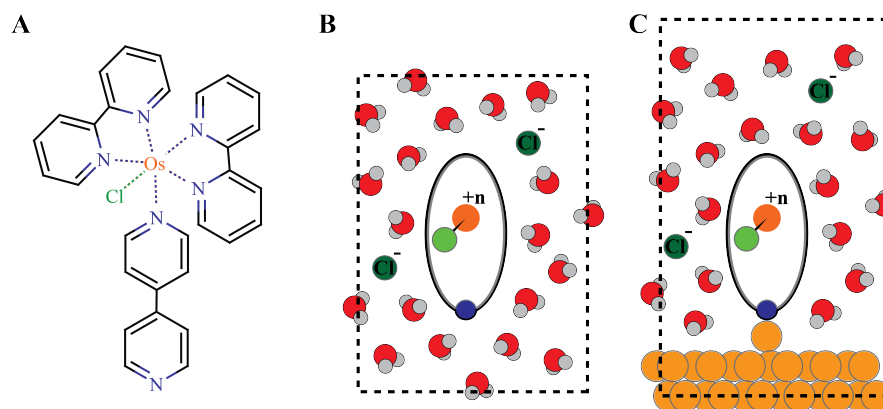


Figure 25: **A:** The Os^{+n}PoP complex, or $[\text{Os}(\text{bpy})_2(\text{PoP})\text{Cl}]$ ($\text{bpy} = 2,2'$ -bipyridine, $\text{PoP} = 4,4'$ -bipyridine). Note that the PoP ligand has a non-ligated nitrogen atom with an electron pair - which is suitable for substrate surface linking. **B:** A variety of molecular dynamics systems are addressed, where the pertinent redox states of the complex (+2 and +3) is controlled either trivially by removing electrons from the computational system, or with the addition of counter-anions (chloride). **C:** The analysis is, moreover, extended to the solvent-substrate surface interface - here $\text{Au}(111)$ - as in the *in situ* STM experiments.

8.2 COMPUTATIONAL PARAMETERS

The computational parameters presented in section 7.1 apply here, with the following addition. To accommodate for the dimensions of the polypyridine osmium complex in molecular dynamics simulations a large cell with periodic boundary conditions was filled with water (198 molecules) and the simulation box size adjusted such that the density is $\approx 1.0 \text{ g/cm}^3$ (resulting dimensions were 16.7, 22.8 and 16.3 Å). After thermalising the system with molecular dynamics a large cavity was cut out fitting the the vacuum relaxed complex. In this way the density should remain approximately the same [145] - and the complex is surrounded by about 2-3 solvation shells. A second system was also constructed in an analogous manner, but now with 732 water molecules (resulting dimensions of 28.5, 31.5 and 28.5 Å) - and the dynamics here done solely with the QM/MM scheme. The bond constraint strategies for the Langevin-RATTLE dynamics and Lennard-Jones pair potential constants for the QM/MM interface are presented in Figure 11 (pg. 44) and Table 1 (pg. 23), respectively.

8.2.1 Redox State Control

A major challenge in DFT is to describe charged species in periodic systems. For example, without any solvent and resulting screening effects the $\text{Os}^{2+}\text{PoP-A}(111)$ and $\text{Os}^{3+}\text{PoP-Au}(111)$ species do not form (**D** in Figure 26) - a non-physical system composed of a partially

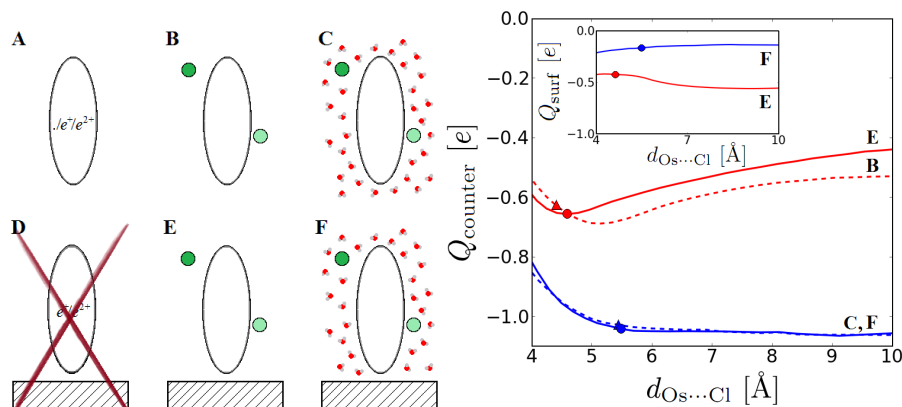


Figure 26: **Left:** Schematic of the various systems investigated. The oval represents the osmium polypyridine complex, Figure 25. The oxidation state of the complex was addressed in a variety of ways. **A:** the oxidation state (+1,+2 and +3) of the isolated complex is controlled by removing zero, one or two electrons from the computational system. In **B, C, E** and **F** this is instead achieved by adding one or two chloride counter-anions to the computational system. In **C** and **F** the complex and counter-anion are solvated with water. In **E** and **F** the complex is, furthermore, adsorbed on a metal surface (Au(111)). In **D** it is emphasized that the redox state can not be controlled by removing electrons from the system when the complex is adsorbed on a metal surface. **Right:** The solvent is found to be crucial in the charge transfer and stabilization between the osmium complex and chloride counter-anion(s), as evident in the charge profiles presented. The profile shows the charge of one of the counter-anions, Q_{counter} , as it systematically moved closer and further from the osmium metal center, $d_{\text{Os}\dots\text{Cl}}$. Without the solvent only a partial charge is transferred, both in the free solute and adsorbed states. Furthermore a large charge transfer exists between the osmium complex and surface, Q_{surf} , without solvent screening as shown in the inset. In all cases the fully solvated complex and counter-anion systems were comparable to the solvated charge complexes - in both nuclear structure (bond lengths) and electronic structure - revealed by extensive molecular dynamics simulations.

charged surface and complex is formed, and the chemical identity of the complex in the +2 and +3 redox states lost. This was addressed first by introducing suitable counter-anions to form overall neutral pairs, and later extended to the solvated case where it was found that the solvent provides crucial charge screening effects which greatly stabilize the two charged species - and meaningful redox states of the complex were formed, both in the free solute and adsorbed state on Au(111) surfaces. The systems and main results are presented in Figure 26.

To expand upon the results above the same systems were addressed with the QM/MM code, where the osmium complex and chloride ions were treated at the full QM level - and all solvent molecules are treated classically. Molecular dynamics simulations were performed on the osmium complex depicted in Figure 25B. In this setup the redox states: +2 and +3 were controlled adding one or two chloride atoms to the system. Table 8 collects major bond lengths for the two different redox states, and compares the QM and QM/MM cases.

Table 8: Metal to ligand bond lengths (in Å) and total charge of the complex, Q_{com} , of the structures B shown in Figure 25. The structures and charge on the osmium complex is compared for the full QM and the QM/MM cases, where in the latter all solvent is treated classically.

	B^+Cl^-		$B^{2+}2Cl^-$	
	QM(H ₂ O) ₁₆₈	QM(H ₂ O) ₁₆₆	MM(H ₂ O) ₁₆₈	MM(H ₂ O) ₁₆₆
Os-Cl _{lig}	2.47	2.35	2.46	2.35
Os-N _{PoP}	2.13	2.15	2.13	2.15
Os-N _{avg}	2.09	2.07	2.09	2.08
Q_{com} [e]	1.07	1.84	0.99	1.97

The average bond lengths are found to be more or less the same in the full QM simulations compared to the QM/MM results. This is observed for both the +2 and +3 redox states, which are controlled by the presence of the chloride counter-anions. Moreover, the classically described solvent enhances the charge on both ions - for example the charge on the complex is closer to integer values in the QM/MM case. This is due to the fact that there is no overlap between the electronic states of complex and counter-anion with the solvent in the QM/MM case - the solvent has no electronic states. In the QM case such an overlap exists which results in an 'apparent' partial charge transfer.

8.2.2 Free Energy Surfaces

The free energy surfaces for the osmium complexes were generated in an analogous manner to the transition metals presented in the reaction schematic Figure 17. The total reaction is $Os^{2+}-Os^{3+} \rightarrow Os^{3+}-Os^{2+}$, where the forward and reverse reaction electronic gaps are combined to generate sufficient statistics. All values are though reported as half-reaction values - since we are interested in single-molecule reorganization as in the *in situ* STM experiments.

First a system comprised of the osmium complex and 168 water molecules was addressed at the full QM level, and the free energy

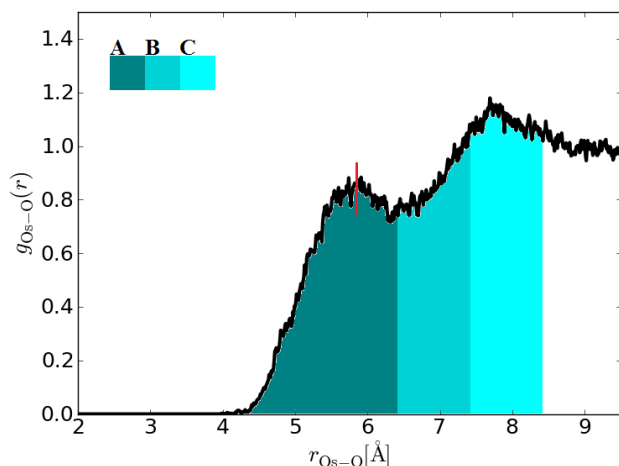


Figure 27: The radial distribution of oxygen in water around the osmium polypyridine complex. After running extensive QM/MM simulations the same configurations were used to analyze the free energy surface, but now with the water treated at the QM level up to the distance indicated by the A, B and C color scheme. Corresponding model cartoons and free energy surfaces are presented in Figure 28. The red line indicates the estimated ionic radius of the complex used in the Marcus model analysis (see text for details).

surface generated to give the reorganization energy and barrier. To explore the efficiency of the QM/MM code a second system was analyzed as well, but now with 732 water molecules. At first all water molecules of the latter system are described classically and a vast phase-space generated with molecular dynamics. In a second step the initial-final state electronic gap is re-evaluated - but now with some of the closest solvent molecules to the complex described at the QM level. Figure 27 presents the radial distribution function of osmium to oxygen distances, and describes the 'post'-sampling process. Figure 28 presents the resulting free energy surfaces - which shows clearly the effect of the solvents dielectric response on the electronic gap.

The free energies of reorganization and barrier are collected in Table 9. The free energy of reorganization and barrier for the half-reaction is found to be 0.63 and 0.16 eV, respectively, at the full QM level. In the QM/MM case, where the complex is solely treated with QM, the same quantities are found to be 1.21 and 0.31 eV, which is roughly an increase of 1.8 in accordance with the difference in the electrostatic constants of the QM vs. MM water. The inner sphere reorganization energy is much smaller in this case compared to the hexaaqua complexes presented in Chapter 7, or only about 0.1 eV. By re-evaluating the initial-final state potential energy gap with varying QM solvent we find that the values converge rapidly - for example the free en-

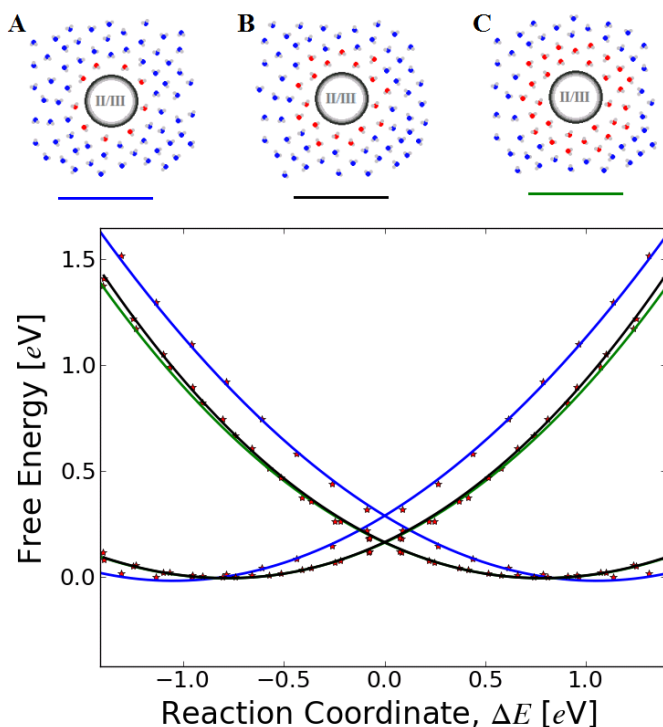


Figure 28: Free energy surfaces generated for varying degree of quantum solvent - systems **A**, **B** and **C** show the expansion of the QM treatment around the osmium complex. The phase-space is sampled first with QM/MM, where all solvent molecules are described classically. For the free energy surface analysis the energy gap between the initial and final state is evaluated but with all solvent molecules within the radial bounds indicated in Figure 27 are treated also with QM. In this way the dielectric response of the solvent is gradually reintroduced in a step-by-step fashion until convergence is achieved.

Table 9: Free energies of reorganization and free energy barriers, in [eV]. Full QM is compared to the QM/MM expansion process, see Figure 27-case **C**, which is deemed converged. QM/MM(o) refers to the case where none of the solvent is treated with QM. For comparison the Marcus model is used, eq. 129, but now with computational PBE [A] and TIP3P [B] dielectric constants, which should compare to the QM and QM/MM(o) results respectively.

	QM	QM/MM(C)	QM/MM(o)	Marcus [A]	Marcus [B]
λ_{reo}	0.63	0.68	1.21	0.82	1.35
ΔF^\ddagger	0.16	0.17	0.31	0.21	0.34

ergy surface where the solvent molecules up to a 7.3 Å radial bound around the complex are treated with QM is almost the same as in the case of 8.3 Å radial bound. Furthermore, at that level the free energies of reorganization and barrier for the QM/MM(C) system is 0.68 and 0.17 eV, in very good agreement with the full QM results. At the 8.3 Å

radial bound each energy gap evaluation roughly includes 90 water molecules on average, and as seen in the radial distribution function of Figure 27 corresponds roughly to two solvation shells. Note that we require less than half the solvent used in the full QM calculations to reach convergence.

The change in the initial-final state potential energy gap and hence reorganization energy between the QM and QM/MM cases is, as mentioned before, due to the dielectric response of the QM water. This change is furthermore apparent when using the Marcus model, eq. 129 (pg. 71), to estimate the outer reorganization energy - which is evaluated for this system by using the ionic radius shown in Figure 27, and the dielectric constants for PBE and TIP3P water. These models, denoted Marcus [A] and Marcus [B] in Table 9, are in fair agreement with the full QM and QM/MM results - although in both cases larger by about 0.14-0.19 eV. This is again due to either a erroneous estimation of the ionic radius, as well as poor choice of dielectric constants. The trend is though exactly as expected - with an enhancement of a factor of 1.8 in the reorganization energy - as observed for the QM versus QM/MM simulations.

8.2.3 Conclusion and Outlook

Using appropriate counter-anions the redox state of an osmium complex is controlled by chemical means. This is in solution and at the solvent/substrate interface. The solvent plays a crucial role in stabilizing both ions, by providing strong charge screening effects. This was, moreover, observed in the QM/MM simulations as well.

Free energies and free energy barriers were generated for the complex at the full QM level. By using the QM/MM method a large system - composed of the complex and 700 water molecules - was simulated and from the QM/MM phase space the solvent response was systematically re-introduced, and the resulting free energies converged to the full QM case.

This seamless jump between QM and QM/MM is very promising for large and complex simulations as the majority of the computational time is thermalisation and phase-space sampling. The option of treating the sampling with QM/MM offers a great and efficient way to introduce other complexities, such as hybrid-GGA functionals - to better represent the solvent response and/or the internal reorganization energy.

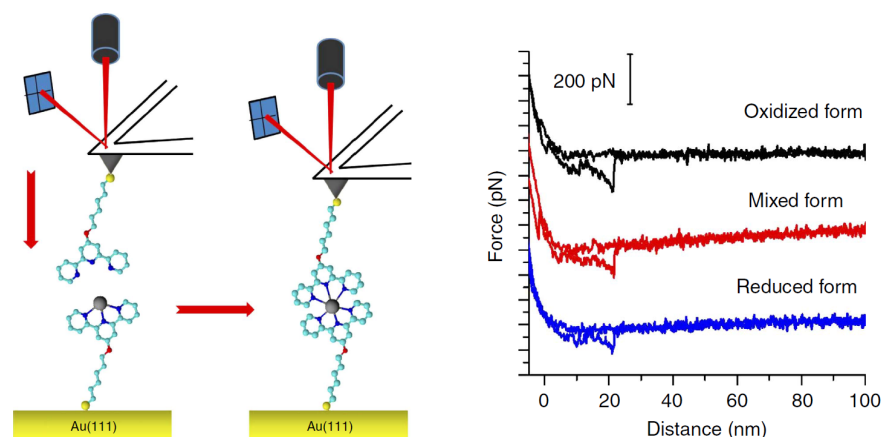


Figure 29: **Left:** Working principles of the electrochemical AFM force spectroscopy performed. The AFM cantilever, to which terpy-C6-S is attached, approaches a mono-layer of Os^{+n} -terpy-C6-S on Au(111). As the tip approaches a bond is formed between the two species. The cantilever deflection - which is determined from the position of the reflected laser - is translated in to forces as it is retracted from the sample. **Right:** typical force-extension curves from the ECAFM experiments performed on the Os-terpy-C6-S-Au(111) system. This is for different working potentials which correspond to the fully oxidized state (+3), partially reduced state (equilibrium of +2/+3) and the reduced state (+2) viewed top to bottom, respectively. From a multitude of such experiments the average forces for the different redox states was determined; Os^{+3} gives 130 ± 60 pN, $\text{Os}^{+2/+3}$ gives 100 ± 30 pN and Os^{+2} gives 80 ± 30 .

8.3 OSMIUM TERPYRIDINE

Here an experimental methods similar to the electrochemical *in situ* STM is used - electrochemical atomic force microscopy (ECAFM), where both the single-molecule coordinative forces can be addressed and the redox state of a osmium terpyridine (terpy) complex controlled. A schematic of the working principles of the AFM experiments is presented in Figure 29.

Using sophisticated experimental methods the single-molecule coordinative bond is both formed and ruptured in a controlled fashion where the redox state of the complex is, furthermore, addressable. Hence, this method offers force-spectroscopy. The effects of the redox state change are evident: in the Os^{2+} case the average Os-terpy bond force is found to be 80 ± 30 pN, while for the Os^{+3} case is 130 ± 60 pN.

8.3.1 DFT Simulations

The aim of this DFT computational work is to address key factors which influence the metal to ligand binding in the $\text{Os}(\text{terpy})_2$ complex - and compare those factors when the complex is in the two different redox states, $[\text{Os}(\text{terpy})_2]^{2+}$ and $[\text{Os}(\text{terpy})_2]^{3+}$. The complexity of the simulations is kept low - for example bulk solvent and counter-anions are not included. Main focus is on exploring how strongly the osmium metal, in the two different redox states, binds to the terpyridine ligand - through coordinating to either one, two or three nitrogens of the tridentate ligand. This is achieved by systematically pulling the bond apart while allowing other degrees of freedom to relax at each stage - and the resulting potential energy change is translated into pulling forces as a function of the bond length change.

8.3.1.1 Computational Parameters

All calculations are performed with the real-space DFT code GPAW [18, 19]. The Kohn-Sham states are represented in terms of numerical atomic orbitals of the double- ζ with polarization (*dzp*) quality, and the potential is represented on a real space grid with $0.18(\pm 0.01)$ Å grid spacing. The exchange-correlation (xc) energy is approximated with the PBE [32] functional, and the core electrons are treated with the PAW [40] method. A quasi-Newton scheme is used to relax structures with a convergence criteria of the forces at 0.05 eV/Å. Magnetic states of the two redox states are, furthermore, analyzed with the hybrid-GGA xc-functionals PBEo [146] and B3LYP [147], using PBE relaxed structures. The charge density of the system and constituents is analyzed with Bader's analysis [46, 48], which gives localized charges for each atom comprising the molecular system.

8.3.2 Rotational PES of Terpyridine

As a first step the potential energy surface of terpy was calculated as a function of the rotation of the two side pyridine units, Figure 30. The results show that terpy favors a planar geometry, with the two end pyridines in *trans* configuration relative to the middle group - with the nitrogen atoms then oriented as follows: $\text{N}\uparrow\text{N}\downarrow\text{N}\uparrow$. The potential energy cost for rotating a pyridine side group by 180° - to the *cis* configuration - is found to be 0.3 eV, consistent with previous work [148]. Rotating the second side unit to the *cis* configuration - forming $\text{N}\downarrow\text{N}\downarrow\text{N}\downarrow$ - has the same potential energy barrier of 0.3 eV. As a consequence the *cis* configuration is 0.6 eV less stable than the *trans*. The conjugation properties are not affected by the orientations of the terpy nitrogen atoms - and we find that the potential energy cost of the rotation is rooted mainly in steric or electrostatic repulsions be-

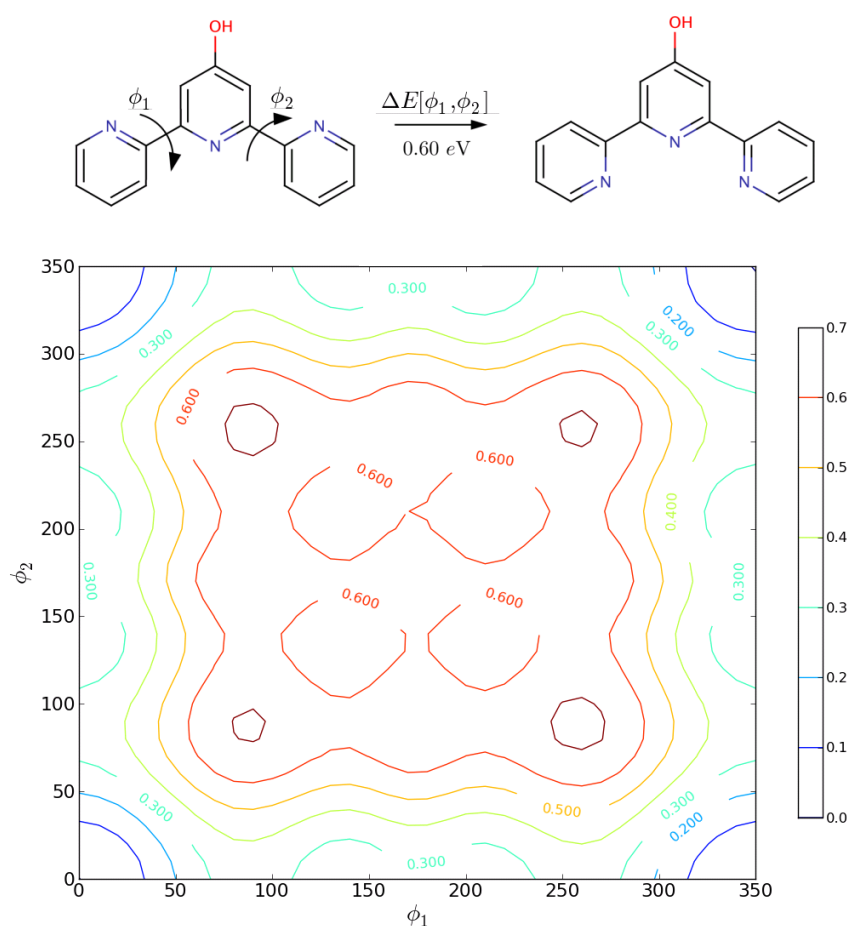


Figure 30: Potential energy surface of pyridine rotation of terpyridine, see top schematic. The most favorable structure is where the three nitrogen atoms are oriented as follows: $N\uparrow N\downarrow N\uparrow$, which is the zero-point reference in the PES. Rotating one pyridine group such that the nitrogen points downwards costs 0.3 eV, and rotation of both side pyridines to form $N\downarrow N\downarrow N\downarrow$ costs about 0.6 eV in total. This rotational barrier is due to coulomb interactions between the charged nitrogen atoms (see for example Figure 31), which have a full lone pair.

tween the charged nitrogen atoms and their lone-pair. This view is backed up by the Bader's analysis presented in Figure 31

With the rotational cost in mind one can assume that it is unlikely that all or even two of the nitrogen atoms are oriented towards the osmium metal center when ligation takes place. This would, moreover, be hindered by the presence of a water ligand as shown in Figure 32.

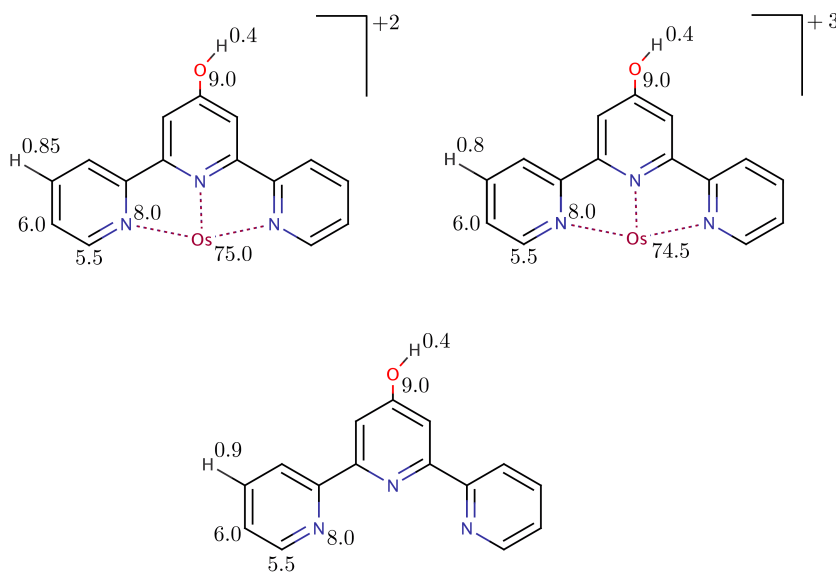


Figure 31: Bader's analysis of Os^{2+} and Os^{3+} complexes, ligated to a single terpy. For reference the charge of a lone terpy is presented as well. Only a single hydrogen is shown for clarity, and the charge values presented are in all cases average values for the atoms in similar positions.

8.3.3 Magnetic States and Charge

Possible high-spin (HS) and low-spin (LS) magnetic states were analysed for both redox states - Os^{2+} is a d^6 species with possible spin state of 0 and 4, whereas Os^{3+} is a d^5 species with possible spin states of 1 and 5. The potential energy of these states was calculated for the various configurations presented in Figure 32, as well as for $[\text{Os}(\text{terpy})(\text{H}_2\text{O})_3]^{2+/3+}$ and $[\text{Os}(\text{H}_2\text{O})_6]^{2+/3+}$, and the HS/LS gap for each species and redox state evaluated: $\Delta E_{\text{HS/LS}}^{n+} = E_{\text{HS}}^{n+} - E_{\text{LS}}^{n+}$. In all cases the low-spin states were considerably more stable for all complexes and both redox states, with very similar $\Delta E_{\text{HS/LS}}$ values evaluated with the PBE, PBEo and B3LYP functionals. The PBE gaps for $[\text{Os}(\text{terpy})_2]^{2+/3+}$ were found to be $\Delta E_{\text{HS/LS}}^{2+} = 2.21$ and $\Delta E_{\text{HS/LS}}^{3+} = 2.31$ eV, while for $[\text{Os}(\text{H}_2\text{O})_6]^{2+/3+}$ $\Delta E_{\text{HS/LS}}^{2+} = 3.81$ and $\Delta E_{\text{HS/LS}}^{3+} = 4.47$ eV. Oddly the introduction of water as ligands instead of the terpy increases the splitting between the magnetic states, contrary to the spectrochemical series [149] where pyridine is a stronger splitter.

Figure 31 presents the atomic charges of terpy and osmium. The resulting electron distribution is reasonable. For example, all nitrogen donor atoms are negatively charged with a full lone-pair, which explains why the *trans*-configuration is favored. The charge is acquired mainly from neighboring carbon atoms in the conjugated system. The

positive charge of the hydrogen atoms in the conjugate system varies from 0.1-0.05. Notably the electron distribution of the terpy nitrogen, oxygen, and carbon atoms is not significantly perturbed by the addition of osmium in either of the two oxidation states. Oxidation of Os^{2+} to Os^{3+} , however, results in shared electron donation from the metal center and terpy ligands, with half an electron loss from Os. The rest of the hole is distributed in the conjugate system, mainly registered as a slight loss of charge on the aromatic hydrogen atoms with the average charge being 0.15 and 0.20 per hydrogen atoms, for the Os^{2+} and Os^{3+} redox states, respectively.

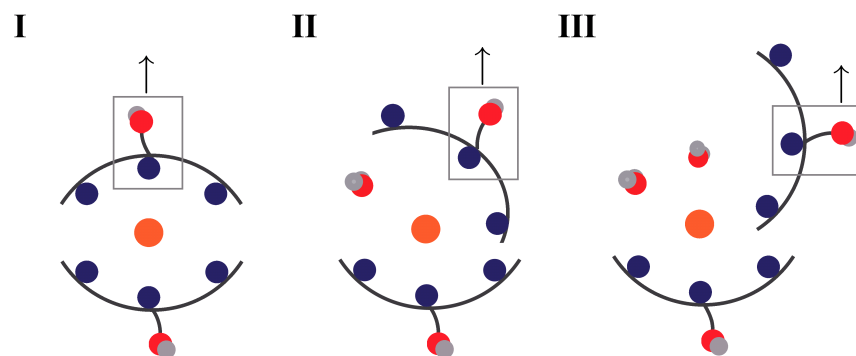


Figure 32: Schematic of the possible coordination of $\text{Os}(\text{terpy})$ with terpy and water, $[\text{Os}(\text{terpy})_2(\text{H}_2\text{O})_n]^{2+/3+}$. Osmium - orange, nitrogen - blue, oxygen - red and hydrogen - grey. The carbons, hydrogens and overall structure of terpyridine is simplified for clarity and is represented with the dark-grey stick figure. Three configurations are examined for both the magnetic state analysis and the bond breaking simulations. In the simulations the carbohydrate linking group is replaced with a hydroxyl group. **I:** $\text{Os}(\text{terpy})_2$ - osmium in octahedral ligand environment provided by the three nitrogen atoms of two terpy molecules. **II:** $\text{Os}(\text{terpy})_2(\text{H}_2\text{O})$ - osmium coordinated through two nitrogen atoms of one terpy ligand. The non-bonding pyridine group rotates by about 90° to accommodate the water molecule occupies the sixth site. **III:** $\text{Os}(\text{terpy})_2(\text{H}_2\text{O})_2$ - osmium coordinated to a single nitrogen atom of one terpy ligand - of a side group - with two water molecules occupying the other coordination sites.

8.3.4 Simulated Bond Breaking

Structural differences between the octahedral $[\text{Os}(\text{terpy})_2]^{2+}$ and $[\text{Os}(\text{terpy})_2]^{3+}$ were found to be minimal. In their vacuum relaxed structures the Os-N bond length at the middle pyridine ligand is around 2.01 Å for both redox states. The other two Os-N bond lengths are slightly different: about 2.10 and 2.05 Å for Os^{2+} and Os^{3+} , respectively. So, to address the $\text{Os}^{2+/3+}$ pulling energy a reference structure was created by relaxing all structures during the bond breaking at a charge of 2.5. The

schematic and caption of Figure 33 present the overall simulation process. In this way the potential energy, and difference, of the integer redox states are based on the same structures - with bond lengths of intermediate value (which was also observed for the hexaaqua-transition metals, Figure 19). The pulling energies $E - E[\text{dr}_{\text{Os-N}} = 0]$ - where $E[\text{dr}_{\text{Os-N}} = 0]$ is the potential energy of the fully relaxed system - were calculated for each configuration and plotted against the change in Os-N distance ($\text{dr}_{\text{Os-N}}$) for both redox states. Figure 34 presents the results.

The pulling force is evaluated as the slope of the linear best fits. The slope is steeper, i.e. the pulling forces stronger, when terpy is fully coordinated to Os^{2+} , which changes dramatically when a single or two water molecules are coordinated. The Os^{3+} -terpy bond and force becomes increasingly stronger compared to Os^{2+} . This accords qualitatively with the experimental observations and in particular the $[\text{Os}(\text{terpy})_2(\text{H}_2\text{O})_2]^{2+/3+}$ structure is proposed as the most favorable coordination, considering the mild reaction conditions and the rotations and structure of isolated terpy. To fully coordinate to terpy would require several reorganization steps and more vigorous condition - and result in the reversed stability order in favor of Os^{2+} .

8.3.5 Conclusion and Outlook

All in all the different pulling forces observed for the two different redox states of the osmium complex are rationalized by the DFT simulations in a qualitative fashion - and in particular points towards the crucial role of the solvent and ligand substitution in the pulling process. For a quantitative analysis a more comprehensive simulation scheme is required with full incorporation of solvent and thermodynamic effects.

This can be achieved in a similar manner to the free energy surface analysis discussed in previous Chapters, and in particular using QM/MM to speed up the sampling process. One can envision simulating the configuration phase space of each increment of the bond length changes (which acts as the reaction coordinate, section 6.2), where a portion of the surrounding solvent is treated with QM, centered in a large box of classical solvent which acts as the heat bath.

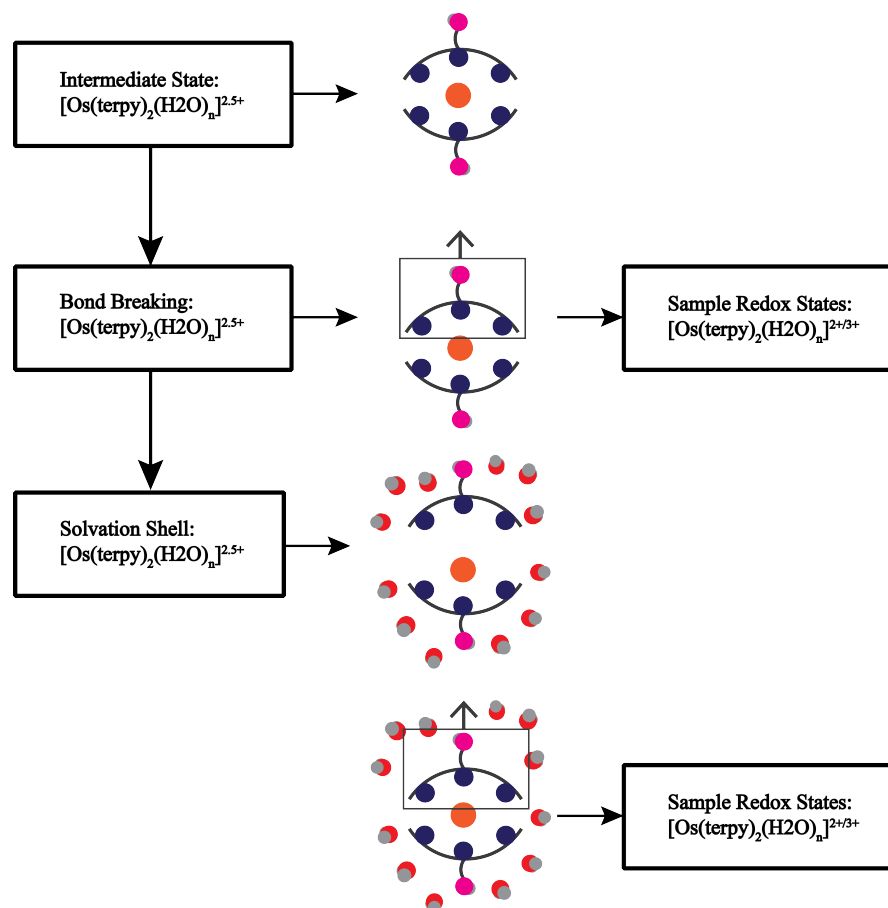


Figure 33: Schematic of the overall bond breaking simulations procedure. Briefly, the target system - see Figure 32 - is relaxed at an intermediate charge state of 2.5. At each interval the osmium to nitrogen distance of the middle unit, or the side unit (structure III in Figure 32), is stretched by 0.2 Å. This distance is kept fixed while all other degrees of freedom are allowed to relax with the same convergence criteria (0.05 eV/Å). The potential energy of the resulting trajectories are then re-evaluated at the +2 and +3 charge states. As a second step a solvation shell - around 25-30 water molecules - is relaxed around the structures, at the intermediate charge, and the potential energy analysis repeated at the integer charges.

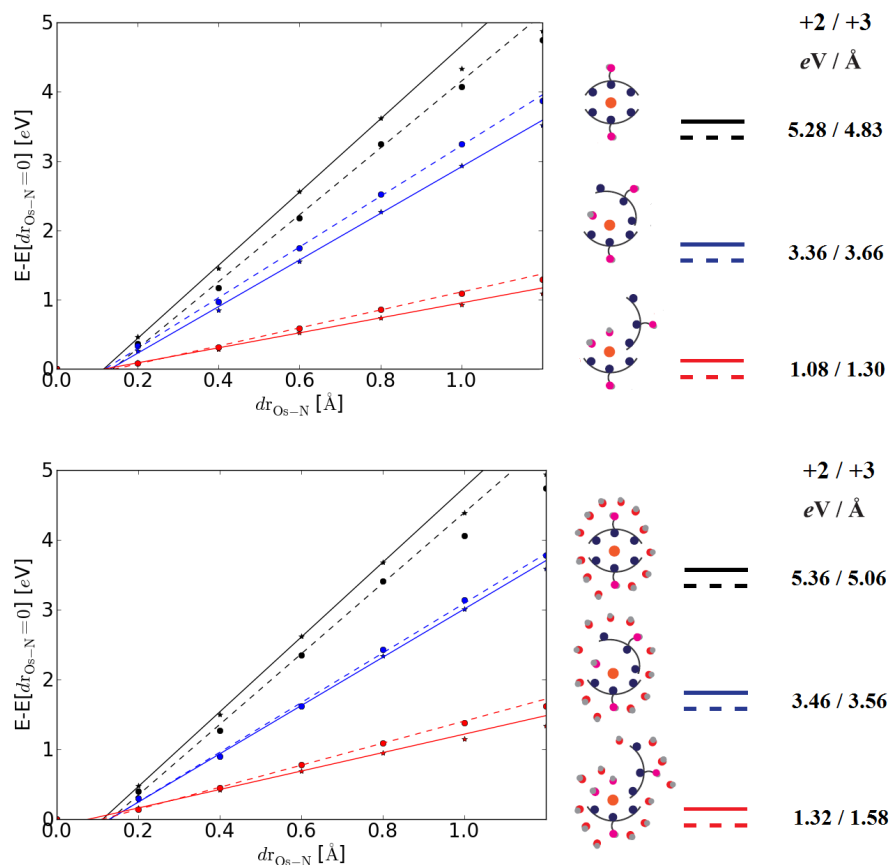


Figure 34: Potential energy changes of the simulated bond breaking for both vacuum (top) and solvated (bottom) systems, for the three different coordination complexes and for both redox states. The solid and broken lines are linear best fits to the +2 and +3 data. The value of the slope is presented to the left, which is interpreted as a the force. It is clear that Os^{+2} favors binding full coordination to terpy, but as water occupies coordinates sites the Os^{3+} -terpy bond becomes stronger. Beyond 0.8-1.2 Å the energy starts to level out (bond breaks), and is flat at a distance of 2.0 Å in all cases. In the 1.2-2.0 Å increment range - in some of the simulations - a hydrogen atom was fully donated from a water ligand to the empty coordination site on terpy - forming a very stable $Os^{2+/3+}$ -OH⁻ and (terpy)⁻H⁺ bonds - which gave a step in the curve.

IRIDIUM-IRIDIUM DIMER

In this Chapter the 'photo'-induced structural changes of a bimetallic iridium-iridium ($d^8 - d^8$) complex are simulated by using the newly implemented QM/MM and MD methods. All of the reported material here is found in paper IV.

Figure 35 presents the iridium-iridium complex, $[\text{Ir}_2(\text{dimen})_4]^{2+}$, and two dynamic structural modes which are highly perturbed upon excitation - it is the objective of this study to simulate and analyze the excitation and resulting changes in these and other modes. In the electron ground state this complex has a σ -antibonding highest occupied molecular orbital (HOMO), while the lowest unoccupied molecular orbital (LUMO) is described as σ -bonding [150, 151]. As a result there is a considerable structural change upon electronic excitation from the HOMO to the LUMO, and in particular a dramatic change in the metal-to-metal distance. This has been observed experimentally with x-ray scattering measurements on both $[\text{Rh}_2(\text{dimen})_4]^{2+}$ [152] and $[\text{Ir}_2(\text{dimen})_4]^{2+}$ [153] - where the change in the distance was 0.86 Å and 1.4 Å, respectively.

9.1 COMPUTATIONAL METHODS

The electronic ground state and molecular dynamics are carried out with the newly implemented Langevin-RATTLE and QM/MM schemes. The $\text{Ir}_2(\text{dimen})_4^{2+}$ complex is treated quantum mechanically with GPAW [18, 19] at the PBE [33] level of theory, using a *dzp* basis set to describe the valence electrons of the $(\text{dimen})_2$ ligand and a *tzp* basis for the valence electrons of the iridium metals. The basis set and grid spacing dependence of the iridium-iridium distance was examined and found to be converged at a grid-spacing of < 0.22 at the *dzp* level. During the simulations and collection of data the grid spacing is in the range 0.16-0.19 Å. The solvent is acetonitrile described with the three-point interaction site potential of Guardia et. al. [53], and an analysis of the RDFs generated from full classical and QM/MM results presented in Figure 15, pg. 50. The vdW parameters and molecular bond constraint strategy for this species is presented in Figure 11 (pg. 44) and 4 (pg. 22). The molecular dynamics systems were made by first prethermalising a box of $28 \times 28.5 \times 31.5$ Å containing acetonitrile at ambient conditions (density 0.786 g/cm³). A cavity is cut out fitting the complex, and the resulting number of acetonitrile molecules is 237.

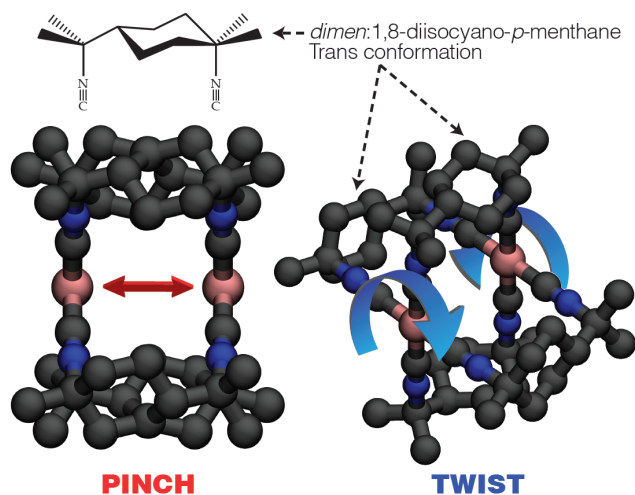


Figure 35: The two main dynamic, structural modes of $[\text{Ir}_2(\text{dimen})_4]^{2+}$, here shown without the hydrogens for clarity, and in the conformer employed for these studies. The 1,8-diisocyno-*p*-menthane (dimen) ligand provides the optimal compromise between flexibility and rigidity for large, but controllable structural changes e.g. by electronic excitation. Electronically exciting this complex promotes an electron from the antibonding HOMO to the bonding LUMO, effectively forming a chemical bond between the Ir atoms [150, 151, 154].

The Langevin thermostat is set to 300 K. A trajectory of 18.21 ps was simulated at a time-step of 2 fs for the ground-state (GS) electronic configuration.

To simulate the excited state 40 snapshots were selected (strategically) from the GS trajectory, and the electronic state changed to the excited state (ES) by changing and fixing the magnetic state from a singlet (GS) to a triplet (ES). This effectively promotes an electron to the LUMO, causing the desired structural changes. A total of 140 ps were simulated with a resolution of 1 fs, and used in the analysis of the various ES dynamic structure modes.

9.2 RESULTS

The major dynamic structure modes from the molecular dynamics runs are collected and presented in Figure 36. First, the mean Ir-Ir distance in the excited state is found to be 2.98 Å, compared to 2.90 Å from x-ray scattering experiments [153]. The oscillation period for the mean pinch is found to be $\approx 70 \text{ cm}^{-1}$, in excellent agreement with experiments by Hartsock et. al. [154]. An analysis of the breathing mode gives a similar period, or about $\approx 74 \text{ cm}^{-1}$. This means that experimentally a deconvolution of these two modes is not possible. No period is available for the twist mechanism, but a delayed mechanism

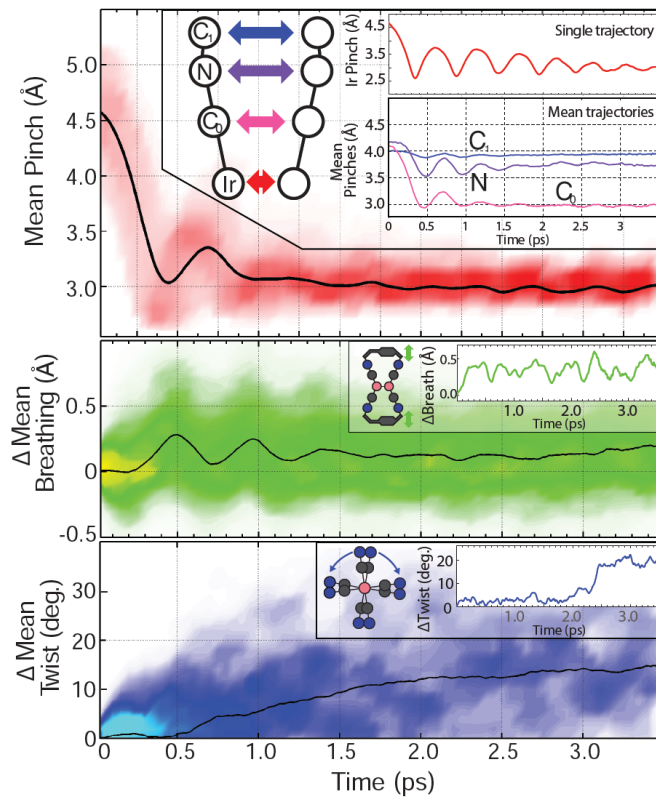


Figure 36: The mean Ir-Ir pinching (top), breathing (middle), and twisting (bottom) as a function of time after excitation. The twist is defined as the change in dihedral angle beyond time $t = 0$. The shaded background represents the binned count - or statistics - of observing these values over all of the sampled trajectories. This population loses its pinch phase within a ps, while the single trajectory-pinch oscillation dies out much slower (top inset). However, the mean phase of the breathing mode is sustained for almost 2 ps. Interestingly, the pinching and breathing modes display the same oscillation period - which means that they are obscured in spectroscopic experiments. The second and third inset show a typical phase of this particular mode from a single trajectory.

is observed starting at 0.5 ps where the complex begins to twist.

A detailed analysis of the dynamic structure modes in vacuum revealed, furthermore, the crucial role of the solvent in facilitating energy dissipation after excitation occurs. This was mainly mediated through the the breathing mode of the complex - and results in, for example, a longer coherent motion in the pinching mode compared to vacuum calculations.

9.3 FINAL REMARKS

In this study the efficiency of both the Langevin-RATTLE and QM/MM scheme are used to sample a vast phase-space for a complex system - displaying a dramatic structural change upon oxidation. With the data available the mean period of the major dynamic structure modes were analyzed, and shown to compare well to x-ray diffraction and spectroscopic experiments. Furthermore, a previously hidden mode (breathing mode) is observed which is here accessible to the computational simulations, but obscured during experiments. All simulations employ modest approximations, like the GGA based functional, and simple magnetic state change to effectively simulate the excited-state. Moreover, the solvent is treated classically and acts here as both a heat source and sink - e.g. following the abrupt change from the ground state to the excited state the resulting potential energy change is dissipated in to the solvent through the breathing mode.

Part IV

SUMMARY

SUMMARY

The theoretical tools used in this work have been presented along with several tests for a variety of systems to show their general properties and expected behavior. The constant temperature molecular dynamics - with molecular bond constraints - are used throughout this work and is a general code applicable to most systems. The classical mechanics potential and code is used for simple solvent models only - and has not been tested for general purposes. However, the formulations are simple and the literature vast on such methods.

The hybrid-classical and quantum mechanics code was applied to a limited number of systems; quantum mechanical hexaaqua transition metals, osmium polypyridine complex and an iridium-iridium dimer complex - in classically described bulk water or acetonitrile. The method itself accepts general charge parameters and Lennard-Jones potential parameters - hence, extension to different types of systems is facilitated and relatively straightforward. This will with no doubt be the case in future studies.

Both the molecular dynamics and QM/MM methods are combined in the phase-space configuration sampling of a complex system. There it was shown that accurate results can be retrieved with a simple 'post'-sampling scheme. This is very appealing as the computational cost sits mainly in the sampling - and with the efficiency of QM/MM will allow for additional complexity in the simulation of free energy surfaces.

A range of electron-charge transfer systems were addressed and free energy surfaces generated. The results were rationalized with both experimental results and classical analytical expressions - with clear steps towards improved accuracy. Furthermore, two bias methods were compared - one based on the conventional fractional number of electrons approach - and the other using a coupling parameter to mix two electronic states. The conventional method of using partially charged systems was found to be troublesome, to say the least. Although slightly more expensive the coupling parameter method is by far more convenient, and is recommended as the choice for driving simulations where single or both reactants are treated within the same simulation cell in DFT simulations.

BIBLIOGRAPHY

- [1] C. Li, I. Pobelov, T. Wandlowski, A. Bagrets, A. Arnold, and F. Evers, *J. Am. Chem. Soc.* **130**, 318 (2008).
- [2] W. Haiss, R. J. Nichols, H. van Zalinge, S. J. Higgins, D. Bethell, and D. J. Schiffrin, *Phys. Chem. Chem. Phys.* **6**, 4330 (2004).
- [3] W. Haiss, T. Albrecht, H. van Zalinge, S. J. Higgins, D. Bethell, H. Höbenreich, D. J. Schiffrin, R. J. Nichols, A. M. Kuznetsov, J. Zhang, et al., *J. Phys. Chem. B* **111**, 6703 (2007).
- [4] T. Albrecht, K. M.-Poulsen, J. B. Christensen, A. Guckian, T. Bjørnholm, J. G. Vos, and J. Ulstrup, *Faraday Discuss.* **131**, 265 (2006).
- [5] T. Albrecht, K. M.-Poulsen, J. B. Christensen, A. Guckian, J. Hjelm, T. Bjørnholm, and J. Ulstrup, *J. Am. Chem. Soc.* **128**, 6574 (2006).
- [6] J. Zhang, Q. Chi, T. Albrecht, A. M. Kuznetsov, M. Grubb, A. G. Hansen, H. Wackerbarth, A. C. Welinder, and J. Ulstrup, *Electrochim. Acta* **50**, 3143 (2005).
- [7] A. M. Kuznetsov and J. Ulstrup, *Electron Charge Transfer in Chemistry and Biology* (Wiley, New York, 1999).
- [8] J. Zhang, A. M. Kuznetsov, I. G. Medvedev, Q. Chi, T. Albrecht, P. S. Jensen, and J. Ulstrup, *J. Chem. Rev.* **108**, 2737 (2008).
- [9] A. M. Kuznetsov and J. Ulstrup, *J. Chem. Phys. A* **104**, 11531 (2000).
- [10] J. Wang, P. Cieplak, and P. Kollman, *J. Comp. Chem.* **21**, 1049 (2000).
- [11] Y. Duan, W. Chun, S. Chowdhury, M. C. Lee, G. Xiong, W. Zhang, R. Yang, P. Cieplak, R. Luo, T. Lee, et al., *J. Comp. Chem.* **24**, 1999 (2003).
- [12] S. J. Weiner, P. A. Kollman, D. A. Case, U. C. Singh, C. Ghio, G. Alagona, S. Profeta, and P. J. Weiner, *J. Am. Chem. Soc.* **106**, 765 (1984).
- [13] S. J. Weiner, P. A. Kollman, D. T. Nguyen, and D. A. Case, *J. Comp. Chem.* **7**, 230 (1986).
- [14] W. D. Cornell, P. Cieplak, C. I. Bayly, I. R. Gould, K. M. Merz, D. M. Ferguson, D. C. Spellmeyer, T. Fox, J. W. Caldwell, and P. A. Kollman, *J. Am. Chem. Soc.* **117**, 5179 (1995).

- [15] A. K. Rappé, C. J. Casewit, W. A. Colwell, W. A. Goddard III, and W. M. Skiff, *J. Am. Chem. Soc.* **114**, 10024 (1992).
- [16] W. Kohn, *Rev. Mod. Phys.* **71**, 1253 (1999).
- [17] M. J. Frisch, G. W. Trucks, H. B. Schlegel, G. E. Scuseria, M. A. Robb, J. R. Cheeseman, G. Scalmani, V. Barone, B. Mennucci, G. A. Petersson, et al. (2009), gaussian Inc. Wallingford CT 2009.
- [18] J. J. Mortensen, L. B. Hansen, and K. W. Jacobsen, *Phys. Rev. B* **71**, 035109 (2005).
- [19] J. Enkovaara, C. Rostgaard, J. J. Mortensen, J. Chen, M. Dulak, L. Ferrighi, J. Gavnholt, C. Glinsvald, V. Haikola, H. A. Hansen, et al., *J. Phys.: Condens. Matter* **22**, 253202 (2010).
- [20] J. M. Soler, E. Artacho, J. D. Gale, A. García, J. Junquera, P. Ordejón, and D. Sánchez-Portal, *J. Phys.: Condens. Matter* **14**, 2745 (2002).
- [21] G. Kresse and J. Furthmüller, *Phys. Rev. B* **54**, 11169 (1996).
- [22] M. Born and R. Oppenheimer, *Ann. Physik* **84**, 457 (1927).
- [23] D. A. McQuarrie, *Quantum Chemistry, Volume 100 Physical Chemistry Series* (1983), university Science Books.
- [24] C. D. Sherrill and H. F. Schaefer III, *Adv. Quant. Chem.* **34**, 143 (1999).
- [25] P. Hohenberg and W. Kohn, *Phys. Rev.* **136**, B864 (1964).
- [26] W. Kohn and L. J. Sham, *Phys. Rev.* **140**, 1133 (1965).
- [27] J. P. Perdew and K. Schmidth, *CP577*, 1 (2001), ed. Doren, V. V. et. al.
- [28] R. M. Martin, *Electronic Structure: Basic Theory and Practical Methods* (2004), cambridge University Press, New York.
- [29] D. Ceperley and B. J. Alder, *Phys. Rev. Lett.* **45**, 566 (1980).
- [30] J. P. Perdew and Y. Wang, *Phys. Rev. B* **45**, 13244 (1992).
- [31] J. P. Perdew and A. Zunger, *Phys. Rev. B* **23**, 5048 (1981).
- [32] J. P. Perdew, K. Burke, and M. Ernzerhof, *Phys. Rev. Lett.* **77**, 3865 (1996).
- [33] J. P. Perdew, K. Burke, and M. Ernzerhof, *Phys. Rev. Lett.* **77**, 3865 (1996).
- [34] A. D. Becke, *Phys. Rev. A* **38**, 3098 (1988).

- [35] C. Lee, W. Yang, and R. G. Parr, *Phys. Rev. B* **37**, 785 (1988).
- [36] S. Kurth, J. P. Perdew, and P. Blaha, *Int. J. Quant. Chem.* **75**, 889 (1999).
- [37] Y. Zhang and W. Yang, *Phys. Rev. Lett.* **80**, 890 (1998).
- [38] B. Hammer, L. B. Hansen, and J. K. Nørskov, *Phys. Rev. B* **59**, 7413 (1999).
- [39] H. Hellman, *J. Chem. Phys.* **3**, 61 (1934).
- [40] P. E. Blöchl, *Phys. Rev. B* **50**, 17953 (1994).
- [41] G. Kresse and D. Joubert, *Phys. Rev. B* **59**, 1758 (1999).
- [42] A. H. Larsen, M. Vanin, J. J. Mortensen, K. S. Thygesen, and K. W. Jacobsen, *Phys. Rev. B* **80**, 195112 (2009).
- [43] H. Hellmann, *Einführung in die Quantenchemie* (1937), franz Deuticke: Leipzig.
- [44] R. P. Feynman, *Phys. Rev.* **56**, 340 (1939).
- [45] R. A. Mulliken, *J. Chem. Phys.* **23**, 1833 (1955).
- [46] R. F. W. Bader, *Atoms in Molecules: A Quantum Theory* (Oxford University Press, New York, 1990).
- [47] D. F. Guerra, J. Handgraaf, E. J. Baerends, and F. M. Bickelhaupt, *J. Comput. Chem.* **25**, 189 (2004).
- [48] W. Tang, E. Sanville, and G. J. Henkelman, *J. Phys.: Condens. Matter* **21**, 084204 (2009).
- [49] J. E. Lennard-Jones, *Proc. R. Soc. Lond. A* **106**, 463 (1924).
- [50] F. London, *Trans. Faraday Soc.* **33**, 8 (1937).
- [51] L. Monticelli and P. D. Tieleman, *Meth. Mol. Biol.* **924**, 197 (2013).
- [52] W. L. Jorgensen, J. Chandrasekhar, J. D. Madura, R. W. Impey, and M. L. J. Klein, *J. Chem. Phys.* **79**, 926 (1983).
- [53] E. Guàrdia, R. Pinzoón, J. Casulleras, M. Orozco, and F. J. Luque, *Mol. Sim.* **26**, 287 (2001).
- [54] T. Schnabel, J. Vrabc, and H. Hasse, *J. Mol. Liq.* **05** (2009).
- [55] A. K. Al-Matar and D. A. Rockstraw, *J. Comp. Chem.* **25**, 660 (2004).
- [56] F. Cuadros, I. Cachadiña, and A. Ahumada, *Mol. Eng.* **6**, 319 (1996).

- [57] H. A. Lorentz, *Ann. d. Phys. und Chemie* **12**, 127 (1881).
- [58] D. Berthelot, *Comptes Rendus* **T126**, 1703 (1898).
- [59] M. Waldman and A. T. Hagler, *J. Comp. Chem.* **25**, 660 (2004).
- [60] P. P. Ewald, *Ann. Phys. Leipzig* **64**, 253 (1921).
- [61] K. P. Jensen and W. L. Jorgensen, *J. Chem. Theory. Comput.* **2**, 1499 (2006).
- [62] N. L. Allinger, X. Zhou, and J. Bergsma, *J. Mol. Struct. (THEOCHEM)* **312**, 69 (1994).
- [63] A. Warshel, *Nature* **260**, 679 (1976).
- [64] B. B. Lev, D. R. Salahub, and S. Y. Noskov, *Interdiscip. Sci. Comput. Life Sci.* **2**, 12 (2010).
- [65] B. B. Lev, B. Roux, and S. Y. Noskov, *J. Chem. Theory Comput.* **9**, 4165 (2013).
- [66] S. Keinan, R. Venkatramani, A. Balaeff, and D. N. Beratan, *J. Phys. Chem. C* **114**, 20496 (2010).
- [67] A. Warshel, P. K. Sharma, M. Kato, Y. Xiang, H. B. Liu, and M. H. M. Olsson, *Chem. Rev.* **106**, 3210 (2006).
- [68] H. Hu and W. Yang, *Annu. Rev. Phys. Chem.* **59**, 573 (2008).
- [69] M. W. van der Kamp and A. J. Mulholland, *Biochemistry* **52**, 2708 (2013).
- [70] H. Takahashi, T. Hori, H. Hashimoto, and T. Nitta, *J. Comp. Chem.* **22**, 1252 (2001).
- [71] A. Crespo, D. A. Scherlis, M. A. Martí, P. Ordejón, and D. A. Estrin, *J. Phys. Chem. B* **107**, 13728 (2003).
- [72] H. M. Senn and W. Thiel, *Angew. Chem. Int. Ed.* **48**, 1198 (2009).
- [73] S. P. de Visser, *Biochem. Soc. Trans* **37**, 373 (2009).
- [74] A. Laio, J. VandeVondele, and U. Rothlisberger, *J. Chem. Phys.* **116**, 6941 (2002).
- [75] H. Takahashi, H. Ohno, R. Kishi, M. Nakano, and N. Matabayasi, *J. Chem. Phys.* **129**, 205103 (2008).
- [76] M. Eichinger, P. Tavan, J. Hutter, and M. Parrinello, *J. Chem. Phys.* **110**, 10452 (1999).
- [77] X. Xu and W. A. Goddard, *J. Phys. Chem. A* **108**, 2305 (2004).

- [78] J. C. Grossman, E. Schwegler, E. W. Drager, F. Gygi, and G. Galli, *J. Chem. Phys.* **120**, 200 (2004).
- [79] P. H.-L. Sit and N. Marzari, *J. Chem. Phys.* **122**, 204510 (2005).
- [80] P. Demontis, S. Spanu, and G. B. Suffritti, *J. Chem. Phys.* **114**, 7980 (2001).
- [81] Y. Ma and S. H. Garofalini, *Mol. Sim.* **31**, 739 (2005).
- [82] K. Nam, J. L. Gao, and D. York, *Theory Comput.* **1**, 2 (2005).
- [83] J. L. Gao and C. Alhambra, *J. Chem. Phys. A* **107**, 1212 (1997).
- [84] H. Hao and Y. Weitao, *Annu. Rev. Phys. Chem.* **59**, 573 (2008).
- [85] T. Darden, D. York, and L. Pedersen, *J. Chem. Phys.* **98**, 10089 (1993).
- [86] T. Laino, F. Mohamed, and M. Parrinello, *J. Chem. Theory Comput.* **2**, 1370 (2006).
- [87] D. Zahn, B. Schilling, and S. M. Kast, *J. Phys. Chem. B* **106**, 10725 (2002).
- [88] P. Brommer, P. Beck, A. Chatzopoulos, F. Gähler, J. Roth, and H.-R. Trebin, *J. Chem. Phys.* **132**, 194109 (2010).
- [89] D. Wolf, P. Keblinski, S. R. Phillpot, and J. Eggerbrecht, *J. Chem. Phys.* **110**, 8254 (1999).
- [90] C. J. Fennell and J. D. Gezelter, *J. Chem. Phys.* **124**, 234104 (2006).
- [91] D.-L. Chen, A. C. Stern, B. Space, and J. K. Johnson, *J. Phys. Chem. A* **114**, 10225 (2010).
- [92] Y. Yonezawa, *J. Chem. Phys.* **136**, 244103 (2012).
- [93] D. Frenkel and B. Smit, *Understanding Molecular Simulation: From Algorithms to Applications* (Academic Press, San Diego, 2001).
- [94] W. F. van Gunsteren and H. J. C. Berendsen, *Mol. Phys.* **45**, 637 (1982).
- [95] Brünger, A. and Brook, C. L. and Karplus, M., *Chem. Phys. Lett.* **105**, 495 (1984).
- [96] E. V.-Eijnden and G. Ciccotti, *Chem. Phys. Lett.* **429**, 310 (2006).
- [97] L. Verlet, *Phys. Rev.* **159**, 98 (1967).
- [98] H. C. Andersen, *J. Comp. Phys.* **54** (1983).

- [99] A. K. Soper and M. G. Phillips, *Chem. Phys.* **107** (1986).
- [100] J. Kästner, *WIREs Comp. Mol. Sci.* **1**, 932 (2011).
- [101] G. M. Torrie and J. P. Valleau, *Chem. Phys. Lett.* pp. 578–581 (1974).
- [102] G. M. Torrie and J. P. Valleau, *J. Comp. Phys.* **23**, 187 (1977).
- [103] R. A. Kuharski, J. S. Bader, D. Chandler, M. Sprik, M. L. Klein, and R. W. Impey, *J. Chem. Phys.* **89**, 3248 (1988).
- [104] C. Dellago, B. P. G., and D. Chandler, *J. Chem. Phys.* **108**, 9236 (1998).
- [105] A. M. Ferrenberg and R. H. Swendsen, *Phys. Rev. Lett.* **63**, 1195 (1989).
- [106] S. Kumar, D. Bouzida, R. H. Swendsen, P. A. Kollman, and J. M. Rosenberg, *J. Comp. Chem.* **13**, 1011 (1992).
- [107] M. Souaille and B. Roux, *Comp. Phys. Comm.* **135**, 40 (2001).
- [108] S. R. Bahn and K. W. Jacobsen, *Comput. Sci. Eng.* **4**, 56 (2002).
- [109] H. C. Andersen, *J. Comp. Phys.* **52**, 24 (1983).
- [110] D. A. Johnson and P. G. Nelson, *Inorg. Chem.* **34**, 5666 (1995).
- [111] H. Montgomery, R. V. Chastain, and E. C. Lingafelter, *Acta Cryst.* **20**, 731 (1966).
- [112] H. Montgomery and E. C. Lingafelter, *Acta Cryst.* **17**, 1478 (1964).
- [113] J. K. Beattie, S. P. Best, S. P. Skelton, and A. H. White, *J. Chem. Soc., Dalton Trans.* **10**, 2105 (1981).
- [114] S. P. Best, J. K. Beattie, and R. S. Armstrong, *J. Chem. Soc., Dalton Trans.* **12**, 2611 (1984).
- [115] B. S. Brunschwig, C. Creutz, D. H. Macartney, T. K. Sham, and N. Sutin, *Faraday Discuss. R. Soc. Chem.* **74**, 113 (1982).
- [116] M. Eshel and A. Bino, *Inorg. Chim. Acta* **320**, 127 (2001).
- [117] K. P. Jensen, B. O. Roos, and U. Ryde, *J. Chem. Phys.* **126**, 014103 (2007).
- [118] K. P. Jensen, *J. Phys. Chem. A* **113**, 10033 (2009).
- [119] P. Delahay, *Chem. Phys. Lett.* **87**, 607 (1982).
- [120] P. Delahay and A. Dziedzic, *J. Chem. Phys.* **80**, 5793 (1984).

- [121] P. Delahay, K. von Burg, and A. Dziedzic, *Chem. Phys. Lett.* **79**, 157 (1981).
- [122] N. Sutin, *Theory of electron transfer reactions. In electron transfer and electrochemical reactions; Photochemical and other energized reactions* (1986), zuckermann, J. J. Ed., VCH: New York.
- [123] R. A. Marcus, *Faraday Discuss. Chem. Soc.* **29**, 21 (1960).
- [124] R. A. Marcus, *J. Chem. Phys.* **24**, 966 (1956).
- [125] R. A. Marcus, *J. Chem. Phys.* **24**, 979 (1956).
- [126] R. A. Marcus, *J. Chem. Phys.* **26**, 867 (1957).
- [127] R. A. Marcus, *J. Chem. Phys.* **26**, 872 (1957).
- [128] M. French and R. Redmer, *Phys. Plasmas* **18**, 043301 (2011).
- [129] K. M. Rosso and J. R. Rustad, *J. Phys. Chem. A* **104**, 6718 (2000).
- [130] D. P. Fernández, Y. Mulev, A. R. H. Goodwin, and J. M. H. Levelt Sengers, *J. Phys. Chem. Ref. Data* **24** (1995).
- [131] W. C. Schumb, M. S. Sherrill, and S. B. Sweetser, *J. Am. Chem. Soc.* **59**, 2360 (1937).
- [132] M. Uudsemaa and T. Tamm, *J. Phys. Chem. A* **107**, 9997 (2003).
- [133] G. Jones and J. H. Colvin, *J. Am. Chem. Soc.* **65**, 1563 (1944).
- [134] G. von Grube and L. Z. Schlecht, *Electrochem.* **32**, 178 (1926).
- [135] L. Ciavatta and M. Grimaldi, *J. Inorg. Nucl. Chem* pp. 3071–3082 (1969).
- [136] H. Diebler and N. Sutin, *J. Phys. Chem.* **68**, 174 (1964).
- [137] S. G. Bratsch, *J. Phys. Chem.* **18**, 1 (1989).
- [138] A. J. Bard, R. Parsons, and J. Jordan, *Standard Potentials in Aqueous Solutions* (1985), marcel Dekker, New York.
- [139] S. Bogusz, T. E. Cheatham, and B. R. Brooks, *J. Chem. Phys.* **108**, 7070 (1998).
- [140] Höchtl, P. and Boresch, S. and Bitomsky, W. and Steinhauser, O., *J. Chem. Phys.* **109**, 4927 (1998).
- [141] Vladimirov, E. and Ivanova, A. and Rösch, N., *J. Chem. Phys.* **129**, 194515 (2008).
- [142] P. H.-L. Sit, M. Cococcioni, and N. Marzari, *Phys. Rev. Lett.* **97**, 028303 (2006).

- [143] J. Gavnholt, T. Olsen, M. Engelund, and J. Schiøtz, *Phys. Rev. B* **78**, 075441 (2008).
- [144] T. Olsen, J. Gavnholt, and J. Schiøtz, *Phys. Rev. B* **79**, 0354403 (2009).
- [145] R. Spezia, C. Bresson, C. D. Auwer, and M. P. Gaigeot, *J. Phys. Chem. B* **112**, 6490 (2008).
- [146] C. Adamo and V. Barone, *J. Chem. Phys.* **110**, 6158 (1999).
- [147] P. J. Stephens, F. J. Devlin, C. F. Chabalowski, and M. J. Frisch, *J. Phys. Chem.* **98**, 11623 (1994).
- [148] M. G. B. Drew, J. Hudson, P. B. Iveson, M. L. Russell, J.-O. Liljezin, M. Skålberg, L. Spjuth, and C. Madic, *J. Chem. Soc., Dalton Trans.* **18**, 2973 (1998).
- [149] G. L. Miessler and D. A. Tarr, *Inorganic Chemistry* (2004), 3rd ed., Pearson Prentice Hall, New Jersey.
- [150] K. R. Mann, J. G. I. Gordon, and H. B. Gray, *J. Am. Chem. Soc.* **97**, 3553 (1975).
- [151] M. D. Roundhill, H. B. Gray, and C. Che, *Acc. Chem. Res.* **22**, 55 (1989).
- [152] P. Coppens, O. Gerlits, I. I. Vorontsov, A. Kovalevsky, Y. Chen, T. Graber, M. Gembicky, and I. Novozhilova, *Chem. Comm.* **19**, 2144 (2004).
- [153] K. Haldrup, T. Harlang, M. Christensen, A. Dohn, T. B. van Driel, K. S. Kjær, N. Harrit, J. Vibenholt, L. Guerin, M. Wulff, et al., *Inorg. Chem.* **50**, 9329 (2011).
- [154] R. W. Hartsock, W. Zhang, M. G. Hill, B. Sabat, and K. J. Gaffney, *J. Phys. Chem. A* **115**, 2920 (2011).


PUBLICATIONS - PAPER I

Ab Initio Calculations of the Electronic Properties of Polypyridine Transition Metal Complexes and Their Adsorption on Metal Surfaces in the Presence of Solvent and Counterions

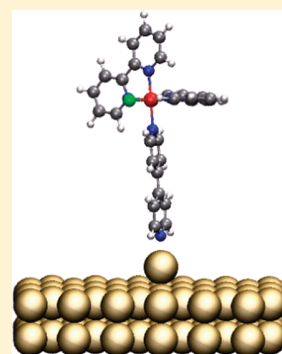
E. Ö. Jónsson,[†] K. S. Thygesen,[†] J. Ulstrup,[‡] and K. W. Jacobsen^{*,†}

[†]CAMD, Department of Physics, Technical University of Denmark, DK - 2800 Kgs. Lyngby, Denmark

[‡]Department of Chemistry, Technical University of Denmark, DK - 2800 Kgs. Lyngby, Denmark

 Supporting Information

ABSTRACT: Os(II)/(III) and Co(II)/(III) polypyridine complexes in aqueous solution are robust molecular entities both in freely solute state and adsorbed on Au(111)- and Pt(111)-electrode surfaces. This class of robust coordination chemical compounds have recently been characterized by electrochemical scanning tunneling microscopy (in situ STM). The Os-complexes were found to display strong tunneling spectroscopic (STS) features at the level of resolution of the single molecule while STS features of the Co complexes, although clear, were much weaker. The data was framed by concise but phenomenological theory of interfacial electrochemical electron transfer extended to the electrochemical in situ STM configuration. With a view on first-principle insight into the in situ STM behavior of robust redox (as opposed to nonredox) molecules, we present in this report a density functional theory (DFT) study of the complexes in both free and adsorbate state, in either state exposed to both stoichiometric counterions and a large assembly of solvent water molecules. The oxidation states of the complexes were controlled, first by introducing chlorine counter atoms followed by spontaneous attraction of electrons from the complexes, also at first in electrostatically neutral form. Second, the solvent is found to provide strong dielectric screening of this charge transfer process and to be crucial for achieving the full chemically meaningful charge separated ionic oxidation states. The molecular charge and structure of the complexes in the presence of the solvent, are conserved upon adsorption, whereas the structural features of the different oxidation states are completely lost upon adsorption under vacuum conditions. Detailed microscopic insight such as offered by the present study will be important in molecular-based approaches to “smart” redox molecules enclosed in in situ STM or other nanoscale and single-molecules scale configurations in condensed matter environments.



INTRODUCTION

The quest for ever smaller electronic components has prompted equally increasing efforts in “bottom up” approaches that start with a single or a small collection of molecules. New experimental tools such as the scanning tunneling microscopes (STM), nanogap electrodes and electrode arrays, and break-junction techniques^{1–7} as well as new theoretical and computational tools have here been essential.^{4–10} As a result, structural mapping and electronic conductivity right down to the level of the single molecule are now increasingly well understood. Most studies have addressed what could be denoted as “simple” molecules; that is, the molecules are structurally small and any HOMO or LUMO strongly off resonance with the Fermi levels of the enclosing electrodes. Conductance through the molecules is therefore represented as tunneling, or superexchange through a potential barrier determined by the MOs of the molecule. From the perspective of possible molecular scale device function, molecules with “smart” properties are, however, needed. Such molecules are, for example, redox molecules with a single or several redox centers and with low-lying electronic levels (LUMOs or HOMOs) that can be physically populated at low bias voltage. In this way new efficient electron transport channels

are opened or closed in given voltage ranges.⁷ Moreover, redox molecules such as some large organic molecules or transition metal complexes can be inserted into three-electrode configurations, where the third electrode, the gate, is present in addition to the directly enclosing source and drain electrodes. The option of both transistor (amplifier) and rectifier function at the single-molecule level are opened in this way.

“Smart” molecules in the sense noted offer other perspectives. Transistor- and rectifier-like functions are operative at ambient temperatures and in condensed matter environment, say in aqueous environment. The latter has been demonstrated particularly by (in situ) STM^{4–6,11,12} where the substrate and tip correspond to the source and drain electrodes in solid-state transistors and rectifiers, and the electrochemical reference electrode to the gate electrode. Both strong on–off amplification and large rectification ratios have been observed, but the device characteristics are obviously broadened by the strong coupling between the molecular electron transfer (ET) center(s)

Received: January 27, 2011

Revised: April 29, 2011

Published: July 12, 2011

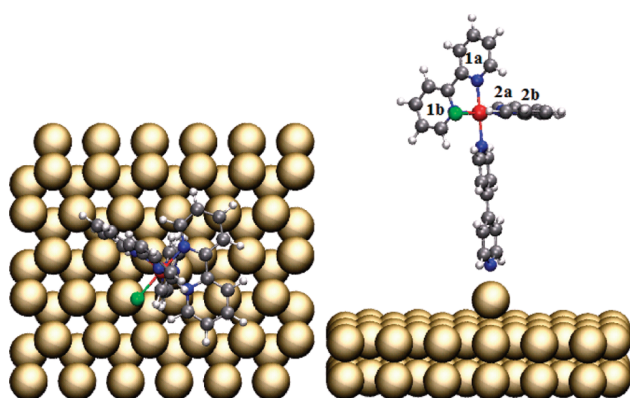


Figure 1. General setup of the adsorption systems. Left: top view of $M(n)POP$ or $[M(bpy)_2(POP)Cl]$ ($bpy = 2,2'$ -bipyridine, $POP = 4,4'$ -bipyridine and $M = Os$ or Co), on a $6 \times 6 \times 2$ (111) metal surface, either Au or Pt. The formal oxidation state of the unperturbed complex is +1 due to the chloride ligand. The complex is presented in the CPK color code: carbon is gray, nitrogen blue, hydrogen white, chloride green, and the metal center red. Right: side view of the same system, showing the perpendicular geometry of the complex relative to the surface and adatom. The labeling of individual pyridines is presented for the assignment of specific metal center to ligand bond lengths in the text.⁴¹

and the dynamic fluctuations of the environmental nuclear configurations.

Condensed matter ET through a redox molecule enclosed between two nanogap electrodes or between an in situ STM substrate surface and tip, including the dynamic solvent has been approached theoretically based on notions from interfacial electrochemical ET.^{7,13,14} These efforts have provided the basis for two important correlations specific for electrochemically controlled single-molecule conductivity. One is the correlation between the tunneling current and the overpotential at fixed bias voltage, i.e., for parallel variation of the electrochemical substrate and tip potentials. This is equivalent to current/gate voltage correlations in solid state transistors. The other one is the current/bias voltage correlation at fixed electrochemical potential of the substrate electrode. Further theoretical modeling was rooted in dielectric continuum theory. The overall character of the formalism is that of a parametrized phenomenological theory emerging from molecular electrochemical ET theory, but with all parameters clearly defined and accessible to first-principle computations.^{4,13–15}

The phenomenological approach enables inclusion of other important effects such as ionic strength, the potential distribution in the tunneling gap, and the importance of electronic coherence and simultaneous transfer of a manifold of electrons in a single molecular in situ STM event. We report here first steps toward a first-principle molecular approach to interfacial electrochemical ET for electrochemical in situ STM and STS redox molecules. Specific target molecules are polypyridine osmium and cobalt complexes for which detailed experimental data are available.^{11,12} The setup of the molecular systems are shown in Figure 1 and the different ways to incorporate the presence of counterions, metal surfaces, and water solvent are shown schematically in Figure 2. Our focus is 3-fold. One focus point is the role of the counterions of the doubly and triply positively charged complex cations. Our strategy here is to add cation and anion species in electrostatically neutral stoichiometric equivalents and compute the resulting charge distribution by ab initio approaches, so to

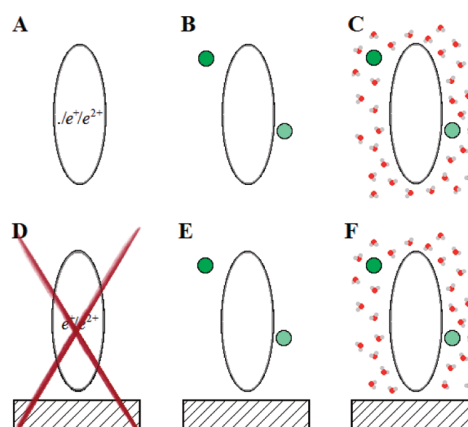


Figure 2. Schematics of all the systems investigated. The ellipse represents the $M(n)POP$ complex. In A the oxidation state (+1, +2, and +3) of the isolated complex is controlled by removing zero, one or two electrons from the simulation cell. In B, C, E, and F this is instead achieved by adding counterions (chlorine). In C and F the counterion and complex are further solvated with water. In E and F the complex is adsorbed on a metal surface. Figure D illustrates that it is not possible to change the oxidation state of the adsorbed complex by simply removing electrons from the simulation cell as these electrons will be removed from the Fermi level of the metal. A and B are also investigated in detail with molecular dynamics simulations with the simulation cells constructed in a different manner than for systems C and F. This is explained in the text.

speak letting the molecular entities redistribute the electronic charge themselves. The second focus is to undertake similar first-principles computations, supported by molecular dynamics simulations, when an assembly of water molecules is present. The adsorbed state of the whole solute molecular transition metal complex unit on both a Au(111) and Pt(111) surface is the third focus. A crucial outcome of the study is that solvation of both the cationic complexes themselves and the counter anions is essential to preserve the chemical identity of the complex cation and anion (chloride), in both the free solute state and the solute adsorbed state. Strong electronic delocalization occurs in vacuum environment, at complete variance with experimental interfacial electrochemical ET and STM/STS in situ observations.^{11,12}

METHODS

All calculations were performed with the real-space DFT code GPAW.^{16,18} The electronic wave functions were represented in terms of numerical atomic orbitals corresponding to double- ζ with polarization (DZP)¹⁸ and the potential represented on a real space grid with a $0.18(\pm 0.01)$ Å grid spacing. The exchange-correlation energy was approximated with the PBE¹⁹ functional and the core electrons described with the PAW method.²⁰ The Au(111) and Pt(111) surfaces were modeled as two layers of 6×6 atoms with lattice constants of 4.176 and 3.981 Å, respectively. Periodic boundary conditions were applied along the surface plane and the Brillouin zone was sampled on a 2×2 Monkhorst–Pack k-point grid. All structural relaxations were treated with a quasi-Newton scheme with a force tolerance of 0.05 eV/Å. The two metal layers were always kept fixed at their bulk lattice constants, while all other degrees of freedom were allowed to relax. All odd-electron systems were unrestricted (spin-polarized).

Table 1. Metal-to-Ligand Bond Lengths (in Å), HOMO-LUMO Energy Gap (Kohn–Sham Gap), Δ_{gap} , Magnetic Moment, μ , and Total Charge of the Complex, Q_{com} , of the Structures A and B Shown in Figure 2^a

	A	A ⁺	B ⁺ Cl [−]	A ²⁺	B ²⁺ 2Cl [−]	A (H ₂ O) ₁₆₈	A ⁺ (H ₂ O) ₁₆₈	B ⁺ Cl [−] (H ₂ O) ₁₆₇	A ²⁺ (H ₂ O) ₁₆₈	B ²⁺ 2Cl [−] (H ₂ O) ₁₆₆
Os–Cl _{lig}	2.42	2.39	2.42	2.33	2.40	2.50	2.48	2.47	2.36	2.35
Os–N _{POP}	2.09	2.13	2.12	2.14	2.14	2.11	2.14	2.13	2.16	2.15
Os–N _{1a}	2.07	2.06	2.05	2.08	2.07	2.07	2.07	2.07	2.08	2.08
Os–N _{1b}	2.05	2.06	2.07	2.09	2.08	2.07	2.07	2.07	2.08	2.08
Os–N _{2a}	2.06	2.05	2.06	2.10	2.03	2.04	2.06	2.06	2.09	2.09
Os–N _{2b}	2.07	2.08	2.08	2.11	2.09	2.06	2.08	2.08	2.10	2.10
Δ_{gap} [eV]	0.07	1.25	1.12	0.05	0.37	0.59	1.34	1.32	0.35	0.23/1.83
μ [μ_{B}]	1	0	0	1	1	1	0	0	1	1/0
Q_{com} [e]	0.00	1.00	0.72	2.00	1.03	0	1.09	1.07	1.94	1.84
Co–Cl _{lig}	2.42	2.25	2.30	2.23	2.28	**	**	**	2.26	2.26
Co–N _{POP}	2.16	2.45	2.42	2.01	2.00	1.93	1.97	1.96	2.00	2.00
Co–N _{1a}	2.11	2.14	2.12	1.96	1.94	1.89	1.95	1.95	1.95	1.95
Co–N _{1b}	2.05	1.94	1.95	1.95	1.95	1.88	1.94	1.94	1.95	1.95
Co–N _{2a}	2.10	1.94	1.94	1.97	1.95	2.07	2.11	2.09	1.97	1.98
Co–N _{2b}	2.10	1.93	1.94	1.96	1.95	1.96	1.95	1.93	1.96	1.96
Δ_{gap} [eV]	0.32	0.80	0.74	1.02	2.31	0.27	1.39	0.96	1.67	1.76
μ [μ_{B}]	2	1	1	0	0	2	1	1	0	0
Q_{com} [e]	0.00	1.00	0.71	2.00	1.21	0	1.14	1.13	1.96	1.88

^a The upper and lower parts of the table present results for the osmium and cobalt complexes, respectively. The three left columns show results for vacuum and the three right columns the results for water obtained by averaging from the Verlet dynamics. For the dynamics systems the bond lengths and magnetic moment are averaged over a 2 ps interval. The HOMO-LUMO gap and the complex charge were analyzed from 40 individual snapshots of the systems, at a 48 fs interval.

Verlet dynamics were performed to sample the phase space of water solvated complexes. A time step of 4 fs was allowed by constraining selected degrees of freedom of the hydrogen bonds. A large cell with periodic boundary conditions was filled with water (198 molecules) and the simulation cell size adjusted such that the density was 1.0 g/cm³. After relaxing the system a cavity was cut out fitting the vacuum relaxed complexes (and counterion(s)). This should reproduce the desired density of 1.0 g/cm³ as discussed by Spezia and associates.²¹ Structural data and the electronic density were analyzed over a 2 ps interval after allowing the system to equilibrate from 600 to 300 K over 0.5 ps.

RESULTS AND DISCUSSION

The Os and Co complexes addressed are identified in Figure 1. A “mined” adatom was inserted between the adsorbate and surface. There is an additional energy associated expenditure with the “mining” process. The ultimate stronger electronic coupling ensures, however, favorable energetics on molecular adsorption to the adatom compared with adsorption on the flat surface, as shown for bipyridines by Stadler et al.⁸ and for phenanthroline by Zhang and co-workers.²² Figure 2 shows a schematic view of the various complexes in free vacuum and solute molecular states, and in the adsorbed state on a Au(111) or Pt(111) surface in contact either with vacuum or an assembly of solvent water molecules.

Gas Phase Complexes. We consider first the vacuum states of system A of Figure 2, regarded as a reference system, but also representing a gas phase ionization process. Selected metal-to-ligand bond lengths, the HOMO–LUMO energy gaps (the difference in the Kohn–Sham eigenvalues), Δ_{gap} , and magnetic moments, μ , for both the osmium and cobalt complexes in each oxidation state are presented in Table 1. The cationic charge,

Q_{com} , of the complexes is also presented, and was analyzed with Bader’s analysis,²³ using a relatively new grid-based algorithm.²⁴ The labeling of specific metal center-to-nitrogen bonds of the 4,4′-bipyridine heteroligand are presented in Figure 1.

The structural changes for the osmium complex as the oxidation state is changed is only minute. There is at most a 0.09 Å change in the Os–Cl_{lig} bond length over the whole Os(A) to Os(A²⁺) transition and even less for the other metal–ligand bond lengths (“A” represents the neutral complex with a single negatively charged Cl[−] ligand, i.e., Os(I), while A⁺ and A²⁺ represent Os(II) and Os(III), respectively). This is expected for an electron-rich late-row transition metal. The bond lengths of Os(A⁺) are in fair agreement with both the crystal structure of Ryabov and associates²⁵ and the relaxed structures of Os(A⁺) and Os(A²⁺) obtained in the DFT computational study of O’Boyle and co-workers,²⁶ at the DZ/B3LYP level. The crystal structure showed, for example, Os–Cl_{lig} is 2.42 Å and Os–N_{POP} is 2.10 Å compared to our 2.39 and 2.13 Å, respectively. In general the bond lengths agree within 2%. All possible magnetic states were sampled as for a metal center in a perfect octahedral ligand field. The low-spin configurations were found to be the most stable in all cases, as in the calculations of O’Boyle et al.

The Co(A) to Co(A²⁺) transition is accompanied by much more pronounced structural changes, as generally observed for early transition metals as their electronic density is more amenable to redox changes due to lower nuclear charge screening. The most notable changes are in the asymmetric Co–Cl_{lig} and Co–N_{POP} bonds. The former changes from 2.42 to 2.25 Å and the latter from 2.16 to 2.45 Å over a single oxidation from Co(A) to Co(A⁺). The most stable spin state of Co(A) is found to be the triplet, which accords with a d⁸ electronic configuration with degenerate e_g orbitals. Low spin is, however, found for the Co(A²⁺) d⁷ configuration. This is in contrast with magnetic

susceptibility measurements of crystals of related cobalt polypyridine compounds, such as $[\text{Co}(\text{II})(\text{bpy})_3]$ and $[\text{Co}(\text{II})(4\text{-terpyridone})_2]$.^{27–30} $[\text{Co}(\text{II})(\text{bpy})_3]$ is generally regarded as a high-spin complex but with a small energy difference between the high- and low-spin states.³¹

The PBE or GGA functionals do not, however, in general capture weakly separated high- and low-spin states, as these functionals favor low-spin states for early transition metal complexes due to spurious self-interaction errors.^{32,33} On the other hand, the PBE functional has been found to predict accurate bond lengths and spin states for a number of first row diatomic transition metal compounds,³⁴ compared to the more accurate hybrid functionals such as TPSSH and B3LYP. The energy differences between high- and low-spin configurations are, however, much higher for the simple diatomics than for a transition metal in a six-coordinated ligand sphere. In any case, whether this particular cobalt complex is more stable in the high- or low-spin state in vacuum or solution does not change the essential results of using counter atoms/anions to control the charge state of the cationic complex. The spin states were restricted to the most stable PBE magnetic state in all cases.

Even though the structural changes were small for the osmium complex major electronic structure changes were apparent. The same goes for the cobalt complex. Projected density of states revealed that the highest occupied molecular orbital (HOMO) was metal-, metal-, and ligand-based for $\text{Os}(\text{A})$, $\text{Os}(\text{A}^+)$, and $\text{Os}(\text{A}^{2+})$, respectively, with highly varying Δ_{gap} of 0.07, 1.12, and 0.05 eV. Cobalt showed similar electronic structural changes and very similar metal-, metal-, and ligand-based HOMO in the same order of oxidation states from A to A^{2+} . Δ_{gap} rises consistently from 0.32 via 0.74 to 1.02 eV as the oxidation state increases.

Counter ion effects were incorporated next, represented by the complex counterion analogues of A^+ and A^{2+} in system B, Figure 2. The complex and counterions were at first combined as electrostatically neutral moieties $\text{B}(\text{I}) + \text{Cl}$ and $\text{B}(\text{I}) + 2\text{Cl}$ ($\text{B}(\text{I})$ again represents Os in the oxidation state +1, with a single Cl^- ligand). These were then allowed to relax electronically toward adjacent cationic and anionic clusters B^+Cl^- and $\text{B}^{2+}2\text{Cl}^-$, Table 1 (B^+ and B^{2+} for short here). The $\text{Os}(\text{B}^+)$ and $\text{Os}(\text{B}^{2+})$ complexes do capture similar structural changes as their A^+ and A^{2+} counterparts but with bond length discrepancies up to 0.07 Å in the $\text{Os}-\text{Cl}_{\text{lig}}$ bond and the trans $\text{Os}-\text{N}_{2\text{a}}$ bonds of $\text{Os}(\text{B}^{2+})$. The effect of the counterions on the ligand structure around the metal center is much more pronounced in the two oxidation states in the cobalt case. The agreement between the bond lengths of $\text{Co}(\text{A}^{+/2+})$ and $\text{Co}(\text{B}^{+/2+})$ species clearly shows that the counterions in fact induce structural changes in much the same way as removing electrons from the simulation cell. As noted, however, the electronic structure undergoes considerable changes as electrons are removed from the complexes. These changes were not reproduced in the presence of the counterions. This is evident by the emerging charges on the complexes, Q_{com} , which is for example 1.03e versus 2e in $\text{Os}(\text{B}^{2+})$ and $\text{Os}(\text{A}^{2+})$, respectively. The electron density of the complexes is simply not the same. Bader's analysis also showed that a large fraction of the charge transferred from the complex cation to the counter anions was localized on the ligands closest to the counteranion. Hence, delocalized electronic states are observed, resulting in a fractional charge distribution between the counterion and complex, as well as a mixed complex-counterion projected density of states for the HOMOs and a different Δ_{gap} . Such delocalized states are often encountered in the LDA or GGA approximations

to charge transfer systems in DFT, the best known case being the half electron occupation in $(\text{H}-\text{H})^+$ and is due to self-interaction errors.³⁵ The gas phase complexes do not therefore reach a truly ionic character, which was instead found next to be closely controlled by strong solvation effects.

Solvated Complexes. Solvation and associated charge localization was addressed by Verlet molecular dynamics computations on $\text{A}^{+/2+}$ and $\text{B}^{+/2+}$ in the presence of solvent, as outlined in the Methods section. The averaged bond lengths, HOMO–LUMO gap, Δ_{gap} , and the averaged charge, Q_{com} , of the complexes are given in Table 1. Clearly the charge transfer to the counterions is greatly stabilized in the presence of the solvent when comparing Q_{com} of $\text{M}(\text{B}^{+/2+})$ in vacuum and the solvated state $\text{M}(\text{B}^{+/2+})$. The positive charges of the single and double counterion systems, with solvent, are in fact close to the fully ionized values of 1e and 2e. The charge of $\text{Os}(\text{B}^{2+})$ and $\text{Os}(\text{A}^{2+})$ are now 1.84e versus 1.94e, with even better agreement for the lower oxidation state. The same goes for the cobalt complexes. Integer values are not observed as the positive charges on the complexes are perturbed by the highly polarized water molecules. The averaged bond lengths of the A- and B-systems are in excellent agreement, and in most cases bond lengths are within 0.01 Å, when comparing solvated $\text{A}^{+/2+}$ and solvated $\text{B}^{+/2+}$.

Two discrepancies between the solvated A and B systems are, however, observed. One is for the cobalt complex in the oxidation state +2. It is well-known that many cobalt(I/II) complexes with halide ligands are labile toward substitution with water ligands.³⁶ This is displayed in the dynamics runs of $\text{Co}(\text{A})(\text{H}_2\text{O})_{168}$, $\text{Co}(\text{A}^+)(\text{H}_2\text{O})_{167}$, and $\text{Co}(\text{B}^+)(\text{H}_2\text{O})_{167}$. The cobalt complex is found to assume a square pyramidal structure as the chloride ligand is lodged away. A complete ligand exchange reaction is, however, not seen over the 2 ps of simulation time. $\text{Co}(\text{A}^+)(\text{H}_2\text{O})_{168}$ and $\text{Co}(\text{B}^+)(\text{H}_2\text{O})_{167}$ undergo different trajectories over the 2 ps; hence, the averaged complexes are different, mainly in the Δ_{gap} which differs by almost 0.4 eV. The metal-to-ligand bond lengths agree within 0.02 Å and the observed charge on the complex within 0.01e. As the oxidation state increases further, either by removing an electron as in $\text{Co}(\text{A}^{2+})(\text{H}_2\text{O})_{168}$ or adding a second counterion as in $\text{Co}(\text{B}^{2+})(\text{H}_2\text{O})_{166}$ this lability toward water is lost. No ligand exchange takes place and the complexes become stable in the solvent environment. This further supports our approach as both the solvated charged systems and the counterion systems display the exact same chemistry and stability. On average the $\text{Co}(\text{A}^{2+})(\text{H}_2\text{O})_{168}$ and $\text{Co}(\text{B}^{2+})(\text{H}_2\text{O})_{166}$ complexes agree very well both structurally and electronically. Minute differences are seen in the Δ_{gap} at 0.09 eV, and Q_{com} at 0.08e.

The second discrepancy is seen for the osmium complex in the oxidation state +3, $\text{Os}(\text{A}^{2+})(\text{H}_2\text{O})_{168}$ and $\text{Os}(\text{B}^{2+})(\text{H}_2\text{O})_{167}$. To aid in calculation convergence, a finite Fermi width of the electronic distribution was employed. This resulted in the $\text{Os}(\text{B}^{2+})(\text{H}_2\text{O})_{166}$ complex to be found in two states. One which has a small Δ_{gap} and a magnetic moment of 1, in agreement with the $\text{Os}(\text{A}^{2+})(\text{H}_2\text{O})_{168}$ system, the other one which is nonmagnetic, i.e., an even occupation of spin-up and -down states. This discrepancy could be amended by using a more accurate functional not subjected to the same degree of self-interaction errors. Δ_{gap} would also be higher such that the finite Fermi width would no longer level the spin-up and spin-down channels. Even though the solvated counterion complex is found in the two states the averaged ligand structure around the metal center does not change. Bond lengths of $\text{Os}(\text{A}^{2+})(\text{H}_2\text{O})_{168}$ and $\text{Os}(\text{B}^{2+})(\text{H}_2\text{O})_{166}$ agree

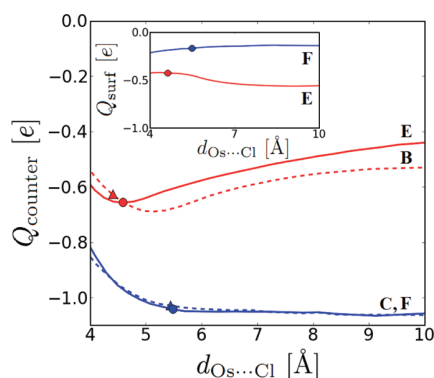


Figure 3. Charge of counterion, or collective charge on counterion and solvent, Q_{counter} , at the sampled osmium to counterion distances $d_{\text{Os}\cdots\text{Cl}}$. The inset depicts the surface charge, Q_{surf} , for systems E and F at the same intervals. Red and blue lines represent the vacuum and solvated systems, respectively. The solid and broken lines indicate whether the complex is in the adsorbed state on Pt(111) or isolated, respectively. Filled triangles and circles indicate the equilibrium $d_{\text{Os}\cdots\text{Cl}}$ distances.

very well with a difference of at most 0.01 Å. This simply reflects how stable the ligand environment is around the osmium metal center, as it only slightly changes upon oxidation and does not change due to specific magnetic ordering.

Solvated Complexes on Metal Surfaces. The essential differences between the nature of the charge transfer in the presence of the solvent and the nonsolvated complexes under the influence of counterions, isolated (system B and C) and in the adsorbed state (system E and F), are presented in Figure 3. A small number, 26–45, of water molecules were relaxed around the complex and counterion in C, amounting to a single solvation shell. The resulting system was then placed on a surface, system F. All systems were analyzed in the following way. The metal center to counterion distance, $d_{\text{Os}\cdots\text{Cl}}$, was varied over the range 4–10 Å, at 0.1 Å intervals. At each interval the charge on the counterion, or counterion and surrounding solvent, Q_{counter} , was analyzed with Bader's analysis.^{23,24} The results in Figure 3 are for a single counterion, the osmium metal center, and the Pt(111) surface. Analogous results were observed for either one or two counterions, the cobalt center and a Au(111) surface (or any combination thereof).

The B and C systems represent the free complex ionic systems. The delocalized nature of the charge transfer in the nonsolvated system, B, is again clearly seen, here in the Q_{counter} profile against $d_{\text{Os}\cdots\text{Cl}}$. A fractional charge is found throughout, ranging from -0.64 to -0.43 e. As a first approximation the observed charge transfer can be factored into two components. A constant charge transfer between counterion and complex, which is only partial due to the self-interaction errors, and a local polarization term, which is relaxed as the counterion moves away (or toward) the complex. This charge transfer is dramatically changed in the presence of the solvent in system C. An almost constant charge transfer of nearly integer value is observed over an $d_{\text{Os}\cdots\text{Cl}}$ interval larger than the equilibrium value at 5.5 Å. This indicates both that the self-interaction error has been greatly reduced and that the solvent screens any localized polarization. At short but probably unrealistic distances charge moves back to the complex from the counterion.

Closely similar charge transfer from complex to counterion is obtained for the systems in the adsorbed states, systems E and F, compared to their nonadsorbed counterparts B and C,

respectively. The Q_{counter} profiles of the solvated systems F and C are almost identical over the whole interval. A small difference of about 0.08e between the Q_{counter} profiles of E and B is, however, found. This is due to an additional charge transfer component, from the complex ion to the surface, Q_{surf} (inset in Figure 3). The nonsolvated complex, E, displays a Q_{surf} range of 0.45e to 0.53e. The range can be related to the smaller distance dependent charge transfer to the counterion. When the charge transfer between the complex and counterion is relaxed the complex ion has more charge to donate to the surface. In contrast, the solvated system F displays an almost constant charge transfer term from the complex ion to the surface, of approximately 0.19e. Clearly the nature of the interaction between the surface and complex is completely altered when the solvent is present. The presence of the surface does not perturb the charge transfer from the complex to the counterion in the solvated case. To analyze this further a range of nonsolvated complexes with or without counterions in the adsorbed states on both Au(111) and Pt(111) were analyzed, and the adsorption energy, E_{ads} , versus the charge transfer from the complex to the surface, Q_{surf} , mapped.

All nonsolvated complexes were found to adsorb strongly with varying adsorption energy, E_{ads} , in the range -1.3 to -2.0 eV and -2.2 to -2.9 eV on Au(111) and Pt(111), respectively. The strongest adsorption is observed for systems without counterions. There was, however, no direct correlation between the adsorption energy and the number of counterions. Bader's analysis showed that both the range and the strong adsorption was due to substantial charge transfer, here from the complex ion to the surface, i.e., oxidation, with an approximately linear relation between the charge transferred and E_{ads} . After the oxidation the structure of all of the complexes, of the same metal center type, relaxed to almost the same ligand to metal geometry. The complexes with different numbers of counter anions became completely featureless. Overall adsorption geometries, for all systems, remained the same as depicted in Figure 1, i.e., the complex standing on one "leg" bound to the surface via the pendant nitrogen. A more detailed account of the adsorption behavior of pyridines, and the M(n)POP complexes as well as of some derivatives is given in the Supporting Information.

In contrast, a consistent value of both charge transferred and adsorption energy is found for all the complexes in the presence of solvent. The values were largely independent of the oxidation states M(II) or M(III), and different only for the two metal surfaces, viz. -1.6 and -2.0 eV for Au(111) and Pt(111), respectively. Furthermore, the nuclei of the complexes do not relax to a new geometry, meaning that the complexes retain the same structure as their cationic charge in the free solute state. The small charge transfer from the complexes to the surface agreed well with the charge transferred from a lone bipyridine molecule to the surface. Using Bader's analysis, this weak polarization could be localized in the region between the binding nitrogen and the surface adatom. This means that the nature of the adsorption is the same for the solvated transition metal complex via the pendant ligand and the lone ligand. This agrees, moreover with experimental isotherms of a similar complex, $[\text{Os}(+2/+3)(\text{bpy})_2(\text{P3P})\text{Cl}]$,³⁷ as well as with adsorption isotherms for pyrazine³⁸ and bipyridine.³⁹

The experimental adsorption energies are found to be about -0.3 eV, and the resulting bond described as being of weak chemisorption nature. This has been verified by computational work on bipyridine⁴⁰ and Os(+2)POP by O'Boyle,²⁶ and now by the present work which has shown that solvated M(+2/+3)POP

complexes and bipyridine all adsorb with very similar adsorption energy and other adsorption characteristics. It is to be emphasized that the solvent is essential in preserving both the cationic character of the complexes and in providing the desired robustness when the complexes are brought into the adsorbed state. The adsorption energy values found in the present study are, however, relatively high compared to both previous calculations and experimental observations. This is due to the use of the PBE functional, the finite numerical atomic orbital basis, the finite number of surface layers and the presence of the adatom.

CONCLUSION

We have used quantum chemical ab initio computations combined with molecular dynamics to study a class of electrochemically active transition metal complexes based on osmium and cobalt central metal ions and polypyridine ligands. The complexes both in their free and solute state and in the adsorbed state on Au(111) and Pt(111) surfaces in contact with a large assembly of solvent water molecules, were addressed. The calculations have relied on approximations with fairly modest constraints such as the numerical atomic orbital basis sets and the PBE functional. Counter anions were included and different oxidation states of the complex cations constructed by first introducing the complex and anion components in electrostatically neutral form, followed by electronic relaxation and charge separation into cationic complex and anionic counter moiety (chloride ions).

The solvent was found to be crucial in the stabilization of chemically and physically truly (solvated) cationic and anionic molecular entities. Only partial electronic charge transfer occurs in the absence of the solvent. This is due to insufficient screening of self-interaction and local polarization unless solvent molecules and strong solvation forces are present. Strong solvation effects also provide the appropriate robustness of the complexes so that they retain their cationic character as they are brought to adsorb on the Au(111) and Pt(111) surfaces.

The combined approach applies generally to molecular redox species including transition metal complexes as well as redox metalloproteins in free and adsorbed solute states. In future work we shall address the effects of solvent and intramolecular configurational fluctuations with a view on combining this approach with interfacial electrochemical electron transfer processes and electrochemical in situ scanning tunneling microscopy of redox-gated molecules such as reported recently.^{11,12}

ASSOCIATED CONTENT

Supporting Information. Adsorption energies versus the charge transferred from complex to surface are provided for pyrazine, POP, P2P, M(n)POP, M(n)P2P (P2P is 1,2-bis(-4-pyridyl)ethane), and [M(n)(bpy)₃], in the presence of zero, one, or two counteranions in the adsorbed state on both Au(111) and Pt(111) surface. The results of [M(n)(bpy)₃] at the DZP/PBE level of theory are also compared to DZP/RPBE. The RPBE functional⁴² is known to provide more accurate adsorption energies. This material is available free of charge via the Internet at <http://pubs.acs.org>.

AUTHOR INFORMATION

Corresponding Author

*E-mail: kwj@fysik.dtu.dk.

ACKNOWLEDGMENT

Financial support from the Danish Research Council for Technology and Production Sciences and the Villum Kann Rasmussen Foundation to J.U. is acknowledged. We further acknowledge support from the Danish Center for Scientific Computing (DCSC). The Center for Atomic-scale Materials Design (CAMD) is sponsored by the Lundbeck Foundation.

REFERENCES

- Reed, M. A.; Zhou, C.; Muller, C. J.; Burgin, T. P.; Tour, J. M. *Science* **1997**, *278*, 252–254.
- Xiao, X.; Xu, B.; Tao, N. J. *Nano Lett.* **2004**, *4*, 267–271.
- Li, X. L.; He, H. X.; Xu, B. Q.; Xiao, X. Y.; Nagahara, L. A.; Amlani, I.; Tsui, R.; Tao, N. J. *Surf. Sci.* **2004**, *573*, 1–10.
- Li, C.; Pobelov, I.; Wandlowski, T.; Bagrets, A.; Arnold, A.; Evers, F. *J. Am. Chem. Soc.* **2008**, *130*, 318–326.
- Haiss, W.; Nichols, R. J.; van Zalinge, H.; Higgins, S. J.; Bethell, D.; Schiffrin, D. J. *Phys. Chem. Chem. Phys.* **2004**, *6*, 4330–4337.
- Haiss, W.; Albrecht, T.; van Zalinge, H.; Higgins, S. J.; Bethell, D.; Höbenreich, H.; Schiffrin, D. J.; Nichols, R. J.; Kuznetsov, A. M.; Zhang, J.; Chi, Q.; Ulstrup, J. *J. Phys. Chem. B* **2007**, *111*, 6703–6712.
- Zhang, J.; Chi, Q.; Albrecht, T.; Kuznetsov, A. M.; Grubb, M.; Hansen, A. G.; Wackerbarth, H.; Welinder, A. C.; Ulstrup, J. *Electrochim. Acta* **2005**, *50*, 3143–3159.
- Stadler, R.; Thygesen, K. S.; Jacobsen, K. W. *Phys. Rev. B* **2005**, *72*, 241401.
- Bagrets, A.; Arnold, A.; Evers, F. *J. Am. Chem. Soc.* **2008**, *130*, 9013–9018.
- Strange, M.; L-Acevedo, O.; Häkkinen, H. *Phys. Chem. Lett.* **2010**, *1*, 1528–1532.
- Albrecht, T.; M-Poulsen, K.; Christensen, J. B.; Guckian, A.; Bjørnholm, T.; Vos, J. G.; Ulstrup, J. *Faraday Discuss.* **2006**, *131*, 265–279.
- Albrecht, T.; M-Poulsen, K.; Christensen, J. B.; Hjelm, J.; Bjørnholm, T.; Ulstrup, J. *J. Am. Chem. Soc.* **2006**, *128*, 6574–6575.
- Kuznetsov, A. M.; Ulstrup, J. *Electron Transfer in Chemistry and Biology: An Introduction to the Theory*, 1st ed.; John Wiley & Sons Ltd.: West Sussex, 1999.
- Zhang, J.; Kuznetsov, A. M.; Medvedev, I. G.; Chi, Q.; Albrecht, T.; Jensen, P. S.; Ulstrup, J. *Chem. Rev.* **2008**, *108*, 2737–2791.
- Kuznetsov, A. M.; Ulstrup, J. *J. Phys. Chem. A* **2000**, *104*, 11531–11540.
- Mortensen, J. J.; Hansen, L. B.; Jacobsen, K. W. *Phys. Rev. B* **2005**, *71*, 035109.
- Enkovaara, J. et al. *J. Phys.: Condens. Matter* **2010**, *22*, 253202.
- Larsen, A. H.; Vanin, M.; Mortensen, J. J.; Thygesen, K. S.; Jacobsen, K. W. *Phys. Rev. B* **2009**, *80*, 195112.
- Perdew, J. P.; Burke, K.; Ernzerhof, M. *Phys. Rev. Lett.* **1996**, *77*, 3865.
- Blöchl, P. E. *Phys. Rev. B* **1994**, *50*, 17953.
- Spezia, R.; Bresson, C.; Auwer, C. D.; Gageot, M.-P. *J. Phys. Chem. B* **2008**, *112*, 6490–6499.
- Cafe, P. F.; Larsen, A. G.; Yang, W.; Bilic, A.; Blake, I. M.; Crossley, M. J.; Zhang, J.; Wackerbarth, H.; Ulstrup, J.; Reimers, J. R. *J. Phys. Chem. C* **2007**, *111*, 17285–17296.
- Bader, R. F. W. *Atoms in Molecules: A Quantum Theory*; Oxford University Press: New York, 1990.
- Tang, W.; Sanville, E.; Henkelman, G. *J. Phys.: Condens. Matter* **2009**, *21*, 084204.
- Ryabov, A. D.; Roznyatovskaya, N. V.; Suwinska, K.; Revenco, M.; Ershov, A. Y. *J. Biol. Inorg. Chem.* **2003**, *8*, 815–22.
- O'Boyle, N. M.; Albrecht, T.; Murgida, D. H.; Cassidy, L.; Ulstrup, J.; Vos, J. G. *Inorg. Chem.* **2007**, *46*, 117–24.
- Szalda, D. J.; Creutz, C.; Mahajan, D.; Sutin, N. *Inorg. Chem.* **1983**, *22*, 2372–379.

- (28) Sieber, R.; Decurtins, S.; S.-Evans, H.; Wilson, C.; Yufit, D.; Howard, J. A. K.; Capelli, S. C.; Hauser, A. *Chem.—Eur. J.* **2000**, *6*, 361.
- (29) Gaspar, A. B.; Muñoz, M. C.; Niel, V.; Real, J. A. *Inorg. Chem.* **2001**, *40*, 9–10.
- (30) Hauser, A.; Amstutz, N.; Delahaye, S.; Sadki, A.; Schenker, S.; Sieber, R.; Zerara, M. *Struct. Bonding (Berlin)* **2004**, *106*, 81–96.
- (31) Krivokapic, I.; Zerara, M.; Daku, M. L.; Vargas, A.; Enachescu, C.; Ambrus, C.; T.-Piggott, P.; Amstutz, N.; Krausz, E.; Hauser, A. *Coord. Chem. Rev.* **2007**, *251*, 364.
- (32) Leung, K.; Rempe, S. B.; Schultz, P. A.; Sproviero, E. M.; Batista, V. S.; Chandross, M. E.; Medforth, C. J. *J. Am. Chem. Soc.* **2006**, *128*, 3659–3668.
- (33) Neese, F. *J. Biol. Inorg. Chem.* **2006**, *11*, 702–711.
- (34) Jensen, K. P.; Roos, B. O.; Ryde, U. *J. Chem. Phys.* **2007**, *126*, 014103.
- (35) Cohen, A. J.; M.-Sánchez, P.; Yang, W. *Science* **2008**, *321*, 792.
- (36) Miessler, G. L.; Tarr, D. A. *Inorganic Chemistry*, 3rd ed.; Pearson Prentice Hall: NJ, 2004.
- (37) Forster, R. J.; O’Kelly, J. P. *J. Electrochem. Soc.* **2001**, *148*, E31–E37.
- (38) Iannelli, A.; Merza, J.; Lipkowski, J. *J. Electroanal. Chem.* **1994**, *376*, 49–57.
- (39) Stolberg, L.; Morin, S.; Lipkowski, J.; Irish, D. E. *J. Electroanal. Chem.* **1991**, *307*, 241–262.
- (40) Bilic, A.; Reimers, J. R.; Hush, N. S. *J. Phys. Chem. B* **2002**, *106*, 6740–6747.
- (41) Humphrey, W.; Dalke, A.; Schulten, K. *J. Mol. Graphics* **1996**, *14*, 33–38. VMD was developed by the Theoretical and Computational Biophysics Group in the Beckman Institute for Advanced Science and Technology at the University of Illinois at Urbana-Champaign.
- (42) Hammer, B.; Hansen, L. B.; Nørskov, J. K. *Phys. Rev. B* **1999**, *59*, 7413.

Supporting Information

Ab initio calculations of the electronic properties of polypyridine transition metal complexes and their adsorption on metal surfaces in the presence of solvent and counter ions

E. Ö. Jónsson,¹ K. S. Thygesen,¹ J. Ulstrup² and K. W. Jacobsen¹

¹ Department of Physics

² Department of Chemistry

Technical University of Denmark, DK - 2800 Kgs. Lyngby, Denmark

FIG. S1: Schematic of the adsorption systems investigated

FIG. S2: Adsorption energy versus the charge transfer *from* complex cation *to* the surface, for pyridines, M(n)P0P and M(n)P2P

FIG. S3: Adsorption energy versus the charge transfer *from* complex cation *to* the surface, for [M(n)(bpy)₃]

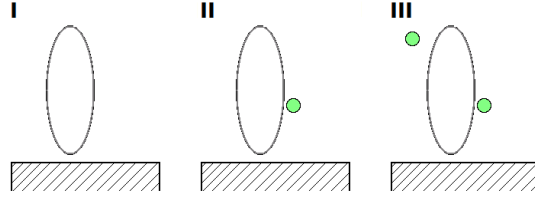


FIG. S 1: Schematic of the systems investigated. The ellipse represents the adsorbing complex. Three complexes are considered: $M(n)P0P = [M(n)(bpy)_2(P0P)Cl]$ (bpy is 2,2'-bipyridine and P0P is 4,4'-bipyridine), $M(n)P2P = [M(n)(bpy)_2(P2P)Cl]$ (P2P is 1,2-bis(-4-pyridyl)ethane) or $[M(n)(bpy)_3]$. The complexes are in the presence of zero, one or two counter ion (chloride), labeled I, II and III, respectively. The surfaces are either Au(111) or Pt(111). An adatom of the same metal is inserted between the adsorbing species and the surface. The overall adsorption geometry is that of a complex standing on one "leg", i.e. perpendicular to the surface.

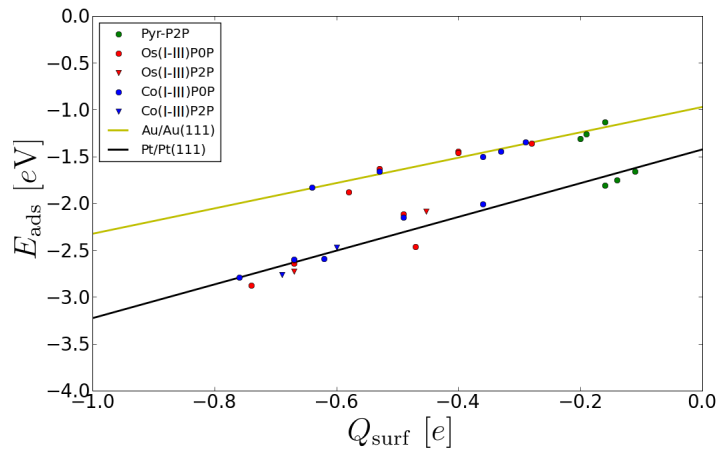


FIG. S2: Adsorption energy, E_{ads} , versus the charge transferred *from* complex to surface, Q_{surf} . A linear relation exists between E_{ads} and Q_{surf} as seen by the yellow and black linear fits for adsorption on to Au(111) and Pt(111), respectively. Filled blue and red circles present values for the M(n)P0P species, and filled blue and red triangles for the M(n)P2P species (see caption of FIG. S1 for definition), where red is for complexes with an osmium metal center and blue for complexes with a cobalt metal center. The green filled circles present data for, in order from weakest to strongest adsorption, pyrazine (Pyr), P0P and P2P. There is no real correlation between the number of counter anions and the strength of the adsorption. The I species (FIG. S1) is, however, generally found to adsorb most strongly. The data for M(n)P2P shows that this charge transfer does not depend strongly on the distance from the metal center to the surface, as the P2P ligand is longer than P0P.

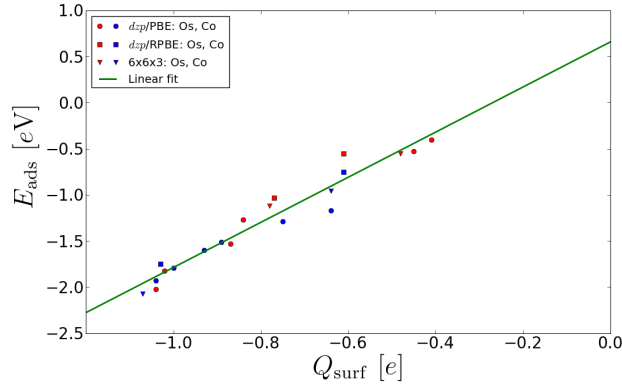


FIG. S3: Adsorption energy, E_{ads} , versus the charge transferred *from* complex to surface, Q_{surf} , for $[M(n)(\text{bpy})_3]$ osmium and cobalt complexes, in the presence of zero, one or two counter ions (see FIG. S1). Note that this complex does not have a pendant nitrogen which can directly bind to the surface adatom (as for the P0P and P2P ligands). The green line presents a linear fit to all the data, i.e. adsorption on both Au(111) and Pt(111). The results of DZP/PBE (filled circles) are almost identical to DZP/RPBE (filled squares). RPBE gives more accurate adsorption energies where there is any electronic density present at the interface between the adsorbate and surface. Furthermore, changing the number of surface layers to three (filled triangles) does not change the results. Note that closely lying circles, squares and triangles owe to the same system (i.e. number of counter anions). This shows that the adsorption process is clearly oxidative in nature when in vacuum, and not dependent on the surface type. With that in mind one can clearly relate the adsorption behavior of $M(n)\text{P0P}$ and $M(n)\text{P2P}$ on to Au(111) and Pt(111) as an oxidative process plus an additional surface dependent term (hence the different lines in FIG. S2).

PAPER II

An efficient qm/mm scheme to explore electron transfer reactions in solution

1 Abstract

We present a hybrid DFT-QM/MM scheme implemented for the grid-based projector augmented wave code GPAW. Our focus is on charge transfer reactions between atoms or molecules in condensed matter environments, and in particular on the evaluation of free energy surfaces. We have selected robust but computationally cheap methods to deal with periodic systems such that a variety of chemical reactions can readily be explored - and even extended to the semi-infinite surface/solvent interface in mixed QM/MM systems. The general nature of the code, however, allows one to go well beyond our particular goals. We use simple point-charge models to greatly speed up the relevant configuration phase-space sampling required in the context of charge transfer and examine two different biasing methods to efficiently reach non-equilibrium configurations. The methodology to approach charge transfer reactions is briefly reviewed and applied on several first row hexaaqua transition metal complexes where the reaction and phase-space configuration sampling methods, and finite basis effects, are investigated. Furthermore, the approach is applied to a more complex system where the efficiency of the QM/MM code is advantageous for the phase-space sampling, and use a simple post sampling scheme to construct free energy surfaces comparable in accuracy to full QM sampling. We observe excellent agreement with studies employing similar methods and arrive at a qualitative agreement with experimental free energies, but with clear steps to improve our models towards greater accuracy.

2 Introduction

Electron transfer (ET) reactions are of fundamental importance to the chemical processes in biochemistry, (photo-)electrochemistry, homo- and heterogeneous (surface) catalysis, as well as to the relatively new field of scanning tunnelling spectroscopy (STS), which is a two step interfacial charge transfer process with electrochemical control. This unique method has unprecedented control over the electrochemistry, particularly in the sense of 'smart' molecules where the redox state of the molecule and surface-electrode to tip-electrode potential bias are controlled separately. This control has been demonstrated for osmium and cobalt polypyridine complexes which

showed transistor-like rectifying behaviour [56, 38, 37, 2, 3]. Not only does this experimental method offer direct insight into the operation of nano-scale electronic devices but this observed transistor-like functionality is explained with the phenomenological theory of interfacial electrochemical ET theory [56, 97, 50, 98, 51]. This includes well defined parameters accessible through experimental work, and *ab initio* and coupled classical methods employed in this work.

The electron transfer reaction, albeit conceptually the simplest of the chemical reactions, still presents a considerable computational challenge. Under electrochemical conditions the reactions take place in solution which can be strongly coupled to the localized molecular charge, hence, accurate simulations often require considerable conformation sampling of the condensed matter environment. Furthermore, the molecular species involved in the charge transfer process can be chemically linked such that the initial and final electronic states overlap. In this regard charge transfer reactions are divided into two categories: non-adiabatic and adiabatic. It is understood that the thermodynamic reaction barrier is almost purely due to the environmental response in the former case, whereas the barrier is strongly affected in the latter due to the chemical link, or electronic state overlap.

Combined (or hybrid) quantum mechanical / molecular mechanics (QM/MM) methods provide an efficient and often accurate potential energy description of chemical and biological simulations. Such methods have been essential in simulating and understanding the role of the environment in chemical and biological reactions [89, 25, 90, 91, 16, 67], where the strategy is to describe the chemically reactive centre(s) and closest surroundings (e.g. a transition metal complex, protein reaction centre) with *ab initio* electronic structure methods and the enclosing environment with classical potentials. The evident gain in using this method is that by coupling to molecular dynamics one can greatly speed up the conformational sampling to map the response of the environment to a transferring charge.

Here we present our recently developed QM/MM code and apply two different methods to traverse the configuration phase space in the context of electron transfer reactions between transition metals in water. We use constant temperature molecular dynamics with molecular bond constraints to speed up sampling. All simulation methods and analysis applied in the ET context are based on general formulations and hence are applicable to other types of chemical reactions. Our QM/MM code employs a simple point

charge model for the MM part and can be used to treat different types of solvents, and has already been used in a molecular dynamics study of a double centred iridium-iridium complex in acetonitrile [24]. To sample the configuration phase space we use a biased sampling scheme, or umbrella sampling (US) [81], where a order parameter is systematically controlled to simulate initial, intermediate and final state configurations of the charge transfer process. Such biased sampling schemes in combination with QM/MM have been extensively used for ET reactions [41, 73, 47, 48, 71, 96].

This work is organized as follows: sections 3 and 4 introduce our in-house QM and MM codes, with section 4 focusing on our particular QM/MM implementation which uses a recent and simple method to treat periodic boundary conditions. Section 5 briefly presents concepts for free energy surface analysis and outlines the biased sampling methods that we use. Sections 6-8 present computational details and results: section 7 deals with symmetric and asymmetric charge transfer between aqueous first row transition metals: vanadium, chromium, manganese, iron and cobalt, where the donor and acceptor in the reaction are infinitely far apart. Here the relevant free energies are solved for following the methodology presented in section 5, and compares two bias methods as well as simulations performed with full QM versus QM/MM. Finally, section 8 presents a more comprehensive analysis on the benefit of QM/MM to ET and redox state control, on a system comprised of a larger polypyridine osmium complex.

3 ASE and GPAW

The Atomic Simulation Environment (ASE) [5] code is written in Python and offers a user friendly and highly flexible environment to create and further manipulate atomistic objects. The ASE package takes care of both setting up atomistic simulations and performing nuclear dynamics with a range of additional analytic tools available, while the quantum mechanical energy and force calculations are performed by external first principles 'calculators' with well defined interfaces to ASE (see ASE home wiki.fysik.dtu.dk/ase/).

The QM code used in this work is the Grid-based Projector Augmented-Wave code GPAW [63, 27, 54], which offers a highly parallelized all-electron density functional theory (DFT) calculator object, written in Python/C. In addition to a variety of valence basis functions and exchange-correlation functionals from the *libxc* library [60] to solve for the ground state elec-

tronic density, GPAW includes coherent transport calculations, TD-DFT [88], linear response [94], Δ SCF [35, 65] and much more (see GPAW home wiki.fysik.dtu.dk/gpaw/).

In the following we describe the implementation of a QM/MM scheme in ASE/GPAW, as well as thermodynamic methods and tools to explore free energy surfaces and redox processes. The bulk of the QM/MM and thermodynamic code constructed here is written in Python [83, 4] and integrated into ASE, hence most of the QM/MM code is applicable to any QM code with an ASE-calculator interface.

4 The General QM/MM Scheme

In DFT the total energy is obtained by minimizing a functional of the electronic density. This provides a convenient framework for describing systems containing both quantum parts with a certain electronic density and classical degrees of freedom which influence the quantum system through electrostatic interactions. We thus use the following total energy expression

$$E_{\text{tot}} = E_{\text{KS}} + E_{\text{QM/MM}} + E_{\text{MM}} \quad (1)$$

where the total energy functional is given by the well known Kohn-Sham functional for the QM system, E_{KS} , a classical part, E_{MM} , which only depends on the classical degrees of freedom, and a mixed term, $E_{\text{QM/MM}}$, which couples the QM and classical degrees of freedom.

We ascribe a point charge value, q_i , and a Cartesian coordinate, τ_i , to the atoms comprising the MM part, and write the QM/MM interaction scheme as

$$E_{\text{QM/MM}} = \sum_{i=1}^C q_i \int \frac{n(\mathbf{r})}{|\mathbf{r} - \tau_i|} d\mathbf{r} + \sum_{i=1}^C \sum_{\alpha=1}^A \frac{q_i Z_\alpha}{|\mathbf{R}_\alpha - \tau_i|} + E_{\text{LJ}} \quad (2)$$

where $n(\mathbf{r})$ is here the spatial electronic density of the quantum region, and Z_α and \mathbf{R}_α are the charges and Cartesian coordinates of the quantum nuclei, respectively. The first term on the rhs. expresses the Coulomb interaction of the point charges and the ground state electronic density. This term leads to an additional contribution to the potential of the QM system

$$v_{\text{MM}} = \frac{\delta E_{\text{QM/MM}}}{\delta n(\mathbf{r})} = \sum_{i=1}^C \frac{q_i}{|\mathbf{r} - \tau_i|} \quad (3)$$

so that the total effective potential of the Kohn-Sham scheme which is solved with GPAW becomes

$$v_{\text{eff}}^{\text{tot}} = v_{\text{H}} + v_{\text{xc}} + v_{\text{ext}} + v_{\text{MM}} \quad (4)$$

where v_{H} , v_{ext} and v_{xc} are the Hartree, electron-nuclei and exchange-correlation potentials, respectively. In this way the ground state electronic density is solved for with electrostatic effects due to the presence of the MM system by the self-consistent cycle in GPAW. This includes the electronic contribution to the forces exerted on the quantum nuclei, F_{α}^{ele} . Similarly for the second term on the rhs. of eq. 2, which is the Coulomb interaction between the point charges and quantum nuclei, we define another classical potential

$$v_{\text{MM}}^{\alpha} = \frac{\delta E_{\text{QM/MM}}}{\delta Z_{\alpha}} = \sum_i^C \frac{q_i}{|\mathbf{R}_{\alpha} - \tau_i|} \quad (5)$$

which we evaluate analytically but with modifications presented in sections 4.2 and 4.3

Finally E_{LJ} , the last term on the right hand side of eq. 2, denotes the Lennard-Jones [55] (LJ) potential interaction between the constituents of the classical and quantum parts, with the generic 12-6 repulsive-attractive form

$$E_{\text{LJ}} = \sum_{i=1}^C \sum_{\alpha=1}^A 4\epsilon_{\alpha i} \left[\left(\frac{\sigma_{\alpha i}}{|\mathbf{R}_{\alpha} - \tau_i|} \right)^{12} - \left(\frac{\sigma_{\alpha i}}{|\mathbf{R}_{\alpha} - \tau_i|} \right)^6 \right] \quad (6)$$

where $\epsilon_{\alpha i}$ and $\sigma_{\alpha i}$ are the energy and size parameters, respectively, controlling the depth and position of the αi pair LJ-potential minimum. The LJ potential and parameters are discussed the next section since it is also present between the classical point charges.

4.1 Classical and Lennard-Jones Potential

The potential energy of the classical point charge system in eq. 1, E_{MM} , can be further divided into two parts; a covalent part describing the internal structure of a classical molecule, and a non-covalent part describing classical inter-molecular interactions

$$E_{\text{MM}} = E_{\text{covalent}} + E_{\text{non-covalent}} \quad (7)$$

In this study we work with solvent models where the internal degrees of freedom are fixed so the focus is on the non-covalent part. Hence, our E_{MM} is simply

$$E_{\text{MM}} = \sum_{i < j} \left[\frac{q_i q_j}{\tau_{ij}} + 4\epsilon_{ij} \left\{ \left(\frac{\sigma_{ij}}{\tau_{ij}} \right)^{12} - \left(\frac{\sigma_{ij}}{\tau_{ij}} \right)^6 \right\} \right] \quad (8)$$

where τ_{ij} is the distance between point charges. The first term on the rhs. is the Coulomb interaction between point charges of different molecules and defines the third classical potential

$$v_{\text{MM}}^j(\tau_j) = \frac{\delta E_{\text{MM}}}{\delta q_j} = \sum_{i \neq j}^C \frac{q_i}{|\tau_j - \tau_i|} \quad (9)$$

The potentials in eq. 3 and 5, and eq. 9 above are all of the same r^{-1} form and hence require special treatment in both the short and long range limits. This is discussed in sections 4.2 and 4.3.

The second part on the rhs. is the Lennard-Jones potential between the classical molecules and is analogous to eq. 6. This potential approximates physically important interspecies interactions where the r^{-12} term is attributed to Pauli repulsion but is an approximation only, whereas the r^{-6} term describes long-range attraction (van der Waals interactions) [57]. Due to the very short range of both contributions the potential is not given any special treatment in the case of periodically repeated systems, so interactions are cut-off at nearest neighbor cells. However, the energy and size parameters need to be constructed for the cross-relation between say point charge i and quantum nuclei α .

Several combination rules exist which are usually based on simple arithmetic or geometric mean [58, 8] and have been systematically tested for a range of gaseous or condensed systems [69, 1, 17]. More in depth studies [1] have focused on a simple rule by Waldman-Hagler (WH) [87]

$$\begin{aligned}\sigma_{\alpha i} &= \left[\frac{\sigma_{\alpha\alpha}^6 + \sigma_{ii}^6}{2} \right]^{\frac{1}{6}} \\ \epsilon_{\alpha i} &= \frac{2\sigma_{\alpha\alpha}^3 \sigma_{ii}^3}{\sigma_{\alpha\alpha}^6 + \sigma_{ii}^6} \sqrt{\epsilon_{\alpha\alpha} \epsilon_{ii}}\end{aligned}\tag{10}$$

with no added computational complexity. Classical simulations where energy and size parameters are evaluated with the WH method above were found to reproduce experimental rare-gas binding curves, yet retain the same relative accuracy in more complex or condensed systems, compared to simulations using the simpler and more common combination schemes [1, 87].

4.2 Short-Range Electrostatics

The classical potential of eq. 3 requires special treatment at both the short and long distance limits. In the former case the point charges will sometimes be within the grid space for the QM system (see top of Figure 1) so one must take care if the divergence of the potential associated with a point charge is close to a grid point. This is also known as the electron spill-out problem [53, 78, 26], where the electronic density of a quantum system clusters around such artificial potential wells. To avoid this problem an appropriate smoothing function is applied to the point charge potential [77, 78, 26, 53], usually of Gaussian shape, but here we use the simple function of Laio et. al. and transform eq. 3 to

$$v_{\text{MM}}(\mathbf{r}^\gamma) = \sum_{i=1}^C \frac{q_i}{r^\gamma}\tag{11}$$

where

$$\frac{1}{r^\gamma} = \frac{\gamma^4 - r_i^4}{\gamma^5 - r_i^5}\tag{12}$$

and r_i denotes $|\mathbf{r} - \tau_i|$, or the distance between point charge i and the real-space grid point \mathbf{r} . The value of γ controls the smoothing and is 0.20 Å in this work, and has been found to work quite well for different types of point charges (H and O of TIP3P water in this work, and C, N and O of a simple acetonitrile model [24]).

For simplicity and consistency in the derivation of the long-range approximations (section 4.3) the classical potentials of eqs. 5 and 9, which are not subject to the spill-out problem, are smoothed in the same way

$$v_{\text{MM}}^{\alpha}(\mathbf{R}_{\alpha}) \rightarrow v_{\text{MM}}^{\alpha}(\mathbf{R}_{\alpha}^{\gamma}) \quad (13)$$

and

$$v_{\text{MM}}^j(\tau_j) \rightarrow v_{\text{MM}}^j(\tau_j^{\gamma}) \quad (14)$$

Figure 1 presents hydrogen bonding curves for the MM/MM case versus the QM/MM case employing the smoothed potentials above. The hydrogen binding energy for the MM/MM is evaluated with the last part of eq. 8, using partial charge values and LJ parameters from the TIP3P model [45]. The QM/MM hydrogen binding energy is given by

$$E_{\text{bond}} = E_{\text{KS}}[\text{H}_2\text{O}, v_{\text{MM}}(\mathbf{r}^{\gamma})] + \sum_{\alpha}^A Z_{\alpha} v_{\text{MM}}(\mathbf{R}_{\alpha}^{\gamma}) + E_{\text{LJ}} - E_{\text{KS}}[\text{H}_2\text{O}] \quad (15)$$

where $E_{\text{KS}}[\text{H}_2\text{O}]$ and $E_{\text{KS}}[\text{H}_2\text{O}, v_{\text{MM}}(\mathbf{r}^{\gamma})]$ are the potential energy of a water molecule in vacuum and the potential energy of water influenced by the point charges through the smoothed potential (eq. 4). The second and third term on the rhs. are the classical-quantum nuclei and LJ interactions. The Lennard-Jones parameters of the TIP3P model are used for both the intra-point charge interactions as well as the point charge to quantum nuclei interactions.

Two QM/MM cases are presented in Figure 1 where in one case a quantum hydrogen forms a bond with a classical oxygen, and in the second case a quantum oxygen forms a bond with a classical hydrogen. There is a very smooth transition between the two cases, with only minor discrepancies between the two curves. Furthermore, the QM/MM and MM/MM curves are very similar, with only a 0.02 eV difference between the hydrogen bond minima. A similar collection of binding interactions between classical and quantum acetonitrile is presented in the Supplementary Information.

4.3 Long-Range Electrostatics

We aim at describing systems containing molecules and solvent interacting with a solid surface. It is therefore preferable to be able to treat periodically

repeated systems. The objective is to approximate the external potentials of eqs. 11, 13 and 14 on the periodic lattice common to the real-space grid, quantum nuclei, and point-charges, respectively.

Consider the summation over the periodic lattice $\mathbf{a} = n\mathbf{l} = \{nl_x, nl_y, nl_z\}$ (see Figure 2A) such that

$$E_{\text{MM}}^{\text{coul}} = \frac{1}{2} \sum_{i,j}^C \sum_{n=0}^C \prime \frac{q_i q_j}{|\tau_{ij} + \mathbf{a}|} \quad (16)$$

where the vector $n = (n_x, n_y, n_z)$ denotes the three-dimensional periodicity of the simulation cell, of side lengths $\mathbf{l} = (l_x, l_y, l_z)$. The prime indicates that at $n = 0$ we have $i \neq j$, and $\sum_{i,j}^C = \sum_i^C \sum_j^C$. It is well known that a direct truncation of eq. 16 at some cut-off distance R_c leads to severe errors in the electrostatics between periodically repeated images. The problem of approximating such infinite summations is a long standing one and is most often addressed with the Ewald summation technique (original paper [29]) [22, 59, 64, 34, 39, 18, 52]. The common strategy is to recast eq. 16 to a more manageable form with separate short and long range components

$$E_{\text{MM}}^{\text{coul}} = \frac{1}{2} \sum_i^{C'} \left(\sum_{\substack{j \neq i \\ \tau_{ij} \leq R_c}}^{C'} \frac{q_i q_j}{\tau_{ij}^\gamma} - \sum_{\substack{j \neq i \\ \tau_{ij} \leq R_c}}^{C'} \frac{q_i q_j}{\tau_{ij}} \right) + \frac{1}{2} \sum_{i,j}^C \sum_{n=0}^C \prime \frac{q_i q_j}{|\tau_{ij} + \mathbf{a}|} \quad (17)$$

where the terms in the parenthesis are cut-off at R_c and the summation is over C' which indexes point charges in the nearest neighbour cells (see Figure 2B), while the last term extends over all distances. Note that the last term on the rhs. includes, and hence cancels, the second term in the parenthesis. In this way the smoothed potential is connected to the basic Coulomb form at the cut-off distance. The last term on the rhs. which requires periodic treatment is furthermore split in to two components [29]

$$\frac{1}{2} \sum_{i,j}^C \sum_{n=0}^C \prime \frac{q_i q_j}{|\tau_{ij} + \mathbf{a}|} = E_1 + E_2 \quad (18)$$

where

$$E_1 = \frac{1}{2} \sum_{i,j}^C \sum_{n=0}^{\infty} \frac{q_i q_j \operatorname{erfc}(\kappa |\tau_{ij} + \mathbf{a}|)}{|\tau_{ij} + \mathbf{a}|} - \lim_{\tau_{ij} \rightarrow 0} \left\{ \frac{1}{2} \sum_i^C \frac{q_i^2 \operatorname{erf}(\kappa \tau_{ij})}{\tau_{ij}} \right\} \quad (19)$$

$$E_2 = \frac{1}{2} \sum_{i,j}^C \sum_{n=0}^{\infty} \frac{q_i q_j \operatorname{erf}(\kappa |\tau_{ij} + \mathbf{a}|)}{|\tau_{ij} + \mathbf{a}|} \quad (20)$$

The second term on the rhs. of 19 is the point self energy correction. With the proper choice of the splitting coefficient, κ , E_1 converges rapidly in real space, while E_2 is treated in reciprocal space and requires summation over several periodic images. However, by applying the method of Wolf et. al. [92] the E_2 term becomes negligible and the Coulomb summation becomes a direct real space summation with linear scaling ($O(N)$).

In their original work Wolf et. al. noted that the Coulomb interactions of the systems under scrutiny; systems comprised of ordered and disordered polar media like crystals, liquids and interfaces; showed Coulomb asymptotic behaviour of order r^{-5} due to strong charge screening effects. By applying a careful charge neutralization procedure for each particle of the system nice asymptotic behaviour was realized, and a suitable real-space cut-off found.

As noted before a simple cut-off at some arbitrary R_c of eq. 16 leads to severe errors. The errors can be dramatically reduced with the inclusion of a charge neutralization term, E_i^{neu} , specific to each point charge comprising the system. The Coulomb energy of individual point charges in the Wolf scheme read

$$E_i^{\text{coul}} = \sum_{\substack{j \neq i \\ \tau_{ij} \leq R_c}}^{C'} \frac{q_j q_i}{\tau_{ij}} - E_i^{\text{neu}} + O(R_c^{-2}) \quad (21)$$

with errors now of the order of R_c^{-2} . What the charge neutralization amounts to is to find the limit of the Coulomb potential around partial charge i at the cut-off distance - which in turn defines the image charge, Φ_i , on the spherical truncation surface surrounding i , or

$$\Phi_i = \sum_{\substack{j \neq i \\ \tau_{ij} \leq R_c}}^{C'} \frac{q_j}{R_c} \quad (22)$$

and the correction term becomes simply

$$E_i^{\text{neu}} \equiv q_i \Phi_i \quad (23)$$

This method has been used for both classical and hybrid simulations and has been found to retain comparable accuracy for ionic and polar systems when compared to the full Ewald summation method [53, 95, 59, 22, 13]. Applying the cut-off method to eq. 17, where the last term is replaced by E_1 , results in

$$\begin{aligned} E_{\text{MM}}^{\text{coul}} \approx & \frac{1}{2} \sum_i^{C'} \sum_{\substack{j \neq i \\ \tau_{ij} \leq R_c}}^{C'} \left(\frac{q_i q_j}{\tau_{ij}^\gamma} - \frac{q_i q_j}{\tau_{ij}} + \frac{q_i q_j \text{erfc}(\kappa \tau_{ij})}{\tau_{ij}} \right. \\ & \left. - \left\{ \frac{q_i q_j}{R_c^\gamma} - \frac{q_i q_j}{R_c} + \frac{q_i q_j \text{erfc}(\kappa R_c)}{R_c} \right\} \right) \\ & - \left(\frac{1}{2R_c^\gamma} - \frac{1}{2R_c} + \frac{\text{erfc}(\kappa R_c)}{2R_c} + \frac{\kappa}{\sqrt{\pi}} \right) \sum_i^C q_i^2 \end{aligned} \quad (24)$$

where in the second line the charge neutralization terms are collected (and R_c^γ is simply eq. 12 applied on R_c), and the last line presents the point self-energy terms. The general smoothed and truncated classical point charge potential, acting on some arbitrary point r_j , can then be defined as

$$\begin{aligned} v_{\text{MM}}[r_j, \tau_i] = \frac{\delta E_{\text{MM}}^{\text{coul}}}{\delta q_j} = & \sum_{\substack{i=1 \\ r_{ij} \leq R_c}}^{C'} q_i \left(\frac{1}{r_{ij}^\gamma} - \frac{1}{r_{ij}} + \frac{\text{erfc}(\kappa r_{ij})}{r_{ij}} \right. \\ & \left. - \left\{ \frac{1}{R_c^\gamma} - \frac{1}{R_c} + \frac{\text{erfc}(\kappa R_c)}{R_c} \right\} \right) \end{aligned} \quad (25)$$

which is then also the final form of eqs. 3 and 5 in the periodic lattice, one simply changes the coordinate variable. The total potential energy of the hybrid QM/MM scheme takes the form

$$\begin{aligned} E_{\text{tot}} = & E_{\text{KS}}[n(\mathbf{r}), v_{\text{MM}}[\mathbf{r}, \tau_i]] + \sum_{\alpha=1}^A Z_\alpha v_{\text{MM}}[\mathbf{R}_\alpha, \tau_i] + E_{\text{LJ}}[\mathbf{R}_\alpha, \tau_i] \\ & + E_{\text{MM}}^{\text{coul}}[\tau_j, \tau_i] + E_{\text{LJ}}[\tau_j, \tau_i] \end{aligned} \quad (26)$$

where eq. 25 is now added to the effective potential in the KS scheme, and the same potential applies to the point charge to quantum nuclei Coulomb interactions (second term on the rhs.).

4.4 Forces

The forces on the quantum nuclei is composed of the following terms

$$F_\alpha = -\frac{\delta E_{\text{KS}}[\mathbf{R}_\alpha]}{\delta R_\alpha} - \frac{\delta E_{\text{QM/MM}}[\mathbf{R}_\alpha, \tau_i]}{\delta R_\alpha} \quad (27)$$

where the first term on the rhs. expresses the forces due to the electronic density and is solved for by GPAW [63, 27, 54], with of course the point-charge potential included in the effective KS potential. The second term can be further divided in to two terms

$$-\frac{\delta E_{\text{QM/MM}}[\mathbf{R}_\alpha, \tau_i]}{\delta R_\alpha} = -Z_\alpha \frac{\delta v_{\text{MM}}[\mathbf{R}_\alpha, \tau_i]}{\delta R_\alpha} - \frac{\delta E_{\text{LJ}}[\mathbf{R}_\alpha, \tau_i]}{\delta R_\alpha} \quad (28)$$

where the second term on the rhs. are the forces due to the interaction with the point charge through the Lennard-Jones potential and is a simple derivative of eq. 6. The first term is a derivative of eq. 25 with the cut-off terms included such that the forces go to zero at the cut-off distance, in line with the potential

$$F_\alpha^{\text{MM}} = -Z_\alpha \sum_{\substack{i=1 \\ r_{i\alpha} \leq R_c}}^{C'} q_i \left(\frac{1}{dr_{i\alpha}^\gamma} - \frac{1}{r_{i\alpha}^2} - \frac{\text{erfc}(\kappa r_{i\alpha})}{r_{i\alpha}^2} - \frac{2\kappa \exp(-\kappa^2 r_{i\alpha}^2)}{\sqrt{\pi} r_{i\alpha}} \right. \\ \left. + \frac{1}{dR_c^\gamma} + \frac{1}{R_c^2} - \frac{\text{erfc}(\kappa R_c)}{R_c^2} - \frac{2\kappa \exp(-\kappa^2 R_c^2)}{\sqrt{\pi} R_c} \right) \quad (29)$$

where $1/dr_{i\alpha}^\gamma$ refers to the derivative of the smearing expression in eq. 12 with respect to the coordinate of the quantum nuclei.

The total forces acting on point charge i contains several terms

$$\begin{aligned}
& - \frac{\delta E_{\text{MM}}^{\text{coul}}[\tau_j, \tau_i]}{\delta \tau_i} - \frac{\delta E_{\text{QM/MM}}[\mathbf{R}_\alpha, \tau_i]}{\delta \tau_i} - \frac{\delta E_{\text{LJ}}[\tau_j, \tau_i]}{\delta \tau_i} = \\
& - \sum_{\substack{i=1 \\ r_{ij} \leq R_c}}^{C'} q_j \frac{\delta v_{\text{MM}}[\tau_j, \tau_i]}{\delta \tau_i} - \int n(\mathbf{r}) \frac{\delta v_{\text{MM}}[\mathbf{r}, \tau_i]}{\delta \tau_i} - \sum_{\substack{i=1 \\ r_{i\alpha} \leq R_c}}^{C'} Z_\alpha \frac{\delta v_{\text{MM}}[\mathbf{R}_\alpha, \tau_i]}{\delta \tau_i} \\
& - \frac{\delta E_{\text{LJ}}[\tau_j, \tau_i]}{\delta \tau_i} - \frac{\delta E_{\text{LJ}}[\mathbf{R}_\alpha, \tau_i]}{\delta \tau_i} \tag{30}
\end{aligned}$$

where the three terms in the second line are the same as eq. 29 with the appropriate coordinate and summation change. The middle term requires a numerical summation over all the grid points to which the electronic density is ascribed, and is the most time consuming step of the QM/MM method. Finally, there are two force components due to Lennard-Jones potential in the last line: one for the point charge to point charge interaction (eq. 8) and second term for the point charge to quantum nuclei interaction.

5 Free Energy Surfaces

In diabatic ET theory a charge is transferred from donor molecule or atom, D^1 , to acceptor molecule or atom, A^0 . Together the donor and acceptor form the initial and final state

$$\begin{aligned}
& i) D^1 + A^0 \\
& f) D^0 + A^1 \tag{31}
\end{aligned}$$

where in the final state the donor and acceptor have changed their electronic states, from the 1- to 0-state, and from the 0- to 1-state, respectively. The potential energy of the initial state can be defined as

$$E_i(R^N) = U_i + \epsilon_i(R^N) \tag{32}$$

where U_i is the gas phase energy of the solutes in the electronic configuration corresponding to the initial state. R^N denotes a nuclear configuration of solvent and solute. $\epsilon_i(R^N)$ denotes the solvent-solute interactions in this electronic state. The same definition is valid for the final state so one can write

$$\begin{aligned}\Delta E(R^N) &= E_f(R^N) - E_i(R^N) \\ &= \Delta\epsilon(R^N) + U_f - U_i\end{aligned}\tag{33}$$

where

$$\Delta\epsilon(R^N) = \epsilon_f(R^N) - \epsilon_i(R^N)\tag{34}$$

$\Delta\epsilon(R^N)$ describes the difference between the interaction of the solvent with the initial and final state electronic configurations - which differ only by the position of the transferring electron charge - for a given nuclear configuration R^N .

We can define the transition state nuclear coordinates in terms of the potential energy difference between the initial and final states as the configurations where the potential energy gap closes (Franck-Condon principle) $\Delta E(R^N) = 0$. This means that at R^\ddagger we must have

$$\epsilon_f(R^\ddagger) - \epsilon_i(R^\ddagger) = -(U_f - U_i)\tag{35}$$

i.e. the nuclear configurations which close the initial-final state potential energy gap induce a change in the electronic interaction between the nuclear environment and transferring charge equal to the constant internal energy difference. To calculate the energy one must both sample numerous configurations as well as statistically unlikely configurations.

5.1 The Free Energy Function

Free energy is a thermodynamic state function, of e.g. $E_i(R^N)$, and in ET theory has a well defined free energy function of the potential energy difference of eq. 33, or

$$F_i(x) = -\frac{1}{\beta} \ln \int dR^N \delta(x - \Delta E(R^N)) \exp(-\beta E_i(R^N))\tag{36}$$

where $\beta = (k_B T)^{-1}$, the inverse of the thermal energy. The integral is the statistical mechanical probability of observing a particular value x of the potential energy gap while the system is in the i state, or

$$F_i(x) = -\frac{1}{\beta} \ln[P_i(x)] + F_i^*\tag{37}$$

where F_i^* is the free energy of the state. This separation is achieved if one factors out the probability from eq. 36

$$P_i(x) = \frac{\int dR^N \delta(x - \Delta E(R^N)) \exp(-\beta E_i(R^N))}{\int dR^N \exp(-\beta E_i(R^N))} \quad (38)$$

so the free energy can here be expressed as

$$F_i(x) = -\frac{1}{\beta} \ln[P_i(x)] - \frac{1}{\beta} \ln \int dR^N \exp(-\beta E_i(R^N)) \quad (39)$$

the second term on the rhs. defines F_i^* . This term is not computed in practice (or evaluated experimentally) but the first term and hence relative free energy and differences for this state are readily calculated. For example, the free energy transition state barrier is

$$\begin{aligned} \Delta F^\ddagger &= F_i(x^\ddagger) - F_i(x_{\min}) \\ &= F_i(\Delta E(R^\ddagger)) - F_i(\Delta E(R_{\min}^N)) \end{aligned} \quad (40)$$

where x_{\min} gives the minimum of the F_i free energy surface.

The same definitions hold for the final state, e.g. it is a thermodynamic state function, and we can write the free energy function as

$$F_f(x) = -\frac{1}{\beta} \ln \int dR^N \delta(x - \Delta E(R^N)) \exp(-\beta E_f(R^N)) \quad (41)$$

which is analogous to eq. 36 and contains an unknown free energy for this state, F_f^* . Now by defining $E_f(R^N)$ in terms of $E_i(R^N)$ (rearranging eq. 33) and inserting in to the above one gets

$$\begin{aligned} F_f(x) &= -\frac{1}{\beta} \ln \int dR^N \delta(x - \Delta E(R^N)) \exp(-\beta(E_i(R^N) + \Delta E(R^N))) \\ F_f(x) &= x - \frac{1}{\beta} \ln \int dR^N \delta(x - \Delta E(R^N)) \exp(-\beta E_i(R^N)) \\ F_f(x) &= x + F_i(x) \end{aligned} \quad (42)$$

The last relation shows that the two surfaces cross at ΔF^\ddagger , or simply

$$F_f(x^\ddagger) - F_i(x^\ddagger) = 0 = x^\ddagger \quad (43)$$

where x^\ddagger is equivalent to eq. 35. Furthermore, knowing one surface the other can be derived in relative terms. The rhs. of eq. 39, which defines F_i^* (and F_f^*), does not need to be known to get relative free energy differences between the states. They have the same free energy function with one translated by the coordinate x . Figure 4 presents two ideal free energy curves and their relations.

6 Biased or Driven Sampling Methods

In a free energy analysis where one seeks to map the free energy change as a system goes from an initial to final state (eq. 31) a considerable sampling is required for accurate results. Furthermore, during constant temperature simulations the system will spend most time near equilibrium so the reaction coordinate x is poorly sampled at the transition state and beyond. To bridge the gap between the two states various methods have been devised to drive the reaction from one state to the other, hence allowing sampling in otherwise statistically unlikely regions along the reaction coordinate.

Accelerated sampling methods in this respect can be divided into two classes: (A) methods modifying the energy expression to reduce the thermodynamic barrier, hence allowing more frequent sampling of out of equilibrium coordinates or (B) restricting the sampling to all degrees of freedom except the reaction coordinate, which is then in some way systematically controlled [46, 33]. The Umbrella Sampling method (US) [80, 81] is one form of (A) where the reaction coordinate is sampled by using a bias potential which drives the reactants from one charge state to the other. This does not restrict any degrees of freedom hence the full momentum space is sampled. In its simplest form it reads

$$E_j^b(R^N) = E_i(R^N) + W_j(\Delta E(R^N)) \quad (44)$$

where $E_j^b(R^N)$ is the energy of an intermediate state j , having mixed characteristics of the initial and final state - the superscript denotes that it is a biased sampling - and $W_j(\Delta E(R^N))$ is a biasing potential which brings the system from the initial state to intermediate states and is here a function of the reaction coordinate which is to be sampled.

A linear coupling parameter, η_j , can be employed which mixes the initial

and final state in a straightforward manner

$$\begin{aligned} E_j(R^N) &= (1 - \eta_j)E_i(R^N) + \eta_j E_f(R^N) \\ &= E_i(R^N) + \eta_j \Delta E(R^N) \end{aligned} \quad (45)$$

and has values in the range $0 \leq \eta_j \leq 1$ which obviously brings the system from the initial to final state. In this case the biasing potential is then defined as $W_j(\Delta E(R^N)) = \eta_j \Delta E(R^N)$. The reaction coordinate can then be readily explored by doing calculations on the initial and final state in parallel, allowing transition into the intermediate state configurations by tuning η_j . This amounts to running molecular dynamics using the same linear combination of the forces

$$\begin{aligned} \mathbf{F}_j(R^N) &= (1 - \eta_j)\mathbf{F}_i(R^N) + \eta_j \mathbf{F}_f(R^N) \\ &= \mathbf{F}_i(R^N) + \eta_j (\mathbf{F}_f(R^N) - \mathbf{F}_i(R^N)) \end{aligned} \quad (46)$$

where \mathbf{F}_i and \mathbf{F}_f represent the force vectors of the atoms in the initial and final state electronic configurations, respectively.

A more conventional way to drive the reaction is to use partial transferring charges [96, 71, 86, 79] and run molecular dynamics with forces from actual (although quite unphysical) intermediate states

$$j) \quad D^{1-\Delta q_j} + A^{+\Delta q_j} \quad (47)$$

In the same fashion as the parameter η_j the partial charge has the range, $0 \leq \Delta q_j \leq 1$, and again obviously brings the system from the initial to final state. In terms of a biasing potential we can rewrite eq. 44 as

$$\begin{aligned} E_j^b(R^N) &= E_i(R^N) + \frac{\Delta E_{q_j}(R^N)}{\Delta E(R^N)} \Delta E(R^N) \\ &= E_i(R^N) + \eta_{q_j} \Delta E(R^N) \end{aligned} \quad (48)$$

where $\Delta E_{q_j}(R^N) = E_{q_j}(R^N) - E_i(R^N)$, the potential energy difference between the partially charged state and the initial state. There is no guarantee that $\Delta q_j = \eta_j$ for a given partial charge, or in other words that the partial charge gap $\Delta E_{q_j}(R^N)$ is a linear function of $\Delta E(R^N)$, with an intersection at zero. As seen and discussed in the results section 7 applying eq. 48 requires additional steps when using the partial charge to drive the reaction.

6.1 Weighted Histogram Analysis Method

The Weighted Histogram Analysis Method (WHAM) as first presented by Ferrenberg and Swendsen [31] is an optimized way to analyse data generated with Monte-Carlo simulations. This method was later extended to the general umbrella sampling and related methods [49, 74], which makes WHAM ideal for constant temperature MD simulation methods such as employed here, where biased sampling windows are used to bridge sampling between two states. Here we follow the basic formulation in [74] and apply a self-consistent WHAM code to connect biased sampling windows using the coupling parameter, η_j , and partial charge, Δq_j .

The probability of observing a particular value of the reaction coordinate, $\Delta E(R^N)$, from a sampling produced by running MD on biased systems, $E_j^b(R^N)$, produces a biased probability - $P_j^b(\Delta E(R^N))$. The relation of the biased probability to the unbiased one is given by

$$P_j^u(\Delta E(R^N)) = e^{\beta[W_j(\Delta E(R^N)) - f_j]} P_j^b(\Delta E(R^N)) \quad (49)$$

where f_j is the free energy change in the system by introducing the biasing potential $W_j(\Delta E(R^N))$. The probability curve for the initial state is written as linear combination of the unbiased probability distributions from the j simulation windows

$$P_i(\Delta E(R^N)) = C \sum_{j=1}^N p_j(\Delta E(R^N)) P_j^u(\Delta E(R^N)) \quad (50)$$

where N runs over all simulation windows, C is a normalization constant, and $p_j(\Delta E(R^N))$ are the weights of the sampling windows which are to be determined and are strongly dependent on the choice of the coupling parameter η_j , or the partial charge Δq_j .

Requiring the weights to be normalized and to minimize the statistical error results in [49, 74]

$$\begin{aligned} P_i(\Delta E(R^N)) &= C \sum_{j=1}^N \frac{n_j e^{-\beta[W_j(\Delta E(R^N)) - f_j]}}{\sum_{k=1}^N n_k e^{-\beta[W_k(\Delta E(R^N)) - f_k]}} P_j^u(\Delta E(R^N)) \\ &= C \sum_{j=1}^N \frac{n_j}{\sum_{k=1}^N n_k e^{-\beta[W_k(\Delta E(R^N)) - f_k]}} P_j^b(\Delta E(R^N)) \end{aligned} \quad (51)$$

where n_j are the number of unique samplings in window j . The free energy change due to the biasing potential, which is an unknown quantity, can be solved for using the following equation

$$\begin{aligned}
e^{-\beta f_j} &= \int dR^N e^{-\beta[W_j(\Delta E(R^N))]} P_i(\Delta E(R^N)) \\
&= C \int dR^N \sum_{j=1}^N \frac{n_j e^{-\beta[W_j(\Delta E(R^N))]} P_j^b(\Delta E(R^N))}{\sum_{k=1}^N n_k e^{-\beta[W_k(\Delta E(R^N)) - f_k]}} \quad (52)
\end{aligned}$$

This equation presents a self-consistent way to solve for the free energy change due to the biasing potential. Note that the biasing potential defined by $\Delta q_j, \eta_j = 1$ in turn fully defines the final state, and the difference $f_1 - f_0$ is then the relative free energy difference between the initial and final state. Finally, the biased probabilities of the simulation windows j are here computed as normalized histograms

$$P_j^b(x) \equiv \frac{1}{n_j} \sum_{l=1}^{n_j} \delta(x - \Delta E(R_{j,l}^N)) \quad (53)$$

where $R_{j,l}^N$ is a selection of coordinates from the configuration phase space and is generally (due to obvious limitations) not a complete sampling of the phase space.

7 Computational Parameters

All electron ground state calculations were performed with the real-space DFT code GPAW [63, 27, 54], where the core electrons are described with the Projector Augmented-Wave method (PAW) [10]. The electronic wave functions describing the valence-electrons are represented with a numerical atom-centered orbital basis corresponding to the double- ζ with polarization (dzp) quality. The effective external potential, and the grid-based wave functions, are represented on a real-space grid with a $0.18(\pm 0.01)$ Å spacing. Exchange-correlation energy is approximated with the GGA functional of Perdew-Burke-Ernzerhof (PBE) [66].

Structural relaxations and molecular dynamics are available in ASE [5]. We used a Quasi-Newton scheme with force tolerance of $0.05 \frac{eV}{\text{\AA}}$ to relax bulk systems (e.g. a transition metal complex adsorbed on a surface), whereas vacuum systems are relaxed with a convergence criteria of $0.01 \frac{eV}{\text{\AA}}$. Constant

temperature MD are run with an in-house Langevin integrator, employing the RATTLE scheme to fix bond lengths. All oxygen to hydrogen bond lengths and angles were constrained, which allows for a MD step size of 1-4 fs. We use a time step of 1 fs, and for the phase space sampling each state (initial, intermediate(s) and final) was thermalised for 10 ps before data collection, which was also run for another set of 10 ps.

The first-row transition metal complexes are placed in a 10^3 \AA^3 cubic cell, along with 31 water molecules - which corresponds approximately to the density of water at ambient conditions, or 1.00 g/cm^3 . The temperature in the Langevin simulations is set to 400 K, which was found to give good agreement between simulated water at the PBE level and experimental water [72, 36]. To accommodate for the dimensions of the polypyridine osmium complex a large cell with periodic boundary conditions was filled with water (198 molecules) and the simulation size adjusted such that the density was 1.00 g/cm^3 (resulting dimension were 16.7, 22.8 and 16.3 \AA in xyz respectively). After relaxing the system a cavity was cut out fitting the vacuum relaxed complex. With this procedure the density should remain approximately the same [75] - and the complex is surrounded by 2-3 solvation shells. A second system was also constructed in analogous manner, but now with 732 water molecules (resulting dimensions of 28, 31.5 and 28.5 \AA) - and the dynamics and phase space sampling for that system was done solely with the QM/MM code.

8 Aqueous Transition Metal Complexes

Here the methodology presented in Section 5 is applied to the symmetric and asymmetric electron transfer reactions of the hexaaqua coordinated first row transition metals: vanadium (V), chromium (Cr), manganese (Mn), iron (Fe) and cobalt (Co), exchanging the +2 and +3 redox states. We have omitted results for titanium (Ti), nickel (Ni) and copper (Cu) which require further investigation due to, among other, the spurious formation of pentaqua complexes in partially charged systems. Figure 5 presents the computational reaction set up. The majority of the results for the various system are at the QM level with the exception of Fe where the symmetric reaction is explored at the QM/MM level. Here we focus on the structure of the charge states, redox potential differences and the reorganization energies of the transition metals listed above, and compare the two methods of using a coupling parameter η_j or partial charge Δq_j to drive the reactions.

8.1 Structural Changes and Redox Potentials

From the molecular dynamics trajectories which were run for 10 ps in each sampling windows, the radial distribution of metal to oxygen (M-(OH₂)) distances were analysed for the initial, intermediate and final states. Figure 7 presents sample radial distribution functions of iron and chromium at the +2 and +3 charged states, with indicators showing the estimated centre of the peaks. All radial distribution functions for the various metals are presented in the Supplementary Information. The first sharp peak represents the metal to ligand bond lengths, and the second broad peak the first solvation shell. Peak positions for the metals are collected in Table 1, along with bond lengths determined experimentally from crystal structures.

The metal to oxygen bond lengths determined from the RDF of all investigated species are in good agreement with experimental structures, with the computational bond lengths consistently larger, but only by 0.01-0.06 Å. Vacuum bond lengths were calculated as well and are within 0.01-0.03 Å of the values determined from the RDFs. Cr(+2), Mn(+3) and Co(LS+2) all show Jahn-Teller distortions in vacuum, which are largely suppressed in the MD simulations for Mn(+3) and Co(LS+2) hence only a single convoluted bond length can be determined. There is though a clear sign of the distortion in the RDF of Cr(+2) (Fig. 7), with the bond length along the distorted axis estimated at 2.44 Å. Accurate determination is however difficult as the relative occurrence of the distorted bond length is low. This indicates that there is a frequent change in which ligand pair occupies the distorted axis during our MD simulations.

The position of the first solvation shell was also estimated, and the approximate centres are reported in Table 1. Although a crude estimate, it does show that the peaks are farthest away from the transition metal species with the longest ligand bonds and that the peak centre shifts towards the metal centre by 0.10-0.18 Å upon oxidation.

8.2 Free Energy Surfaces

Data for the free energy surface analysis is collected by running molecular dynamics on states defined with either the coupling parameter or partial charge, at the same intervals, of $\Delta q_j, \eta_j = [0, 0.25, 0.5, 0.75, 1.0]$. Figure 8 presents radial distribution functions for the initial, intermediate and final

states for the V^{2+} - V^{3+} transition using both bias methods.

Intermediate state peak positions of the RDFs are in general the same within ± 0.01 Å when comparing the two bias methods. The peak positions are furthermore shifted by the same fractional value as the bias parameter, e.g. the difference in peak position between intermediate state at $\eta_j, \Delta q_j = 0.5$ to the initial state is 0.07 Å which is 0.5 of the distance between the initial and final state peaks (0.14 Å). This was observed for all intermediate states and all metals meaning that the internal structure truly changes by the same fraction which controls the bias potential.

As discussed in sections 6 and 6.1 both the driven sampling and application of WHAM requires the knowledge of the biasing potential as defined in eq. 44. In the case where the partial charge is used as a parameter to drive the reaction this potential is written as a simple function of the partially charge energy gap and the initial-final state gap, assuming linearity. This linearity is not observed due to, among other, self-interaction error of the partially charged systems, inherent to DFT. In order to apply the umbrella sampling and WHAM formalism we perform a trivial linearisation by first order fitting to the $\Delta E_q(R^N)/\Delta E(R^N)$ ratio. Eq. 48 thus becomes

$$E_j^b(R^N) = E_i(R^N) + \eta_{q_j}^{\text{LIN}} \Delta E(R^N) + C \quad (54)$$

where $\eta_{q_j}^{\text{LIN}}$ and C are the slope and intersect of the linear equation. The slope is found, in all cases and for all metals, to be the same as the coupling parameter η_j within ± 0.03 . The fitting procedure of this ratio for vanadium, as an example, gives a slope of $\eta_{q_j}^{\text{LIN}} = [0.23, 0.5, 0.74]$ for intermediate states with the partial charges $q_j = [0.25, 0.5, 0.75]$. Figure 9 presents a sample data analysis and linear fit.

Figure 10 presents sample free energy surfaces for vanadium using both bias methods in the form of unbiased probabilities from each sampling window eq. 49. A plot of the associated weights, $p_j(x)$, are overlaid which show that in this case the intermediate state data overlap considerably as their weights do not reach a value of one. Similar plots of the free energy of the unbiased probabilities and weight components of the other metals are presented in Supplementary Information.

The unbiased probabilities and associated weights were then combined to make the final free energy surface, see Figure 11, from where reorganiza-

tion energies and barriers are determined. Table 2 collects these values for all metals and the two bias methods. The free energy barriers vary from about 0.4-0.7 eV but deviates by ± 0.02 -0.04 eV when comparing the two bias methods. The reorganization energies range from 1.66-2.82 eV, and evidently varies quite a lot between metals. Between the two bias methods the values deviate by 0.06-0.15 eV, and the relation of the reorganization energy to the barriers is found to be consistently $\lambda_{\text{reo}}/4 \approx \Delta F^\ddagger$, in accordance with the Marcus relations.

By subtracting the inner reorganization energy, λ_{in} , from the calculated total reorganization energy one gets an estimate of the contribution of the outer sphere reorganization energy, λ_{out} , which is associated with the shift in the position of the first-solvation shell peak. The λ_{in} is defined as the potential energy difference between the initial and final electronic states evaluated in the relaxed structures of the hexaaqua complexes in vacuum.

$$\lambda_{\text{out}} = \lambda_{\text{reo}} - \lambda_{\text{in}} \quad (55)$$

and as seen in column six of Table 3 the λ_{out} are of similar magnitude for all the metals, in the range: 1.18-1.35 eV, which is more in line with classical models of the reorganization. The largest internal reorganization energy is found for the metal species which display the Jahn-Teller effect in vacuum (and during the MD simulations), which makes perfect sense as those structures deviate more from their redox counterpart. The simulation methods and set up is the same in all cases hence one would expect a very similar response from the solvent to the redox change on the central metal ion. The outer sphere reorganization energy can here be compared to the Marcus model, which is derived for the interaction of ions with a continuous medium (the solvent) extending from the ion-to-medium radius, R^q , to infinity. This model gives

$$\lambda_{\text{out}} = \frac{1}{4\pi\epsilon_0} \left(\frac{1}{\epsilon^{\text{op}}} - \frac{1}{\epsilon^{\text{s}}} \right) \left(\frac{1}{2R^{2+}} + \frac{1}{2R^{3+}} - \frac{1}{R_{if}} \right) \quad (56)$$

where ϵ_0 is the permittivity of free space, and ϵ^{op} and ϵ^{s} are the optical and static dielectric constants of water. R^q is the ionic radius for the metal states, and are here simply taken as the estimated position of the first solvation shell peaks presented in Table 1. Finally R_{if} is the distance between the ions which are infinitely far apart in our simple simulations scheme so this term is omitted. We are performing the simulations with water described with the PBE functional, which has an estimated optical dielectric constant

of 2.0 from computations employing the same functional at ambient temperatures [32]. The experimental values of ϵ^{op} and ϵ^{s} for water at ambient conditions are 1.77 and 78.4 [30]. This means, according to eq. 56, that the higher constant of the PBE water in our simulations will result in the underestimation of the reorganization energy.

The outer reorganization energies from the Marcus model are 0.26-0.36 eV larger than the simulated values, which could be due to the fact that we are using a very small number of water molecules to represent the non-local dielectric, and so the actual optical and static dielectric constants are larger in our simulations. For example a value of $\epsilon^{\text{op}} = 2.2$ would bring the Marcus model values in accordance with our simulations. The experimental values from source A (see Table 2) are all very close in value or 2.02-2.26 eV, whereas our simulations range from 1.66-2.82 eV, and it is clear that the internal reorganization energy plays the role in differentiating between the various transition metals. The trend in our computational values is better reflected in more recent experimental values (source B) where the values range from 2.1-3.5 eV, and also in the computational study of Rosso et. al. [68] where both the internal and outer-sphere reorganization terms of the same metal species are analysed in detail. Our simulations are lacking important factors - in the experiments it is understood that there is an optimal distance between the reaction centres before charge transfer occurs, most often taken as the hard-sphere distance between the reaction centres - and the resulting solvation shell overlap effects and charge interaction terms are missing in our simulation as the two reaction centres are treated at an infinite separation.

8.3 Redox Potentials

We are performing QM calculations on charged and periodic systems which employ the standard uniform neutralizing background. This shifts the relative potential of differently charged systems [11] hence the redox potential of the various $\text{M}^{2+/3+}$ reactions can not be accurately determined. However, using the known reduction potential of $\text{Fe}^{2+/3+}$ versus the standard hydrogen electrode (SHE), $E_{\text{Fe,SHE}}^{2+/3+} = -0.771$ eV, the redox potential of the other transition metals can be determined from the free energy difference between the initial and final states of asymmetric $\text{Fe}^{2+}\text{-M}^{3+} \rightarrow \text{Fe}^{3+}\text{-M}^{2+}$ reactions. In this way we solve for the redox potential of the other metals relative to SHE with

$$E_{\text{M,SHE}}^{3+/2+} = \Delta F^0 - E_{\text{Fe,SHE}}^{2+/3+} \quad (57)$$

This difference is solved for self-consistently using the WHAM formalism in eq. 52. In order to solve it one starts with an initial array of the f_j values corresponding to the $\eta_j = [0, 0.25, 0.5, 0.75, 1.0]$ states and at convergence subtracts any residual f_i (initial state $\eta_j = 0$). This gives the relative free energies of the intermediate, f_j , and final state f_f ($\eta_j = 1.0$). In that way $\Delta F^0 = f_f$. Table 4 collects the estimated redox potentials of the metals, and compares to experimental values and other computational results.

The relative redox potentials of V, Cr and Co are in fair agreement with experiment, differing by only 0.05-0.1 eV. Results for Mn are however not, and differ by 0.4 eV, but are in line in all cases with the trend and value of computational results employing a similar exchange-correlation functional (GGA) and a larger basis set [82]. In those simulations the transition metals were placed in an idealised cage consisting of eighteen water molecules and then embedded in to a continuous electrostatic media to represent the bulk solvent.

8.4 Efficient Phase-Space Sampling

Here we explore the symmetric reaction of Fe^{2+} - Fe^{3+} in more detail where first the difference of using a relatively cheap basis set versus a complete basis set is compared, and second where we use the cheaper QM/MM calculator (see Figure 5B) to sample an adequate phase-space for free energy analysis. Note that the free energy analysis requires accurate potential energy gaps between the initial and final state, so after an adequate phase-space sampling with QM/MM a subspace is selected (every tenth image) the potential energy gap is evaluated with full QM calculations. The resulting potential energy gap from QM/MM calculations will be too large due to the role of dielectric response of the solvent, which is lacking in the simple three-site solvent model used here - e.g. for TIP3P ϵ^{op} is found to be ≈ 1.1 [40, 84] which according to eq. 56 increases the reorganization energy and hence the potential energy gap considerably (or by a factor of 1.8).

Figure 12 presents two free energy curves where the basis set dependence is compared. Table 5 collects the free energies of reorganization and barrier for both basis sets, and for the case where the phase-space is sampled with QM/MM. We compare these results to the simulations of Sit et. al. [71] where we have matched the system size, number of water molecules

and exchange-correlation functional. In their calculations they employ a plane-wave basis to describe the valence electrons, where here we use a comparable purely grid-based basis set where the only convergence parameter is the spacing between individual points [63, 27].

All in all there is good agreement between the free energy barriers when comparing the two different basis sets, 0.45 eV vs. 0.39 eV for the fd and *dzp* basis respectively, and only a slight difference when comparing the same basis but different sampling method. There is also excellent agreement between our results and the one of Sit et. al., and the cases where the phase space is generated with the QM/MM calculator. Considering the total reorganization energy there is a noticeable difference between the basis, or up to 0.22 eV. This difference is largely explained with the difference in the energy of internal reorganization. The outer-sphere reorganization is due to the change in localized charge on a central metal surrounded by water ligands - so there is little to no overlap between the electronic states of the solvent and the charge carrying electronic state on the metal - hence there should be little difference in λ_{out} between the two basis sets. The energy due to the internal structural change is another matter, and is strongly dependant on the basis which describes the various overlaps between the metal and ligands - hence internal bonding. In the fd case $\lambda_{\text{int}} = 0.56$ eV so $\lambda_{\text{out}} = 1.24$ in excellent agreement with the *dzp* results of $\lambda_{\text{out}} = 1.22$ eV (see Table 3).

In terms of the total computational time needed we find that the QM/MM, QM(*dzp*) and QM(fd) scale as 1:4:10. Although the fd is considerably more expensive - and too expensive for systems beyond a few hundred atoms particularly when one needs a considerable phase-space sampling - we find that the optimal choice for further study is to use QM/MM to sample the phase space and then use the fd basis, or *dzp* basis if the internal energy reorganization is small, to analyse the potential energy gap. .

9 Polypyridine Osmium Complex

Here we explore the utility and efficiency of the QM/MM code by applying it to the redox-state control and free energy analysis of a large polypyridine osmium complex, Figure 13. We have previously addressed the same polypyridine complexes at the QM level and observed that the solvation of both the cationic osmium complex and the anionic chloride counter-anions is crucial

in stabilizing the localized charges on both ions, in both the free solute state and the solute adsorbed state [44]. Here we expand upon that analysis and evaluate the osmium system with the QM/MM calculator. These are mixed systems of a large osmium complex and counter-anions which are described with QM, and a surrounding solvent described with MM - all evaluated within the same cell, or boundary. Table 6 presents the average metal to ligand bond lengths as well as the charge on the osmium complex, Q_{com} , which is controlled by the number of chloride counter-anions.

The average bond lengths are found to be more or less the same in the full QM calculations compared to the QM/MM. This is observed for both the +2 and +3 redox states, which are here controlled by the presence of the chloride counter-anions. Moreover, we also find that the classical solvent enhances the charge separations between the ions. For example the charge on the complex is closer to the integer values of +1 and +2 in both QM/MM cases - with one or two chloride counter-anions, respectively. This is simply due to the fact that there is no overlap between the electronic states of the classical solvent molecules - as there are none - with the electronic states of the charged complex. In the full QM case such an overlap exists which results in an apparent partial charge transfer to the solvent.

9.1 Free Energies of Reorganization and Barriers

Using the same procedure and reaction schematic as outlined in Section 5 and Figure 5 the free energy surfaces for the Os(II)P0P-Os(III)P0P transition was constructed. This was first done for a system comprised of the complex and 168 water molecules, all at the full QM level. For a complex of this size this corresponds to approximately 2-3 solvation shells. As a second step we utilize the efficiency of the QM/MM code and simulate the same reaction again, but now with 732 water molecules. At first all solvent molecules are treated classically - but the initial-final state energy gap is re-evaluated with varying number of the solvent molecules at the QM level. Figure 14 presents the resulting free energy surfaces and Figure 15 presents the radial expansion. Table 7 collects the free energies of reorganization and barriers - and compares the full QM results to the QM/MM, with and without the solvent expansion.

The free energy of reorganization and barrier for the half-reaction is found to be 0.63 and 0.16 eV, respectively, at the full QM level. In the QM/MM case, where the complex is solely treated with QM, we find the same quantities to

be 1.21 and 0.31 eV, which is roughly an increase of 1.8 in accordance with the difference in the electrostatic constants of the QM vs. MM water. The inner sphere reorganization energy is much smaller in this case compared to the hexaaqua complexes, or only about 0.1 eV. By re-evaluating the initial-final state potential energy gap with varying QM solvent we find that the values converge rapidly - for example the free energy surface where the solvent molecules up to a 7.3 Å radial bound around the complex are treated QM is almost the same as in the case of 8.3 Å radial bound. Furthermore, at that level the free energies of reorganization and barrier for the QM/MM(C) system is 0.68 and 0.17 eV, in very good agreement with the full QM results. At the 8.3 Å radial bound each energy gap evaluation roughly includes 90 water molecules on average, and as seen in the radial distribution function of Figure 15 corresponds roughly to two solvation shells. Note that we require less than half the solvent used in the full QM calculations to reach convergence.

The change in the initial-final state potential energy gap and hence reorganization energy between the QM and QM/MM cases is, as mentioned before, due to the dielectric response of the QM water. This change is furthermore apparent when using the Marcus model, eq. 56, to estimate the outer reorganization energy - which is evaluated for this system by using the ionic radius shown in Figure 15, and the dielectric constants for PBE and TIP3P water. These models, denoted Marcus [A] and Marcus [B] in Table 7, are in fair agreement with the full QM and QM/MM results - although in both cases larger by about 0.14-0.19 eV. This is again due to either a erroneous estimation of the ionic radius, as well as poor choice of dielectric constants. The trend is though exactly as expected - with an enhancement of a factor of 1.8 in the reorganization energy - as observed for the QM vs. QM/MM simulations.

10 Conclusion and Outlook

In the present study we have outlined our newly implemented hybrid-QM/MM code coupled to our in-house QM calculator. The methodology to approach charge transfer reactions was briefly reviewed and applied on several hexaaqua transition metals, where two biased sampling methods were compared - which give the same results - as well as the effects of the finite basis and phase-space configuration sampling. In the asymmetric charge transfer case

we can, furthermore, estimate the redox potentials of the various transition metals with a suitable choice of a reference value. We also find that we can use the QM/MM code to efficiently do the configuration phase-space sampling, and get the same results as full QM free energy simulations by calculating the initial-final state potential energy gap - as a post sampling process - at the full QM level. This is more evident in the case of the polypyridine osmium complex where we perform a systematic expansion of QM treatment of the solvent around the complex, and find that the values quickly converge from the QM/MM to the QM value with inclusion of roughly two solvation shells.

We observe the same trend in the computed reorganization energy (and barrier) compared to experiment, but our values are lower due to several factors such as the relatively high dielectric response of PBE solvent, limited number of solvent molecules and the infinite separation of the donor and acceptor molecules in our ET reactions. However, steps towards improvement are clear - for example systems composed of two integer charged species can be simulated in DFT using the relatively simple Δ SCF scheme [35, 65] or by using a special penalty xc-functional [71]. Furthermore, the computational dielectric properties of water can be greatly improved with hybrid functionals [93] and does not pose a serious addition to the computational cost in the free energy analysis as QM/MM provides an efficient way of thermalization and phase-space sampling with molecular dynamics.

References

- [1] A. K. Al-Matar and D. A. Rockstraw. *J. Comp. Chem.*, 25:660, 2004.
- [2] T. Albrecht, K. M.-Poulsen, J. B. Christensen, A. Guckian, T. Bjørnholm, J. G. Vos, and J. Ulstrup. *Faraday Discuss.*, 131:265–279, 2006.
- [3] T. Albrecht, K. M.-Poulsen, J. B. Christensen, A. Guckian, J. Hjelm, T. Bjørnholm, and J. Ulstrup. *J. Am. Chem. Soc.*, 128:6574–6575, 2006.
- [4] D. Ascher, P. F. Dubois, K. Hinsien, J. Hugunin, and T. Oliphant. *Numerical Python*. Lawrence Liverpool National Laboratory, California, USA, 2001.

- [5] S. R. Bahn and K. W. Jacobsen. An object-oriented scripting interface to a legacy electronic structure code. *Comput. Sci. Eng.*, 4:56–66, 2002.
- [6] A. J. Bard, R. Parsons, and J. Jordan. *Standard Potentials in Aqueous Solutions*. 1985. Marcel Dekker, New York.
- [7] J. K. Beattie, S. P. Best, S. P. Skelton, and A. H. White. Structural studies on the caesium alums, $\text{CsM}^{III}[\text{SO}_4]_2\cdot 12\text{H}_2\text{O}$. *J. Chem. Soc., Dalton Trans.*, 10:2105–2111, 1981.
- [8] D. Berthelot. *Comptes Rendus*, T126:1703, 1898.
- [9] S. P. Best, J. K. Beattie, and R. S. Armstrong. Vibrational spectroscopic studies of trivalent hexa-aqua-cations: single-crystal Raman spectra between 275 and 1200 cm^{-1} of the caesium alums of titanium, vanadium, chromium, iron, gallium, and indium. *J. Chem. Soc., Dalton Trans.*, 12:2611–2624, 1984.
- [10] P. E. Blöchl. Projector augmented-wave method. *Phys. Rev. B*, 50(24):17953, 1994.
- [11] S. Bogusz, T. E. Cheatham, and B. R. Brooks. Removal of pressure and free energy artifact in charged periodic systems via net charge corrections to the Ewald potential. *J. Chem. Phys.*, 1998, volume=.
- [12] S. G. Bratsch. *J. Phys. Chem.*, 18:1–21, 1989.
- [13] P. Brommer, P. Beck, A. Chatzopoulos, F. Gähler, J. Roth, and H.-R. Trebin. Direct Wolf summation of a polarizable force field for silica. *J. Chem. Phys.*, 132(19):194109, 2010.
- [14] B. S. Brunschwig, C. Creutz, D. H. Macartney, T. K. Sham, and N. Sutin. The role of inner-sphere configuration changes in electron-exchange reactions of metal complexes. *Faraday Discuss. R. Soc. Chem.*, 74:113, 1982.
- [15] L. Ciavatta and M. Grimaldi. The potential of the couple $\text{Mn(III)}\leftrightarrow\text{Mn(II)}$ in aqueous 3 M HClO_4 . *J. Inorg. Nucl. Chem.*, (31):3071–3082, 1969.
- [16] W. D. Cornell, P. Cieplak, C. I. Bayly, I. R. Gould, K. M. Merz, D. M. Ferguson, D. C. Spellmeyer, T. Fox, J. W. Caldwell, and P. A. Kollman. A Second Generation Force Field for the Simulation of Proteins, Nucleic Acids, and Organic Molecules. *J. Am. Chem. Soc.*, 117(19):5179–5197, 1995.

- [17] F. Cuadros, I. Cachadiña, and A. Ahumada. Determination of Lennard-Jones Interaction Parameters Using a New Procedure. *Mol. Eng.*, 6:319–325, 1996.
- [18] T. Darden, D. York, and L. Pedersen. Particle mesh Ewald: an N-log(N) method for Ewald sums in large systems. *J. Chem. Phys.*, 98:10089–92, 1993.
- [19] P. Delahay. Correlation between thermal electron transfer in solution and photoelectron emission. *Chem. Phys. Lett.*, 87(6):607–611, 1982.
- [20] P. Delahay and A. Dziedzic. Inner-sphere reorganization in optical electron transfer. *J. Chem. Phys.*, 80:5793–5798, 1984.
- [21] P. Delahay, K. von Burg, and A. Dziedzic. Photoelectron Emission Spectroscopy of Inorganic Cations in Aqueous Solution. *Chem. Phys. Lett.*, 79(1):157–161, 1981.
- [22] P. Demontis, S. Spanu, and G. B. Suffritti. Application of the Wolf method for the evaluation of Coulombic interactions to complex condensed matter systems: Aluminosilicates and water. *J. Chem. Phys.*, 114(18):7980, 2001.
- [23] H. Diebler and N. Sutin. The Kinetics of Some Oxidation-Reduction Reactions Involving Manganese(III). *J. Phys. Chem.*, 68:174–180, 1964.
- [24] A. O. Dohn, E. O. Jonsson, N. E. Henriksen, K. W. Jacobsen, and K. B. Møller. Direct dynamics studies of a transition metal complex. 2014.
- [25] Y. Duan, W. Chun, S. Chowdhury, M. C. Lee, G. Xiong, W. Zhang, R. Yang, P. Cieplak, R. Luo, T. Lee, J. Caldwell, J. Wang, and P. Kollman. *J. Comp. Chem.*, 24(16):1999–2012, 2003.
- [26] M. Eichinger, P. Tavan, J. Hutter, and M. Parrinello. *J. Chem. Phys.*, 110(21):10452, 1999.
- [27] J. Enkovaara, C. Rostgaard, J. J. Mortensen, J. Chen, M. Dulak, L. Ferrighi, J. Gavnholt, C. Glinsvald, V. Haikola, H. A. Hansen, H. H. Kristoffersen, M. Kuisma, A. H. Larsen, L. Lehtovaara, M. Ljunberg, O. Lopez-Acevedo, P. G. Moses, J. Ojanen, T. Olsen, V. Petzold, N. A. Romero, J. Stausholm, M. Strange, G. A. Tritsarlis, M. Vanin, M. Walter, B. Hammer, H. Häkkinen, G. K. H. Madsen, R. M. Nieminen, J. K. Nørskov, M. Puska, T. T. Rantala, J. Schiøtz, K. S. Thygesen,

- and K. W. Jacobsen. Electronic structure calculations with GPAW: a real-space implementation of the projector augmented wave-method. *J. Phys.: Condens. Matter*, 22:253202, 2010.
- [28] M. Eshel and A. Bino. Polynuclear chromium(III) carboxylates Part 2. Chromium(III) acetate - what's in it? *Inorg. Chim. Acta*, 320:127–132, 2001.
- [29] P. P. Ewald. *Ann. Phys. Leipzig*, 64:253, 1921.
- [30] D. P. Fernández, Y. Mulev, A. R. H. Goodwin, and J. M. H. Levelt Sengers. A Database for the Static Dielectric Constant of Water and Steam. *J. Phys. Chem. Ref. Data*, 24(1), 1995.
- [31] A. M. Ferrenberg and R. H. Swendsen. *Phys. Rev. Lett.*, 63(12):1195, 1989.
- [32] R. French, M. abd Redmer. Optical properties of water at high temperature. *Phys. Plasmas*, 18:043301.
- [33] D. Frenkel and B. Smit. *Understanding Molecular Simulation: From Algorithms to Applications*. Academic Press, San Diego, 2001.
- [34] J. L. Gao and C. Alhambra. A hybrid semiempirical quantum mechanical and lattice-sum method for electrostatic interactions in fluid simulations. *J. Chem. Phys. A*, 107:1212–1217, 1997.
- [35] J. Gavnholt, T. Olsen, M. Englund, and J. Schiøtz. *Phys. Rev. B*, 78:075441, 2008.
- [36] J. C. Grossman, E. Schwegler, E. W. Drager, F. Gygi, and G. Galli. Towards an assessment of the accuracy of density functional theory for first principles simulations of water. *J. Chem. Phys.*, 120:200, 2004.
- [37] W. Haiss, T. Albrecht, H. van Zalinge, S. J. Higgins, D. Bethell, H. Höbenreich, D. J. Schiffrin, R. J. Nichols, A. M. Kuznetsov, J. Zhang, Q. Chi, and J. Ulstrup. *J. Phys. Chem. B*, 111:6703–6712, 2007.
- [38] W. Haiss, R. J. Nichols, H. van Zalinge, S. J. Higgins, D. Bethell, and D. J. Schiffrin. *Phys. Chem. Chem. Phys.*, 6:4330–4337, 2004.
- [39] H. Hao and Y. Weitao. Free Energies of Chemical Reactions in Solution and in Enzymes with Ab Initio Quantum Mechanics / Molecular Mechanics Methods. *Annu. Rev. Phys. Chem.*, 59:573–601, 2008.

- [40] Höchtl, P. and Boresch, S. and Bitomsky, W. and Steinhauser, O. Rationalization of the dielectric properties of common three-site water models in terms of their force field parameters. *J. Chem. Phys.*, 109(12):4927.
- [41] J.-K. Hwang and A. Warshel. *J. Am. Chem. Soc.*, 109:715, 1987.
- [42] D. A. Johnson and P. G. Nelson. Factors Determining the Ligand Field Stabilization Energies of the Hexaaqua 2+ Complexes of the First Transition Series and the Irving-Williams Order. *Inorg. Chem.*, 34:5666–5671, 1995.
- [43] G. Jones and J. H. Colvin. *J. Am. Chem. Soc.*, 65:1563, 1944.
- [44] E. Ö. Jónsson, K. S. Thygesen, and J. Ulstrup. *J. Phys. Chem. B*, 115(30):9410, 2011.
- [45] W. L. Jorgensen, J. Chandrasekhar, J. D. Madura, R. W. Impey, and M. L. J. Klein. *J. Chem. Phys.*, 79:926, 1983.
- [46] J. Kästner. Umbrella Sampling. *WIREs Comp. Mol. Sci.*, 1:932–942, 2011.
- [47] G. King and A. Warshel. *J. Chem. Phys.*, 93(12):8682, 1990.
- [48] R. A. Kuharski, J. S. Bader, D. Chandler, M. Sprik, M. L. Klein, and R. W. Impey. *J. Chem. Phys.*, 89:3248, 1988.
- [49] S. Kumar, D. Bouzida, R. H. Swendsen, P. A. Kollman, and J. M. Rosenberg. *J. Comp. Chem.*, 13:1011, 1992.
- [50] A. M. Kuznetsov and J. Ulstrup. *Electron Charge Transfer in Chemistry and Biology*. Wiley, New York, 1999.
- [51] A. M. Kuznetsov and J. Ulstrup. *J. Chem. Phys. A*, 104:11531–11540, 2000.
- [52] T. Laino, F. Mohamed, and M. Parrinello. An Efficient Linear-Scaling Electrostatic Coupling for Treating Periodic Boundary Conditions in QM/MM Simulations. *J. Chem. Theory Comput.*, 2:1370, 2006.
- [53] A. Laio, J. VandeVondele, and U. Rothlisberger. A Hamiltonian electrostatic coupling scheme for hybrid Car-Parrinello molecular dynamics simulations. *J. Chem. Phys.*, 116(16):6941, 2002.

- [54] A. H. Larsen, M. Vanin, J. J. Mortensen, K. S. Thygesen, and K. W. Jacobsen. Localized atomic basis set in the projector augmented wave method. *Phys. Rev. B*, 80:195112, 2009.
- [55] J. E. Lennard-Jones. *Proc. R. Soc. Lond. A*, 106(738):463–477, 1924.
- [56] C. Li, I. Pobelov, T. Wandlowski, A. Bagrets, A. Arnold, and F. Evers. *J. Am. Chem. Soc.*, 130:318–326, 2008.
- [57] F. London. The General Theory of Molecular Forces. *Trans. Faraday Soc.*, 33:8–26, 1937.
- [58] H. A. Lorentz. *Ann. d. Phys. und Chemie*, 12:127, 1881.
- [59] Y. Ma and S. H. Garofalini. Atomistic insights into the conversion reaction in iron fluoride: A dynamically adaptive force field approach. *Mol. Sim.*, 31(11):739, 2005.
- [60] M. A. L. Marques, M. J. T. Oliveira, and T. Burnus. Libxc: a library of exchange and correlation functionals for density functional theory. *Comp. Phys. Commun.*, 183:2272–2281, 2012.
- [61] H. Montgomery, R. V. Chastain, and E. C. Lingafelter. The Crystal Structure of Tutton’s Salts. V. Manganese Ammonium Sulfate Hexahydrate. *Acta Cryst.*, 20:731, 1966.
- [62] H. Montgomery and E. C. Lingafelter. The crystal structure of Tutton’s Salts. II. Magnesium ammonium sulfate hexahydrate and nickel ammonium sulfate hexahydrate. *Acta Cryst.*, 17:1478, 1964.
- [63] J. J. Mortensen, L. B. Hansen, and K. W. Jacobsen. Real-space grid implementation of the projector augmented wave method. *Phys. Rev. B*, 71:035109, 2005.
- [64] K. Nam, J. L. Gao, and D. York. An efficient linear-scaling Ewald method for long-range electrostatic interactions in combined QM/MM calculations. *Theory Comput.*, 1:2, 2005.
- [65] T. Olsen, J. Gavnholt, and J. Schiøtz. *Phys. Rev. B*, 79:0354403, 2009.
- [66] J. P. Perdew, K. Burke, and M. Ernzerhof. Generalized Gradient Approximation Made Simple. *Phys. Rev. Lett.*, 77:3865, 1996.

- [67] A. K. Rappé, C. J. Casewit, W. A. Colwell, W. A. Goddard III, and W. M. Skiff. UFF, a Full Periodic Table Force Field for Molecular Mechanics and Molecular Dynamics Simulations. *J. Am. Chem. Soc.*, 114:10024–35, 1992.
- [68] K. M. Rosso and J. R. Rustad. Ab Initio Calculations of Homogeneous Outer Sphere Electron Transfer Rates: Application to $M(\text{OH}_2)_6^{3+/2+}$ Redox Couples. *J. Phys. Chem. A*, 104:6718, 2000.
- [69] T. Schnabel, J. Vrabc, and H. Hasse. Unlike Lennard-Jones Parameters for Vapor-Liquid Equilibria.
- [70] W. C. Schumb, M. S. Sherrill, and S. B. Sweetser. *J. Am. Chem. Soc.*, 59:2360, 1937.
- [71] P. H.-L. Sit, M. Cococcioni, and N. Marzari. Realistic Quantitative Description of Electron Transfer Reactions: Diabatic Free-Energy Surfaces from First-Principles Molecular Dynamics. *Phys. Rev. Lett.*, 97:028303, 2006.
- [72] P. H.-L. Sit and N. Marzari. Static and dynamical properties of heavy water at ambient conditions from first-principles molecular dynamics. *J. Chem. Phys.*, 122:204510, 2005.
- [73] B. B. Smith, A. Staib, and J. T. Hynes. *J. Chem. Phys.*, 176:521, 1993.
- [74] M. Souaille and B. Roux. Extension to the weighted histogram analysis method: Combining umbrella sampling with free energy calculations. *Comp. Phys. Comm.*, 135:40, 2001.
- [75] R. Spezia, C. Bresson, C. D. Auwer, and M. P. Gaigeot. Solvation of Co (III)-Cysteinato Complexes in Water: A DFT-based Molecular Dynamics Study. *J. Phys. Chem. B*, 112(20):6490–6499, 2008.
- [76] N. Sutin. *Theory of electron transfer reactions. In electron transfer and electrochemical reactions; Photochemical and other energized reactions.* 1986. Zuckermann, J. J. Ed., VCH: New York.
- [77] H. Takahashi, T. Hori, H. Hashimoto, and T. Nitta. A hybrid QM/MM method employing real space grids for QM water in the TIP4P water solvents. *J. Comp. Chem.*, 22(12):1252–1261, 2001.
- [78] H. Takahashi, H. Ohno, R. Kishi, M. Nakano, and N. Matabayasi. *J. Chem. Phys.*, 129:205103, 2008.

- [79] I. Tavernelli, R. Vuilleumier, and M. Sprik. *Phys. Rev. Lett.*, 881:213002, 2002.
- [80] G. M. Torrie and J. P. Valleau. *Chem. Phys. Lett.*, (28):578–581, 1974.
- [81] G. M. Torrie and J. P. Valleau. *J. Comp. Phys.*, 23:187–199, 1977.
- [82] M. Uudsemaa and T. Tamm. *J. Phys. Chem. A*, 107:9997, 2003.
- [83] G. van Rossum and F. L. Drake (eds). *Python Reference Manual*. PythonLabs, Virginia, USA, 2001.
- [84] E. Vladimirov, A. Ivanova, and R
- [85] G. von Grube and L. Z. Schlecht. . *Electrochem.*, 32:178–186.
- [86] R. Vuilleumier, M. Sprik, and A. Alavi. *J. Mol. Struct.*, 506:343, 2000.
- [87] M. Waldman and A. T. Hagler. *J. Comp. Chem.*, 25:660, 2004.
- [88] M. Walter, H. Hä kkinen, L. Lehtovaara, M. Puska, J. Enkovaara, C. Rostgard, and J. J. Mortensen. *J. Chem. Phys.*, 128:244101, 2008.
- [89] J. Wang, P. Cieplak, and P. Kollman. *J. Comp. Chem.*, 21(12):1049, 2000.
- [90] S. J. Weiner, P. A. Kollman, D. A. Case, U. C. Singh, C. Ghio, G. Alagona, S. Profeta, and P. J. Weiner. A new force field for molecular mechanical simulation of nucleic acids proteins. *J. Am. Chem. Soc.*, 106(3):765–784, 1984.
- [91] S. J. Weiner, P. A. Kollman, D. T. Nguyen, and D. A. Case. An all atom force field for simulations of proteins and nucleic acids. *J. Comp. Chem.*, 7:230–252, 1986.
- [92] D. Wolf, P. Keblinski, S. R. Phillpot, and J. Eggerbrecht. Exact method for the simulation of Coulombic systems by spherically truncated, pairwise r^{-1} summation. *J. Chem. Phys.*, 110:8254, 1999.
- [93] X. Xu and W. A. Goddard. Bonding Properties of the Water Dimer: A Comparative Study of Density Functional Theories. *J. Phys. Chem. A*, 108:2305–2313, 2004.
- [94] J. Yan, J. J. Mortensen, and K. W. Jacobsen. *Phys. Rev. B*, 83:245122, 2011.

- [95] D. Zahn, B. Schilling, and S. M. Kast. Enhancement of the Wolf Damped Coulomb Potential: Static, Dynamic, and Dielectric Properties of Liquid Water from Molecular Simulation. *J. Phys. Chem. B*, 106:10725–10732, 2002.
- [96] X. Zeng, H. Hu, A. J. Cohen, and W. Yang. *J. Chem. Phys.*, 128:124510, 2008.
- [97] J. Zhang, Q. Chi, T. Albrecht, A. M. Kuznetsov, M. Grubb, A. G. Hansen, H. Wackerbarth, A. C. Welinder, and J. Ulstrup. *Electrochim. Acta*, 50:3143–3159, 2005.
- [98] J. Zhang, A. M. Kuznetsov, I. G. Medvedev, Q. Chi, T. Albrecht, P. S. Jensen, and J. Ulstrup. *J. Chem. Rev.*, 108:2737–2791, 2008.

11 FIGURES

Table 1: The hexaaqua coordination, $R_{(\text{OH}_2)_6}$, and first solvation shell, R_{sol} , peak position of the transition metals at the +2 and +3 states. The hexaaqua coordination is compared to crystal structures of the metals at the two different redox states. The radial distribution functions for all the metals at the initial and final states are presented in supplementary information. The last column lists the computational metal to oxygen bond lengths for the complexes in vacuum, $R_{(\text{OH}_2)_6}^{\text{vac}}$. All values are in angstroms.

Metal	$R_{(\text{OH}_2)_6}$				R_{sol}		$R_{(\text{OH}_2)_6}^{\text{vac}}$	
	+2	Exp.	+3	Exp.	+2	+3	+2	+3
V	2.17	2.14 ^a	2.03	2.00 ^d	4.27	4.17	2.15	2.06
Cr	2.44	2.30 ^f	1.99	1.96 ^{d,g}	4.20	4.10	2.35	2.01
		2.07 ^f					2.09	
Mn	2.19	2.18 ^{a,b}	2.00	1.99 ^d	4.32	4.23	2.19	2.16
							2.00	
Fe	2.13	2.12 ^a	2.03	1.99 ^e	4.21	4.07	2.13	2.05
Co(LS)	2.02		1.93	1.87 ^d	4.15	3.97	2.17	1.94
							2.00	
Co(HS)	2.10	2.09 ^a	2.03		4.26	4.12	2.10	2.04

(a) Johnson et. al. [42], references therein; (b,c) Montgomery et. al. [61, 62]; (d) Beattie et. al. [7]; (e) Best et. al. [9]; (f) Brunschwig et. al. [14]; (g) Eshel, Bino [28]

Table 2: Free energy barrier, ΔF^\ddagger , and reorganization energy, λ_{reo} , collected from free energy surfaces created with intermediate states using either the coupling parameter η_j (eq. 45), or partial charge Δq_j (eq. 48).

Metal	ΔF^\ddagger		λ_{reo}	
	η_j	Δq_j	η_j	Δq_j
V	0.47	0.45	1.90	1.80
Cr	0.70	0.74	2.82	2.97
Mn	0.62	0.64	2.46	2.55
Fe	0.42	0.39	1.66	1.58
Co(HS)	0.44	0.45	1.74	1.80
Co(LS)	0.68	0.71	2.73	2.81

Table 3: Free energy barrier, ΔF^\ddagger , energy of reorganization, λ_{reo} , and internal reorganization energy, λ_{in} , for the first row transition metals, estimated using the procedure described in section 5 and a single point vacuum calculation, respectively. (Quasi-)Experimental reorganization energies are found here [19, 20, 21], and a collection of more recent values from various sources here [76] (exp. B). Also presented are outer-sphere reorganization energy, $\lambda_{\text{out}} = \lambda_{\text{reo}} - \lambda_{\text{in}}$. The last column presents the outer sphere reorganization energy estimated with the Marcus model, eq. 56 (see text for details).

Metal	ΔF^\ddagger	λ_{reo}	exp. A	exp. B	λ_{int}	λ_{out}	calc.
V	0.47	1.90	2.13	2.69	0.72	1.18	1.50
Cr	0.70	2.82	2.05	3.47	1.58	1.24	1.54
Mn	0.62	2.46	2.02	3.26	1.26	1.20	1.48
Fe	0.42	1.66	2.11	2.10	0.44	1.22	1.55
Co(HS)	0.44	1.84	2.26	2.24	0.68	1.16	1.52
Co(LS)	0.68	2.73			1.38	1.35	1.59

Table 4: Initial-final state free energy difference, f_f , between $\text{Fe}^{2+} + \text{M}^{3+} \rightarrow \text{Fe}^{3+} + \text{M}^{2+}$. The free energy difference is solved for self-consistently using the WHAM method. From the difference the experimental redox potential of $\text{Fe}^{3+/2+}$: 0.771 eV [70] is added to give a computational estimate of the $\text{M}^{3+/2+}$ redox potential (see text for details), which is compared to experiments. The computational results are from [82], where the redox potential is estimated with a simpler scheme using DFT at a similar level of theory.

$\text{M}^{3+/2+}$	f_f	$E_{\text{M}}^{3+/2+}$	exp.	comp.
V	-0.98	-0.21	-0.26 ^{a,f}	-0.17
Cr	-1.15	-0.38	-0.42 ^{b,f}	-0.50
Mn	0.37	1.14	1.54 ^{c,f}	1.21
Co(HS)	1.05	1.82	1.92 ^{d,f}	1.75
Co(LS)	0.30	1.07		1.10

(a) Jones et. al. [43]; (b) von Grube et. al. [85]; (c) Ciavatta et. al. [15]; (d) Diebler et. al. [23]; (e) Bratsch et. al. [12]; (f) Bard, Parson and Jordan [6]

Table 5: Free energy barrier and reorganization energy for the $\text{Fe}^{2+} \rightarrow \text{Fe}^{3+}$ reaction. The fd results are on par with Sit et al. which is a plane-wave based DFT calculation employing the same xc functional. QM/MM parenthesis refers to the case where the phase space is first created with the WOLF-QM/MM method (see schematic Figure 5), but energy gaps and WHAM parameters are re-evaluated with full QM calculations at the indicated basis level.

	fd	fd(QM/MM)	dzp	dzp(QM/MM)	Sit et al.
ΔF^\ddagger	0.45	0.44	0.39	0.40	0.44
λ	1.80	1.75	1.58	1.60	1.77

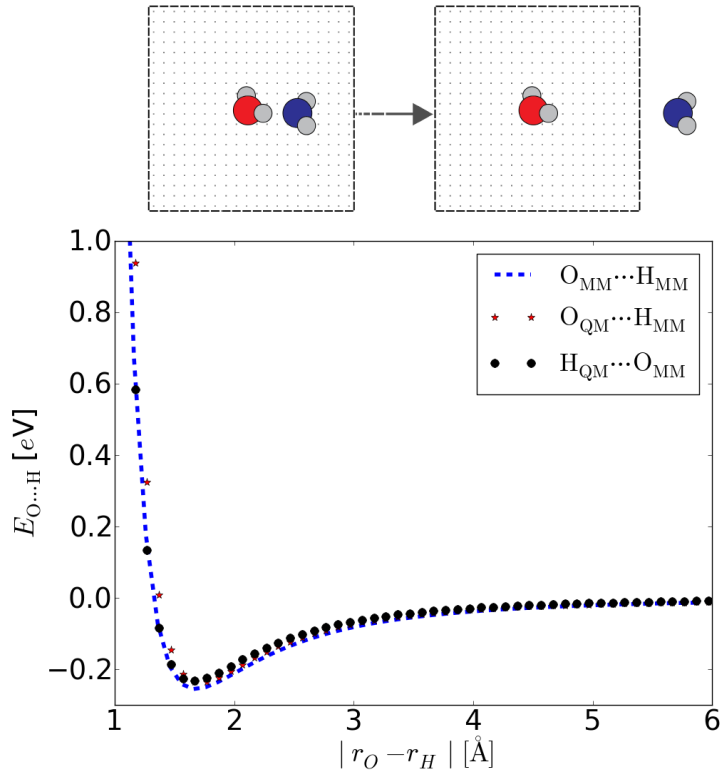


Figure 1: **Top:** The computational setup for the hydrogen bond analysis between a classical and quantum water molecule. The classical point charges begin within the grid space of the QM system which extends to 4.0 Å in all directions, viewed from the quantum oxygen. The classical molecule is systematically moved away until the quantum-hydrogen to classical-oxygen length is 6.0 Å which brings it well outside the quantum grid space. **Bottom:** The hydrogen binding energy between a classical and quantum molecule, compared to the classical to classical case. The classical to quantum is furthermore split in to two cases; first a quantum oxygen interacts with a classical hydrogen, and second, a quantum hydrogen interacts with a classical oxygen. The blue broken curve is the electrostatic potential of eq. 8, using parameters for the rigid TIP3P water model [45]. The red stars and black dots are the hybrid QM/MM cases, $O_{QM} \cdots H_{MM}$ and $H_{QM} \cdots O_{MM}$ respectively, where $E_{bond} = E_{QM/MM} - E_{KS}(H_2O)$, or eq. 2 with the smoothed coulomb potential of eq. 11, minus the potential energy of quantum water in vacuum.

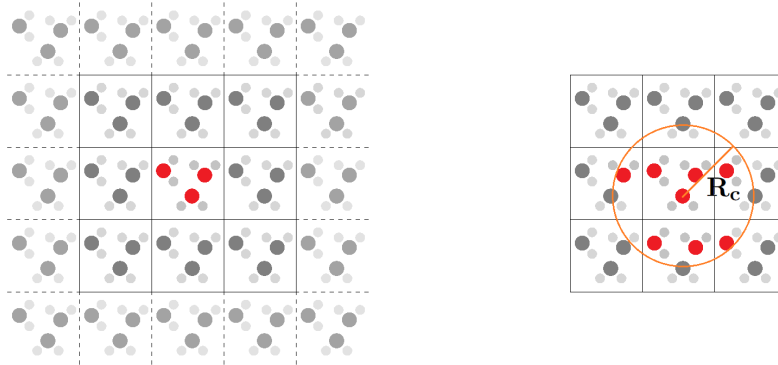


Figure 2: A typical simulation consist of atomic objects and a well defined simulation cell of dimension l_x , l_y and l_z . For a (semi-)infinite simulation we refer to the periodic lattice $\mathbf{a} = n\mathbf{l} = \{nl_x, nl_y, nl_z\}$. **A:** Schematic of the real-reciprocal space Ewald summation. Depending on the system, a typical Ewald summation includes at least the nearest neighbours in the real space part, plus a reciprocal sum which extends much greater (e.g. $n = 9$). **B:** Truncated Wolf scheme. For a system where $R_c < l_x, l_y, l_z$, the Wolf method amounts to a single real-space summation over the nearest neighbour cells only ($\{n \in [-1, 0, 1]\}$).

Table 6: Metal to ligand bond lengths (in Å) and total charge of the complex, Q_{com} , of the structures B shown in FIG. 13. The structures and charge on the osmium complex is compared for the full QM and the QM/MM cases, where in the latter all solvent is treated classically.

	B^+Cl^-	$\text{B}^{2+}2\text{Cl}^-$	B^+Cl^-	$\text{B}^{2+}2\text{Cl}^-$
	QM(H_2O) ₁₆₈	QM(H_2O) ₁₆₆	MM(H_2O) ₁₆₈	MM(H_2O) ₁₆₆
Os-Cl _{lig}	2.47	2.35	2.46	2.35
Os-N _{P0P}	2.13	2.15	2.13	2.15
Os-N _{avg}	2.09	2.07	2.09	2.08
$Q_{\text{com}} [e]$	1.07	1.84	0.99	1.97

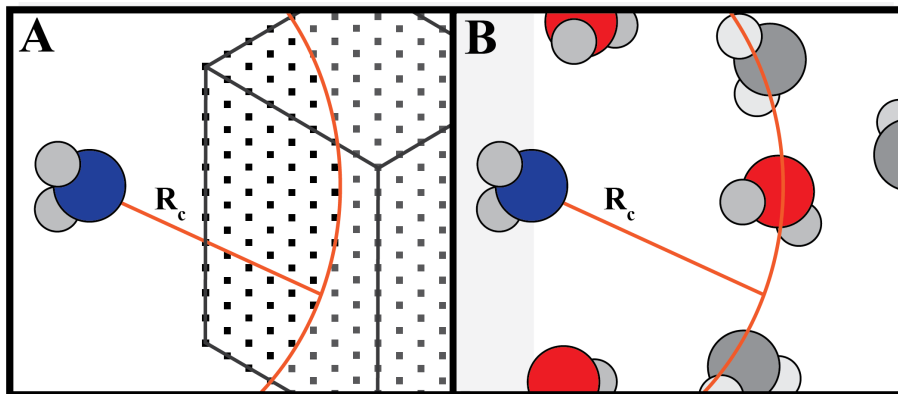


Figure 3: The electrostatic interactions of the classical solvent molecules are truncated at R_c ; here they are depicted as water with the oxygen blue, and the hydrogens grey. **Case A:** In this example the point charge is outside the quantum potential grid space, and due to the cut-off only gives weight to v_{MM} where the grid-points are within the truncated sphere defined by R_c . **Case B:** Here the electrostatic interaction between point charge to quantum nuclei, or point charge to point charge, are cut off at R_c . However, if the principal atom of a simple molecule like water (oxygen) lies within the sphere the whole molecule can be taken into account without the loss of accuracy, i.e. the hydrogens are evaluated if they lie within the interval $|R_c + \Delta_H|$.

Table 7: Free energies of reorganization and free energy barriers, in [eV]. Full QM is compared to the QM/MM expansion process, see Figure 15C, which is deemed converged. QM/MM(0) refers to the case where none of the solvent is treated with QM. For comparison the Marcus model is used, eq. 56, but now with computational PBE [A] and TIP3P [B] dielectric constants, which should compare to the QM and QM/MM(0) results respectively.

	QM	QM/MM(C)	QM/MM(0)	Marcus [A]	Marcus [B]
λ_{reo}	0.63	0.68	1.21	0.82	1.35
ΔF^\ddagger	0.16	0.17	0.31	0.21	0.34

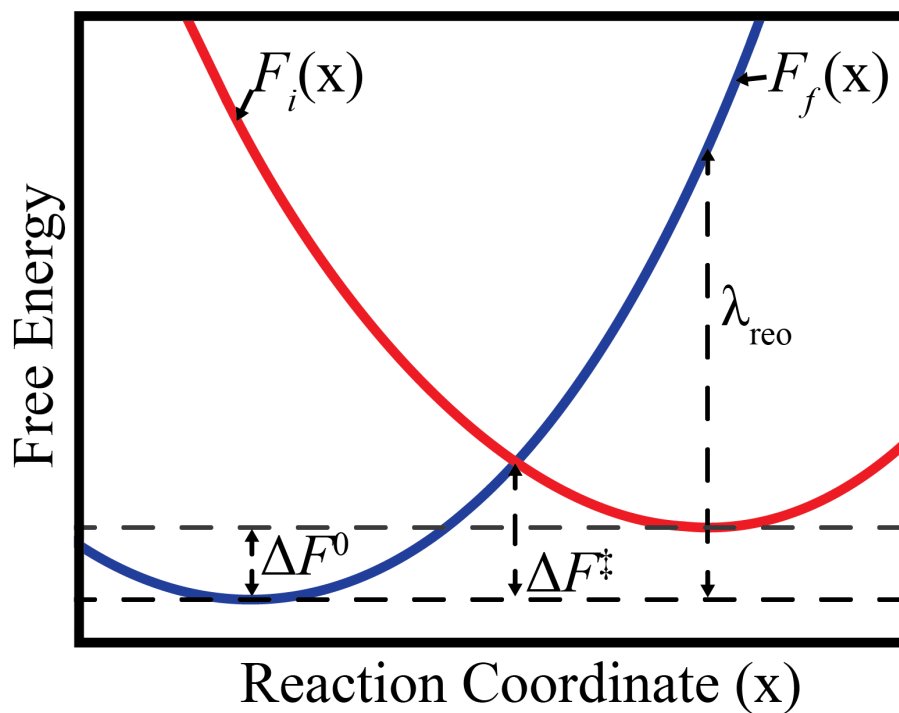


Figure 4: Free energy surfaces for the initial, $F_i(x)$, and the final, $F_f(x)$, states. The parameters pertinent to electron charge transfer are depicted on the graph: ΔF^0 - the free energy difference between the two states (redox potential difference); ΔF^\ddagger - the free energy barrier for the reaction; and λ_{reo} - the reorganization energy of the solvent (nuclear) environment including the internal reorganization of the chemical species under scrutiny.

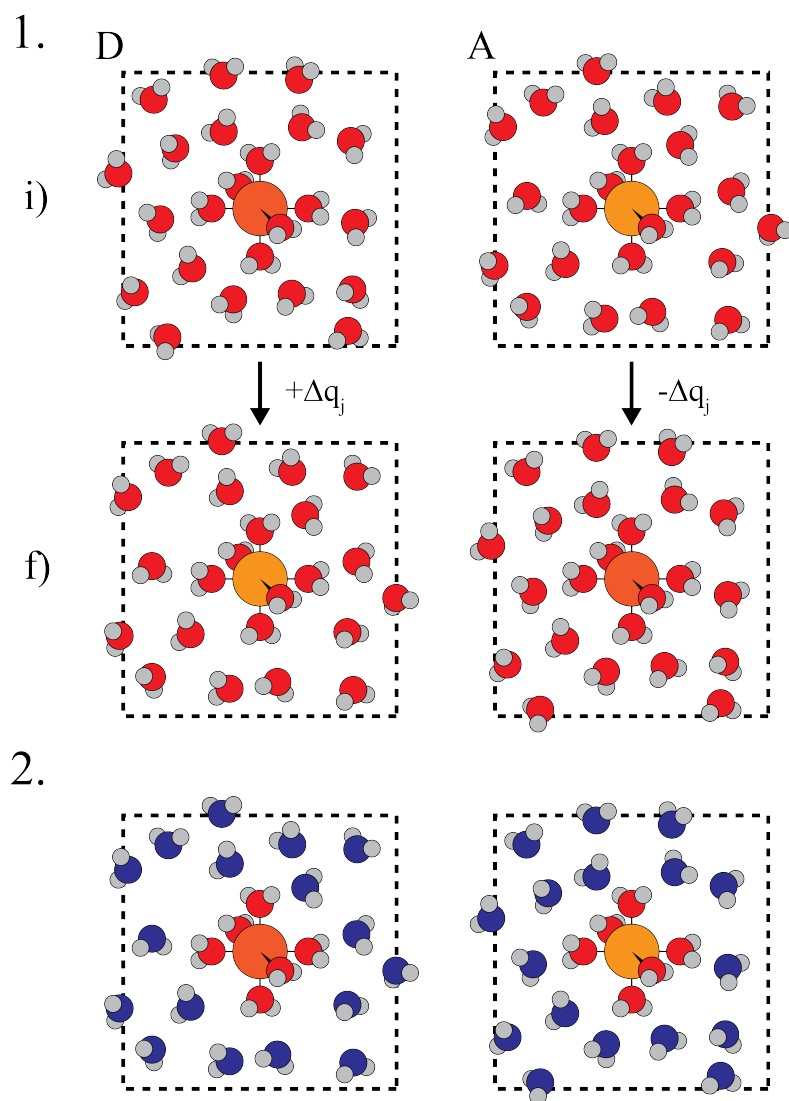


Figure 5: 1. Schematic of the biased sampling methods and reaction centres. The i)initial and f)final states are a combination of two independent charge sites, **Donor** and **Acceptor**. The simulated reaction at **D** is $M^{2+} \rightarrow M^{3+}$ with the reverse reaction taking place at **A**. 2. We also explore the case where the solvent is treated classically, but the inner ligand sphere is kept QM. We have applied the same reaction schematic to the Os(n)POP complex. However, the QM/MM method can not predict accurate reorganization energies as it lacks description of the solvent polarizability, hence we use QM/MM to sample a large phase space, but potential energy values which enter the WHAM scheme are always evaluated with full QM on selected snapshots.

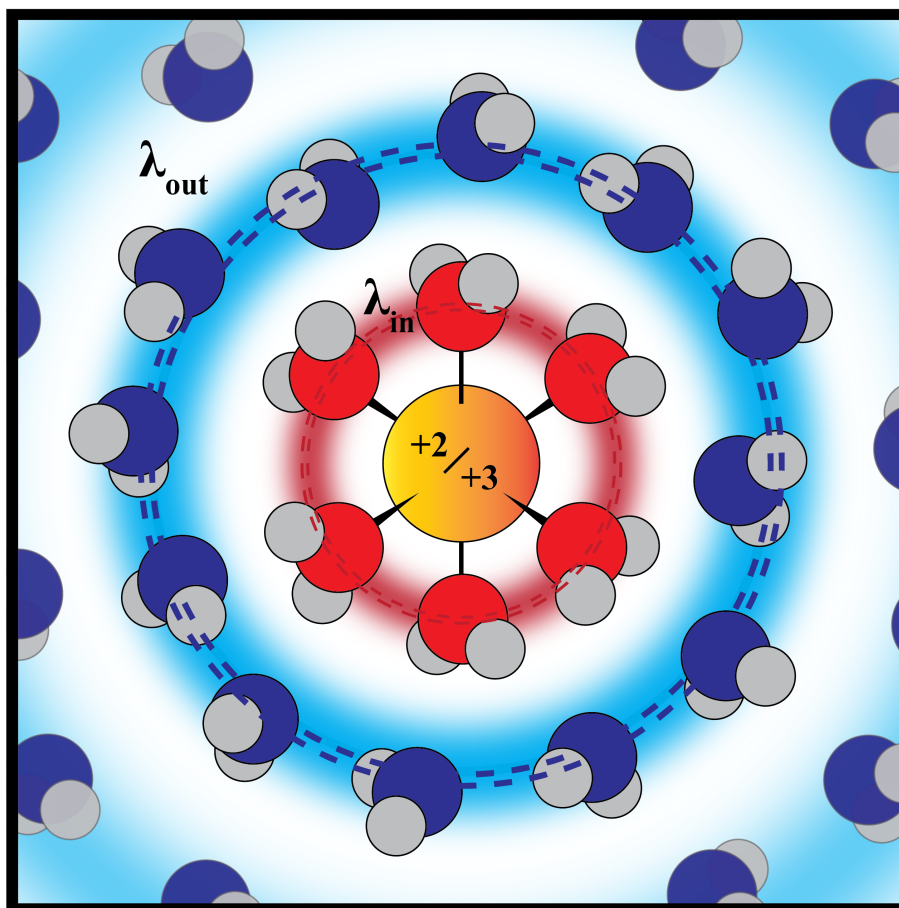


Figure 6: The redox induced radial distribution change around the hexaaqua $M^{2+/3+}$ complexes. The distance is to scale, as well as the given width of each distribution. Centred on each width is the radial distance for state $+3$, with the $+2$ radius presented as the outer ring.

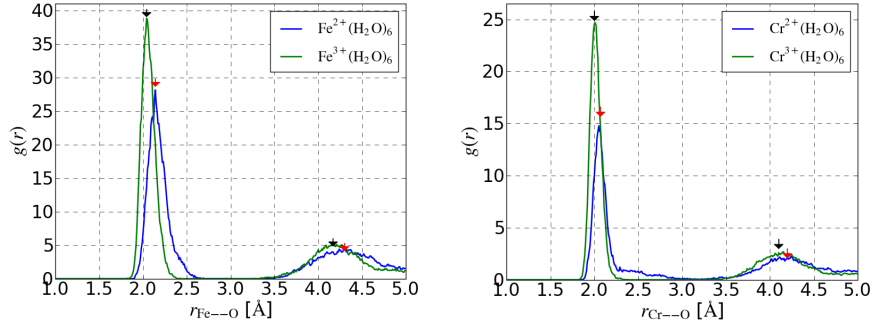


Figure 7: Radial distribution functions for $\text{Fe}^{2+/3+}$ (left) and $\text{Co}^{2+/3+}$ (right). Blue and green RDF are for the +2 and +3 oxidation state. In both cases there is a clear shift of both the internal ligand structure as well as the first solvation shell. Cr^{2+} is a high-spin d^4 species and shows very clear Jahn-Teller distortions in vacuum calculations. The first peak hints of the same effect in the MD simulation, with a relatively low probability, which indicates that the distorted axis switches rapidly between ligand pairs.

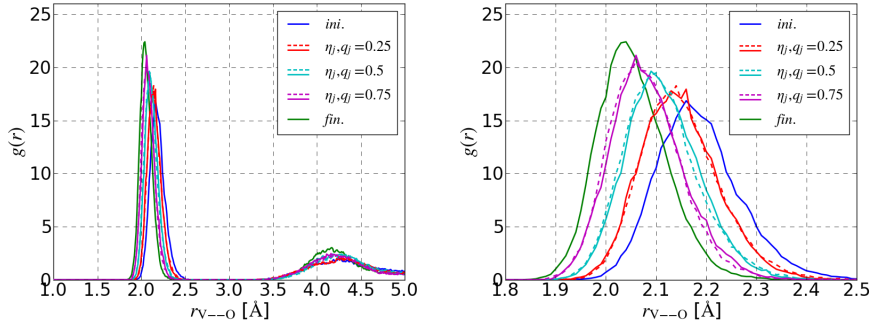


Figure 8: Radial distribution functions (RDFs) of the initial, intermediate and final states of hexaaqua vanadium. The intermediate states sampled by using both the coupling parameter, η_j (broken lines), and partial charge, q_j , are presented. Left: RDFs showing both the ligand and first solvation peaks. Right: zoom in of the ligand peaks, showing the overlap of the intermediate state peaks (broken lines of same color scheme shown in the legend).

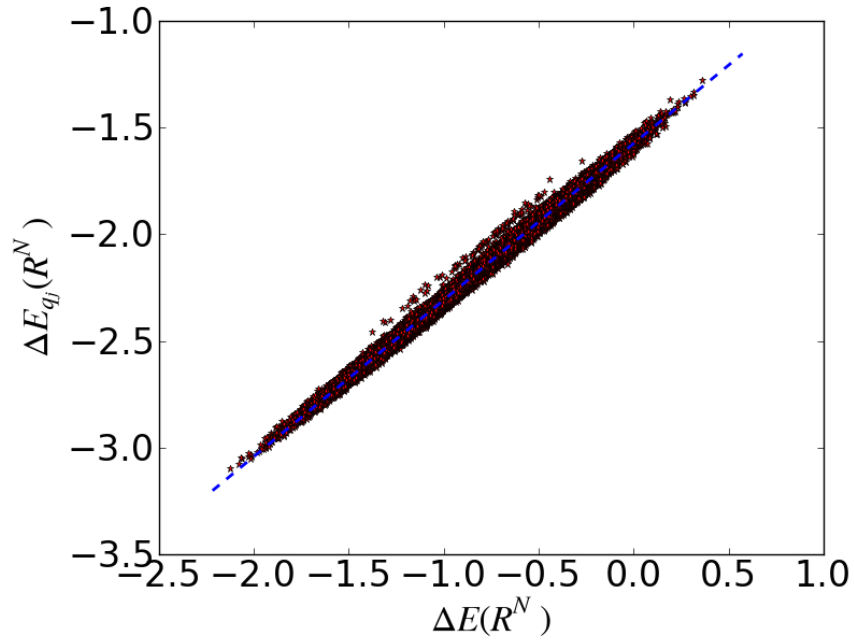
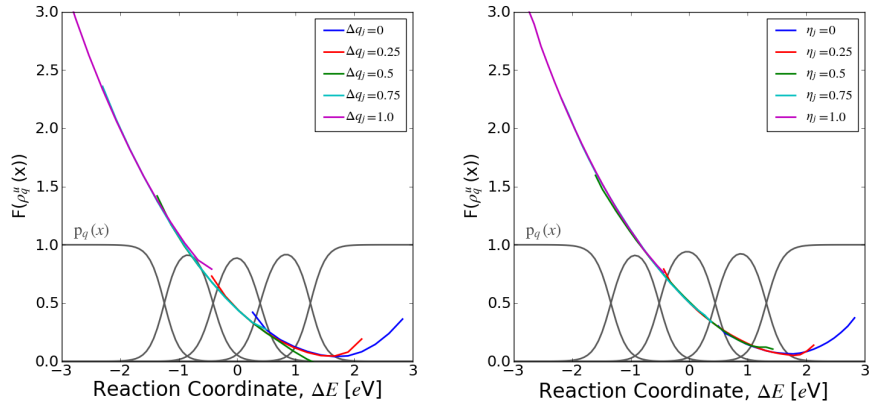


Figure 9: In order to evaluate the biasing potential of eq. 48 for the intermediate, or partially charged, systems the ratio of partial charge potential energy gap $\Delta E_{q_j}(R^N)$ to the initial-final state gap $\Delta E(R^N)$, red stars, is fitted with a first order linear equation, blue broken line. This particular example is from simulations with the $V^{+2.75} - V^{+2.25}$ intermediate state ($\Delta q_j = 0.75$, see Figure 5), where the slope of the best fit is $\eta_{q_j}^{\text{LIN}} = 0.74$, in line with the partial charge.



(a) FES of $V^{2+}-V^{3+} \rightarrow V^{3+}-V^{2+}$, using Δq_j (b) FES of $V^{2+}-V^{3+} \rightarrow V^{3+}-V^{2+}$, using η_j

Figure 10: Example of the free energy surfaces analysis. The plots show the free energy associated with each unbiased probability curve (eq. 49) sampled by setting the coupling parameters η_j , or partial charge Δq_j , to the values indicated in the legend. Also plotted are the associated weights which require the self-consistently solved free energies of perturbation (eq. 52). The final free energy surface is then the linear combination of the product of the weights and unbiased probabilities (eq. 50). Using the coupling parameters to drive the reaction, and this goes for all transition metal, gives a smoother transition, but the two methods give very similar or the same free energy surfaces.

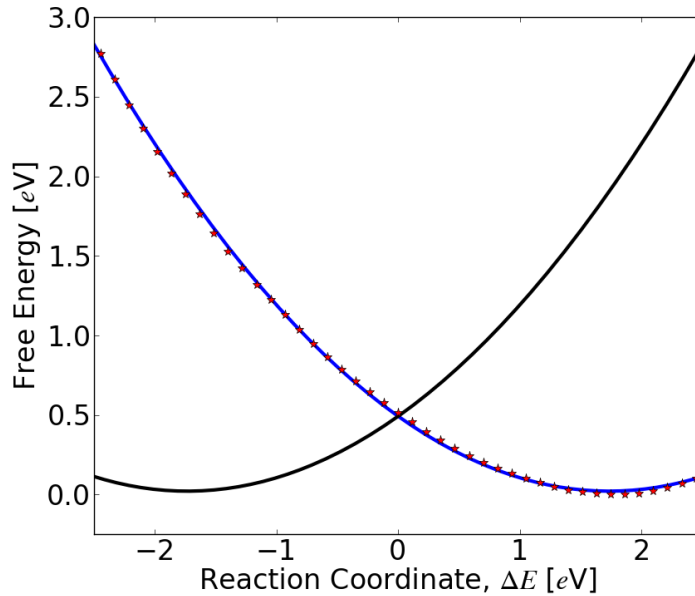


Figure 11: Applying the weights to the unbiased probability curves (see Figure 10) for each sampling window the final free energy surface is constructed. This particular example is for vanadium and the bias method here uses the coupling parameter η_j . The red stars are the WHAM data and the blue curve is a second order best fit. The black curve represents the final state free energy surface which is the same fitted curve but here translated by the reaction coordinate (see eq. 42). The equations of the resulting best fit and translation are used to solve for the reorganization energy (value of initial state curve above final state minima) and the free energy barrier (value of their crossing which is at zero in the symmetric case, eq. 43). The values for both methods and all metals are presented in Table 2. The values presented in Table 3 are collected from the free energy surfaces composed of intermediate states made with the coupling parameter η_j , and are compared to experiment and the Marcus model.

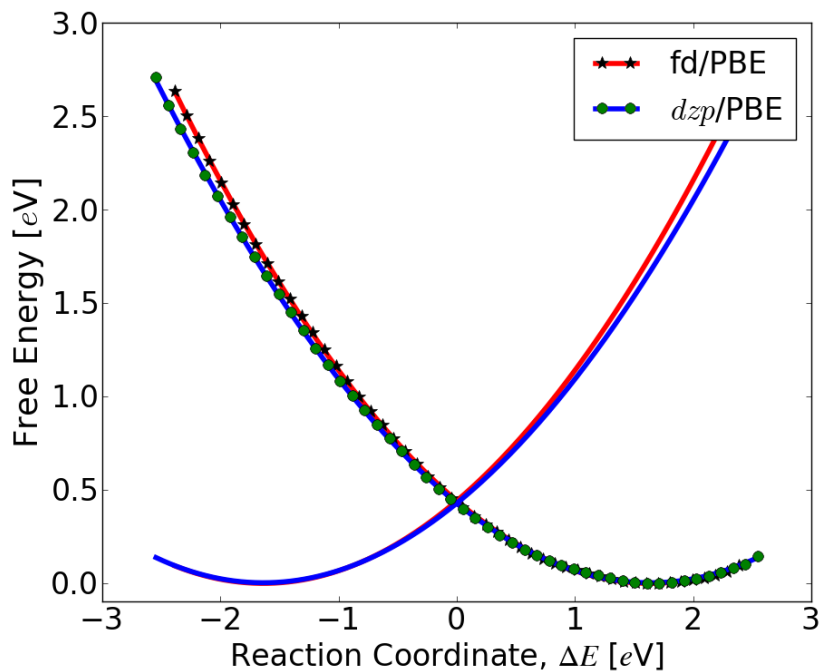


Figure 12: Diabatic free energy surfaces for the ferric-ferrous (Fe^{+2} - Fe^{+3}) charge transfer reaction. It is important to note that we are comparing two different ways KS state expressions: the finite difference (fd) mode, where the basis accuracy depends solely on the grid spacing, and a localized atomic orbital basis of *dzp* quality (a much cheaper option). Time scale of sampling an adequate phase space corresponding to 5 ps per bias window scales as follows: 1:4:10 for the QM/MM, QM(*dzp*) and QM(fd) methods, respectively. The black stars and green dots is the output from the WHAM method, and the red and green curves are second order fits to the data.

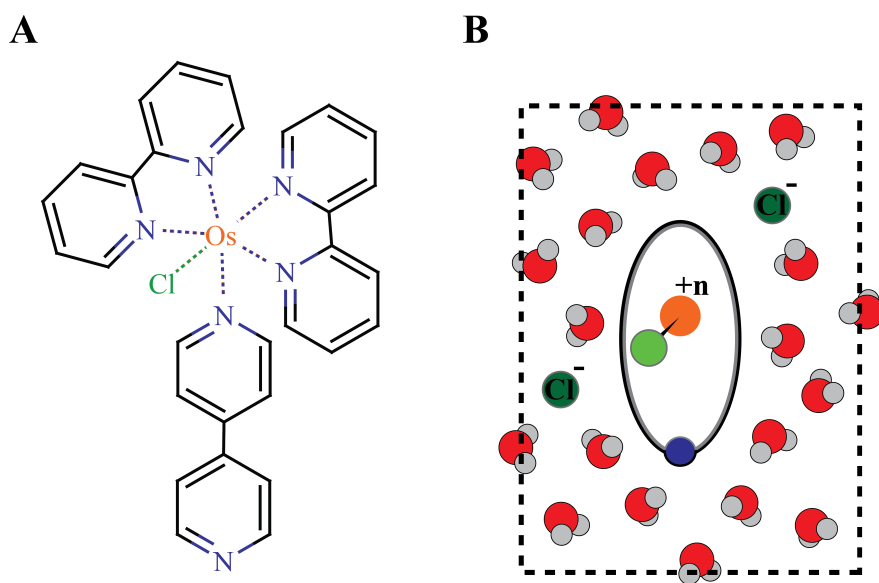


Figure 13: Schematic of the osmium transition metal complex investigated. **A:** $\text{Os}(n)\text{P0P}$ or $[\text{Os}(\text{bpy})_2(\text{P0P})\text{Cl}]$ (bpy = 2,2'-bipyridine, P0P = 4,4'-bipyridine). The formal oxidation state of the transition metal centre is here +1, due to the ionic chloride ligand. Carbons are depicted with the stick model and hydrogens are omitted for clarity. **B:** In the presence of solvent the oxidation state, $+n$, is controlled either trivially by simply removing electron(s) from the computational system, or by introducing additional chlorides as anions.

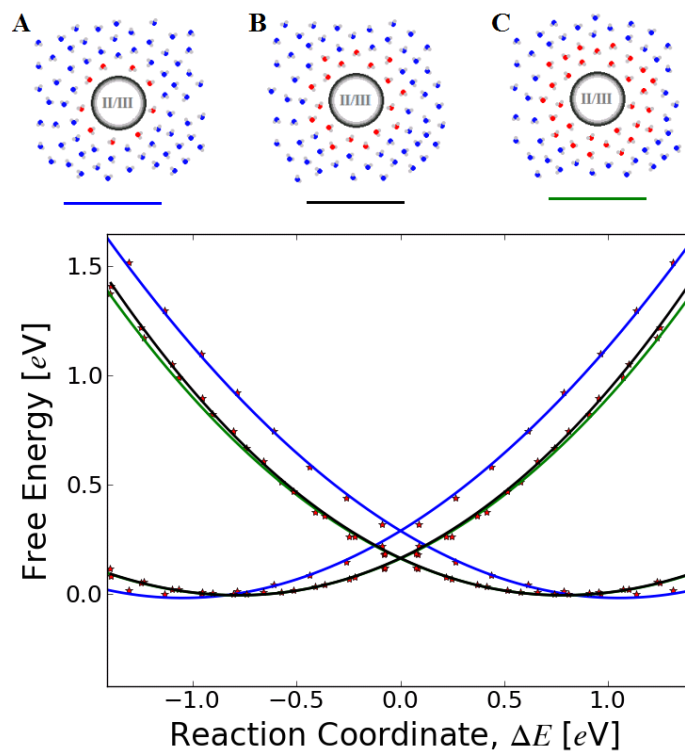


Figure 14: Free energy surfaces generated for varying degree of quantum solvent - systems **A**, **B** and **C** show the expansion of the QM treatment around the osmium complex. The phase-space is sampled first with QM/MM with all solvent molecules at the MM level. For the free energy surface analysis the energy gap between the initial and final state is evaluated but with all solvent molecules within the radial bounds indicated in Figure 15 are treated also with QM. In this way the dielectric response is reintroduced in to the solvent in a step-by-step fashion until convergence is achieved.

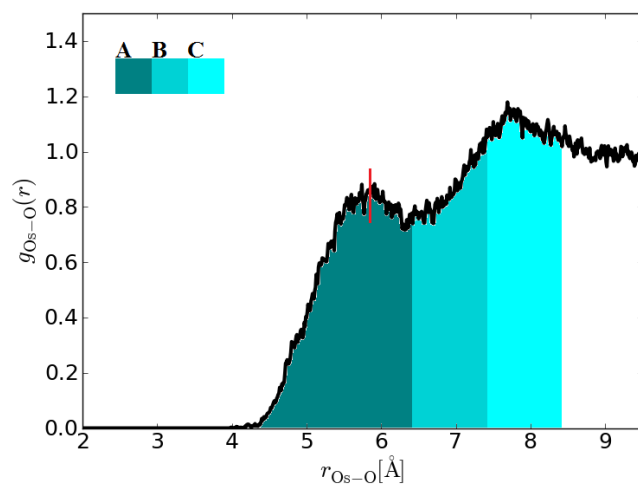


Figure 15: The radial distribution of oxygen in water around the osmium polypyridine complex. After running extensive QM/MM simulations the same configurations were used to analyse the free energy surface, but now with the water treated at the QM level up to the distance indicated by the **A**, **B** and **C** color scheme. Corresponding model cartoons and free energy surfaces are presented in Figure 14. The red line indicates the estimated ionic radius of the complex used in the Marcus model analysis (see text for details).

PAPER III

ARTICLE

Received 26 Jan 2013 | Accepted 6 Jun 2013 | Published 2 Jul 2013

DOI: 10.1038/ncomms3121

Direct measurement and modulation of single-molecule coordinative bonding forces in a transition metal complex

Xian Hao^{1,2}, Nan Zhu¹, Tina Gschneidtn³, Elvar Ö. Jonsson⁴, Jingdong Zhang¹, Kasper Moth-Poulsen³, Hongda Wang², Kristian S. Thygesen⁴, Karsten W. Jacobsen⁴, Jens Ulstrup¹ & Qijin Chi¹

Coordination chemistry has been a consistently active branch of chemistry since Werner's seminal theory of coordination compounds inaugurated in 1893, with the central focus on transition metal complexes. However, control and measurement of metal-ligand interactions at the single-molecule level remain a daunting challenge. Here we demonstrate an interdisciplinary and systematic approach that enables measurement and modulation of the coordinative bonding forces in a transition metal complex. Terpyridine is derived with a thiol linker, facilitating covalent attachment of this ligand on both gold substrate surfaces and gold-coated atomic force microscopy tips. The coordination and bond breaking between terpyridine and osmium are followed *in situ* by electrochemically controlled atomic force microscopy at the single-molecule level. The redox state of the central metal atom is found to have a significant impact on the metal-ligand interactions. The present approach represents a major advancement in unravelling the nature of metal-ligand interactions and could have broad implications in coordination chemistry.

¹Department of Chemistry, Technical University of Denmark, Kemitorvet, Building 207, DK-2800 Kongens Lyngby, Denmark. ²State Key Laboratory of Electroanalytical Chemistry, Changchun Institute of Applied Chemistry, Chinese Academy of Sciences, Changchun 130022, China. ³Department of Chemical and Biological Engineering, Chalmers University of Technology, SE-412 96 Gothenburg, Sweden. ⁴Department of Physics, Technical University of Denmark, DK-2800 Kongens Lyngby, Denmark. Correspondence and requests for materials should be addressed to Q.C. (email: cq@kemi.dtu.dk) or to H.W. (email: hdwang@ciac.jl.cn).

Coordination chemistry has emerged as an overwhelmingly active branch of chemistry since Werner published his seminal theory of coordination compounds in 1893^{1,2}. A wealth of studies have since then been focused on transition metal complexes, driven by their importance in fundamental chemistry, biochemistry, protein science and industrial catalysis applications². In a coordination compound, a central metal atom is bonded to a surrounding array of coordinating ligands². Coordinative bonding is a special class of chemical covalent bonds, often with strong dipolar nature and complex electronic interactions between central metal atom and ligands. Understanding the nature of the coordinative bonding has ever posed and still remains a tremendous challenge. Extensive investigations on metal–ligand interactions have therefore not surprisingly constituted one of the central themes in coordination chemistry.

Nearly all aspects of coordination chemistry, including metal-binding free energies and enthalpies, and bond association/dissociation kinetics so far disclosed are based on average ensemble level information. In the past two decades, the scanning probe microscopies have, however, increasingly enabled non-traditional and single-molecule approaches to physicochemical properties of many important chemical and biological processes³, ranging from electron transfer (ET)^{4–6} and molecular recognition^{7,8} to *in vivo* biochemical processes in a living cell⁹. In terms of transition metal complexes, scanning tunnelling microscopy (STM), particularly electrochemical STM (ECSTM), as an advanced tool has offered detailed mapping of single-molecule conductivity patterns in chemical or/and electrochemical environments^{10–13}. Atomic force microscopy (AFM) imaging and spectroscopy have the power to uncover chemically hidden information that would not be revealed by traditional chemical approaches, for example, mechanical activation of chemical bonds (bond rupture) as well as the influence of stretching forces on chemical reactions^{14–28}. A very recent report shows that molecular conductance and Van der Waals forces can also be measured simultaneously by conducting AFM²⁹.

In comparison to the extensive use of ECSTM in molecular electronics studies^{4–6}, electrochemically controlled AFM (ECAFM) has not been exploited nearly as much. This is owing to technical challenges and the use of AFM in liquid environments so far mostly for biochemistry and molecular biology. ECAFM has, however, offered new perspectives in two recent reports. One study by Gaub and coworkers^{30,31} has shown the feasibility of direct measurement of electrically induced nitrogen–gold bonding via the interaction of DNA fragments with a gold substrate. Another report has demonstrated that significant structural changes of a metalloenzyme can be detected when the enzyme is electrochemically brought from its resting state to its catalytically active state²⁶. In the present work, we address direct measurement of single-molecule coordinative bonding forces in a transition metal complex in different oxidation states by ECAFM. Density functional theory (DFT) simulations are also performed to offer a rationale of the experimental observations.

Results

Synthesis and surface self-assembly of terpyridine ligands. Terpyridine (terpy) was derived with an alkanethiol linker group. Details of the synthesis, chemical structure and molecular dimensions are provided in the Supplementary Information (Supplementary Fig. S1). Thiol derivation enables this ligand to self-assemble onto gold surfaces¹⁰ (Fig. 1a) and gold-coated AFM tips. The self-assembled monolayers (SAMs) of the terpy

derivative on a Au(111) surface with or without osmium (Os) coordination were systematically studied by electrochemistry, ECAFM and ECSTM. Upon the coordination of Os ions to the immobilized terpy (Fig. 1a), the Faradaic signal arising from interfacial ET between Os and the Au(111) electrode was detected directly by cyclic voltammetry (Fig. 1b). The linear relation between the peak current and scan rate is a clear indication that the Os ions are bound to the electrode surface via terpy coordination (Supplementary Fig. S2). Reversible interfacial ET was observed, and the ET rate was estimated as 25 s^{-1} by the Laviron method (Supplementary Fig. S3)^{32,33}. The surface population of terpy, estimated from the reductive desorption (Supplementary Fig. S4), was controlled by adjusting the terpy solution concentration and adsorption time. For the present purpose, the effective surface coverage of $(9.0 \pm 0.8) \times 10^{-11}\text{ mole cm}^{-2}$ (that is, at the submonolayer level) as estimated by the Faradaic charge was used in most measurements.

The surface microscopic structures of the terpy-based SAMs were characterized by AFM and STM imaging in electrochemical environment, which were also used in the AFM force spectroscopy. The AFM images (Fig. 1c and Supplementary Fig. S5) show that the apparent height of the Os–terpy complex is about 2 nm, consistent with the molecular dimensions of the half-coordinated complex (Supplementary Fig. S1). In contrast to physical imaging by AFM, *in situ* STM imaging offers electronic mapping of the molecules and is very sensitive to molecular conductance. Owing to poor conductivity, the terpy SAMs alone show weak STM contrast although the fingerprint features of the SAMs, such as nanoscale pits, are clearly distinguished (Supplementary Fig. S6). The coordination of Os ions to the immobilized terpy results in a dramatic enhancement of molecular conductivity, as shown in Fig. 1d and Supplementary Fig. S7. STM imaging is thus consistent with the electrochemical observations. While the terpy SAMs are redox inert, the Os–terpy SAMs show reversible and fast interfacial ET. Overall, the electrochemical, AFM and STM characterizations support that the terpy SAMs are formed on Au(111) surfaces and can coordinate to Os. This sets a foundation for single-molecule AFM force spectroscopic analysis.

Direct measurement of single-molecule coordination forces.

Figure 2a illustrates the working principles of single-molecule AFM force spectroscopy, which is further detailed in Supplementary Fig. S8. When the AFM tip approaches the sample, tip-bound terpy interacts with Os–terpy on the substrate surface to form the complex $[(\text{Os}(\text{terpy}-(\text{CH}_2)_6\text{-S-Au})_2)^{2+/3+}]$. Retraction of the tip results in dissociation of the Os–terpy bond but does not break the Au–S bond, which is much stronger than the coordinative bond as described below. Force–distance curves for the Os–terpy ligand dissociation process can thus be recorded.

To distinguish what AFM force–distance curves actually record, four experimental configurations were designed as illustrated schematically in Fig. 2b. A series of force spectra (several hundreds to thousands force–distance curves) for each configuration were acquired and statistically analysed. Figure 3a compares representative force–distance curves at open circuit potentials for the four configurations. In configuration (I), Os ions were absent. When the terpy–C₆-S-tip was brought in contact with terpy–C₆-S-Au(111) samples, no specific interaction force was detected (Fig. 3a(I)), that is, no force peak feature is observed. Similar observations apply for configuration (IV) (Fig. 3a(IV)) where Os ions were pre-loaded on both the AFM tip and Au(111) substrate. In contrast, well-defined force–distance curves were recorded with configurations (II) and (III), and characterized by

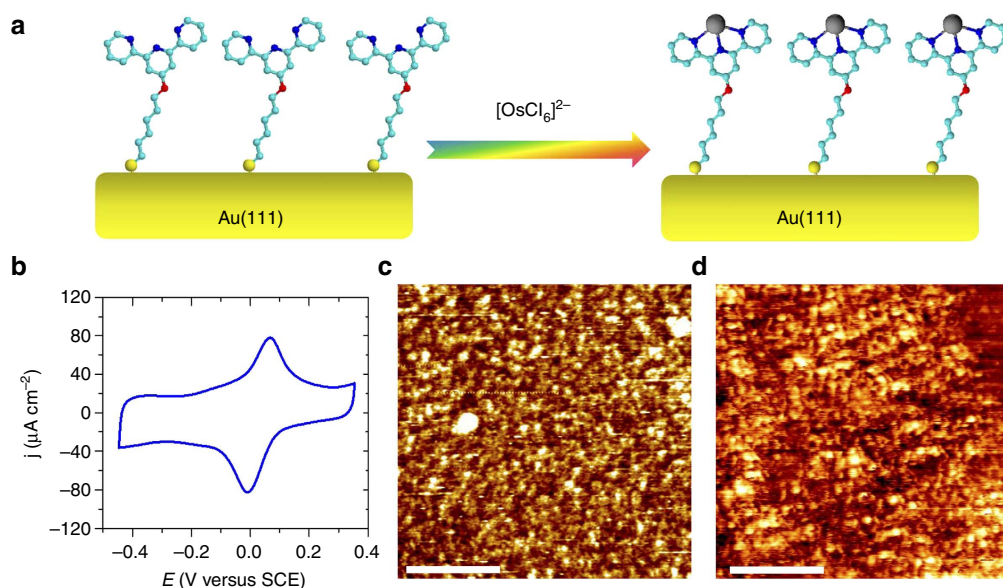


Figure 1 | Surface self-assembly and characterization of terpy ligands. (a) Schematic illustration of terpy molecules self-assembled on a Au(111) surface and the coordinative binding of Os ions (not drawn to scale). (b) Cyclic voltammogram of Os-terpy SAMs obtained with a scan rate of 1 V s^{-1} . (c) An AFM image and (d) a STM image of Os-terpy SAMs on Au(111) surfaces, recorded by ECAFM and ECSTM in phosphate buffer (10 mM, pH 7.0). The STM image recorded with the key parameters: $I_t = 20\text{ pA}$, $V_b = -0.4\text{ V}$, $E_w = -0.02\text{ V}$ (versus SCE). Scan areas: (c) $1,000\text{ nm} \times 1,000\text{ nm}$ and (d) $100\text{ nm} \times 100\text{ nm}$. Scale bar, 250 nm (c) and 25 nm (d).

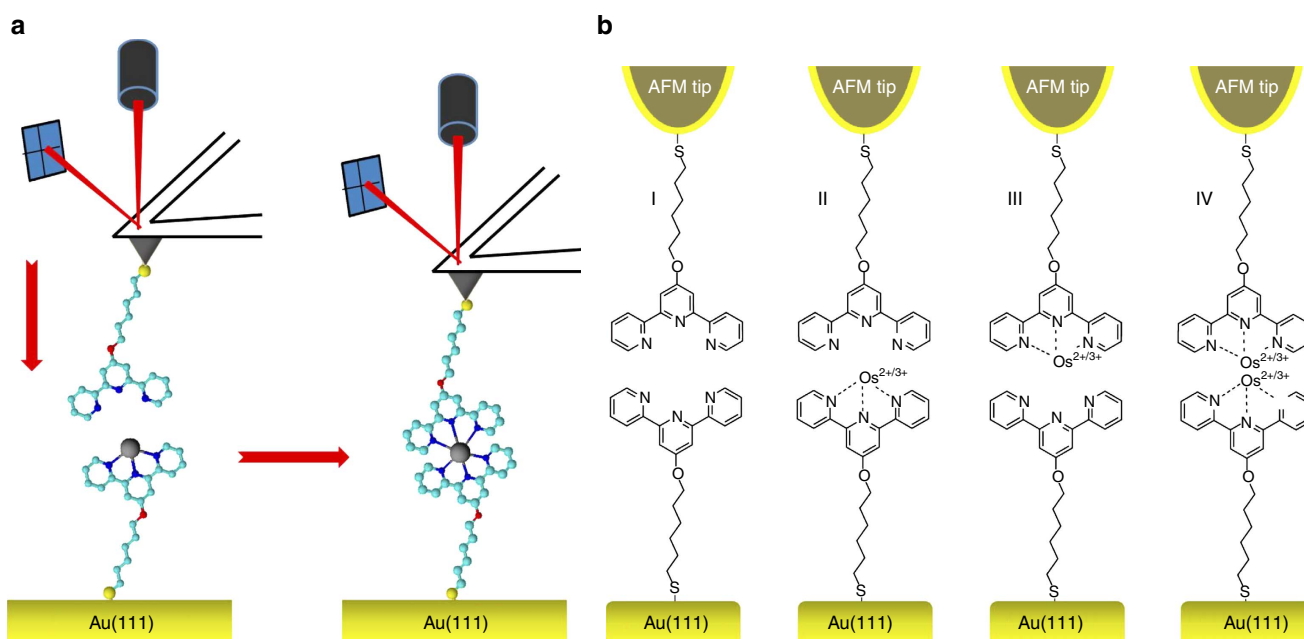


Figure 2 | AFM force spectroscopy and designed experimental configurations. (a) Schematic illustration of measurement principles of the AFM force spectroscopy for the Os-terpy complex. The cantilever deflection is determined by the position of a reflected laser beam and translated into an interaction force transmitted via the samples. The ligand-functionalized tip approaches the sample and is brought to interact with the sample. (b) Schematic illustrations of four types of experimental configurations for measurements of force spectra: (I) absence of Os ions, (II) Os ions pre-bound to the Au(111) substrate, (III) Os ions pre-loaded on the AFM tip and (IV) Os ions pre-loaded on both the substrate and AFM tip.

single force peaks in most cases (Fig. 3a(II),a(III)). Single force peaks suggest that coordination interaction is most likely detected at the single-molecule level, although they do not exclude several possible interactions occurring simultaneously. The peak widths are in the range of only a few nm reflecting convolution with the cantilever motion (Fig. 3). Multiple peaks are only observed in

very few cases, with a probability not more than 5–8% among the featured force spectra. This observation is likely owing to multiple terpy molecules at an AFM tip interacting with the sample occasionally. Owing to low probability and to simplify the data analysis, the force spectra with multiple peaks were not included in our statistical analysis. In addition, it is a challenge to

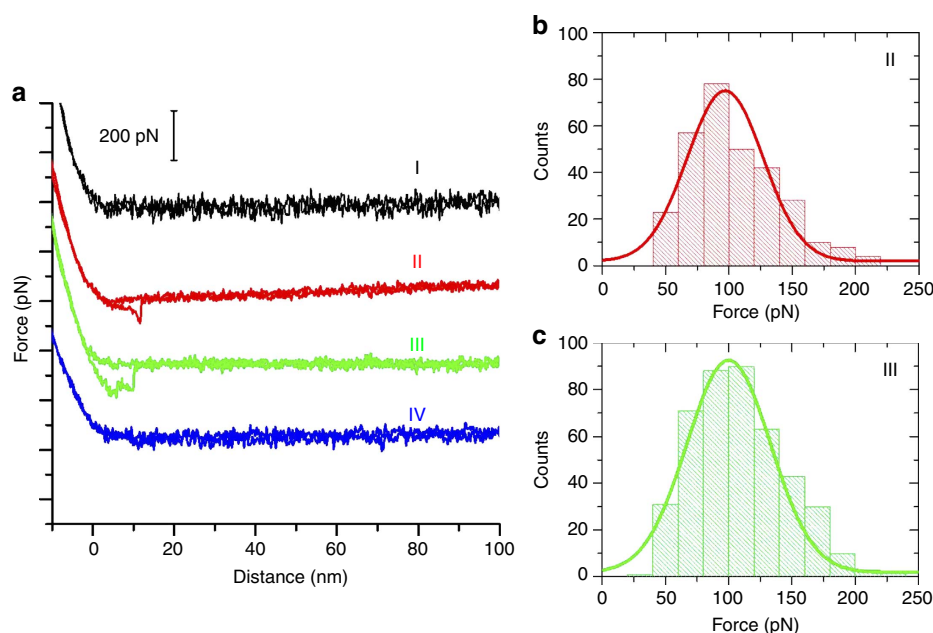


Figure 3 | Single-molecule force spectra in different experimental configurations. (a) Comparison of typical force-extension curves for the four experimental configurations shown in Fig. 2b. The loading rate (LR) of 200 nm s^{-1} was used in recording all the curves. (b,c) The histograms of coordinative force distributions for configurations (II) and (III). The average force is estimated as $97 \pm 35 \text{ pN}$ ($n = 300$) for configuration II and $100 \pm 40 \text{ pN}$ ($n = 432$) for configuration III.

distinguish specific interactions from unspecific ones in some systems. The coordination interaction is regarded as a kind of specific interaction. However, it is unknown to which extent the specificity stands, if compared with the conventional specific interactive systems such as antigen–antibody, substrate–enzyme and ligand–receptor. For example, the same ligand (for example, terpy) can coordinate with various metal ions such as Os, Ru, Zn, Mn and Fe, although with different bonding strength. However, we have designed four experimental configurations as illustrated in Fig. 2b. The results from these configurations show that only configurations II and III yield the featured force spectra, arising from the coordinative interactions. There is no (or extremely few) force spectra with features obtained for configurations I and IV from different batches of samples measured.

Statistical analyses based on hundreds of force curves for each case show that the average force is $100 \pm 40 \text{ pN}$ (Fig. 3b,c), virtually identical for configurations (II) and (III). This value compares well with that for the terpy–Ru system (95 pN , no potential control)²⁷, but is significantly lower than for a covalent bond. For example, previous AFM studies showed that the C–Si bond breaks at 2.0 nN (ref. 17), the Si–Si bond at 2.1 nN (ref. 20) and the Au–S bond at 2.5 nN (ref. 28). The strength of the Os–terpy coordinative bonding is thus about 5% of that for a covalent bond. The coordinative bonds have long been regarded as a special kind of covalent bonds in coordination chemistry. However, it is unknown how strong a coordinative bond should be. The 100 pN force is surprisingly small at first glance. However, the AFM-induced ligand substitution process cannot be regarded solely as a dissociation process. Ligand substitution is instead synchronous dissociation of the outgoing terpy ligand and association of incoming ligands, presumably water molecules to complete the coordination sphere. This notion is supported by the DFT computations, which is described below.

Redox-state-dependent coordinative bonding forces. ECAFM is capable of controlling the redox state of a transition metal

complex and recording force spectra, simultaneously. This ability offers the possibility to explore how the redox state of the metal atom impacts on the bond strength of metal–ligand coordination. In the present case, the Os–terpy SAM is electroactive and its redox state can be controlled by electrochemical potentials applied to the substrate. As recorded by voltammetry (for example, Fig. 1b), the formal redox potential (that is, in the equilibrium redox state) is around $+40 (\pm 5) \text{ mV}$ (versus saturated calomel electrode (SCE)). The observed redox potential accords well with that of the redox pair $\text{Os}^{2+/3+}$ partially coordinated to polypyridine ligands^{10,11}. A large number of force–distance curves for coordinative bonding at different substrate-working potentials were recorded and statistically analysed.

Figure 4a compares typical AFM force spectra recorded at $+185$, -15 and -215 mV , respectively. The corresponding histograms are shown in Fig. 4b–d. In the fully oxidized form (that is, the working potential applied at $+185 \text{ mV}$), the coordinative bonding force was found to be as high as 190 pN , with an average force around 130 pN . The force decreased to about 100 pN , when the Os–terpy complex was partially reduced at -15 mV . The coordinative bonding was further weakened to 80 pN at -215 mV where the complex was in its fully reduced form. More force spectra were recorded at various working potentials and statistically analysed, and the corresponding histograms are shown in Supplementary Fig. S9. The dependence of the average forces on working potentials is shown in Fig. 4e. The redox-state-dependent transition is thus systematic from the fully reduced form to the fully oxidized form, with a sigmoid-like (that is, ‘S’ form) dependence.

As the pioneering introduction of the method by Hinterdorfer *et al.*³⁴, the loading rate (LR)-dependent AFM force spectroscopy has offered an effective approach for estimating key parameters that characterize single-molecular interaction events. The method has been used for a wide range of chemical and biological systems^{35–38}, although in some cases the parameters estimated could differ by an order of magnitude even for the same systems.

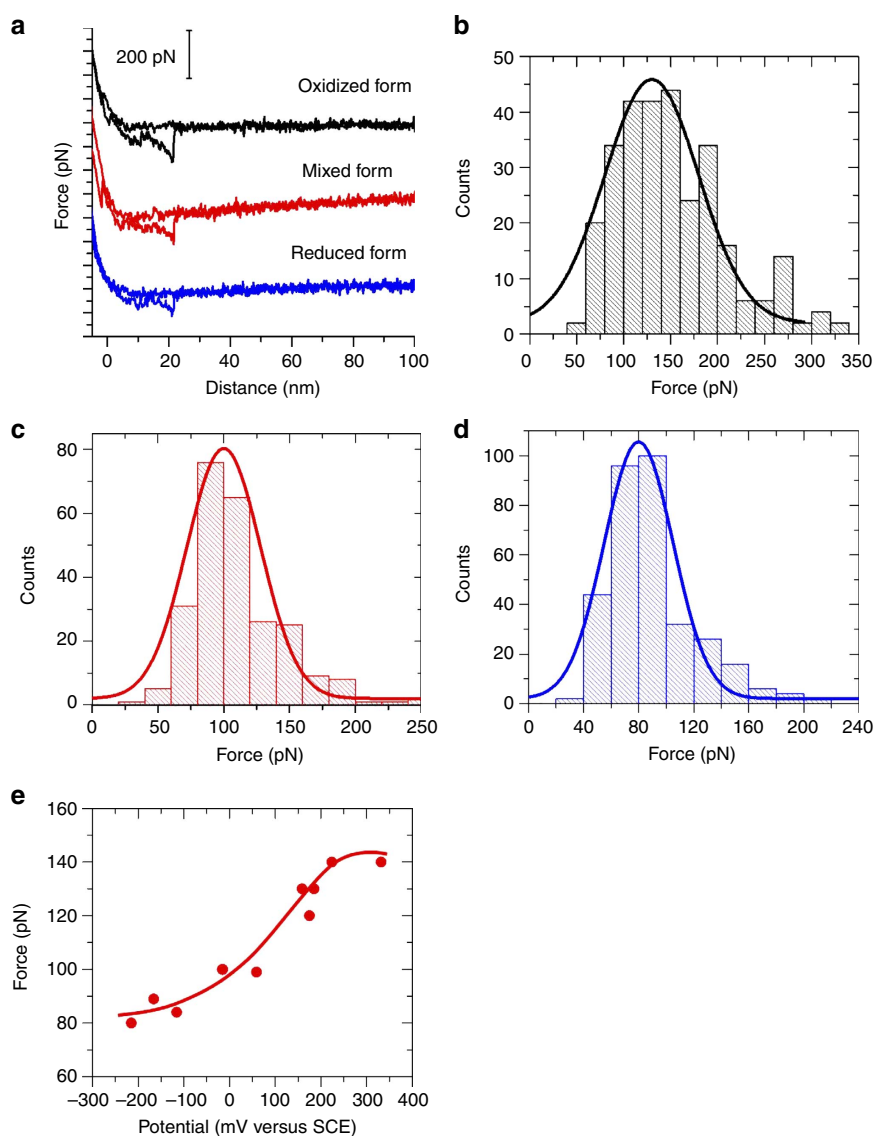


Figure 4 | Transition metal redox-state-dependent coordinative forces. (a) Comparison of typical force-extension curves for interactions between Os-terpy-C6-S-Au(111) substrates and terpy-C6-S-tips (that is, configuration II) at different working potentials (versus SCE) of +185 mV (fully oxidized state), -15 mV (partially reduced but close to the equilibrium form) and -215 mV (fully reduced form). The LR was 200 nm s⁻¹. (b-d) Corresponding histograms of coordination force distributions. The average force based on statistical analyses is: (b) 130 ± 60 pN (*n* = 292) at +185 mV, (c) 100 ± 30 pN (*n* = 250) at -15 mV and (d) 80 ± 30 pN (*n* = 328) at -215 mV. (e) The dependence of average unbinding forces on the redox states controlled by the working potentials; the data used are the average values of three or four sets of independent experimental measurements.

Our AFM measurements were focused on the LR-dependent force spectra at three different oxidation states of the Os-terpy complex. On the basis of statistical analyses of thousands of force spectra, the dependences of the average forces on LRs are presented in Fig. 5. According to the single barrier model, the correlation between the breaking (or unbinding) force and the LR is rationalized by the approximate form (equation 1)^{38,39}.

$$F_u = \frac{k_B T}{\chi_\beta} \ln r + \frac{k_B T}{\chi_\beta} \ln \left(\frac{\chi_\beta}{k_B T k_{\text{off}}} \right), \quad r = k_{\text{eff}} v \quad (1)$$

where F_u is the unbinding force, χ_β is the separation distance (energy barrier) from the equilibrium position, r is the LR, k_{eff} is the effective spring constant of the AFM cantilever used, v is the AFM cantilever retraction velocity, k_{off} is the dissociation kinetic rate constant at zero force, k_B is the Boltzmann constant and T is the Kelvin temperature.

The parameters χ_β and k_{off} can thus be estimated from the slope and intercept of the plot of measured force versus LR, respectively (see for example Fig. 5). A recently reported approach was used to estimate the binding kinetic rate constant (k_{on})³⁷. The apparent dissociation constant (K_d) or affinity constant (K_a) can then be obtained by Equation 2:

$$K_d = k_{\text{off}}/k_{\text{on}} \text{ or } K_a = k_{\text{on}}/k_{\text{off}} \quad (2)$$

furthermore, the activation Gibbs energy (ΔE_a) for dissociation of coordination bonding in different redox states is compared, based on their k_{off} values. The smaller the k_{off} value, the higher the dissociation activation free energy. In order to compare the dissociation activation free energy in different redox states, we define the dissociation activation free energy needed for the oxidized form ($(\Delta E_a)_{\text{Ox}}$) as a unit. The relative activation free energy for the equilibrium ($(\Delta E_a)_{\text{Eq}}$) and reduced ($(\Delta E_a)_{\text{Re}}$)

states is thus obtained using the following relations³⁸.

$$(\Delta E_a)_{\text{Eq}} = -k_B T \ln \left(\frac{k_{\text{off}}(\text{Eq})}{k_{\text{off}}(\text{Ox})} \right) \quad (3)$$

$$(\Delta E_a)_{\text{Re}} = -k_B T \ln \left(\frac{k_{\text{off}}(\text{Re})}{k_{\text{off}}(\text{Ox})} \right) \quad (4)$$

The parameters estimated are summarized in Table 1. These crucial parameters have re-enforced the systematic effects of the redox state on coordinative interactions observed by direct comparison of forces (Fig. 4e), but with more details provided. While all parameters point to the same tendency towards the redox-state effects, their sensitivity and extents could be quite different. The k_{off} values provide a clear distinct by at least a factor of 3 between the fully oxidized and reduced states. The K_d

(or K_a) values are observably different among the redox states, but they are significantly larger than those obtained by traditional average ensemble approaches to terpy-based transition metal complexes in homogenous solution. There are no K_d data available for Os-terpy, but for other transition metals (for example, Mn, Co, Ni, Cd and Fe) K_d is in the range of 10^{-8} to 10^{-3} M, depending on solution pH, ionic strength and the presence or absence of other ligands^{40,41}. On the one hand, the discrepancy could be in part owing to high uncertainty in the estimates of parameter k_{on} by AFM, as also noted by previous reports on other systems³⁴⁻³⁷. On the other hand, a direct comparison is not appropriate because the K_d values are estimated under very different experimental conditions in AFM and in homogenous solution. In homogenous aqueous solutions, the dissociation of the complex occurs spontaneously in the free state. In the AFM configuration, the Os-terpy complex is immobilized on an Au(111) surface and its dissociation is induced by external mechanic forces (that is, through retraction of the AFM cantilever). Direct comparison for other systems has posed similar challenges³⁴⁻³⁸. The relative values of the parameters estimated by AFM force spectroscopy within the same system under different experimental conditions are thus more meaningful. The differences in the dissociation activation free energy are notable but not significant. Nevertheless, in the present case these parameters have offered a possibility of quantitative views on the redox-state-dependent coordinative interactions at the single-molecule level.

The redox-state effects are thus significant. While detailed reasons are not fully understood at present, the different forces reflect higher bonding strengths for Os^{3+} than for Os^{2+} . Earlier DFT studies for a terpy analogue (2,2'-bipyridine) showed that structural changes caused by the central metal redox state switching are insignificant, when the complex is immobilized on Au(111) surfaces^{42,43}. The Os-terpy σ bonding might be stronger for Os^{3+} than for Os^{2+} but this would be counterbalanced in part by relatively poorer π -back donation in the oxidized state. The electronic charge distribution over the complex is different in the two redox states, as charge is relocated from the periphery of the complex to the metal upon oxidation^{42,43}. Besides, different ligand field stabilization energies (LFSEs) could be a factor. The LFSE is higher for $\text{Os}^{2+} d^6$ than for $\text{Os}^{3+} d^5$ in fully hexacoordinated $[\text{Os}(\text{terpy})_2]^{2+/3+}$. The relatively low oxidation potentials observed suggest, however, that full tri-dentate coordination of both terpy ligands is unlikely. Instead, the coordination of residual $\text{H}_2\text{O}/\text{OH}^-$ ligands could lower the oxidation potential and results in a higher LFSE for Os^{3+} than for Os^{2+} . To understand the key factors determining the coordinative bonding strength, we performed DFT modelling and computations.

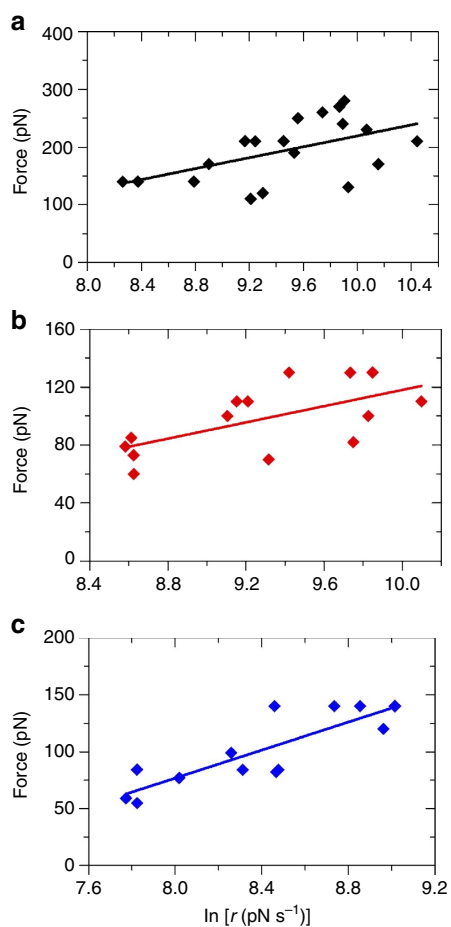


Figure 5 | Dependence of coordinative unbinding forces on LRs. (a) In the oxidized state (+224 mV versus SCE). (b) In the equilibrium state (+37 mV versus SCE). (c) In the reduced state (-166 mV versus SCE). The solid lines represent the best linear fits to the experimental data.

DFT computations of coordination pulling force. DFT modelling was focused on the different bond rupture forces in the oxidized and reduced forms of the complex and the crucial roles of terpy/ H_2O ligand substitution in the bond rupture process.

Table 1 | Comparison of the crucial parameters characterizing Os-terpy coordinative interactions in different oxidation states.

Redox states	$k_{\text{off}}(\text{s}^{-1})$	$k_{\text{on}}(\text{M}^{-1}\text{s}^{-1})$	Stability constant		Relative $\Delta E_a(k_B T)$	$x_\beta(\text{nm})$
			$K_d(\text{M})$	$K_a(\text{M}^{-1})$		
Oxidized form (at +224 mV)	4.5	41	0.11	9.1	—	0.09
Equilibrium (at +37 mV)	11.6	24	0.48	2.1	-0.95	0.15
Reduced form (at -166 mV)	13.9	18	0.77	1.3	-1.13	0.07

Before the direct approach to the pulling forces, the potential energy surfaces of the terpy and H₂O ligand deformation and the electronic structures of the complexes were calculated using the following scheme. The potential energy surface of the terpy ligand was first calculated by rotating two pyridine end units through a whole cycle (Supplementary Fig. S10). The results show that terpy favours a planar geometry, with the two end pyridines in *trans*-configuration relative to the middle pyridine (that is, N↑N↓N↑). The energy cost for rotating a single pyridine unit, converting the pyridines to the *cis* configuration (that is, N↓N↓N↓) is about 0.3 eV, consistent with previous reports⁴⁴. Almost the same energy is required to rotate the second pyridine unit. As a consequence, in terms of energy, the *cis* N↓N↓N↓ configuration is 0.6 eV less stable than the *trans*-configuration. The conjugation properties are not affected by the orientations of the terpy nitrogen atoms because the energy cost is rooted mainly in steric or electrostatic repulsions between the charged nitrogens. This is supported by Bader analysis (Supplementary Fig. S11).

The magnetic properties of the complex were addressed next. Possible low- and high-spin states for Os²⁺ (d⁶) are 0 and 2, and 1/2 and 5/2 for Os³⁺ (d⁵). The energies were calculated for the Perdew–Burke–Ernzerhof (PBE)-relaxed structures of [Os(terpy)₂(H₂O)_n]^{2+/3+} complexes (Fig. 6a) as well as for [Os(terpy)(H₂O)₃]^{2+/3+} and [Os(OH₂)₆]^{2+/3+}. Low-spin states were considerably more stable than high-spin states in all cases, with very similar $\Delta E_{\text{HS/LS}}$ differences for PBE, PBE0 and B3LYP. $\Delta E_{\text{HS/LS}}$ for [Os(OH₂)₆]³⁺ is calculated as 4.3 to 4.5 eV, which is higher but in the same range as 2.3 eV compared with Os³⁺ fully coordinated to two terpy ligands. Bader analysis of Os^{2+/3+}(terpy) fragments was used as a reference (Supplementary Fig. S11). The resulting electron distribution is reasonable. For example, all nitrogen donor atoms are negatively charged with a full lone pair, which explains why the *trans*-configuration is favoured. The charge is acquired mainly from neighbouring carbon atoms. The oxygen donor atoms are also negatively charged, with the bulk of the charge donated by the ligand hydrogen atoms. The positive charge on the hydrogen atoms is fractional, varying from 0.10 to 0.05. Notably the electron distribution at the terpy nitrogen, oxygen and carbon atoms is not significantly perturbed by addition of osmium in either of the two oxidation states. Oxidation of Os²⁺ to Os³⁺, however, results in shared electron donation from the metal centre and terpy ligand, that is, with Os further donating half an electron to the ligand. The rest of the holes are distributed in the whole conjugated system, mainly registered as a slight loss of charge on the aromatic hydrogen atoms with the average charge being 0.15 and 0.20 per hydrogen atom, for the Os²⁺ and Os³⁺ redox states, respectively.

With the electronic and molecular structures available, the Os^{2+/3+} pulling energy was simulated in a final stage. Only very small structural differences between the octahedral [Os(terpy)₂]²⁺ and [Os(terpy)₂]³⁺ were found. The Os–N bond length at the middle pyridine unit is around 2.01 Å for both redox states. The other two Os–N bond lengths are slightly different, that is, about 2.10 and 2.05 Å for Os²⁺ and Os³⁺, respectively. A reference structure was created by relaxing all structures during bond-breaking simulations at a charge of 2.5. The simulations were then started from relaxed geometries of the complexes with varying coordination to terpy and water molecules (Supplementary Information Fig. S12), shifting the middle pyridine unit away within 0.2 Å increments. At each increment, the middle Os–N distance was fixed, while all other degrees of freedom were allowed to relax with the same criteria (0.05 eV Å⁻¹). Figure 6a and Supplementary Fig. S13a show three simulated target configurations. The pulling energies ($E - E[\text{dr}_{\text{Os-N}} = 0]$) for each configuration were calculated and

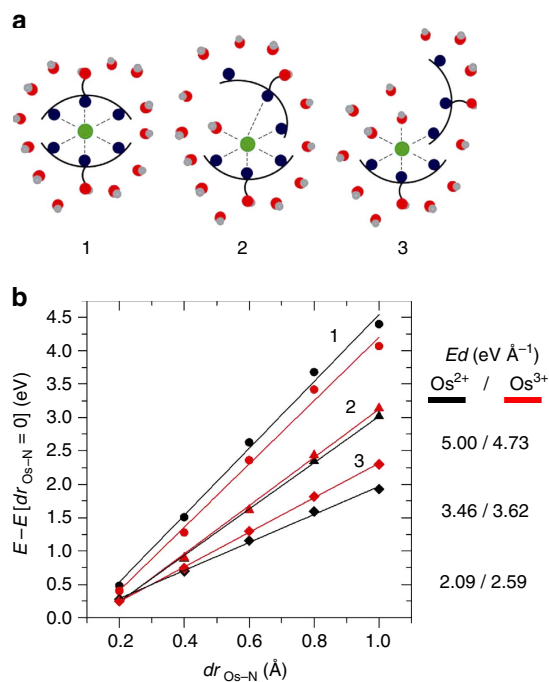


Figure 6 | DFT simulations of the bond-breaking pulling forces in solution environments. (a) Schematic illustrations of the target bond-breaking systems. Three initial configurations examined in the two oxidation states are: (1) [Os(terpy)₂] is osmium in octahedral ligand environment provided by the nitrogen atoms (blue) of two terpy molecules. (2) [Os(terpy)₂(H₂O)] is coordinated to a second terpy molecule through two nitrogen atoms. The non-bonding group is rotated by about 90°, allowing coordination of a water molecule. (3) [Os(terpy)₂(H₂O)₂] is osmium coordinated to a single nitrogen atom of the second terpy ligand, with two water molecules occupying the coordination sites. The middle pyridine unit of terpy was systematically moved by 0.2 Å increments. At each increment, the Os–N distance (of the middle pyridine unit) was kept fixed and all other degrees of freedom allowed to be relaxed. A notable side reaction was the transfer of a proton from a water ligand to a non-coordinated nitrogen of terpy. (b) Potential energy changes of the simulated bond-breaking systems in aqueous solution. Solid lines are linear best fits to the calculated data for Os²⁺ (black lines) and Os³⁺ (red lines), respectively. The slopes were obtained from these linear fits, and the values are listed in the right panel of b. It is clear that the Os²⁺ state favours full binding to terpy, but as water occupies coordination sites the terpy–Os³⁺ bond becomes the stronger. It is noted that the energy starts to level off when the Os-to-terpy distance is beyond 1.0 Å.

plotted against the Os–N distance ($\text{dr}_{\text{Os-N}}$) for both redox states. The change in bond length is not shown beyond 1 Å, which is where the terpy–Os bond starts to break. Notably, proton transfer between a water molecule and a terpy nitrogen atom occurs in some cases, giving a step in the potential energy curve.

The pulling force was evaluated as the slopes of the best linear fits (Fig. 6b and Supplementary Fig. S13) in the energy profile. The slope is steeper, that is, the pulling force stronger when terpy is fully coordinated to Os²⁺, but this changes dramatically when a single or two water molecules are coordinated (Supplementary Fig. S13b). There is then a clear difference in the energy change for the two redox states, with Os³⁺ showing considerably stronger bonding and stronger bond force with two water molecules each occupying a coordination site. The calculated forces thus accord qualitatively with the experimental data and is proposed as the most favourable coordination of Os^{2+/3+} to terpy under the experimental conditions. It is noted that the

quantitative values of the calculated pulling forces are significantly stronger than those observed (that is, nN versus pN). This discrepancy is presumably owing to limitations of the present model. Full coordination would both involve several reorganization steps and more vigorous conditions, and reverse the stability order in favour of Os^{2+} .

To make the simulations closer to the experimental conditions, a solvation shell of 25–30 water molecules around each complex was added. The water molecules were allowed to relax around the complex (Supplementary Fig. S12) and calculations for both redox states in each configuration were carried out. The relation between the pulling energy and the Os–N distance is shown in Fig. 6b. Compared with vacuum (Supplementary Fig. S13b), the addition of a single solvation shell does not change the trend in the relative pulling energy but enhances notably the coordinative bond strength of Os^{3+} (Fig. 6b).

Overall, the DFT simulations suggest the following: the potential surfaces of terpy show that the $\text{N}\uparrow\text{N}\downarrow\text{N}\uparrow$ configuration is favoured over $\text{N}\downarrow\text{N}\downarrow\text{N}\downarrow$; the terpy carbon and hydrogen atoms carry a considerable positive charge; beyond 1 Å where the Os–terpy bond breaks, terpy promotes proton transfer from a H_2O ligand forming a terpy (H^+)– OH^- ligand pair; the terpy nitrogen atoms are negatively charged, but OH^- carries the largest negative charge and interacts more strongly with Os^{3+} than with Os^{2+} ; and the redox state of Os significantly affects the bonding strength. Os^{2+} favours full ligation to terpy, probably owing to larger ligand field stabilization, while Os^{3+} favours coordination to one or two terpy ligands, with the other ligand sites occupied by water. Solvation finally enhances the bond strength and pulling force of Os^{3+} , and favours ligand binding of Os^{3+} over Os^{2+} . The latter accords with the experimental data and points to the crucial role of ligand substitution in the pulling process; although as noted, quantitative accordance requires a more comprehensive computational scheme with full incorporation of the solvent.

Discussion

Coordination interaction is a very broad area in chemistry, because more than half of the elements in the periodic table are transition metals, the chemical properties of which are dominated entirely by coordination chemistry. ET and ligand substitution reactions represent the two major classes of reactivity of transition metal complexes with crucial applications in catalysis, molecular electronics and medical chemistry. However, most studies in coordination chemistry, including metal-binding free energies and enthalpies, and bond association/dissociation kinetics, are based on average and ensemble level approaches.

While studies on ET of transition metal complexes have been conducted intensively (including single-molecule approaches by STM and related techniques), the present work aims to address the other major class, namely ligand substitution processes at the single-molecule level. Such an approach has not been reported before for ligand–metal interactions in controlled oxidation states of the central metal ion and represents therefore a new exploration in coordination chemistry.

In this work, single-molecule force analysis has been achieved by combining several interdisciplinary tools, particularly including ligand design and synthesis, surface self-assembly chemistry, single-crystal electrochemistry, STM imaging, and high-resolution electrochemical AFM force imaging and spectroscopy. The proof-of-concept study is a major focus of this work and has been illustrated well by the Os–terpy systems. The Os–terpy bonds are ruptured at 100 ± 30 pN at open circuit potentials, but at 130 ± 60 pN in the oxidized state of the central metal and at the lower value of 80 ± 30 pN in the reduced state. A remarkable

effect of the redox state on the coordinative bonding is thus experimentally observed. Such effects are further detailed by the crucial parameters obtained, relevant to the coordinative bonding and dissociation processes.

The different pulling forces in the two oxidation states are rationalized by DFT simulations. The computational procedures are rigorous, though the models used at this stage are relatively crude as the bulk solvation is either disregarded or represented by a single solvation shell only. The emerging pulling forces, however, still disclose clearly the kinematic and electronic nature of the molecular scale pulling events, and the subtle interplay between bond stretching and terpy/ H_2O ligand substitution that controls the process. The latter is a rationale even for the qualitative observations. The quantitative values of the emerging pulling forces are still significantly stronger than those observed (nN rather pN ranges) but the accordance can be expected to change drastically by full scale incorporation of solvent molecular assemblies that incorporate both the dynamics of the accompanying terpy/ H_2O ligand substitution and longer-range solvation. Such a study is in progress.

The overall approach demonstrated in this work represents a critical advancement in studying coordination chemistry at the single-molecule level. The observations should add new insight to our understanding of the physicochemical nature of coordinative bonds. The method is expected to apply generally to other transition metal complexes and to impact coordination chemistry and related areas broadly.

The AFM force spectroscopy has shown that a metal–ligand coordinative bonding strength is only equivalent to about 5% of that for a covalent bond. This value appears to be surprisingly smaller than expectation from our traditional understanding of metal–ligand interactions in coordination chemistry, where coordinative bonds are considered as a kind of special covalent chemical bonds. These AFM studies have thus raised several interesting but challenging questions such as: how strong a metal–ligand coordination bond should be; what we can learn more about the physicochemical nature of metal–ligand bonding; and how much external conditions such as solution pH, ionic strength and type of transition metals could affect metal–ligand interactions. These questions would promote refined research in the near future, for example, by systematic design and synthesis of various ligands, including mono-, bi-, tri- and multi-binding sites, and by exploring other transition metals as well as introduction of other complementary tools in addition to AFM.

Methods

Chemicals and reagents. Potassium hexachloro-osmate(IV) with high purity (99.99%) from Aldrich and 2,2': 6',2''terpyridine (99%) from Sigma were used as received. Electrolyte solutions (10 mM, pH 7.0) were prepared from KH_2PO_4 (Sigma-Aldrich, ultrapure 99.99%) and K_2HPO_4 (Fluka, ultrapure 99.99%). KOH (ultrapure 99.99%) obtained from Sigma-Aldrich was used for the experiments of reductive desorption. Absolute ethanol (EtOH) (Ultrapure, Sigma-Aldrich) was used as a solvent for preparation of terpy solutions. Millipore water (18.2 M Ω) was used throughout.

Synthesis and characterization of terpy ligands. Terpy with a 4'-(6-acetylthiohexyloxy) linker group (Supplementary Scheme S1), denoted as terpy- $\text{C}_6\text{-SAC}$, was synthesized by reference to a previously reported procedure with modification^{45,46}, and its structure and chemical properties were systematically characterized. Briefly, to a solution containing compound 1 (1 g, 4 mmol) and anhydrous powdered K_2CO_3 (1.1 g, 8 mmol) in anhydrous dimethylformamide (20 ml), compound 2 (1.72 g, 7.22 mmol) was added. The solution was heated to 70 °C and stirred for 24 h. The reaction mixture was then cooled down, poured into 100 ml of water and subjected to extraction with dichloromethane three times. The combined organic layers were dried over MgSO_4 , filtered and evaporated under reduced pressure. The spectroscopically clean product was obtained after column chromatography (Al_2O_3 , Hex:EA (4:1)) and following recrystallization from

ethanol (1.3 g, 3.2 mmol, yield: 80%). The chemical reaction is illustrated in Supplementary Fig. S15.

Preparation of terpy monolayers on Au(111) surfaces. To prepare the SAMs on substrate Au(111) surfaces and AFM cantilevers, as-synthesized terpy-C₆-SAC solid was dissolved in ultrapure ethanol (EtOH) to prepare the solutions with the concentration range of 0.05–5 mM. For example, about 5 mg terpy-C₆-SAC was dissolved in 5 ml EtOH, leading to a concentration of about 0.5 mM. SAMs were formed by immersing the freshly annealed and hydrogen flame-quenched Au(111) substrates and clean gold-coated AFM tips in terpy-C₆-SAC solutions. After surface modification, the samples were removed from the terpy solution, followed by rinsing with EtOH, Milli-Q water and buffer solution. The samples were then immersed in [OsCl₆]²⁻ containing aqueous solutions (ca. 2 mM) for 3 h. Excess metal compound was removed by rinsing with Milli-Q water. The adsorption time for formation of SAMs on Au(111) surfaces was systematically studied in the range of 2 h to overnight (20 h) with different concentrations of terpy-C₆-SAC solutions. It was found that the closely packed SAM was formed, only when the terpy-C₆-SAC concentration is higher than 3 mM with an overnight adsorption. The effective surface concentration of Os-terpy SAMs on Au(111) surfaces is $9.0 (\pm 0.8) \times 10^{-11} \text{ mol cm}^{-2}$, which was used in most AFM force spectroscopic measurements.

Electrochemistry measurements. Cyclic voltammograms were recorded using a 15 ml, three-compartment cell containing phosphate buffer (10 mM, pH 7.0) as electrolyte solution. A freshly prepared reversible hydrogen electrode served as reference electrode and a Pt wire as counter electrode, respectively. The electrolyte solution was degassed with pure Argon for 1 h before electrochemical experiments. All voltammetric measurements were carried out at room temperature ($23 \pm 2^\circ\text{C}$), using an Autolab PGSTAT12 system controlled by the GPES 4.9 software (Eco Chemie, Netherlands). The reference electrode was calibrated against a SCE after each experiment. All electrochemical potentials are reported versus SCE in this work. Experimental procedures for the pretreatment of Au(111) electrodes and single-crystal electrochemical measurements were similar to those used in our previous reports^{47,48}.

STM imaging. A PicoSPM (Molecule Imaging, USA) including *in situ* STM microscope was used. Au(111) disk electrodes (1.2 cm in diameter) were used as *in situ* STM substrates. A Teflon house-built liquid STM cell, equipped with reference and counter electrodes, was used throughout. The reference electrode was calibrated against a SCE after each experiment. Electrochemically etched Pt/Ir tips (80/20, 0.25 mm in diameter) coated with Apiezon wax served as scanning probe. STM samples were prepared as described above. The detail of experimental procedures on the pretreatment of single-crystal Au(111) substrates and STM imaging can be further referred to our previous reports^{47,48}.

AFM force imaging and spectroscopy. AFM imaging and force spectroscopic measurements were carried out using a Scanning Probe Microscope (Model 5500, Agilent Technologies, Chandler, AZ). The Os-Tpy SAMs on Au(111) were imaged in an AAC (Acoustic Alternating Current) mode AFM. Oxide-sharpened Si₃N₄ probes (Veeco, SNL) with a spring constant of 0.06 N m^{-1} were applied, mostly suitable for the soft organic adlayers. The typical radius of the SNL tip is about 2–10 nm (Manufacturer's homepage). Imaging amplitude was set between 2.0 and 2.5 V. The scanner was calibrated using a Veeco 10- μm pitch calibration grating, each square with a 200 nm depth. Scanning speed was 1.6 Hz. For single-molecule force spectroscopy experiments, an in-house-built electrochemical cell was applied for control of the sample potentials. Each individual gold-coated cantilever used was calibrated in solution using the equi-partition theorem before each experiment to obtain the spring constant (k_{eff}) (with a typical value around 105 pN nm^{-1}). All experiments were carried out at room temperature ($23 \pm 2^\circ\text{C}$) in phosphate buffer (10 mM, pH 7) at a given approaching and pulling speed (for example, 200 nm s^{-1}). Totally over 100 gold-coated AFM cantilevers were used in the AFM experiments. The measurements under each experimental condition were repeated at least three times independently with 4–5 tips used in each set of measurements. Different areas of each sample were measured and the areas were changed after about 50 data points were collected for force spectra.

DFT modelling and computations. All calculations were performed with the real-space Grid-based projector augmented-wave DFT code^{49,50}. Kohn–Sham states were represented in terms of numerical atom centred orbitals of the double- ζ with polarization quality (DZP). The potential was expressed on a real-space grid with $0.18 (\pm 0.01) \text{ \AA}$ grid point spacing. The exchange-correlation (xc) energy was approximated using the PBE functional⁵¹, and the core electrons were described with the PAW method⁵². All structural relaxations were performed with a quasi-Newton scheme at a maximum force tolerance of 0.05 eV \AA^{-1} . Magnetic structures of the two redox states were, furthermore, also analysed with the hybrid-GGA xc-functionals PBE0⁵³ and B3LYP⁵⁴. The charge density of the system was calculated using Bader analysis^{55,56}, which gives localized charges for each atom in the specific system.

References

- Bowman-James, K. Alfred Werner Revisited: the coordination chemistry of anions. *Acc. Chem. Res.* **38**, 671–678 (2005).
- Gispert, J. R. *Coordination chemistry* (Wiley VCH, 2008).
- Claridge, S. A., Schwartz, J. J. & Weiss, P. S. Electrons, photons, and force: quantitative single-molecule measurements from physics to biology. *ACS Nano*. **5**, 693–729 (2011).
- Tao, N. J. Electron transport in molecular junctions. *Nat. Nanotech.* **1**, 173–181 (2006).
- Nichols, R. J., Haiss, W., Higgins, S. J., Leary, E., Martin, S. & Bethell, D. The experimental determination of the conductance of single molecules. *Phys. Chem. Chem. Phys.* **12**, 2801–2815 (2010).
- Zhang, J. *et al.* Single-molecule electron transfer in electrochemical environments. *Chem. Rev.* **108**, 2737–2791 (2008).
- Dupres, V., Verbelen, C. & Dufrene, Y. F. Probing molecular recognition sites on biosurfaces using AFM. *Biomaterials* **28**, 2393–2402 (2007).
- Müller, D. J. & Duferene, Y. F. Atomic force microscopy as a multifunctional molecular toolbox in nanobiotechnology. *Nat. Nanotech.* **3**, 261–269 (2008).
- Müller, D. J., Helenius, J., Alsteens, D. & Duferene, Y. F. Force probing surfaces of living cells to molecular resolution. *Nat. Chem. Biol.* **6**, 383–390 (2009).
- Salvatore, P., Hansen, A. G., Moth-Poulsen, K., Bjørnholm, T., Nichols, R. J. & Ulstrup, J. Voltammetry and *in situ* scanning tunneling spectroscopy of osmium, iron, and ruthenium complexes of 2,2':6',2''-terpyridine covalently linked to Au(111)-electrodes. *Phys. Chem. Chem. Phys.* **13**, 14394–14403 (2011).
- Albrecht, T., Guckian, A., Ulstrup, J. & Vos, J. G. Transistor-like behavior of transition metal complexes. *Nano Lett.* **5**, 1451–1455 (2005).
- Albrecht, T., Moth-Poulsen, K., Christensen, J. B., Hjelm, J., Bjørnholm, T. & Ulstrup, J. Scanning tunneling spectroscopy in an ionic liquid. *J. Am. Chem. Soc.* **128**, 6574–6575 (2006).
- Chi, Q., Zhang, J., Jensen, P. S., Christensen, H. E. M. & Ulstrup, J. Long-range interfacial electron transfer of metalloproteins based on molecular wiring assemblies. *Faraday Discuss.* **131**, 181–195 (2006).
- Janshoff, A., Neitzert, M., Oberdörfer, Y. & Fuchs, H. Force spectroscopy of molecular systems - Single molecule spectroscopy of polymers and biomolecules. *Angew. Chem. Int. Ed.* **39**, 3213–3217 (2000).
- Kienberger, F., Ebner, A., Gruber, H. J. & Hinterdorfer, P. Molecular recognition imaging and force spectroscopy of single biomolecules. *Acc. Chem. Res.* **39**, 29–36 (2006).
- Stroh, C. *et al.* Single-molecule recognition imaging-microscopy. *Proc. Natl. Acad. Sci. USA* **101**, 12503–12507 (2004).
- Grandbois, M., Beyer, M., Rief, M., Clausen-Schaumann, H. & Gaub, H. E. How strong is a covalent bond? *Science* **283**, 1727–1730 (1999).
- Beyer, M. K. & Clausen-Schaumann, H. Mechanochemistry: The mechanical activation of covalent bonds. *Chem. Rev.* **105**, 2921–2948 (2005).
- Rief, M., Gautel, M., Oesterhelt, F., Fernandez, J. M. & Gaub, H. E. Reversible unfolding of individual titin immunoglobulin domains by AFM. *Science* **276**, 1109–1112 (1997).
- Lantz, M. A. *et al.* Quantitative measurement of short-range chemical bonding forces. *Science* **291**, 2580–2583 (2001).
- Garcia-Manyès, S., Liang, J., Szoszkiewicz, R., Kuo, T. L. & Fernandez, J. M. Force-activated reactivity switch in a bimolecular chemical reaction. *Nat. Chem.* **1**, 236–242 (2009).
- Zheng, P. & Li, H. Direct measurements of the mechanical stability of zinc-thiolate bonds in rubredoxin by single-molecule atomic force microscopy. *Biophys. J.* **101**, 1467–1473 (2011).
- Zheng, P. & Li, H. Highly covalent ferric-thiolate bonds exhibit surprisingly low mechanical stability. *J. Am. Chem. Soc.* **133**, 6791–6798 (2011).
- Perez-Jimenez, R. *et al.* Diversity of chemical mechanisms in thioredoxin catalysis revealed by single-molecule force spectroscopy. *Nat. Struct. Mol. Biol.* **16**, 890–896 (2009).
- Alegre-Cebollada, J., Perez-Jimenez, R., Kosuri, P. & Fernandez, J. M. Single-molecule force spectroscopy approach to enzyme catalysis. *J. Biol. Chem.* **285**, 18961–18966 (2010).
- Hao, X., Zhang, J., Christensen, H. E. M., Wang, H. & Ulstrup, J. Electrochemical single-molecule AFM of the redox metalloenzyme copper nitrite reductase in action. *Chem. Phys. Chem.* **13**, 2919–2924 (2012).
- Kudera, M., Eschbaumer, C., Gaub, H. E. & Schubert, U. S. Analysis of metallo-supramolecular systems using single-molecule force spectroscopy. *Adv. Funct. Mater.* **13**, 615–620 (2003).
- Garnier, J., Gauthier-Manuel, B., van der Vegte, E. W., Snijders, J. & Hadziioannou, G. Covalent bond force profile and cleavage in a single polymer chain. *J. Chem. Phys.* **113**, 2497–2503 (2000).
- Aradhya, S. V., Frei, M., Hybertsen, M. S. & Venkataraman, L. Van der Waals interactions at metal/organic interfaces at the single-molecule level. *Nat. Mater.* **11**, 872–876 (2012).
- Erdmann, M., David, R., Fornof, A. R. & Gaub, H. E. Electrically induced bonding of DNA to gold. *Nat. Chem.* **2**, 745–749 (2010).

31. Erdmann, M., David, R., Fornof, A. R. & Gaub, H. E. Electrically controlled DNA adhesion. *Nat. Nanotech.* **5**, 154–159 (2010).
32. Laviron, E. General expression of the linear potential sweep voltammogram in the case of diffusionless electrochemical systems. *J. Electroanal. Chem.* **101**, 19–28 (1979).
33. Jensen, P. S. *et al.* Gold nanoparticle assisted assembly of a heme protein for enhancement of long-range interfacial electron transfer. *J. Phys. Chem. C* **111**, 6124–6132 (2007).
34. Hinterdorfer, P., Baumgartner, W., Gruber, H. J., Schilcher, K. & Schindler, H. Detection and localization of individual antibody-antigen recognition events by atomic force microscopy. *Proc. Natl Acad. Sci. USA* **93**, 3477–3481 (1996).
35. Baumgartner, W. *et al.* Cadherin interaction probed by atomic force microscopy. *Proc. Natl Acad. Sci. USA* **97**, 4005–4010 (2000).
36. Schwesinger, F. *et al.* Unbinding forces of single antibody-antigen complexes correlate with their thermal dissociation rates. *Proc. Natl Acad. Sci. USA* **97**, 9972–9977 (2000).
37. Wildling, L. *et al.* Probing binding pocket of serotonin transporter by single molecular force spectroscopy on living cells. *J. Biol. Chem.* **287**, 105–113 (2012).
38. Zhao, W., Liu, S., Cai, M., Xu, H., Jiang, J. & Wang, H. D. Detection of carbohydrates on the surface of cancer and normal cells by topography and recognition imaging. *Chem. Commun.* **49**, 2980–2982 (2013).
39. Evans, E. & Ritchie, K. Dynamic strength of molecular adhesion bonds. *Biophys. J.* **72**, 1541–1555 (1997).
40. Holyer, R. H., Hubbaerd, C. D., Kettle, S. F. A. & Wilkens, R. G. The kinetics of replacement reactions of complexes of the transition metals with 2, 2', 2''-terpyridine. *Inorg. Chem.* **4**, 622–625 (1966).
41. Shunmugam, R., Gabriel, G. J., Aamer, K. A. & Tew, G. N. Metal-ligand-containing polymers: terpyridine as the supramolecular unit. *Macromol. Rapid Commun.* **31**, 784–793 (2010).
42. Jonsson, E. Ö., Thygesen, K. S., Ulstrup, J. & Jacobsen, K. W. Ab initio calculations of the electronic properties of polypyridine transition metal complexes and their adsorption on metal surfaces in the presence of solvent and counterions. *J. Phys. Chem. B* **115**, 9410–9416 (2011).
43. O'Boyle, N. M., Albrecht, T., Murgida, D. H., Cassidy, L., Ulstrup, J. & Vos, J. G. A density functional theory study of the electronic properties of Os(II) and Os(III) complexes immobilized on Au(111). *Inorg. Chem.* **46**, 117–124 (2007).
44. Drew, M. G. B. M. *et al.* Theoretical and experimental studies of the protonated terpyridine cation. Ab initio quantum mechanics calculations, and crystal structures of two different ion pairs formed between protonated terpyridine cations and nitratolanthanate(III) anions. *J. Chem. Soc., Dalton Trans.* **18**, 2973–2980 (1998).
45. Andres, P. R., Hofmeier, H., Lohmeijer, G. G. B. & Schubert, U. S. Synthesis of 4'-Functionalized 2,2':6',2''-terpyridines via the pyridone route: symmetric and asymmetric bis-complex formation. *Synthesis-Stuttgart* **18**, 2865–2871 (2003).
46. Albrecht, T. *et al.* In situ scanning tunneling spectroscopy of inorganic transition metal complexes. *Faraday Discuss.* **131**, 265–279 (2006).
47. Chi, Q. *et al.* Molecular monolayers and interfacial electron transfer of *Pseudomonas aeruginosa* azurin on Au(111). *J. Am. Chem. Soc.* **122**, 4047–4055 (2000).
48. Chi, Q., Farver, O. & Ulstrup, J. Long-range protein electron transfer observed at the single-molecule level: In situ mapping of redox-gated tunneling resonance. *Proc. Natl Acad. Sci. USA* **102**, 16203–16208 (2005).
49. Enkovaara, J. *et al.* Electronic structure calculations with GPAW: A real-space implementation of the projector augmented-wave method. *J. Phys.: Condens. Matter* **22**, 253202 (2010).
50. Larsen, A. H., Vanin, M., Mortensen, J. J., Thygesen, K. S. & Jacobsen, K. W. Localized atomic basis set in the projector augmented wave method. *Phys. Rev. B* **80**, 195112 (2009).
51. Perdew, J. P., Burke, K. & Ernzerhof, M. Generalized gradient approximation made simple. *Phys. Rev. Lett.* **77**, 3865–3868 (1996).
52. Blöchl, P. E. Projector augmented-wave method. *Phys. Rev. B* **50**, 17953–17979 (1994).
53. Adamo, C. & Barone, V. Toward reliable density functional methods without adjustable parameters: the PBE0 model. *J. Chem. Phys.* **110**, 6158–6170 (1999).
54. Stephens, P. J., Devlin, F. J., Chabalowski, C. F. & Frisch, M. J. Ab initio calculation of vibrational absorption and circular dichroism spectra using density functional force fields. *J. Phys. Chem.* **98**, 11623–11627 (1994).
55. Bader, R. F. W. *Atoms in Molecules: A Quantum Theory* (Oxford University Press, 1990).
56. Tang, W., Sanville, E. & Henkelman, G. A grid-based Bader analysis algorithm without lattice bias. *J. Phys.: Condens. Matter.* **21**, 084204 (2009).

Acknowledgements

We are grateful for the financial support from the Lundbeck Foundation (Grant No. R49-A5331 to Q.C.) and the Danske Universiteter for a postdoc fellowship to X.H. in Denmark. H.W. thanks the support from MOST (Grant No. 2011CB933600), NSFC (Grant No. 21073181) and the '100 Talent Program' of CAS in China. K.M.-P. acknowledges the funding from the Chalmers Materials and Energy Areas of Advance in Sweden. J.U. acknowledges the financial support from the Villum Kann Rasmussen Foundation. K.S.T. acknowledges the support from the Danish Council for Independent Research's Sapere Aude Program (Grant No. 11-1051390). J.Z., H.W., X.H. and Q.C. thank Professor Erkang Wang for the career development with this paper dedicated to the occasion of his 80th birthday.

Author contributions

Q.C. conceived the idea and project. Q.C. and X.H. designed the experiments. X.H. and H.W. performed the AFM measurements and force spectroscopic analysis. N.Z. performed the electrochemical and partial AFM experiments. T.G. and K.M.-P. designed and synthesized the terpy ligands. J.Z. performed the STM imaging analysis. E.O.J., K.S.T., K.W.J. and J.U. contributed the DFT simulations. Q.C., X.H., E.O.J., J.U. and H.W. jointly wrote the paper. All authors discussed the results and commented on the manuscript.

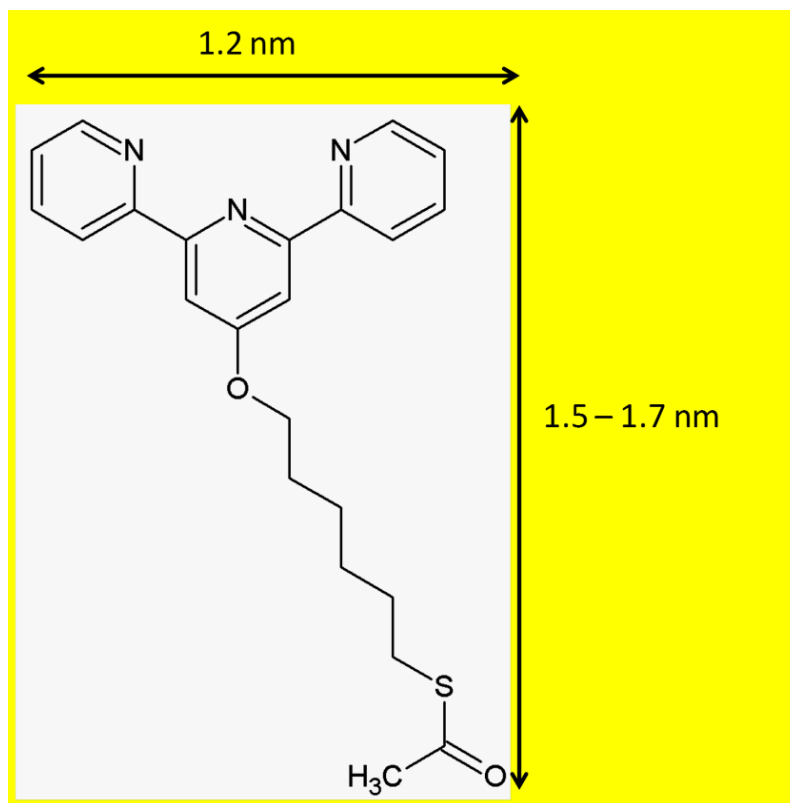
Additional information

Supplementary Information accompanies this paper at <http://www.nature.com/naturecommunications>

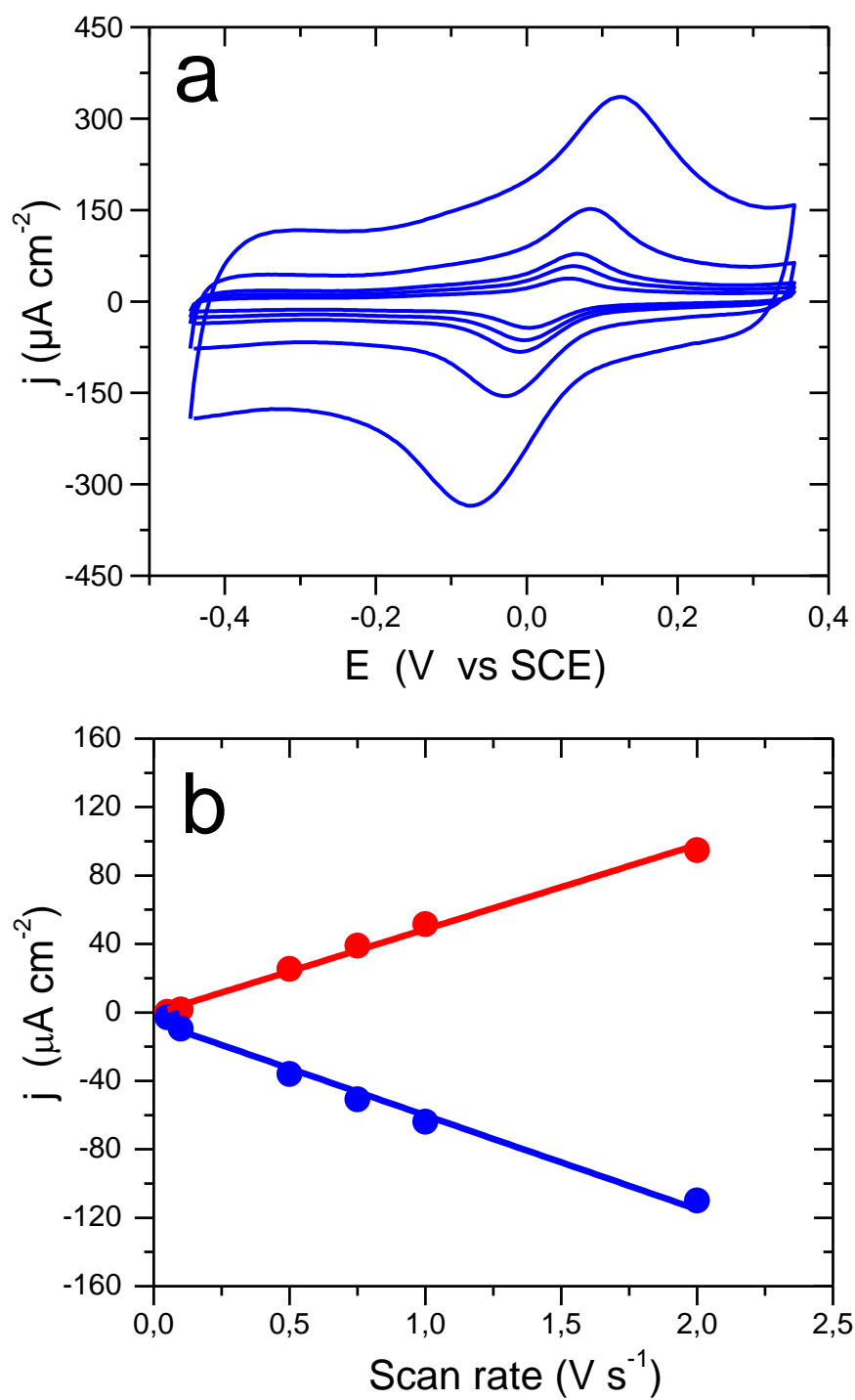
Competing financial interests: The authors declare no competing financial interests.

Reprints and permission information is available online at <http://npg.nature.com/reprintsandpermissions/>

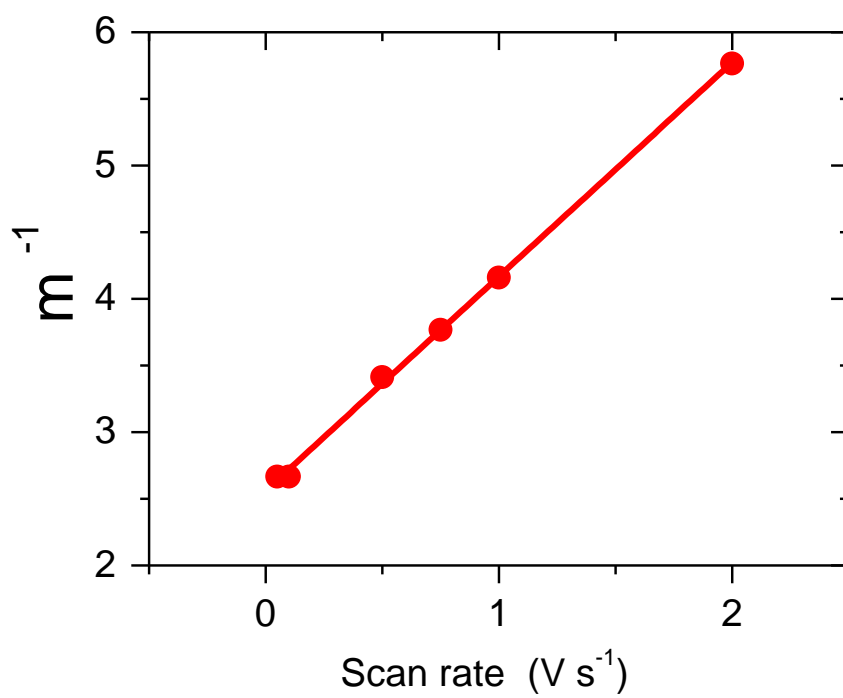
How to cite this article: Hao, X. *et al.* Direct measurement and modulation of single-molecule coordinative bonding forces in a transition metal complex. *Nat. Commun.* **4**:2121 doi: 10.1038/ncomms3121 (2013).



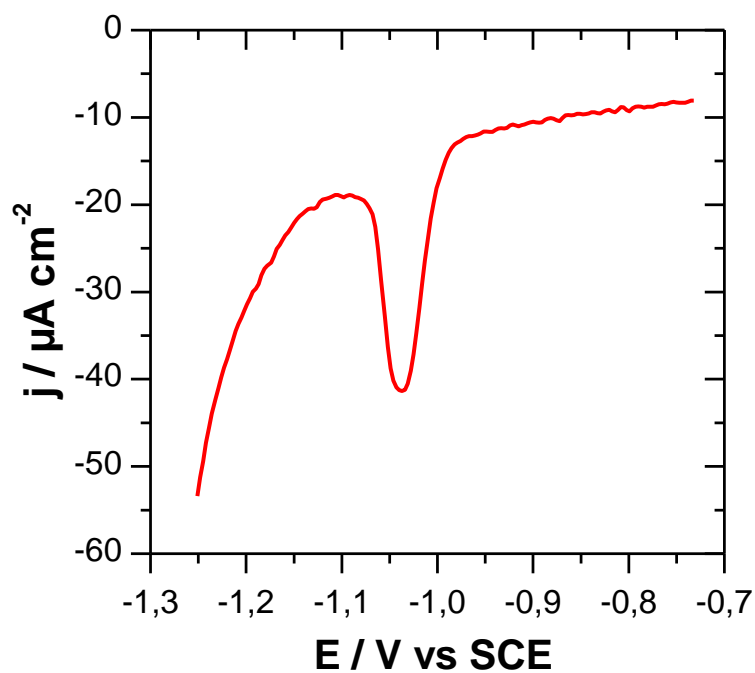
Supplementary Figure S1. Chemical structure and molecular dimensions of the thiolated ligand used in this work, 4'-(6-acetylthiohexyloxy)-2,2':6'2''-terpyridine.



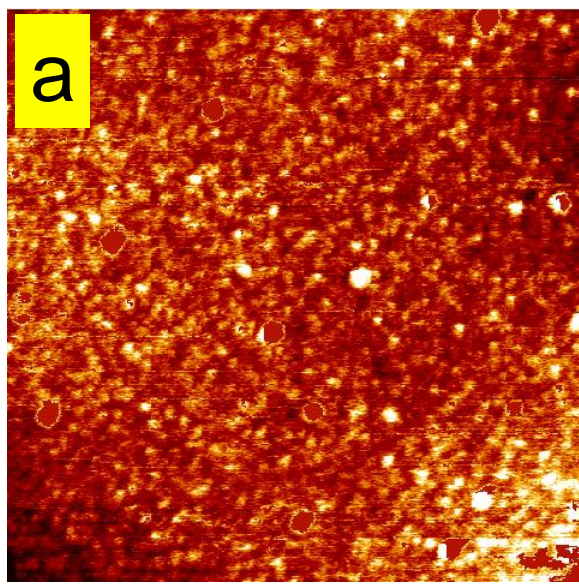
Supplementary Figure S2. Voltammetric measurements: (a) cyclic voltammograms of Os-terpy SAMs on Au(111) surfaces obtained at different scan rates of 0.5, 0.75, 1.0, 2.0, 5.0 V s^{-1} and (b) the correlation between the peak current and scan rate. Electrolyte: phosphate buffer (10 mM, pH 7.0).



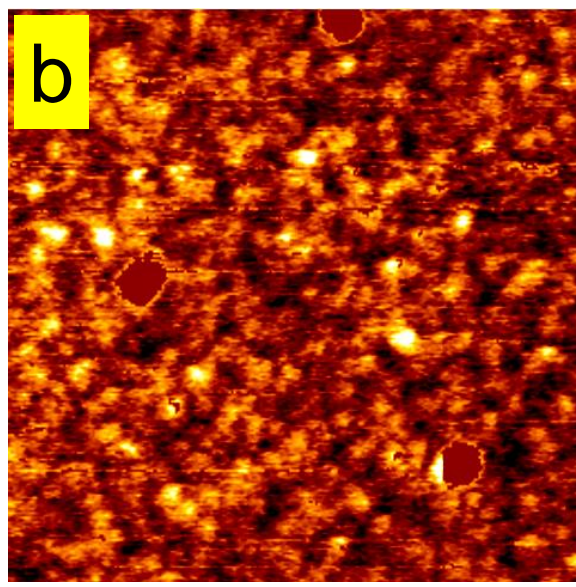
Supplementary Figure S3. A Laviron plot for estimating the rate constant of interfacial electrochemical electron transfer.



Supplementary Figure S4. Linear scan voltammetric curve of reductive desorption of the Os-terpy SAM on Au(111) surface in 0.5 M KOH. Scan rate: 10 mVs⁻¹ (i.e. the electrochemical reaction: Au(111)-S-R + e⁻ → Au(111) + RS⁻) The surface concentration or coverage (Γ) can be estimated by the integration of charge with the equation: $Q = nFA$, where Q is the Faradaic charge of the reduction peak, n the number of electrons transferred, F the Faraday constant, and A the area of working electrode.

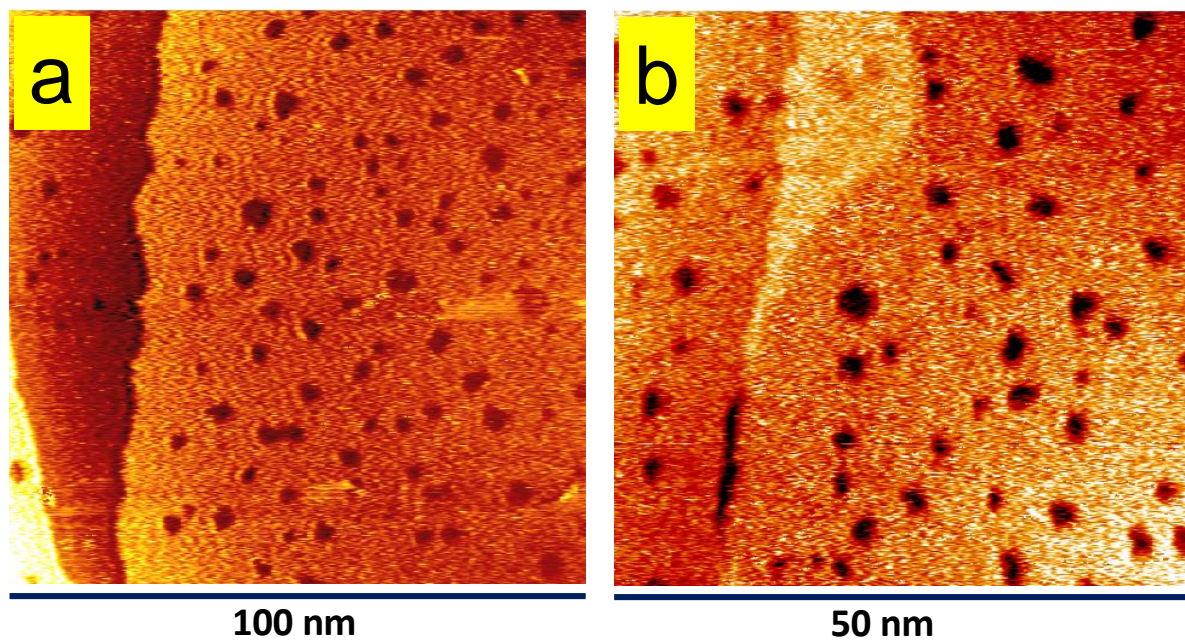


1000 nm

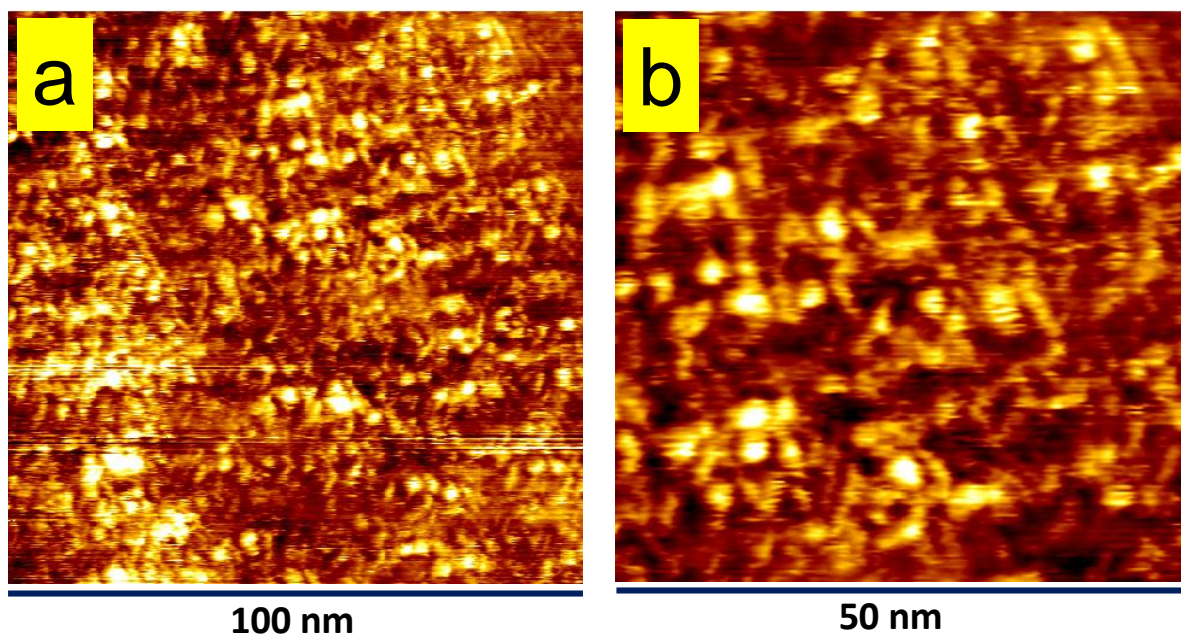


500 nm

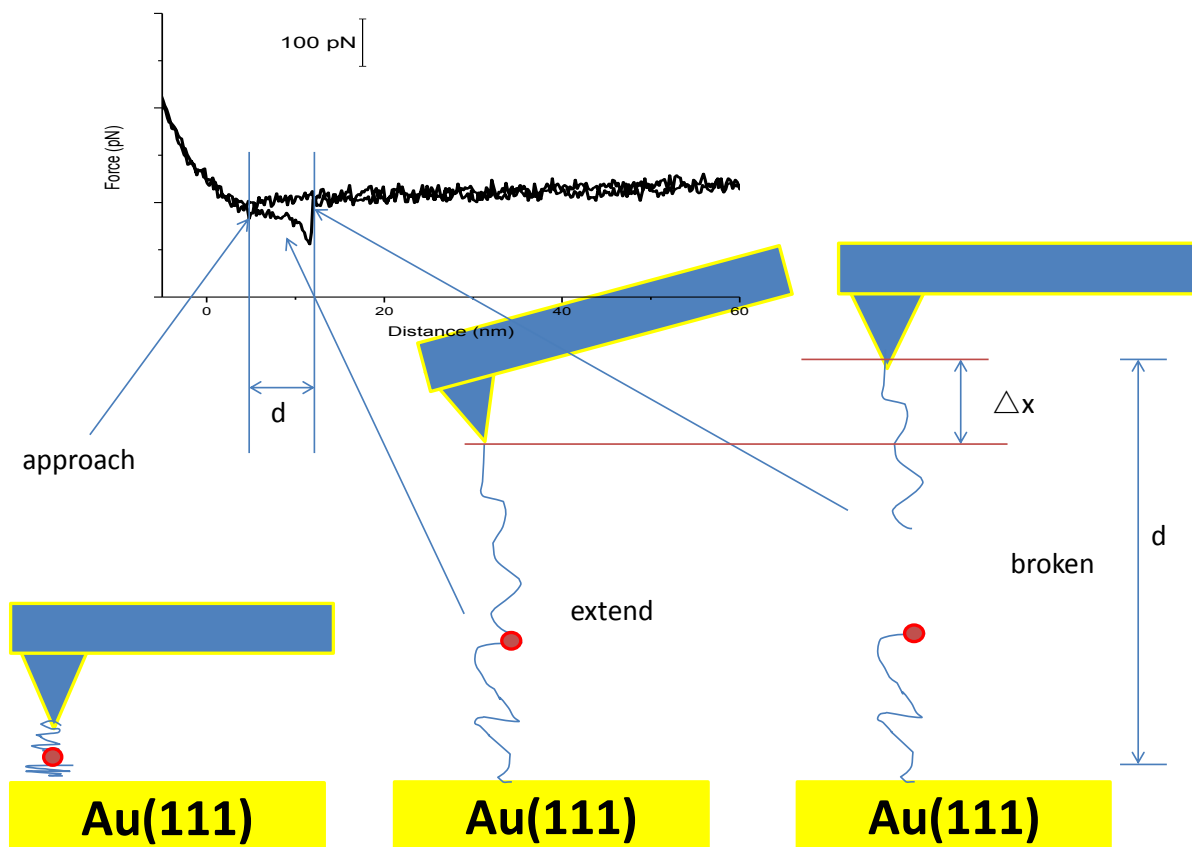
Supplementary Figure S5. AFM images of Os-terpy-C6-S-Au(111) in 10 mM phosphate buffer (pH 7.0). Scan area: (a) 1000 nm x 1000 nm and (b) 500 nm x 500 nm.



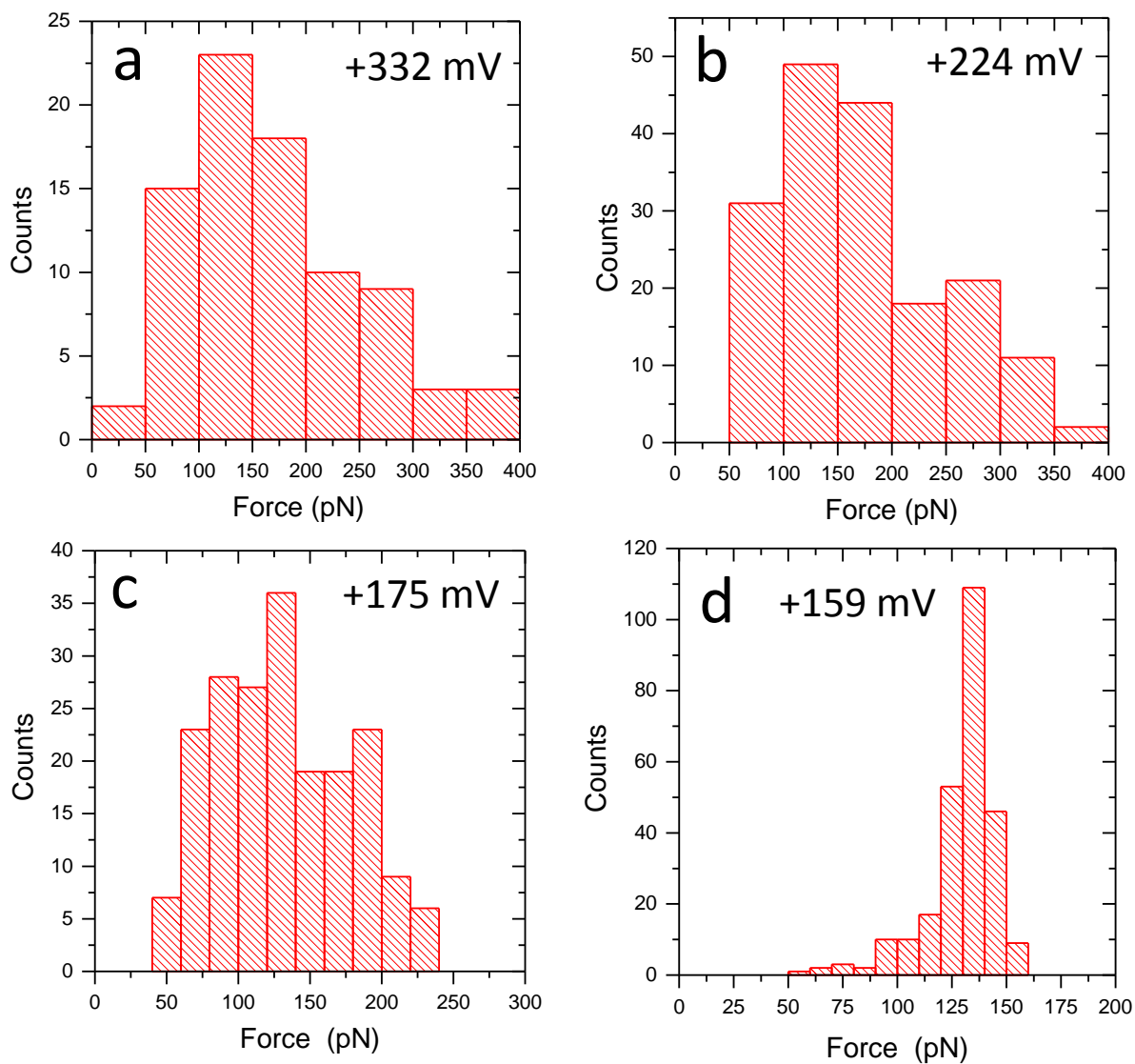
Supplementary Figure S6. STM images of terpy-C6-S-Au(111) (i.e., in the absence of Os ions) in 10 mM phosphate buffer (pH 7.0). Scan area: (a) 1000 nm x 1000 nm and (b) 500 nm x 500 nm (right). $V_b = -0.4$ V, $E_w = -20$ mV vs SCE, $I_t = 30$ pA.



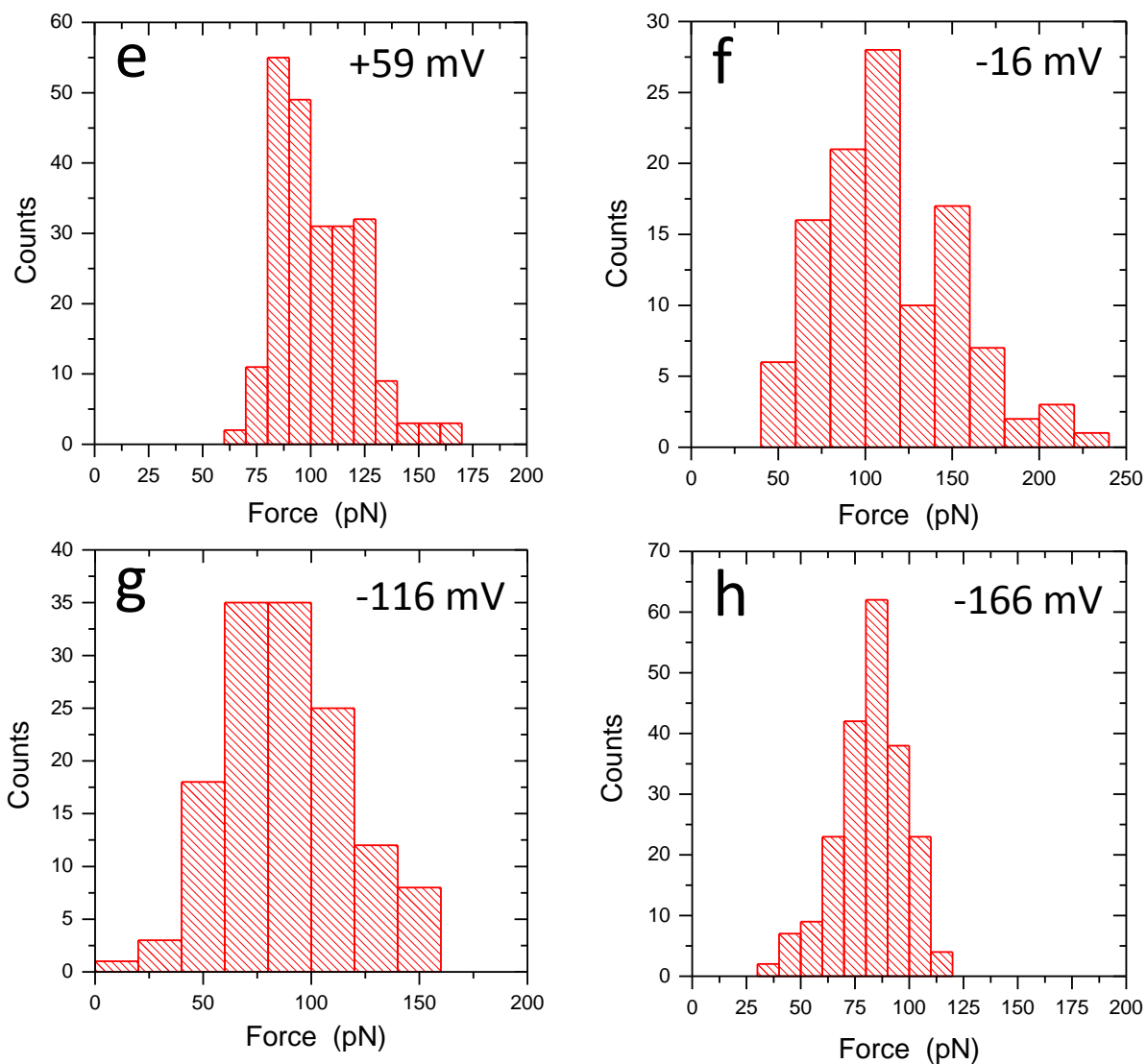
Supplementary Figure S7. STM images of Os-terpy-C6-S-Au(111) (i.e., in the presence of Os ions) in 10 mM phosphate buffer (pH 7.0). Scan area: (a) 1000 nm x 1000 nm and (b) 500 nm x 500 nm (right). $V_b = -0.4$ V, $E_w = -20$ mV vs SCE, $I_t = 20$ pA.



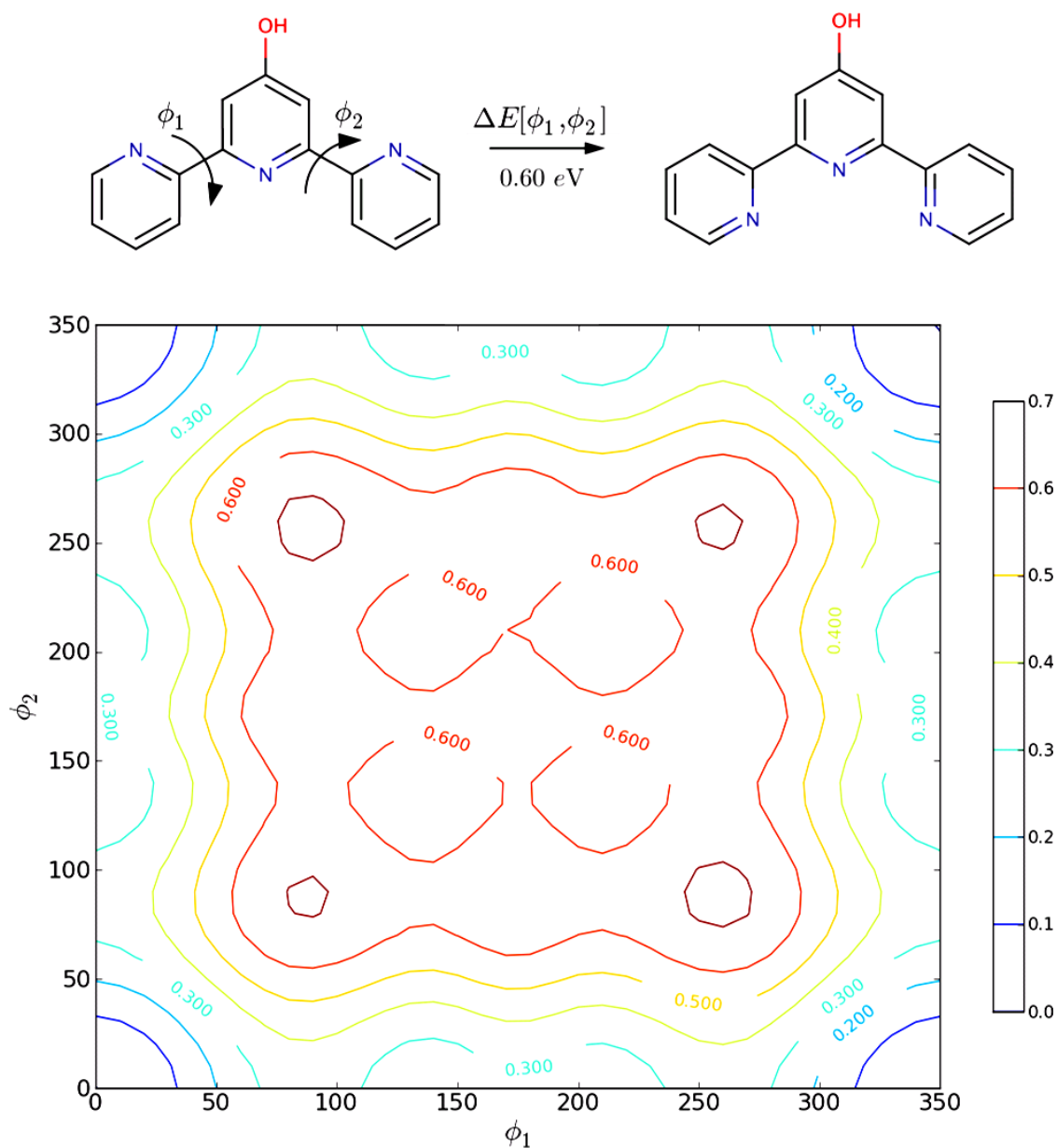
Supplementary Figure S8. Schematic illustration of formation of the force-distance curves in the present AFM measurements. Not drawn to scale. In AFM, the force-distance relation follows relatively straightforward Hooke law, $F = -k\Delta x$, where F is the force measured, k is a constant called the spring constant determined by AFM tip, and Δx is the relative distance (or displacement) of tip deflection. Note that the apparent total distance (d) should include both the linker length and the distance of AFM tip deflection.



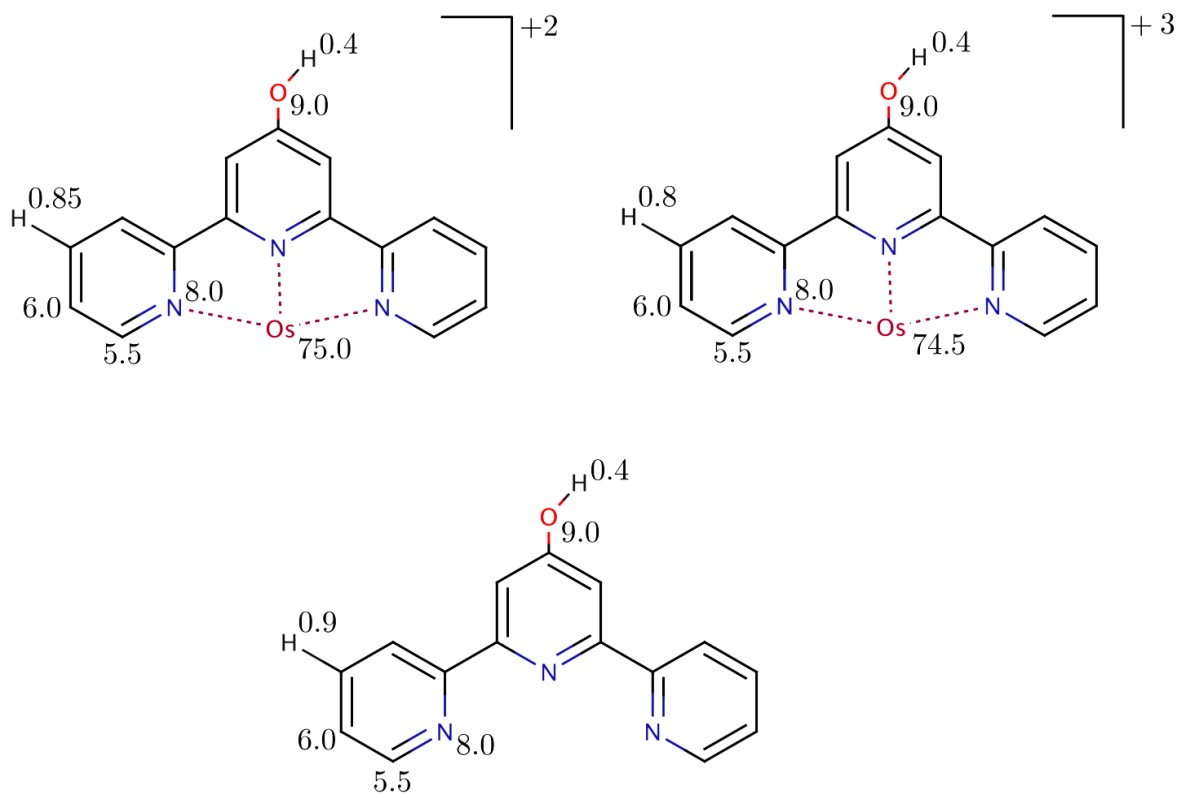
Supplementary Figure S9. Histograms of coordinative force distributions in the different redox states. The applied working potentials (vs SCE) are: (a) +332, (b) +224, (c) +175, (d) +159, (e) +59, (f) -16, (g) -116, and (h) -166 mV.



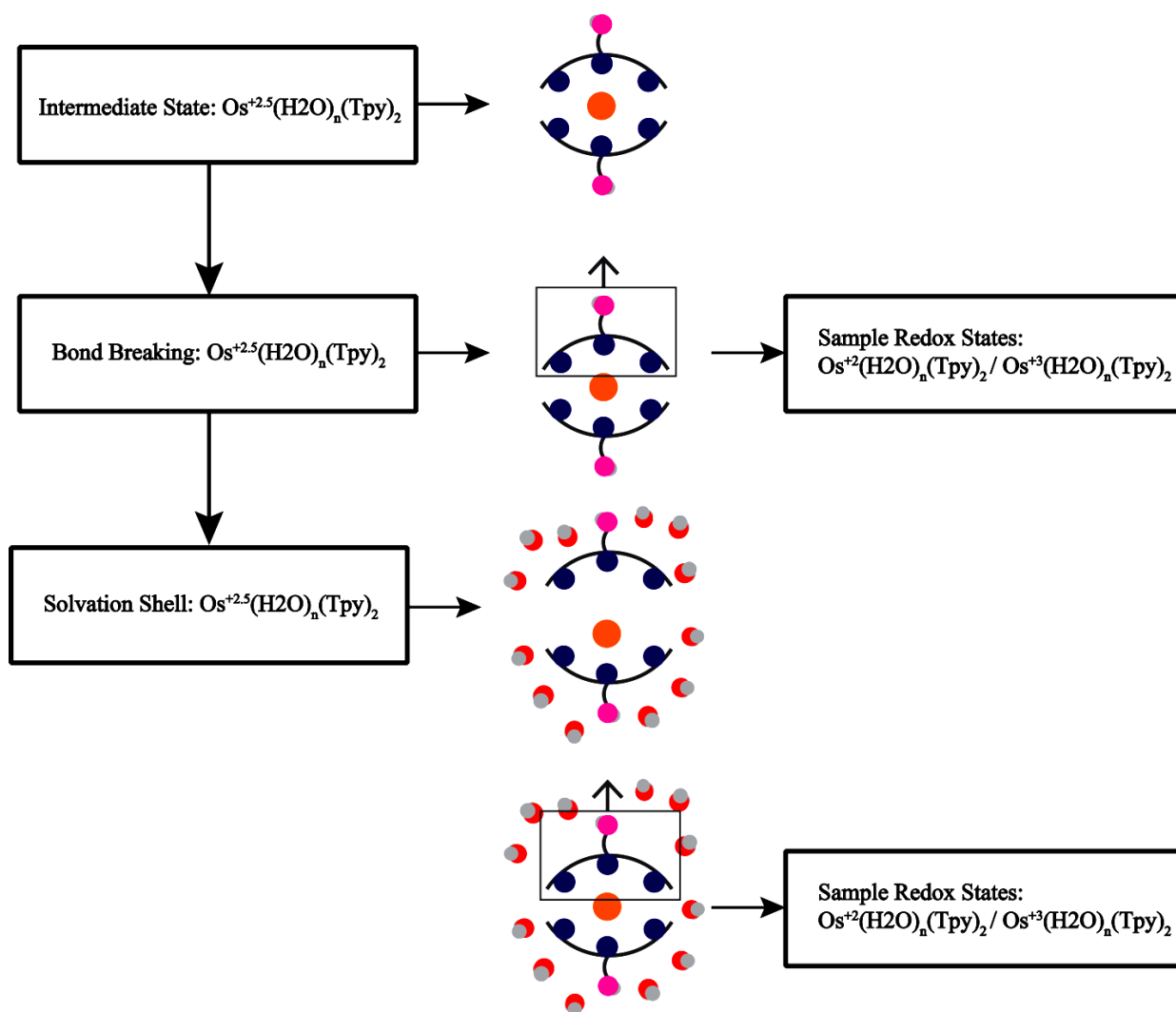
Supplementary Figure S10. Histograms of coordinative force distributions in the different redox states. The applied working potentials (vs SCE) are: (a) +332, (b) +224, (c) +175, (d) +159, (e) +59, (f) -16, (g) -116, and (h) -166 mV.



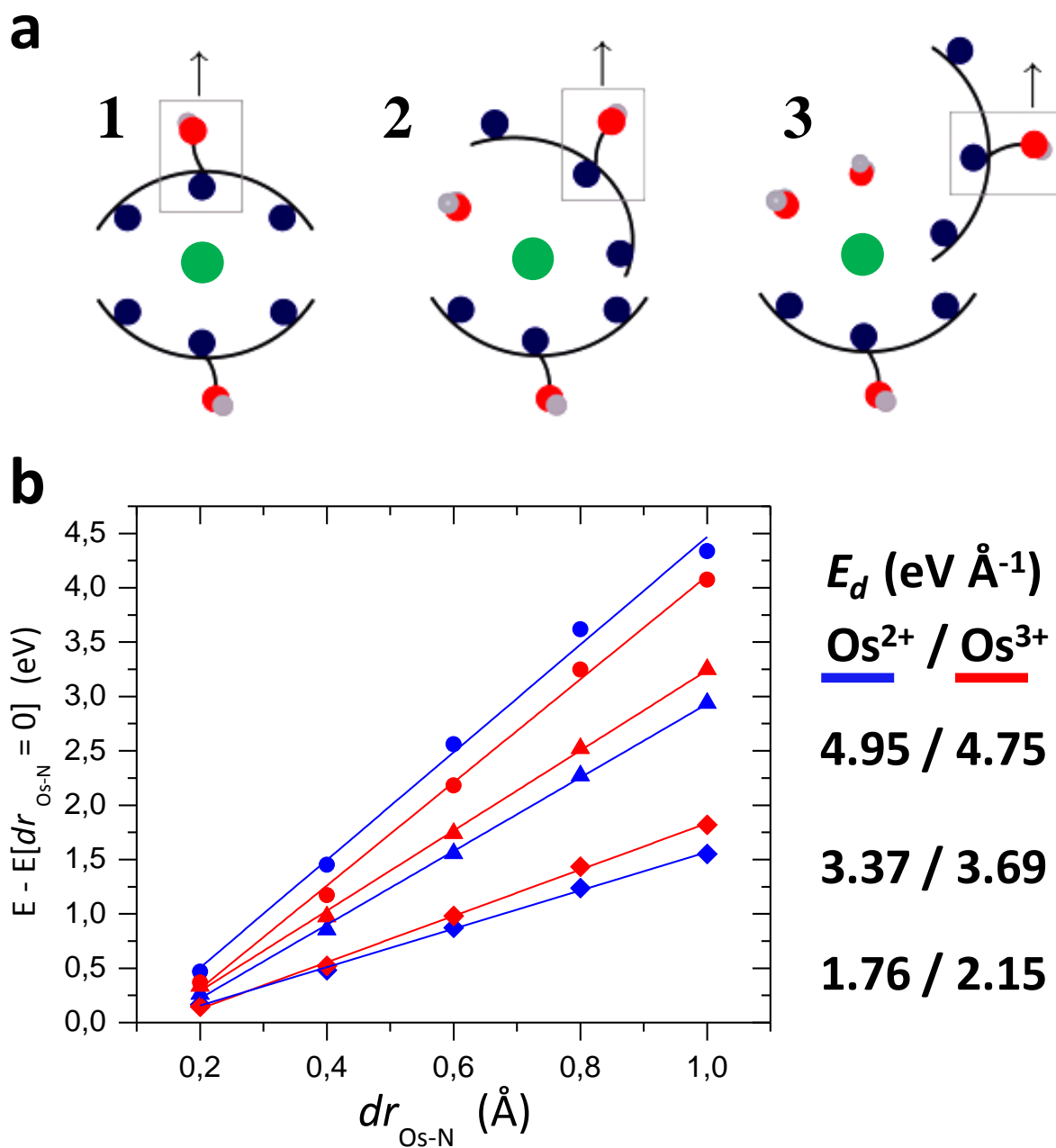
Supplementary Figure S11. **Top**, the schematic illustration of rotating the pyridine units, **Bottom**, Potential energy surface of pyridine unit rotation in the whole terpyridine molecule. The most favorable structure is the zero-point reference. This is where the nitrogens are oriented in configuration $N\uparrow N\downarrow N\uparrow$. Rotating a single nitrogen to point along the middle nitrogen costs 0.3 eV, and the energy cost for the rotation of both to form the $N\downarrow N\downarrow N\downarrow$ configuration is thus added up to 0.6 eV. However, the orientation does not affect the conjugation, because the energy cost is largely due to steric or/and Coulomb interactions among the charged nitrogen atoms.



Supplementary Figure S12. The Bader's analysis of Os^{2+} and Os^{3+} complexes, ligated to a single terpy. The zero charge reference is a lone terpyridine unit. Only a single hydrogen is shown on the terpy unit for simplicity. The values noted are averaged over all atoms in similar positions.

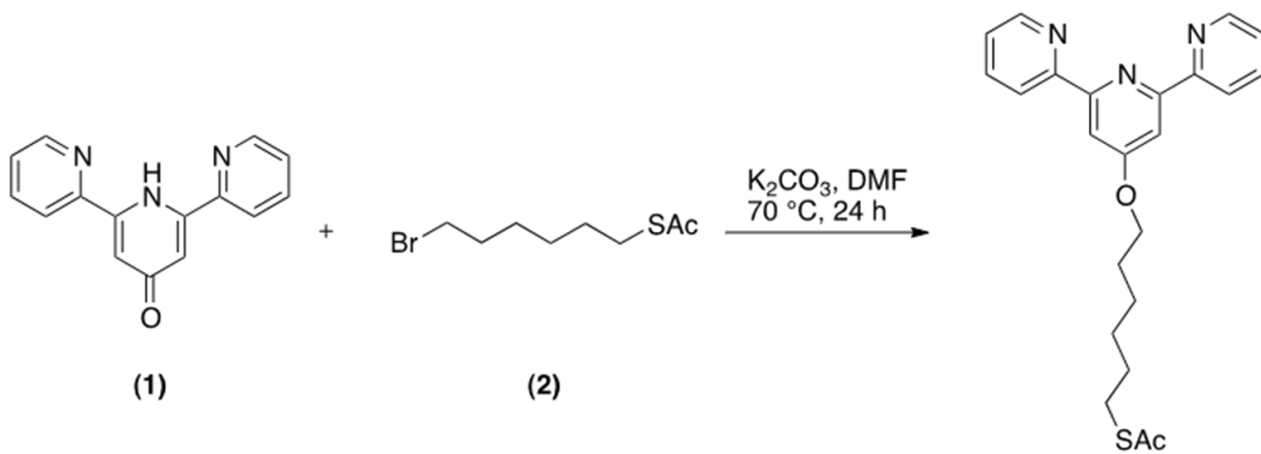


Supplementary Figure S13. Schematic illustration of the overall simulation procedure. Briefly, the target system is relaxed in the intermediate state of charge 2.5. At each interval the osmium to nitrogen distance of the middle unit or the binding unit is stretched by 0.2 Å. This distance is kept fixed but all other degrees of freedom allowed to relax. The resulting trajectories are then sampled at the redox states of Os^{2+} and Os^{3+} . Furthermore, to the last image of the trajectory, where the bond is broken (about 2.0 Å in all cases) and a solvation shell is constructed around the two units. Focus is mainly on the osmium carrying unit. The solvent is allowed to relax at the intermediate state of charge 2.5, but the complex is kept fixed. Finally, the solvated trajectory is sampled again at the Os^{2+} and Os^{3+} redox states.



Supplementary Figure S14. DFT simulations of the bond breaking pulling forces without consideration of solvation effects. a, Schematic illustrations of the target bond breaking systems. Three initial configurations examined in the two oxidation states are: **(1)** $\text{Os}(\text{terpy})_2$ is osmium in octahedral ligand environment provided by the nitrogens (blue) of two terpy molecules. **(2)** $\text{Os}(\text{terpy})_2(\text{H}_2\text{O})$ is coordinated to a second terpy molecule through two nitrogens. The nonbonding group rotates by about 90° , allowing the coordination of a water molecule to the osmium. **(3)** $\text{Os}(\text{terpy})_2(\text{H}_2\text{O})_2$ is osmium coordinated to a single nitrogen of the second terpy ligand, with two water molecules occupying the coordination sites. The middle pyridine unit of terpy was

systematically moved by 0.2 Å increments. At each increment the osmium to nitrogen distance (of the middle pyridine unit) was kept fixed and all other degrees of freedom allowed to be relaxed. A notable side reaction was the transfer of proton from a water ligand to a non-coordinated nitrogen of terpy. **b**, Potential energy changes of the simulated bond breaking systems in vacuum. Solid lines are linear best fits to the calculated data for Os²⁺ and Os³⁺, respectively. The slopes were obtained from these linear fits, and the values are listed in the right pane of **b**. It is clear that the Os²⁺ state favors binding to terpy, but as water occupies coordination sites the terpy-Os³⁺ bond becomes stronger. It is noted that the energy starts to level out when the Os-to-terpy distance is beyond 1.0 Å.



Supplementary Figure S15. Chemical reaction for the synthesis of 4'-(6-acetylthiohexyloxy)-2,2':6'2''-terpyridine.

PAPER IV

Direct dynamics studies of a binuclear metal complex in solution: The interplay between vibrational relaxation, coherence, and solvent effects.

Asmus Ougaard Dohn,^{*,†} Elvar Örn Jónsson,[‡] Kasper Skov Kjær,[‡] Tim Brandt van Driel,[‡] Martin Meedom Nielsen,[‡] Karsten Wedel Jacobsen,[‡] Niels Engholm Henriksen,[†] and Klaus Braagaard Møller[†]

Department of Chemistry, Technical University of Denmark, Building 207, 2800 Kgs. Lyngby, Denmark, and Department of Physics, Technical University of Denmark, Building 307 2800 Kgs. Lyngby, Denmark

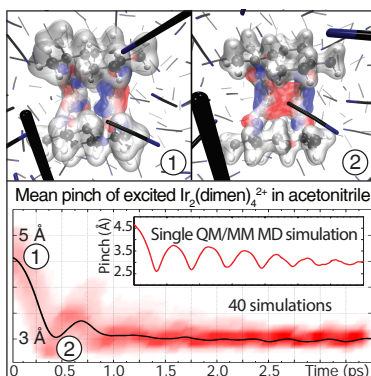
E-mail: asod@kemi.dtu.dk

*To whom correspondence should be addressed

[†]DTU Chemistry

[‡]DTU Physics

Abstract



By using a newly implemented QM/MM multiscale MD method to simulate the excited state dynamics of the Ir₂(dimen)₄²⁺ complex, we report on results that support the two experimentally observed coherent dynamical modes in the molecule, but also reveal a third mode, not distinguishable by spectroscopic methods. We directly follow the channels of energy dissipation to the solvent, and report that the main cause for coherence-decay is the initial wide range of configurations in the excited state population. We observe that the solvent can actually extend the coherence lifetime, by decoupling the internal degrees of freedom in the complex.

Introduction

One way of exploring the dynamical nature of chemical reactions has been facilitated through the study of bimetallic d⁸-d⁸ complexes and their remarkable photochemical properties¹⁻⁷, since their first synthesis almost four decades ago⁵. The focus of this work has been on Ir₂(dimen)₄²⁺ (dimen=1,8-diisocyno-*p*-menthane), a type of molecule which has also shown photoconversion functionality for solar energy storage⁴.

The electronic configuration of this complex features a σ -antibonding highest occupied molecular orbital (HOMO), while the lowest unoccupied molecular orbital (LUMO) is σ -bonding^{1,2}. This causes the complex to undergo large structural changes when photoexcited to the S₁ state with an efficient intersystem crossing to T₁⁸, as was experimentally confirmed for the similar Rh₂(dimen)₄²⁺ complex in the solid phase using time-resolved x-ray diffraction,

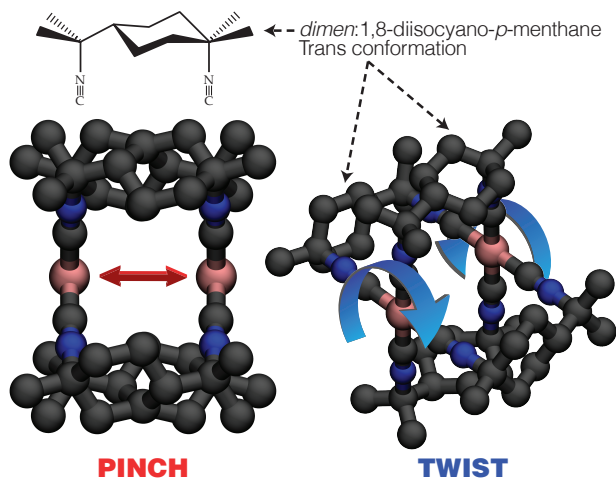


Figure 1: Two of the main dynamic, structural modes of $\text{Ir}_2(\text{dimen})_4^{2+}$, here shown without hydrogens for clarity, and in the conformer employed for these studies. The 1,8-diisocyano-*p*-menthane (dimen) ligand provides the optimal compromise between flexibility and rigidity for large, but controllable structural changes e.g. by electronic excitation. Electronically exciting this complex promotes an electron from the antibonding HOMO to the bonding LUMO, effectively forming a chemical bond between the Ir atoms¹⁻³.

showing a shortening of the metal-metal distance of 0.86 \AA ⁹. Our group observed a contraction of the Ir variant in solution by 1.4 \AA ,¹⁰ using $\sim 100 \text{ ps}$ pulsed synchrotron radiation. We have recently gathered data on this system at the Linac Coherent Light Source (LCLS), to directly probe the coherent motion with x-ray methods, utilizing the higher temporal resolution of x-ray free electron lasers, compared to synchrotron radiation. Analysis is ongoing. Hartsock *et al.*³ has carried out transient spectroscopy measurements on the $\text{Ir}_2(\text{dimen})_4^{2+}$ complex, observing excited state (ES) vibrational wavepackets. These are assigned to the previously mentioned contraction on S_1 , and also a twist of the metal planes in the complex (see fig. 1). Furthermore, the study reports a deformational isomerism which effectively splits the ground state (GS) population in two main structures. This has previously been observed⁶, and is supported by computationally by constrained mappings of the GS energy landscapes¹¹. However, to our knowledge, no attempts (including our own) to freely relax the geometry of the molecule into the short conformer has proved successful, when using DFT methods.

With this work, we aim to expand on the pre-existing knowledge about the system using our newly developed QM/MM Born-Oppenheimer MD (QM/MM BOMD) method¹² to obtain an adiabatic version of the vibrational motion in the single molecule. By utilizing the efficiency of the code, we mimic the coherent motion by exciting a host of different GS configurations and analyse the mean properties of these dynamic trajectories, and their relation to individual excitations. By benchmarking these results against experiments, we obtain information not experimentally distinguishable, such as possible dynamics of spectroscopically dark or obscured modes, direct observation of intra- and intermolecular energy transfer and solvent interactions. Since the electronic structure of the QM part is calculated "on the fly", and no full potential energy surfaces are calculated (or needed) in this direct-dynamics method, we focus on simulating the structural dynamics upon excitation of a population of solvated $\text{Ir}_2(\text{dimen})_4^{2+}$ from the long GS conformer.

Methodology

The Direct-Dynamics simulations were carried out utilizing the Atomic Simulation Environment (ASE)¹³ to interface the QM and MM subsystems. The Grid-based Projector-Augmented Wave Method (GPAW)¹⁴ is used for the QM description. The full details of the method and its interfacing strategy is described elsewhere.¹² The quantum system comprised of the $\text{Ir}_2(\text{dimen})_4^{2+}$ complex is described using DFT with the PBE functional.¹⁵ It was placed in a classically pre-thermalized simulation box of $28 \times 28.5 \times 31.5$ Å containing acetonitrile at 0.786 g/cm^3 . After removal of acetonitrile molecules overlapping with the complex, the total number of classically described acetonitriles was 237. The entire system was then thermalized again, until the temperature was stable at 300 K, as set by the Langevin thermostat applied to the solvent only. For the production run, 18.21 ps of GS trajectory was sampled using 2 fs timesteps.

We simply approximate the experimental excitation by instantaneously promoting a com-

prehensive representation of the GS configuration space to the ES, neglecting effects from finite pulse-widths and bandwidths of real excitation sources (The effect the bandwidth is examined in the SI). The ultrafast ES dynamics take place on S_1 , but since similar binuclear d^8 - d^8 complexes have previously been shown to have the same triplet and singlet surface shapes, only differing in energy,^{16,17} it is possible to carry out T_1 simulations mimicking the S_1 dynamics. Thus, the computational cost is kept within the feasible range for systems of this size by staying within the GS DFT framework on T_1 . This approximation is implied for all the excitations simulated in this work.

Fig 2 shows a GS trajectory from which 40 configurations are promoted to the ES, for a total of 140 ps ES trajectories sampled. The sampling was spaced such as to minimize the correlation between each of the excited state trajectories, while also allowing for comparison of excitations from complexes of similar starting geometries, but with different solvent configurations, and excitations from different starting geometries. The thermostat was turned completely off for these runs. The ES timestep was 1 fs, to allow better resolution and minimize the drift. The maximum observed drift in any of the simulations was 0.40 kJ/mol per atom in the system, over the entire simulation duration.

Results and discussion

The simulations clearly show the Ir-Ir pinch and the dihedral twist (see fig. 3, and videos in SI online), but they reveal more: The ligands expand and contract along the N-C-Ir-C-N directions in the complex. This is best described by plotting the mean of the distances between each carbon in the ligand rings and the one on the opposing side of the entire complex at each time step t . In the following analysis we have incorporated this "breathing mode", and show that it plays an important role in the overall dynamics of this system. The GS trajectory does not exhibit any significant activations of this mode.

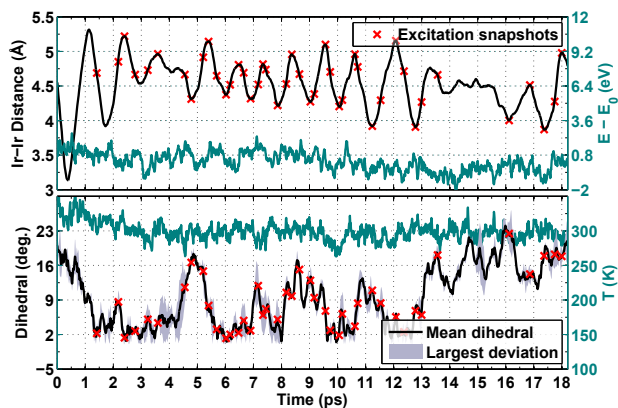


Figure 2: Two of the main structural modes in $\text{Ir}_2(\text{dimen})_4^{2+}$ plotted for the GS trajectory. Top: The Ir-Ir distance. Bottom: The dihedral angle. The teal graphs show the total energy difference during the run (where E_0 is the total energy at the start of the production run) and temperature in the top and bottom graph, respectively. The ES runs were started from the configurations marked with red crosses.

Fig. 3 shows how the pinch and twist modes evolve in time, following excitation, and how they relate to the newly discovered breathing mode. The mean Ir-Ir distance in the population when measured over the last ps of the simulation is 2.98 \AA , which is in very good agreement with previous experimental results from x-ray scattering¹⁰ of 2.90 \AA , given the incomplete basis and the exchange-correlation functional used for the QM part. The second inset in the top figure shows that the pinching motion is limited to the center part of the molecule, affecting the next two atoms adjacent to Ir, but not the outermost parts of the ligands. The mean values of the entire population show oscillatory features, meaning that the motion of each trajectory is in phase with the others, thus showing signs of coherent motion. The excited population loses its mean pinch oscillation amplitude almost before completing a full period, but if the first oscillation period is calculated by doubling the time from the first well to the first top, the period is $\sim 480 \text{ fs}$, or $\sim 70 \text{ cm}^{-1}$. In the work by Hartsock *et al.*³, an observed transient absorption feature with a frequency of 75 cm^{-1} is assigned to the pinching motion, differing only 7 % from the result presented here.

The anharmonicity of the underlying potential, reflected in the direct dynamics, is evident

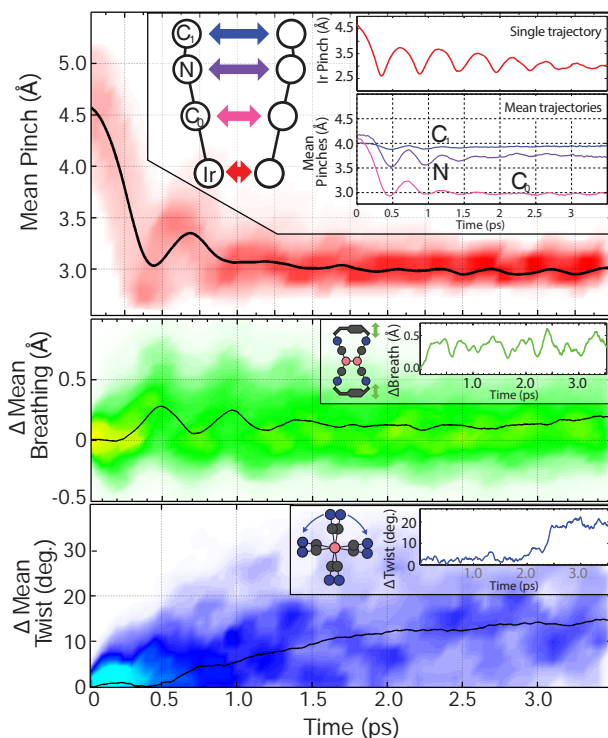


Figure 3: The mean Ir-Ir pinching (top), breathing (middle), and twisting (bottom) as a function of time after excitation. The twist is defined as the change in dihedral angle from the moment of excitation $t = 0$. The shaded background show the binned counts of values from all the trajectories. The bin sizes are 50 fs by 0.1 Å, 0.05 Å, and 2 degrees for the pinching, breathing and twisting, respectively. This population loses its pinch phase within a picosecond, while the single trajectory-pinch oscillation dies out much slower, as can be seen on the top inset. However, the mean phase of the breathing mode is sustained for almost 2 ps. The pinching- and breathing modes share the same oscillation period. The next inset on the top graph show that the pinch is also affecting the adjacent atoms, but not the ligand ends. The last insets show the breathing and twisting of the same single trajectory as the top inset.

from the oscillation in the single trajectory (top inset in fig. 3): It reflects a steeper potential for the short distances, and gentler slope for the long ones. The oscillation becomes more sinusoidal with time, as the trajectory moves closer to the harmonic approximation limit, deeper in the potential. Similarly, the frequency increases as the molecule dissipates its excess vibrational energy, which is also observed for the single trajectory. This is equivalent to anharmonic potentials with Morse-like characteristics. Therefore, it is also expected that the first oscillation period of the population should be somewhat longer than the experimental result, since the latter is first measured at times $t \geq 0.5$ ps after excitation. Also consistent with experimental results³, little to no coherent twist oscillation is observed from excitations that start from the long, eclipsed conformation. However, a delayed twist mechanism is observed for the mean motion, with the molecule starting to twist after roughly 500 fs. The simulation coherence decay is faster than the experimental, if only the pinch is taken into account. However, the breathing mode is coherent for almost 1.5 ps. Furthermore, the frequency of the pinching and breathing is similar: The period from the first to the second top is ~ 450 fs, or ~ 74 cm^{-1} , only 1.3 % slower than the experimental pinch. The first breathing maximum arrives 0.5 ps after excitation, where the experimental fit also starts from³.

The causes of coherence decay can be either statistical or dynamical in nature, i.e. either a result of the difference in initial configurations from which the system is brought up to the excited state or of (stochastic) energy dissipation in each molecule, either through the solvent or through internal degrees of freedom. Examinations of the individual trajectories (fig. 3, top inset) reveal that vibrational relaxation is much slower than the population mean coherence decay, and not very stochastic in nature. Hence, the fast coherence decay of the population mean must originate from the wide range of initial GS configurations. This is supported by a thorough population-partitioning analysis (see SI for details), which shows that exciting a narrow, phase coherent distribution of GS configurations extends the coherence time on the excited state significantly. Our analysis also shows that introduction of

an effective bandwidth in making the ES population, similar to the one of the experimental excitation source³, leads to a somewhat longer excited-state coherence time, although there is no strong correlation between the GS metal-metal vibrational amplitude/phase and the excitation energy.

In order to further understand the effect of the solvent on $\text{Ir}_2(\text{dimen})_4^{2+}$ dynamics, fig. 4 compares the pinch of the single trajectory from the inset of fig. 3 to a group of additional simulations that have progressively more gas-phase character (from bottom to top in the figure). The first noticeable feature is the large intramolecular vibrational energy redistribution (IVR) in the pure gas phase simulation, which is evidently the *only* possible channel for energy dissipation in that system. In this case, the excess vibrational energy is efficiently transferred to the breathing mode, since there is no solvation-cage effects, as seen in fig. 5.

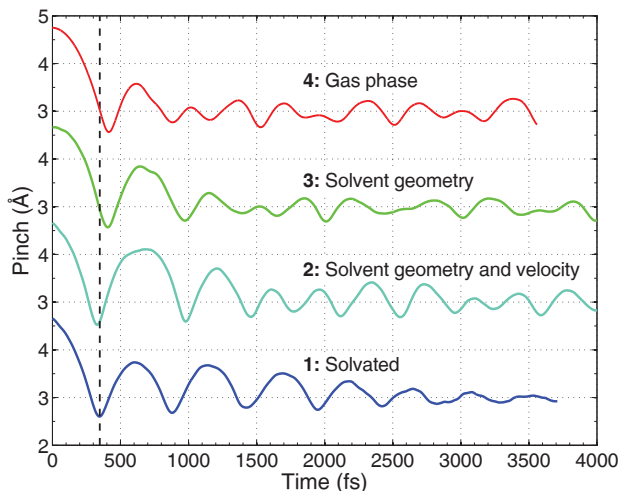


Figure 4: In order to investigate the role of the solvent in the dynamics, three other ES trajectories were also simulated, and shown here, together with a single trajectory from the main production run. **1:** The pinch of the fully solvated complex. **2:** A simulation where the solvent was removed at the time of excitation, but keeping the initial geometry influenced by the solvent, *and* the velocity of the atoms in the complex. **3:** A simulation where only the geometry is kept, while the initial velocities are set to zero. **4:** An excitation started from the gas phase structure of the complex.

Returning to fig. 4, the original trajectory (**1**) was excited from a GS phase space area of already contracting metal atoms, which explains why the first contraction of the metal

atoms in simulations **1** and **2** is faster than in **3** and **4**. The fastest pinch is observed in trajectory **2**, meaning that the solvent interaction of the solvated system must dampen the pinching motion. The second expansion is also shorter in **1**, which is again a cage-effect of the solvent. All in all, for the trajectory of the solvated system, the solvent cage actually facilitates the *extension* of the lifetime of the coherent motion, through decoupling of the internal degrees of freedom in the complex. The flexible dimen ligand can be argued to be

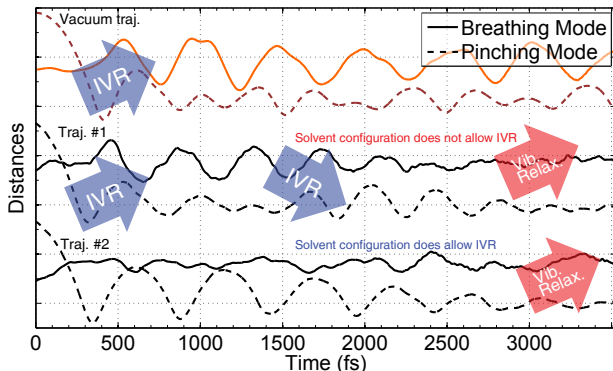


Figure 5: Comparison of the breathing mode in the gas phase trajectory (red) and two trajectories of solvated systems, displaying the energy transfer mechanisms in the system. The two solvate-included trajectories are started from similar GS conditions, but 10 ps apart, so the two accompanying solvent configurations are uncorrelated. The breathing mode amplitude is large compared to the other trajectories, since there is no dampening from the solvent.

the cause of the large amount of IVR observed, delayed by ~ 150 fs since the metals atoms need to contract before a coupling of the two modes is made. Since the breathing motion can be heavily dampened by the solvent cage, it can be expected that the main channel of external vibrational dissipation of energy to the solvent is through the ligands. This is further supported by the comparison in fig. 5: In trajectory 2, the solvent configuration does not allow for IVR to the breathing mode, so the excess excitation energy is contained in the pinch, the motion of which is almost free of small perturbations stemming from electrostatic interactions with the solvent. In the first trajectory, the pinch energy is redistributed almost completely to the breathing mode within 1.5 ps, where solvent-induced interactions perturb the oscillation. Some of the remaining energy is then again transferred back into the pinch

before dissipating further. All in all, this means that vibrational relaxation of $\text{Ir}_2(\text{dimen})_4^{2+}$ through the solvent can only occur in substantial quantities if the energy is efficiently redistributed into the ligand breathing mode.

That the coherence decay is faster than vibrational cooling is in contrast with the findings of van der Veen *et al.*¹⁶ for the bimetallic d^8 - d^8 complex $[\text{Pt}_2(\text{P}_2\text{O}_5\text{H}_2)_4]^{4-}$ in various solvents, where the authors observe that coherence decay occurs on the same time scale as vibrational cooling. While the two complexes are different, and different solvents are used (including protic solvents), they both have coordination sites along the metal atom axis, which could facilitate significant electrostatic- and dispersion interactions with the solvent. Nevertheless, the main difference causing the contrasting results is most likely due to the different rigidities of the two distinct ligand types, where the more flexible dimen ligand allows for a wider range of configurations in the GS ensemble. We emphasize that here, the variation of the GS metal-metal distance (fig. 2) is comparable to the amplitude of the excited state vibration (fig. 3).

Both the $\text{Ir}_2(\text{dimen})_4^{2+}$ and $[\text{Pt}_2(\text{P}_2\text{O}_5\text{H}_2)_4]^{4-}$ experiments represent the formation of a chemical bond in a "scaffolded diatomic". Recently, we have investigated the solvent-induced bond formation in a true diatomic molecule: The ground-state recombination of I_2 , following photo-induced dissociation¹⁸. In this system, we observed the same behaviour as for $\text{Ir}_2(\text{dimen})_4^{2+}$: The coherence decay is much faster than vibrational cooling. However, since I_2 is bound in the ground state, the original GS distribution is very narrow, compared to amplitude of the motion following photo excitation, and it is therefore not a source of decoherence. The cause of I_2 decoherence is still statistical: It is due to the direct interaction with its solvent cage, which lacks in both the order and rigidity compared to the molecular scaffold of the bi-metallic complexes.

Conclusions

In conclusion, this work demonstrates that the implementation using GPAW for the QM description in this multiscale method is capable of producing out-of-equilibrium molecular dynamics with statistical quantities that make it possible to obtain information on the mean dynamics of populations. The experimental Ir-Ir dynamics is reproduced. We observed a, to our knowledge, not previously discovered breathing mode that stays coherent for longer, and helps explain how the energy is transferred to the solvent. We note that the role of the solvent can actually be to *maintain* the coherence, through decoupling of the internal degrees of freedom in the molecule. By looking at the shapes of the individual trajectories, we have argued that the major electrostatic solute-solvent interaction occurs through the ligands for this complex, and that the IVR here is delayed, since the metals need to contract first. At last, the breathing occurs in the ligands, and perpendicular to the pinch axis. As such, the (rigidity of the) ligands play an important role in the complex, both through defining the width of the GS ensemble, which affects the ES population coherence, and as mediators of the solvent interaction.

Acknowledgement

The authors thank Robert W. Hartsock, Kelly Gaffney, & the Center for Molecular Movies for discussion and feedback.

This work was funded by the Lundbeck Foundation.

Supporting Information Available

This material is available free of charge via the Internet at <http://pubs.acs.org/>.

References

- (1) Mann, K. R.; Gordon, J. G. I.; Gray, H. B. Characterization of oligomers of tetrakis(phenyl isocyanide)rhodium(I) in acetonitrile solution. *Journal of the American Chemical Society* **1975**, *97*, 3553–3555.
- (2) Roundhill, M. D.; Gray, H. B.; Che, C. Pyrophosphito-bridged diplatinum chemistry. *Accounts of Chemical Research* **1989**, *22*, 55–61.
- (3) Hartsock, R. W.; Zhang, W.; Hill, M. G.; Sabat, B.; Gaffney, K. J. Characterizing the deformational isomers of bimetallic $\text{Ir}_2(\text{dimen})_4^{2+}$ (dimen = 1,8-diisocyno-*p*-menthane) with vibrational wavepacket dynamics. *Journal of Physical Chemistry A* **2011**, *115*, 2920.
- (4) Mann, K. R.; Lewis, N. S.; Miskowski, V. M.; Erwin, D. K.; Hammond, G. S.; Gray, H. B. Solar-energy storage - production of hydrogen by 546-nm irradiation of a dinuclear Rhodium(ii) complex in acidic aqueous-solution. *Journal of the American Chemical Society* **1977**, *99*, 5525–5526.
- (5) Lewis, N. S.; Mann, K. R.; Gordon, J. G.; Gray, H. B. Oligomerization and 2-center oxidative addition-reactions of a dimeric Rhodium(II) complex. *Journal of the American Chemical Society* **1976**, *98*, 7461–7463.
- (6) Exstrom, C. L.; Britton, D.; Mann, K. R. Structures of $[\text{M}_2(\text{dimen})_4](\text{Y})_2$ (M = Rh, Ir; dimen = 1,8-Diisocyanomenthane; Y = PF₆, Tetrakis[3,5-bis(trifluoromethyl)phenyl]borate, B(C₆H₅)₄) crystals featuring an exceptionally wide range of metal-metal distances and dihedral twist angles. *Inorganic Chemistry* **1996**, *35*, 549–550.
- (7) Harvey, P. D.; Murtaza, Z. Properties of Pd(i)-Pd(i) Bonds - Theoretical and Spectroscopic Study of Pd₂(dmb)_{2x2} Complexes (Dmb = 1,8-Diisocyno-P-Menthane, X = Cl,br). *Inorganic chemistry* **1993**, *32*, 4721–4729.

- (8) Miskowski, V. M.; Rice, S. F.; Gray, H. B. Spectroscopy and Photophysics of $\text{Rh}_2(\text{dimen})_4^{2+}$ (dimen = 1,8-Diisocyanomenthane). Exceptional Metal-Metal Bond Shortening in the Lowest Electronic Excited States. *Inorganic Chemistry* **1994**, *33*, 2799–2807.
- (9) Coppens, P.; Gerlits, O.; Vorontsov, I. I.; Kovalevsky, A.; Chen, Y.; Graber, T.; Gem-bicky, M.; Novozhilova, I. A very large Rh-Rh bond shortening on excitation of the $[\text{Rh}_2(1,8\text{-diisocyano-}p\text{-mentane})_4]^{2+}$ ion by time-resolved synchrotron X-ray diffraction. *Chemical Communications* **2004**, *19*, 2144–2145.
- (10) Haldrup, K.; Harlang, T.; Christensen, M.; Dohn, A.; van Driel, T. B.; Kjær, K. S.; Harrit, N.; Vibenholt, J.; Guerin, L.; Wulff, M. et al. Bond shortening (1.4 Å) in the singlet and triplet excited states of $[\text{Ir}_2(\text{dimen})_4]^{2+}$ in solution determined by time-resolved x-ray scattering. *Inorganic Chemistry* **2011**, *50*, 9329.
- (11) Hunter, B. M.; Villahermosa, R. M.; Exstrom, C. L.; Hill, M. G.; Mann, K. R.; Gray, H. B. M-M Bond-stretching energy landscapes for $\text{M}_2(\text{dimen})_4^{2+}$ (M = Rh, Ir; dimen = 1,8-Diisocyanomenthane) complexes. *Inorganic Chemistry* **2012**, *51*, 6898–6905.
- (12) Jónsson, E. O.; Dohn, A. O.; Ulstrup, J.; Thygesen, K. S.; Jacobsen, K. W. An efficient QMMM scheme to explore electron transfer reactions in solution. *to be submitted* **2014**,
- (13) Bahn, S. R.; Jacobsen, K. W. An object-oriented scripting interface to a legacy electronic structure code. *Computing in Science & Engineering* **2002**, *4*, 55.
- (14) Mortensen, J. J.; Hansen, L. B.; Jacobsen, K. W. Real-space grid implementation of the projector augmented wave method. *Physical Review B* **2005**, *71*, 035109.
- (15) Perdew, J. P.; Burke, K.; Ernzerhof, M. Generalized gradient approximation made simple. *Phys. Rev. Lett.* **1996**, *77*, 3865–3868.

- (16) van der Veen, R. M.; Cannizzo, A.; van Mourik, F.; Vlcek, A. J.; Chergui, M. Vibrational relaxation and intersystem crossing of binuclear metal complexes in solution. *Journal of the American Chemical Society* **2011**, *113*, 305.
- (17) Stiegman, A. E.; Rice, S. F.; Gray, H. B.; Miskowski, V. M. Electronic spectroscopy of d⁸-d⁸ diplatinum complexes. ¹A_{2u}(dσ* → pσ), ³E_u(d_{xz}, d_{yz} → pσ), and ^{3,1}B_{2u}(dσ* → d_{x²-y²) excited states of Pt₂(P₂O₅H₂)₂⁴⁻. *Inorganic Chemistry* **1987**, *26*, 1112.}
- (18) lee, J. H.; Wulff, M.; Bratos, S.; Petersen, J.; Guerin, L.; Leicknam, J. C.; Cammarata, M.; Kong, Q.; Kim, J.; Møller, K. B. et al. Filming the birth of molecules and accompanying solvent rearrangement. *Journal of the American Chemical Society* **2013**, *135*, 3255–3261.

Direct dynamics studies of a binuclear metal complex in solution: The interplay between vibrational relaxation, coherence, and solvent effects. Supporting Info

Asmus Ougaard Dohn,^{*,†} Elvar Örn Jónsson,[‡] Kasper Skov Kjær,[‡] Tim Brandt van Driel,[‡] Martin Meedom Nielsen,[‡] Karsten Wedel Jacobsen,[‡] Niels Engholm Henriksen,[†] and Klaus Braagaard Møller[†]

Department of Chemistry, Technical University of Denmark, Building 207, 2800 Kgs. Lyngby, Denmark, and Department of Physics, Technical University of Denmark, Building 307 2800 Kgs. Lyngby, Denmark

E-mail: asod@kemi.dtu.dk

^{*}To whom correspondence should be addressed

[†]DTU Chemistry

[‡]DTU Physics

Computational Details

The QM/MM MD simulations were made using the QM/MM Scheme presented in¹, which interfaces the two regions through the total energy of the system:

$$E_{\text{tot}} = E_{\text{QM}} + E_{\text{MM}} + E_{\text{QM/MM}} \quad (1)$$

where the three terms represent the energy of the QM subsystem, the MM subsystem and their interaction energy, respectively. The interaction energy consists of a Coulomb term between the electronic density and the classical point charges, a Coulomb term between the nuclei in the QM subsystem and the MM point charges, and a Lennard-Jones (LJ) term:

$$E_{\text{QM/MM}} = \sum_i^{N_{\text{MM}}} q_i \int \frac{n(\mathbf{r})}{|\mathbf{r} - \mathbf{R}_i|} d\mathbf{r} + \sum_i^{N_{\text{MM}}} \sum_{\alpha}^{N_{\text{QM}}} \frac{q_i Z_{\alpha}}{|\mathbf{R}_{\alpha} - \mathbf{R}_i|} + E_{\text{LJ}} \quad (2)$$

$$E_{\text{LJ}} = \sum_i^{N_{\text{MM}}} \sum_{\alpha}^{N_{\text{QM}}} 4\epsilon_{i\alpha} \left[\left(\frac{\sigma_{i\alpha}}{|\mathbf{R}_{\alpha} - \mathbf{R}_i|} \right)^{12} - \left(\frac{\sigma_{i\alpha}}{|\mathbf{R}_{\alpha} - \mathbf{R}_i|} \right)^6 \right] \quad (3)$$

The LJ parameters are combined using the Waldman-Hagler rule.²

The first term in eqn. 1 is evaluated with density functional theory (DFT), using the grid-based projector augmented wave method, implemented in the GPAW package,³ which is modified so that the total effective potential also contains a term from the MM subsystem. The calculations were performed with a localised atomic orbital basis in combination with the real space grid, allowing for high parallelisation as well as fast diagonalization of the principal matrices.

Preliminary Tests

Preliminary calculations showed that a simulation box with 4 Å of vacuum padding in each dimension was enough to fully eliminate effects from truncating the wave functions, so the cell size for each simulation (both GS and ES) was chosen thusly. Test geometry

calculations were performed in vacuum, and the results are shown in fig. 1. The max Ir-Ir

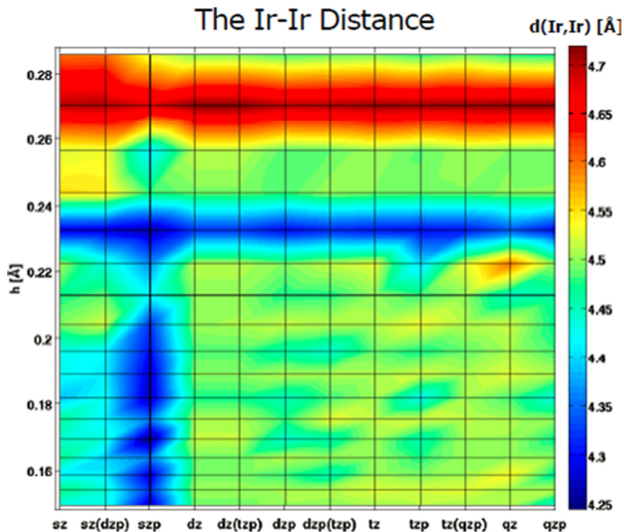


Figure 1: Convergence of the main structural parameter of the complex - the Ir-Ir distance - with respect to the real space grid spacing h , and size of basis set. A stable value for the distance is maintained when employing values of $h < 0.22 \text{ \AA}$ with basis sets of at least double-zeta size. The convergence criteria for each individual relaxation was a maximum force of $0.05 \text{ eV} / \text{ \AA}$ on any of the atoms in the system.

distance difference in the grid spacing region $0.15 \leq h \leq 0.21$ is less than 3.5 % of the largest distance, so instead of fixing the grid spacing to a definite value, it was possible to speed up the simulation even further by keeping the number of grid points to values divisible by eight, i.e. (112,120,112) for the (x,y,z) dimensions. Since the overall size of the molecule varies for each of the initial GS configurations used in the the ES simulations, so does the QM cell, resulting in grid spacings $0.1571 \leq h \leq 0.1931$, well within the converged region shown in fig. 1. The basis set used was of tzp quality for Ir and dzp for the rest of the molecule. The chosen PBE vacuum description overshoots the Ir-Ir distance (as does the mean QM/MM value), when compared to the experimental value of the solvated complex:⁴ 4.3 \AA . Crystalline values range from 3.601 \AA to 4.414 \AA , depending on the type of counter ion.⁵

The Acetonitrile solvent

Since the predominantly used solvent for $\text{Ir}_2(\text{dimen})_4^{2+}$ is Acetonitrile (ACN), a classical, rigid, 3-point interaction potential was adapted from Guardia *et al.*⁶ A simulation box of $28 \times 28.5 \times 31.5 \text{ \AA}$ was filled with 290 ACN molecules and thermalized. An MM production run of 0.5 ns was used to obtain radial distribution functions (RDFs). In order to also confirm a proper QM/MM interfacing, RDFs between a single QM ACN and the remaining MM ACNs were produced, and compared to RDFs obtained only using MM MD. Parallel QM/MM runs with a single QM ACN were branched off the production MM trajectory, interspaced by 500 fs, to avoid any correlation between the new trajectories (see the velocity autocorrelation function inset on fig. 2). A Langevin-type thermostat was used in both the MM and QM/MM runs, with a friction coefficient of 0.05 and 2 fs timesteps. The hydrogens on the QM were constrained using the RATTLE scheme.⁷ Each QM/MM trajectory was thermalized again, before sampling the RDFs. A total of 0.5 ns and 0.25 ns of dynamics were sampled for the MM and QM/MM systems, respectively. There is generally a good agreement between the various descriptions. The literature RDFs⁶ have been produced in the NPT ensemble, which might be the cause of some of the small differences. Furthermore, the electronic structure description used to create the force field is not the same as the one used in the QM/MM simulations, and the force field is not optimized to work in a QM/MM framework.

Further ES population analysis

In principle, an instantaneous excitation corresponds to an infinite bandwidth. However, a more realistic representation of an experiment can be obtained by including an effective, finite bandwidth⁸. This can be included by estimating the effective bandwidth of our range of ES simulations in fig. 3, and compare the pinch oscillation from different, relevant subsets with similar sampling statistics of the entire ES population in fig. 4, to elucidate how this affects the coherence lifetime.

The simplest way to approximate the excitation energy is simply to subtract a single point

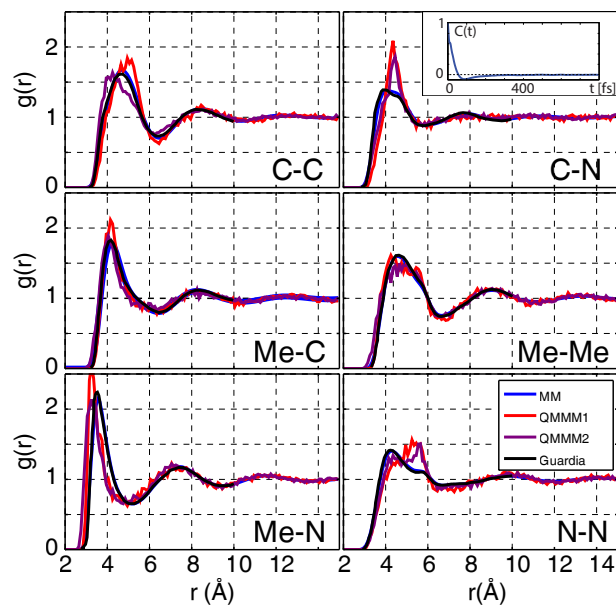


Figure 2: Radial distribution functions (RDFs) of the 6 intermolecular distances of ACN. The RDFs are calculated every 500th fs in trajectories of 0.5 ns and 0.25 ns for the MM and QM/MM systems, respectively. The QM/MM systems are comprised of a single QM ACN in a bath of MM ACN. The QM/MM1 systems are made using methyl-group vdW parameters for the middle Carbon, while QM/MM2 uses aliphatic parameters. There is overall a good agreement between the various description.

energy calculation of the system in T_1 from a single point energy calculation in the S_0 . This is of course a very rough approximation within the chosen theoretical framework. Since the T_1 surface is believed to have a similar shape to the S_1 , but lower in energy^{9,10}, utilizing ground state DFT on T_1 can be expected to introduce the error in the energy giving the largest deviation, and give too low excitation energies. The bandwidth, obtained from looking at the excitation energies of all the excitations, should not be as sensitive to this approximation, since the error introduced should be the same for each of the excitations. Since the 40 excitation configurations were specifically chosen to cover as much of the GS phase space as possible, an extrapolation to the excitation energies of each step in the entire GS trajectory is made, although no clear linear correlation between the Ir-Ir distance and excitation energy is observed. The complex is known to have an absorption maximum

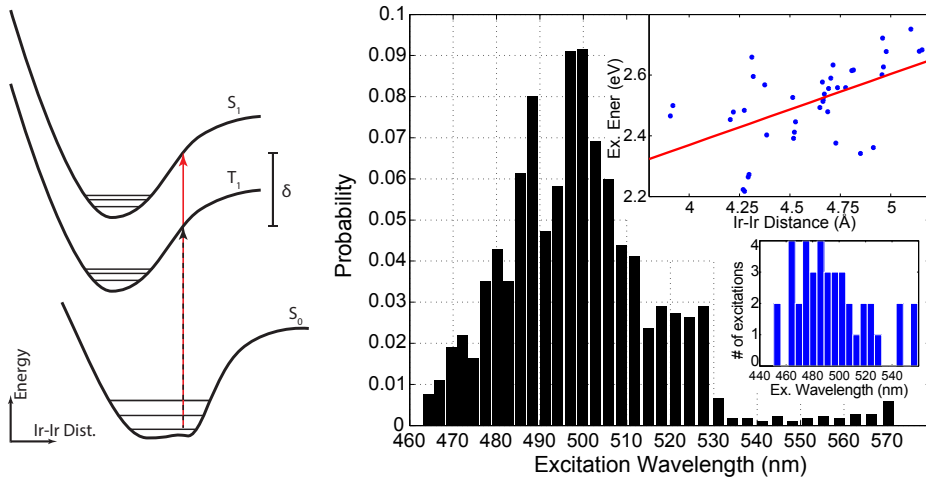


Figure 3: **Left:** Franck-Condon diagram sketching how the experimental excitation is approximated in the simulations, with δ being the error made from exciting to T_1 instead of S_1 . **Right:** Approximation of the effective bandwidth used in creating the excited state population. The excitation energy is approximated by subtracting the single point energy of each initial GS configuration from a single point calculation of its ES spin configuration counterpart. The lower inset shows histogram of these energies, converted to wavelengths, and how many times they appear in the ES population. This is extrapolated to the entire GS trajectory, under the (crude) assumption that the excitation energy is linearly dependent on (and only on) the Ir-Ir distance, shown in the top inset. This relation is then used for obtaining the results shown in the main figure.

assigned to the long and eclipsed conformer at 475 nm¹¹, so it is expected due to the lower

T_1 energy that the simulated excitation peak (fig. 3, left) is located at lower energies. The experimental bandwidth is 18.77 nm, and excitation wavelength is 477 nm¹¹. The total effective bandwidth of the ES production run simulations can be seen from the figure to be at least 100 nm, or 5 times the experimental bandwidth. Fig. 4 shows the Ir-Ir pinch in four

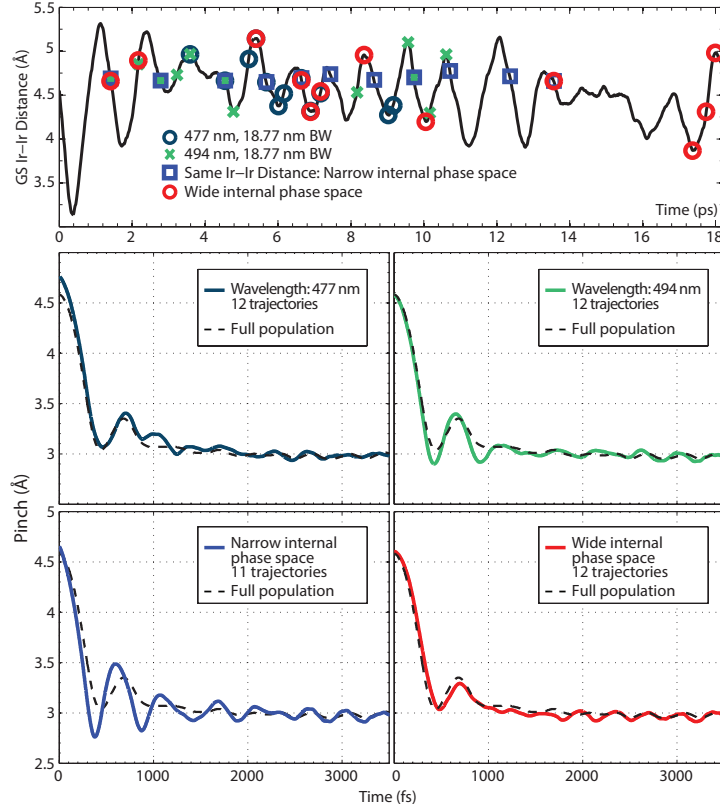


Figure 4: Splitting up the total ES population with respect to excitation energies, or by grouping initial configurations. The top two ES pinch graphs are made from selecting for ES trajectories with excitation energies assumed close to the experimental value and bandwidth. The bottom left subset is made from a narrow internal phase space of initial Ir-Ir distances. The last graph shows the dynamics of a wide phase space, but with the same statistics as the other three subsets.

subsets of the entire phase space of the ES population. The top two are subsets of excitations with energies corresponding to wavelengths of 477 nm and 494 nm, respectively. The first having the same value as in the experiment, and the second is lower in energy to account for the error made in simulating the excitation energies. The bottom left subset is chosen to have the most narrow internal phase space possible, with identical initial Ir-Ir distances,

but different solvent configurations. The last plot shows the pinch in a wide internal phase space, but with similar sampling statistics, allowing for comparison of the four subsets.

As demonstrated in the lower right graph in 4, it is possible to obtain the same coherence-decay time using 12 trajectories as 40, which again means that any changes in coherence time in the other subsets are not simply due to worse statistics. Concentrating on the 477 nm and 494 nm excitation, the coherent pinch amplitude is observed to decay slightly slower than for the full population. Thus, the effective bandwidth in the simulation has, to some extent, an influence on the resulting coherent motion. Therefore, the incoherence in the initial ensemble is the main factor for the coherence decay of the ES population. This result is underpinned by the lower left graph, where the very narrow internal phase space greatly increases the coherence lifetime. This result is not surprising, since the GS pinch oscillation has a similar amplitude as the ES pinch.

References

- (1) Jónsson, E. O.; Dohn, A. O.; Ulstrup, J.; Thygesen, K. S.; Jacobsen, K. W. An efficient QMMM scheme to explore electron transfer reactions in solution. *to be submitted* **2014**,
- (2) Waldman, M.; Hagler, A. New combining rules for rare gas van der waals parameters. *Journal of Computational Chemistry* **2004**, *14*, 1077.
- (3) Mortensen, J.; Hansen, L.; Jacobsen, K. W. Real-space grid implementation of the projector augmented wave method). *Physical Review B* **2005**, *71*, 035109.
- (4) Haldrup, K.; Harlang, T.; Christensen, M.; Dohn, A.; van Driel, T. B.; Kjær, K. S.; Harrit, N.; Vibenholt, J.; Guerin, L.; Wulff, M. et al. Bond shortening (1.4 Å) in the singlet and triplet excited states of $[\text{Ir}_2(\text{dimen})_4]^{2+}$ in solution determined by time-resolved x- ray scattering. *Inorganic Chemistry* **2011**, *50*, 9329.

- (5) Extrom, C. L.; Britton, D.; Mann, K. R. Structures of $[M_2(\text{dimen})_4](Y)_2$ (M = Rh, Ir; dimen = 1,8-diisocyanomenthane; Y = PF₆, Tetrakis[3,5-bis(trifluoromethyl)phenyl]borate, B(C₆H₅)₄) crystals featuring an exceptionally wide range of metal-metal distances and dihedral twist angles. *Inorganic Chemistry* **1996**, *35*, 549.
- (6) Guardia, E.; Pinzón, R.; Casulleras, J.; Orozco, M.; Luque, F. J. Comparison of different three-site interaction potentials for liquid acetonitrile. *Molecular Simulation* **2001**, *26*, 287.
- (7) Andersen, H. C. Rattle: A "velocity" version of the shake algorithm for molecular dynamics calculations. *Journal of Computational Physics* **1983**, *52*.
- (8) Petersen, J.; Henriksen, N. E.; Møller, K. B. Validity of the BersohnZewail model beyond justification. *Chemical Physics Letters* **2012**, *539-540*, 234–238.
- (9) van der Veen, R. M.; Cannizzo, A.; van Mourik, F.; Vlcek, A. J.; Chergui, M. Vibrational relaxation and intersystem crossing of binuclear metal complexes in solution. *Journal of the American Chemical Society* **2011**, *113*, 305.
- (10) Stiegman, A. E.; Rice, S. F.; Gray, H. B.; Miskowski, V. M. Electronic spectroscopy of d⁸-d⁸ diplatinum complexes. $^1A_{2u}(d\sigma^* \rightarrow p\sigma)$, $^3E_u(d_{xz}, d_{yz} \rightarrow p\sigma)$, and $^3,^1B_{2u}(d\sigma^* \rightarrow d_{x^2-y^2})$ excited states of Pt₂(P₂O₅H₂)₂⁴⁻. *Inorganic Chemistry* **1987**, *26*, 1112.
- (11) Hartsock, R. W.; Zhang, W.; Hill, M. G.; Sabat, B.; Gaffney, K. J. Characterizing the deformational isomers of bimetallic Ir₂(dimen)₄²⁺ (dimen= 1,8-diisocyno-*p*-menthane) with vibrational wavepacket dynamics. *Journal of Physical Chemistry A* **2011**, *115*, 2920.